

Multimodal Investigation of Neuronal Responses

Thesis submitted to the University of Nottingham
for the degree of Doctor of Philosophy

Daisie Olivia Pakenham, MSci

March 2021

Contents

ABSTRACT	I
ACKNOWLEDGMENTS	II
1 INTRODUCTION	
1.1 NEUROIMAGING.....	1
1.2 AIMS OF THIS THESIS	2
1.3 THESIS OVERVIEW.....	4
1.4 REFERENCES.....	6
2 MAGNETOENCEPHALOGRAPHY	
2.1 INTRODUCTION	7
2.2 ORIGIN OF MEG SIGNALS	8
2.2.1 <i>Neurons</i>	8
2.2.2 <i>Action Potentials</i>	10
2.2.3 <i>Postsynaptic Potentials</i>	11
2.2.4 <i>Neuronal Origin of MEG</i>	12
2.2.5 <i>Neural Oscillations</i>	13
2.3 DETECTION OF MEG SIGNALS	14
2.3.1 <i>Superconductivity</i>	15
2.3.2 <i>Josephson Junctions</i>	15
2.3.3 <i>DC SQUID</i>	17
2.3.4 <i>Noise Reduction</i>	18
2.3.5 <i>MEG System</i>	20
2.3.6 <i>Source Reconstruction</i>	21
2.3.7 <i>The Forward Problem</i>	22
2.3.8 <i>Multiple Sphere Model</i>	24
2.3.9 <i>The Inverse Problem</i>	25
2.3.10 <i>Beamforming</i>	27
2.3.11 <i>Hilbert Transform</i>	29
2.4 REFERENCES.....	31
3 MAGNETIC RESONANCE IMAGING	
3.1 NUCLEAR MAGNETIC RESONANCE	33
3.1.1 <i>Precession</i>	34
3.1.2 <i>Relaxation</i>	35
3.2 MAGNETIC RESONANCE IMAGING (MRI)	39
3.2.1 <i>Magnetic Field Gradients</i>	40
3.3 MRI SYSTEM.....	42
3.4 IMAGING TECHNIQUES.....	43
3.4.1 <i>2D Gradient Echo Planar Imaging</i>	43
3.4.2 <i>3D Gradient Echo Planar Imaging</i>	44
3.4.3 <i>Accelerated Imaging</i>	46

3.5	STRUCTURAL IMAGING	48
3.5.1	<i>Magnetisation Prepared Rapid Gradient Echo (MPRAGE)</i>	48
3.5.2	<i>Phase Sensitive Inversion Recovery (PSIR)</i>	49
3.5.3	<i>Fast Low Angle Shot (FLASH)</i>	50
3.6	FUNCTIONAL MAGNETIC RESONANCE IMAGING (fMRI)	51
3.6.1	<i>Origin of fMRI Signal</i>	51
3.6.2	<i>Detection of the fMRI Response</i>	54
3.7	REFERENCES	57
4	POST-STIMULUS OSCILLATORY MEG RESPONSES	
4.1	ABSTRACT	60
4.2	INTRODUCTION	61
4.3	METHODS	66
4.3.1	<i>Subjects</i>	66
4.3.2	<i>Motor Paradigm</i>	66
4.3.3	<i>Data Acquisition</i>	68
4.3.4	<i>Pre-processing</i>	68
4.3.5	<i>Post-processing</i>	69
4.4	RESULTS	73
4.4.1	<i>Grip-force and EMG data</i>	73
4.4.2	<i>Beta Responses</i>	74
4.4.3	<i>Alpha Responses</i>	78
4.4.4	<i>Gamma Responses</i>	80
4.5	DISCUSSION	82
4.6	CONCLUSION	86
4.7	REFERENCES	88
4.8	APPENDICES	92
	<i>A. Investigating Baseline</i>	92
	<i>B. Visual Alpha</i>	95
5	EXPLORING TRANSIENT NETWORKS IN TASK-BASED MEG DATA	
5.1	ABSTRACT	97
5.2	INTRODUCTION	99
5.2.1	<i>Aims and Objectives</i>	102
5.3	BACKGROUND THEORY	103
5.3.1	<i>Functional Connectivity</i>	103
5.3.2	<i>Dynamic Functional Connectivity</i>	103
5.3.3	<i>Amplitude Envelope Correlation</i>	104
5.3.4	<i>Leakage</i>	105
5.3.5	<i>HMM Theory</i>	106
5.4	METHODS	110
5.4.1	<i>Data Acquisition</i>	110
5.4.2	<i>Analysis</i>	110
5.5	RESULTS	114
5.5.1	<i>Amplitude Envelope Correlation</i>	114
5.5.2	<i>Hidden Markov Model</i>	118
5.6	DISCUSSION	124

5.7	CONCLUSION	128
5.8	REFERENCES	129
6	INVESTIGATING FMRI POST-STIMULUS RESPONSES	
6.1	ABSTRACT	134
6.2	INTRODUCTION	135
6.2.1	<i>Mechanisms of the BOLD PSU</i>	135
6.2.2	<i>Stimulus Duration in fMRI</i>	139
6.2.3	<i>Aim</i>	141
6.3	OPTIMISATION OF THE VASO-ASL-BOLD SEQUENCE	142
6.3.1	<i>Vascular Space Occupancy (VASO)</i>	142
6.3.2	<i>Arterial Spin Labelling (ASL)</i>	143
6.3.3	<i>Combining BOLD, VASO and ASL</i>	144
6.3.4	<i>Methods</i>	148
6.3.5	<i>Optimisation of the VASO Scheme Using Non-task Data</i>	149
6.3.6	<i>Task Data</i>	155
6.4	ASSESSING THE BOLD PSU USING COMBINED VASO-ASL-BOLD	160
6.4.1	<i>Paradigm</i>	160
6.4.2	<i>Data Acquisition</i>	160
6.4.3	<i>Analysis</i>	162
6.5	RESULTS	171
6.5.1	<i>EMG</i>	171
6.5.2	<i>fMRI Responses</i>	173
6.5.3	<i>Using MEG Regressors in the GLM</i>	179
6.5.4	<i>CMRO₂</i>	185
6.6	DISCUSSION	187
6.7	REFERENCES	196
6.8	APPENDICES	203
A.	<i>Data Quality Assessment</i>	203
B.	<i>Simulating BOLD, VASO and aCBV Time Courses</i>	206
C.	<i>CMRO₂</i>	210
7	USING FMRI TO MAP TOUCH IN FOCAL HAND DYSTONIA	
7.1	ABSTRACT	211
7.2	INTRODUCTION	212
7.2.1	<i>Aims and Hypotheses</i>	218
7.3	METHODS	219
7.3.1	<i>Behavioural Measures</i>	219
7.3.2	<i>fMRI</i>	222
7.4	RESULTS	228
7.4.1	<i>Behavioural Measures</i>	228
7.4.2	<i>fMRI</i>	231
7.5	DISCUSSION	246
7.5.1	<i>Behavioural Measures</i>	246
7.5.2	<i>fMRI</i>	247
7.6	CONCLUSION	251
7.7	REFERENCES	252

7.8	APPENDICES	256
	A. <i>Travelling wave paradigm</i>	256
	B. <i>Handedness questionnaire</i>	258
	C. <i>Dice coefficients</i>	258
8	CONCLUSION	262
8.1	SUMMARY	262
8.2	THE FUTURE	264
8.3	REFERENCES	267

Abstract

This thesis describes an investigation of neuronal responses with both magnetoencephalography (MEG) and functional magnetic resonance imaging (fMRI). MEG and fMRI are widely used in neuroscience. However, aspects of the MEG and fMRI signal are still not well understood, particularly post-stimulus responses – responses which occur after a stimulus has ended. Post-stimulus responses have been shown to correlate with various illnesses and as a result, MEG and fMRI have yet to reach their full potential clinically.

By developing carefully controlled experiments, MEG is used in this thesis to characterise post-stimulus responses to a grip-force task. The results showed that the beta-band post-stimulus response (post-movement beta rebound, PMBR) is modulated by task duration. Functional network analysis, using amplitude envelope correlation and a hidden Markov model, showed that the PMBR re-establishes networks after breaking down during a task, suggesting the PMBR is related to functional connectivity. The results of this thesis provide new information about the nature of the PMBR, demonstrating that it can be systematically controlled by task parameters and provides insight into its generation. It is hoped this research will contribute to a deeper understanding of the PMBR and provide a step forward for its use clinically.

In fMRI, the origin of the post-stimulus response is also poorly understood. To investigate fMRI post-stimulus responses, an MR pulse sequence was developed and optimised to measure blood flow, volume and oxygenation changes simultaneously at 7 T. This was implemented with the grip-force task, allowing direct comparison between MEG and fMRI. This study provides new insights into the fMRI post-stimulus undershoot which warrant further investigation. Understanding the link between fMRI and MEG signals will help further understanding of both modalities and how they relate to neuronal activity.

Finally, the applications of fMRI were explored by comparing fMRI responses in patients with focal hand dystonia (FHD) with healthy controls. 7 T fMRI was used to map cortical fingertip representations and measures were developed to compare overlap of digit representations between patients and healthy controls. This project provided an important opportunity to advance the understanding of FHD and was the first study to use fMRI to explore the effects of treatment on patients with FHD.

Acknowledgments

Writing this thesis would have been impossible without my wonderful supervisors. I would first like to thank Karen Mullinger, who has been the best supervisor I ever could have asked for. Thank you for all your help, guidance and making the time for me over these past four years. Thank you to Sue Francis for all your help with fMRI, particularly with the VASO and TOUCHMAP sections. Thank you to Matt Brookes for all your MEG-wisdom, but especially thank you for all the pints you've bought me throughout my PhD! I am incredibly grateful for all the work they have put in to help this thesis be a success.

I must also credit the following people who have helped me with all aspects of science along the way: George O'Neill, for always being there (to this day) whenever I had an issue with the MEG, Lauren Gascoyne, for answering all my questions whenever I popped into your office, Lucrezia Liuzzi for help with the AEC code, Ellie Wilson for being my MEG problem-solver in the office, Andrew Quinn and Mark Woolrich for helping with the HMM, Michael Asghar for all your help in collecting and analysing the TOUCHMAP data and answering all my endless questions, Rosa Sanchez Panchuelo for help with the TOUCHMAP project and VASO fMRI, and anyone else I have missed! And of course I would like to thank all volunteers who took part in these studies.

To the people of the SPMIC, past and present, thank you for making the SPMIC feel like home and making this PhD such an enjoyable experience. Special thanks to Andrew, George and Laura (and the JA pub quiz) for getting me through the darkest times. Thank you to Ben for all our trips to the tea room. Thank you to the whole MEG team for all our amazing conference trips. Thanks to all members of the lunch time quiz for giving me something to look forward to everyday!

Finally, thank you to my family for your love and support throughout these many years of education. Thank you to Gared, without whom I'm not sure I ever would have finished writing this thing. I should also thank my pet Bobby, for your constant company when working from home!

CHAPTER 1

1 Introduction

The human brain is one of the most complex things in the universe. Humanity has tried to understand the brain for millennia, yet how it functions still largely remains elusive. It is only recently that the tools to study the structure and function of the brain *in vivo* have been available.

Whilst the quest to understand the brain for knowledge's sake is an important one, it is the real-world applications that make studying the brain truly worthwhile. Perhaps, if it is possible to image the brain when it is well functioning, it will be possible to understand what goes wrong in the brain in disease, neurological disorders and mental illness. In particular, mental illness is often dismissed as it is seen as something only happening in your head. Yet, because something is happening in your head does not mean it is not real. With modern neuroimaging techniques, it is possible to image neural activity and examine changes in this neural activity in psychiatric disorders.

Beyond understanding the brain, it is conceivable that better neuroimaging techniques will not only lead to diagnosis of conditions, and earlier treatment, but could be used to tailor treatment to an individual and monitor treatment throughout – so called precision medicine. Medicine is usually thought of in terms of being applied to a population, but with increasing data on individual patients, medicine can be tailored to the individual with the aim of improving outcomes and reduce side effects.

1.1 Neuroimaging

Neuroscience has been trying to understand the function of the brain for a long time, but it is difficult to investigate neural activity non-invasively. Electrical activity can be measured from the brain by placing electrodes directly on the surface of the brain, or into the brain, but this invasiveness limits its investigational uses. In 1924, Hans Berger first recorded the electrical activity from the brain non-invasively, which he termed the electroencephalogram (EEG) (Berger, 1929). Berger demonstrated that brain activity can be described by waves, such as the alpha rhythm (8 – 12 Hz). It wasn't until much later, due to technological advances in quantum mechanics in superconductors, that magnetoencephalography (MEG), the magnetic counterpart to EEG, was able to be

measured in a practical way (Cohen, 1968). Consequently, whole-head MEG scanners have only been available since the 2000s.

Other imaging modalities, namely x-ray computed tomography (CT), positron emission tomography (PET) and magnetic resonance imaging (MRI) came about in the late 20th century. MRI, unlike CT and PET, offers a means to measure anatomical structure without the use of ionising radiation. Moreover, with the ability to rapidly acquire images, functional MRI (fMRI) was developed in the early nineties to measure the dynamics of brain function, using blood oxygenation as contrast.

Despite these advances in neuroimaging, how the brain functions is still not fully understood, in part due to a lack of understanding of the precise origins of the signals measured by the neuroimaging techniques described. Understanding the brain's function is vital to better understand disease and therefore it is necessary to characterise brain responses. To do this, this thesis uses multimodal techniques (MEG and fMRI) to investigate neuronal responses. MEG measures oscillatory activity directly related to neuronal activity, with high temporal resolution, yet its spatial resolution is hindered by the ill-posed inverse problem. fMRI, on the other hand, has excellent spatial resolution, which is improved with higher field strength, but poorer temporal resolution than MEG. Furthermore, these techniques provide insights into different aspects of brain activity: synchronous firing of neurons from MEG and changes in neuronal metabolic demands as well as physiological changes from fMRI. Therefore, if used in concert, multimodal imaging has the potential to gain greater insights into the true functioning of the brain.

1.2 Aims of This Thesis

This thesis firstly aims to characterise post-stimulus responses, significant changes from baseline in measured brain signal after the end of a stimulus, using both fMRI and MEG. On movement cessation, electrophysiological responses show an increase in amplitude above baseline - the post-movement beta rebound (PMBR). Numerous studies have highlighted the importance of the PMBR, showing how the PMBR is modulated in disease (for example, schizophrenia (Robson et al., 2016), autism (Honaga et al., 2010), stroke (Parkkonen et al., 2017), multiple sclerosis (Barratt et al., 2017) and motor neurone disease (Proudfoot et al., 2017)). For the PMBR to have clinical relevance, it must be fully characterised. It is still unknown how the PMBR modulates with task parameters which is essential to its characterisation. A great deal

of recent research into the PMBR has been performed, yet tasks favour short inter-stimulus-intervals to acquire many repeats, limiting their ability to fully assess the PMBR. This thesis uses a precisely controlled task with long baseline periods to investigate the PMBR.

A large amount of recent research has investigated functional connectivity in the brain. These tools can be used to explore the origins of the PMBR more closely. Most studies have investigated resting state networks, which are limited for studying the PMBR. In this thesis, the functional networks that are present throughout different task stages will be explored, using amplitude envelope correlation and a novel hidden Markov model. An understanding of how brain networks develop during a task will provide further insight into the functional relevance of brain activity during different phases of the task.

The direct relationship between the fMRI responses and neuronal activity is not understood. In particular, a significant component of the fMRI response, post-stimulus responses, have been largely overlooked. Post-stimulus fMRI responses are important as the post-stimulus undershoot (PSU) has been shown to have some neuronal origin and therefore functional relevance, distinct to the information occurring during the stimulus. A key question is what generates the post-stimulus undershoot – does it arise from vascular, metabolic, or neuronal effects? Large amounts of research have tried to answer this, with different measures, but to fully understand the PSU it is necessary to untangle what happens to blood oxygenation, oxygen metabolism, blood volume and blood flow for a task where the underlying neuronal activity is precisely characterised. In this thesis, the aim was to combine measures of cerebral blood volume, cerebral blood flow and blood oxygenation to measure what happens to the post-stimulus undershoot in the same motor task where the MEG response had been characterised and relate the responses measured across modalities.

Finally, the primary blood-oxygen-level-dependent (BOLD) fMRI response can play an important role in understanding neurological disorders. Focal hand dystonia (FHD) is of interest as it has been thought that FHD causes disturbances in the sensory representation of digits in the cortex. However, the research to date has used lower field strength and lower spatial resolution fMRI to investigate FHD. The specific objective of the work in this thesis was to use high spatial resolution fMRI at 7 T to generate maps of digit representation in individual FHD patients and healthy controls, as well as

exploring effects of Botox treatment. This study aims to develop analysis pipelines to optimise the investigation of digit representation, to facilitate research into FHD.

1.3 Thesis Overview

At the beginning of this thesis, the background of MEG and fMRI will be introduced. Chapter 2 describes the theory behind the origins and acquisition of the MEG signal. The neuronal origin of MEG signals is discussed, followed by the physics of superconducting quantum interference devices (SQUIDS) which are most commonly used to detect MEG signals. The analysis methods, used in the experimental work of this thesis, which enable MEG signals measured on the surface of the head to be localised inside the head are then described.

In Chapter 3, the theory behind fMRI is detailed, beginning with a description of the phenomenon of nuclear magnetic resonance. This is followed by the theory of MRI and how an image is generated. Techniques are introduced for fast imaging, including ways to speed up acquisition. Finally, the basics of BOLD fMRI are explained, including the origin of the BOLD signal and the general principles of how fMRI data are acquired and analysed.

Chapter 4, the first experimental chapter, describes the methods and results of a precisely developed grip-force task using MEG to image brain electrophysiology. The aim was to accurately characterise how task duration modulates beta responses. Chapter 5 extends this work, using the same data to further explore the nature of the PMBR using functional connectivity measures. Amplitude envelope correlation is used to investigate connectivity changes throughout a task. Exploiting the high temporal resolution of MEG, novel hidden Markov model analysis is used to investigate networks on a short timescale.

Chapter 6 takes advantage of multimodal imaging, employing the task used in the MEG experiments adapted for an fMRI setting. The aim of this chapter was to establish the origins of the post-stimulus BOLD response to this stimulus. A sequence was optimised to measure cerebral blood volume and flow as well as BOLD to aid interpretation of the origin of the BOLD post-stimulus response and modulation with the task. The aim is that this sequence will better uncover any underlying neural activity than standard BOLD fMRI alone, and aid interpretation of the contribution of the vascular and

neuronal origin to the post-stimulus response. The MEG and fMRI results will also be compared.

Chapter 7 explores the applications of BOLD fMRI to clinical populations. A high spatial resolution BOLD fMRI experiment is conducted on patients with focal hand dystonia with the aim to accurately map the representation of hand digits in the sensorimotor cortex of these patients compared with healthy controls. Analysis pipelines are developed for investigating overlap of digit representations, and the effects of Botox treatment on cortical organisation in patients with FHD is explored for the first time with fMRI.

Finally, Chapter 8 will present the conclusions of this thesis and will explore the potential for future research.

1.4 References

- Barratt, E. L., Tewarie, P. K., Clarke, M. A., Hall, E. L., Gowland, P. A., Morris, P. G., Francis, S. T., Evangelou, N., & Brookes, M. J. (2017). Abnormal Task Driven Neural Oscillations in Multiple Sclerosis: A Visuomotor MEG Study. *Human Brain Mapping, 38*(5), 2441-2453.
- Berger, H. (1929). *Archiv für Psychiatrie und Nervenkrankheiten, 87*(1), 527-570.
- Cohen, D. (1968). Magnetoencephalography: Evidence of Magnetic Fields Produced by Alpha-Rhythm Currents. *Science, 161*(3843), 784.
- Honaga, E., Ishii, R., Kurimoto, R., Canuet, L., Ikezawa, K., Takahashi, H., Nakahachi, T., Iwase, M., Mizuta, I., Yoshimine, T., & Takeda, M. (2010). Post-movement beta rebound abnormality as indicator of mirror neuron system dysfunction in autistic spectrum disorder: An MEG study. *Neuroscience Letters, 478*(3), 141-145.
- Parkkonen, E., Laaksonen, K., Piitulainen, H., Pekkola, J., Parkkonen, L., Tatlisumak, T., & Forss, N. (2017). Strength of ~20-Hz Rebound and Motor Recovery After Stroke. *Neurorehabilitation and Neural Repair, 31*(5), 475-486.
- Proudfoot, M., Rohenkohl, G., Quinn, A., Colclough, G. L., Wu, J., Talbot, K., Woolrich, M. W., Benatar, M., Nobre, A. C., & Turner, M. R. (2017). Altered Cortical Beta-Band Oscillations Reflect Motor System Degeneration in Amyotrophic Lateral Sclerosis. *Human Brain Mapping, 38*, 237-254.
- Robson, S. E., Brookes, M. J., Hall, E. L., Palaniyappan, L., Kumar, J., Skelton, M., Christodoulou, N. G., Qureshi, A., Jan, F., Katshu, M. Z., Liddle, E. B., Liddle, P. F., & Morris, P. G. (2016). Abnormal visuomotor processing in schizophrenia. *Neuroimage Clin, 12*, 869-878.

CHAPTER 2

2 Magnetoencephalography

2.1 Introduction

MEG (magnetoencephalography) is a non-invasive technique that measures the magnetic fields produced by the brain, induced by synchronised currents flowing through neurons. These magnetic fields are on the order of 10^{-14} to 10^{-13} T. Measuring such small fields is challenging, but possible with superconducting quantum interference devices (SQUIDs) (Cohen, 1968; Jaklevic et al., 1964). Currently, most systems use around 300 detectors, which surround the head in an array and can be used to measure neural oscillations and evoked potentials. MEG has excellent temporal resolution as it directly measures changes in neuronal activity.

Conducting a magnetoencephalography experiment firstly involves measuring the extra-cranial magnetic fields. This is performed inside a magnetically shielded room to reduce external noise. Once the measured magnetic fields are collected, the next aim is to reconstruct the sources inside the head which produced the measured magnetic fields to provide a measure of brain activity. The problem is, there are an infinite number of current distributions inside the head that could produce a single measured magnetic field distribution outside the head. This is known as the MEG inverse problem, to which there is no unique solution, but can be overcome with methods such as beamforming (Van Veen & Buckley, 1988; Van Veen et al., 1997).

The result is that MEG allows the study of electrophysiological activity on short time scales, non-invasively. This provides a method to directly study the synchronous firing of neurons within the brain and therefore allows the investigation of brain function. MEG is still fairly uncommon, with only 10 MEG systems in the UK (meguk.ac.uk), largely due to its high price. Yet, MEG has better spatial resolution than its electric counterpart (electroencephalography, EEG) and better temporal resolution than fMRI, and as such holds great promise. In recent years, technological developments have enabled a new type of MEG, namely OPM MEG (optically pumped magnetometer) which uses optical pumping of rubidium atoms to act as a magnetometer. This allows MEG to be performed at room temperature, reducing the costs needed for liquid helium

and allowing the sensors to be placed closer to the head, increasing SNR (Boto et al., 2018). OPM MEG could revolutionise the future of MEG, however, it is still in its infancy and being developed. Therefore, this thesis focuses on the use of SQUID MEG, which was used in experimental Chapters 4 and 5. The data collected in this thesis were recorded on a 275 SQUID CTF MEG system (CTF MEG International Services, Coquitlam, BC), at the Sir Peter Mansfield Imaging Centre, University of Nottingham. The basis of the methods by which to measure magnetic fields from the brain will be explained in this chapter.

2.2 Origin of MEG Signals

2.2.1 Neurons

MEG measures the magnetic fields from the brain, produced by the synchronous firing of millions of neurons. Neurons are electrically excitable nerve cells responsible for information processing within the brain by sending electrical impulses to other neurons. Figure 2.1 shows the schematic of a neuron. A neuron consists of the soma, the cell body which contains the nucleus of the cell; the dendrites, thread-like structures which branch from the soma to receive information from neighbouring cells; and the axon, a single fibre which extends from the soma to carry electrical signals to other neurons, which terminates in a nerve ending. The axon leaves the soma at the axon hillock and the axon may be surrounded by a myelin sheath which electrically insulates the axon to increase transmission speed. The nerve ending of the axon (the presynaptic nerve terminal) connects to another neuron which is referred to as the postsynaptic cell. The presynaptic nerve terminal and postsynaptic membrane make up the synapse, and are separated by a small area called the synaptic cleft, where neurotransmitters are released. The synapse allows electrical stimulation to travel from the nerve ending of one neuron to the dendrite, soma or axon of the next neuron and are the structures by which neurons communicate.

Figure 2.2 shows a diagram of the human brain. The brain is made up of grey matter on the outer surface of the brain, which largely consists of cell bodies and dendrites, and white matter, which is made up of axons. Neurons can take many forms but generally take two main shapes: stellate neurons which have dendrites that propagate in all directions from the soma, and pyramidal neurons which have dendrites oriented parallel to each other, and usually perpendicular to the cortical surface. The schematic in Figure

2.1 shows a pyramidal neuron. A drawing of a cross-section of the cortex is shown in Figure 2.3 showing the laminar structure of neurons in the cortex.

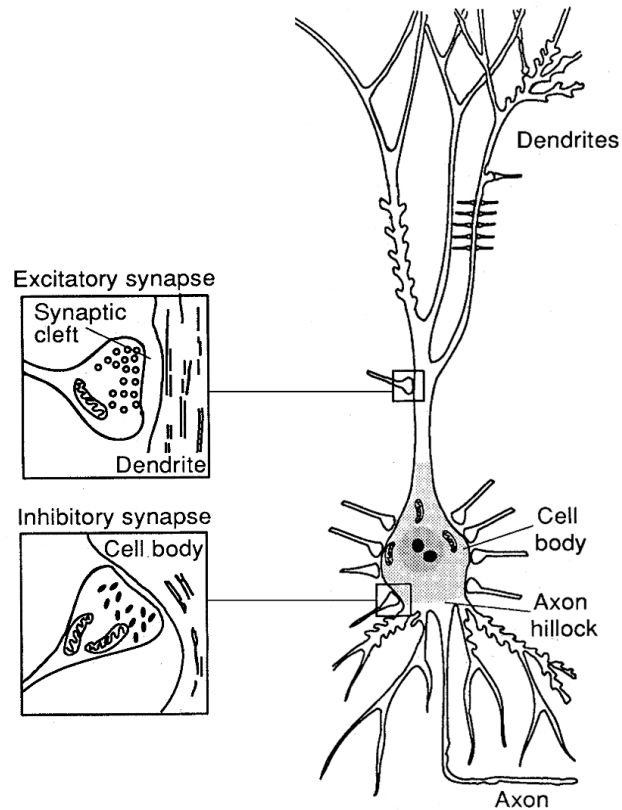


Figure 2.1. Schematic of a pyramidal neuron, where the dendrites are oriented parallel to each other. The cell body contains the nucleus of the cell and the axon extends from the axon hillock. Electrical signals are transmitted to other neurons via synapses, which can be excitatory or inhibitory. Adapted from Hämäläinen et al. (Hämäläinen et al., 1993).

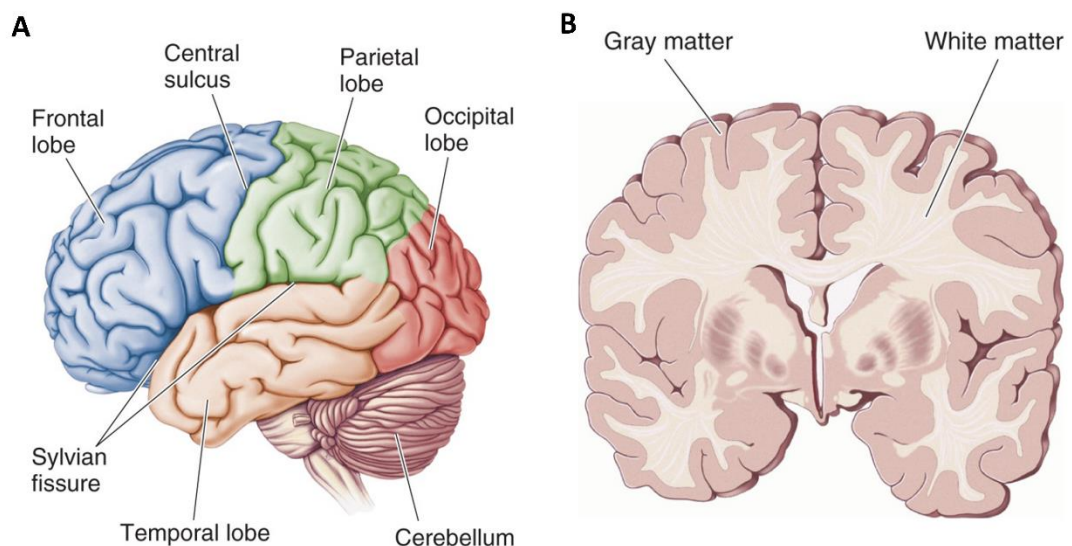


Figure 2.2. Anatomy of the human brain. (A) The cerebrum can be divided into four lobes: frontal, parietal, occipital and temporal. The central sulcus separates the frontal and parietal lobes. (B) A coronal slice through the brain showing the grey and white matter. Adapted from Bear et al. (Bear et al., 2020).

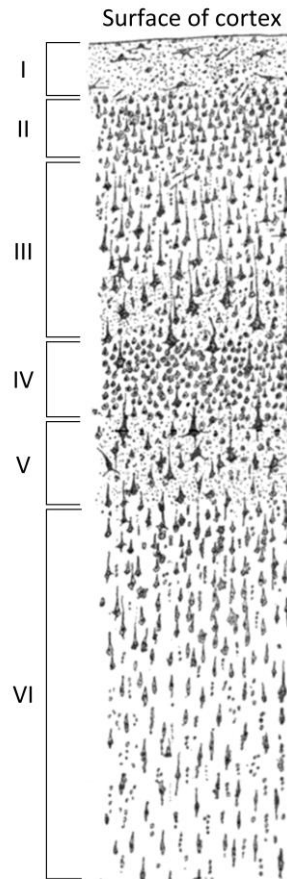


Figure 2.3. Drawing of the cell bodies of neurons in motor cortex, showing laminar structure of layers I-VI, where the surface of the cortex is at the top. Drawing from Ramón y Cajal (Ramón y Cajal, 1899).

2.2.2 Action Potentials

Neurons transmit information via electrical and chemical processes. Neurons are surrounded by a selectively permeable membrane, which changes depending on the electrical potential of the surrounding area. At equilibrium, there is a difference in intracellular and extracellular ion concentrations, resulting in a resting potential of -70 mV between the inside and outside of the cell. If the potential at the axon hillock (Figure 2.1) reaches a certain threshold of around -40 mV, the neuron fires and an action potential is initiated. At this threshold, the permeability of the membrane changes and ion channels are opened, allowing ion flow. This causes a large influx of Na^+ ions into the membrane, resulting in the cell becoming positively charged to approximately +40 mV. This rapid increase in potential is known as the action potential. The action potential triggers neighbouring membranes to change permeability and become depolarised, resulting in the propagation of the action potential along the length of the axon (Figure 2.4). After becoming depolarised, the membrane returns to equilibrium

via outflow of potassium ions causing the membrane to repolarise back to the resting potential. This is achieved by ion pumps which move ions against the concentration gradient. This depolarisation and repolarisation propagates along the axon. Because of this, action potentials can be modelled as two opposite current dipoles, forming a current quadrupole (Figure 2.4). Quadrupole magnetic fields fall off at a rate of $1/r^3$.

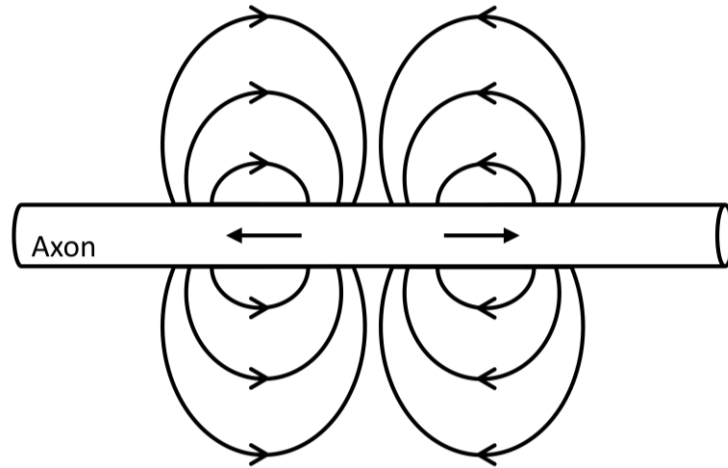


Figure 2.4. Diagram of an action potential propagating along an axon. Two opposing current dipoles (depolarisation and repolarisation) create a current quadrupole which propagates along the axon.

2.2.3 Postsynaptic Potentials

Once the action potential reaches the end of the axon of the presynaptic cell, it triggers the release of neurotransmitters into the synaptic cleft (Figure 2.1). The neurotransmitters travel across the synapse and bind to the dendrites or soma of the postsynaptic cell, opening ion channels at the postsynaptic cell. This allows ions to enter the cell causing a change in potential, which is known as the postsynaptic potential, as well as a current along the direction of the dendrite of the postsynaptic cell (Figure 2.5). Depending whether an excitatory or inhibitory synapse was stimulated, the neuron will either be depolarised (voltage increase, in the case of an excitatory synapse) or hyperpolarised (in the case of an inhibitory synapse, voltage more negative). If enough excitatory synapses are stimulated, the voltage will reach the -40 mV threshold and an action potential will be triggered. In the case of inhibitory synapses, the neuron becomes less likely to fire as the chance of reaching the -40 mV threshold for an action potential to be induced is reduced. The postsynaptic potential decays along the direction of the dendrite. After the postsynaptic potential, ion pumps re-establish equilibrium concentration by expelling ions against the concentration

gradient. This expulsion of ions creates an extracellular current (volume current) in the opposite direction to the postsynaptic current (Figure 2.5).

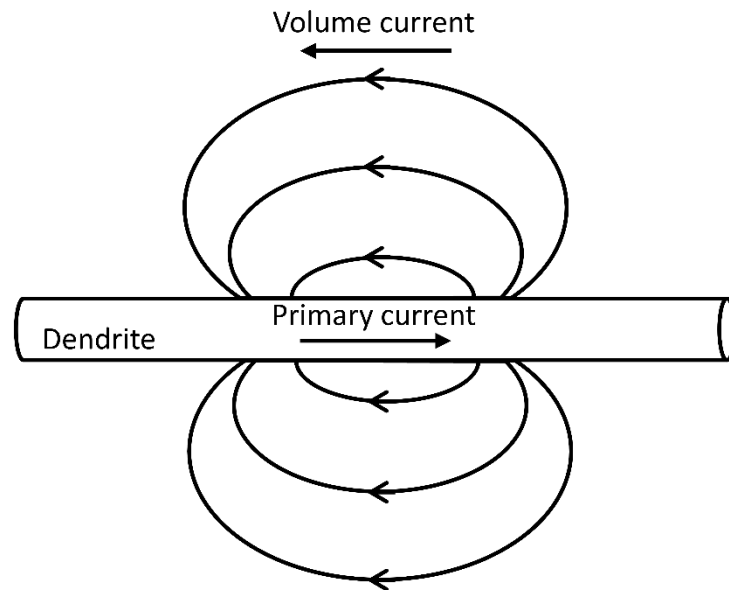


Figure 2.5. Diagram of a current dipole along a dendrite.

2.2.4 Neuronal Origin of MEG

From a distance, this postsynaptic current can be modelled as a dipole oriented along the dendrites. The magnetic field of a dipole falls off at a rate of $1/r^2$. Therefore, at a distance the dendritic current (postsynaptic potential) is larger than the axonal current (action potential). The action potentials also operate on a much smaller timescale than postsynaptic potentials: 2 ms compared to tens of milliseconds, respectively. Therefore, it is unlikely that action potentials make a significant contribution to the MEG signal; instead, MEG signals are thought to originate largely from dendritic currents in postsynaptic potentials (Hansen et al., 2010). Further, the symmetric nature of stellate neurons means that the current is distributed symmetrically, hence the electromagnetic fields produced by stellate neurons cancel out at short distances. In pyramidal neurons, with dendrites parallel to each other and usually perpendicular to the cortical surface, the electromagnetic fields do not cancel out meaning the signals are able to be detected outside the head. Therefore MEG signals are thought to originate from postsynaptic currents of pyramidal neurons.

The detected MEG signal does not originate from a single neuron, rather the synchronous firing of many thousands of neurons. If the average measured MEG signal is around 10 nAm, and the postsynaptic potential is considered to be a current dipole

on the order of 0.29 to 0.90 pAm, this would suggest around 50 000 neurons are needed to be synchronously firing to be detectable with MEG (Murakami & Okada, 2006).

2.2.5 Neural Oscillations

This synchronous firing of thousands of neurons results in rhythmic oscillations. Brain oscillations were first measured in humans by Berger (Berger, 1929), upon the discovery of alpha rhythm (8 – 13 Hz). Spontaneous oscillations have since been categorised into further observed frequency bands: delta (1 – 4 Hz), theta (4 – 8 Hz), beta (13 – 30 Hz) and gamma (30 – 200 Hz). Oscillations are crucial to brain function and the traditional view was that different frequency bands represent different functions, and mediate connections between brain regions. Jasper and Penfield (Jasper & Penfield, 1949) describe early work measuring electrocortical activity, showing different frequency bands associated with different brain regions and give the first description which attempts to characterise rhythms.

A more current theory has provided a model of how neural oscillations communicate across the brain. The idea is that for oscillations to communicate effectively with each other over a long range, the oscillations need to be coherent. This is termed communication by coherence and was proposed by Fries in 2005 (Fries, 2005). The excitability of a neuron is dependent on the phase of the oscillation, such that at the peak of the oscillation spiking occurs. The neuron is also more receptive to signals at the peak. Therefore, if two neuronal populations are in phase, and hence their peak occurs at the same time, they are more likely to be able to send information between each other and be functionally connected.

The amplitude of these oscillations can be modulated by a task. Figure 2.6 shows the time course of the envelope of activity in different frequency bands overlaid in a visual experiment. During the visual stimulus, there is a loss in power in the low frequency bands (alpha and beta) and an increase in power in high frequency bands (gamma). A rebound above baseline can also be observed in the alpha and beta bands, after the stimulus has ended. The decrease in average power of the oscillations in response to a stimulus is known as event related desynchronization (ERD) and the increase in average power of the oscillations is known as event related synchronization (ERS). These changes in neural oscillations have been observed numerous times – Pfurtscheller and Lopes da Silva (Pfurtscheller & Lopes da Silva, 1999) give a review on basic principles

of ERD and ERS in different frequency bands and how to quantify them; Neuper and Pfurtscheller 2001 (Neuper & Pfurtscheller, 2001) discuss features of ERD and ERS in alpha and beta; Pfurtscheller et al. 1996 (Pfurtscheller et al., 1996) gives a review of ERS in the alpha band in EEG; Cheyne 2013 (Cheyne, 2013) gives a more current review on application of MEG in sensorimotor cortex. These responses also occur in many regions of the brain. The precise functional role of ERD and ERS both during and after a stimulus period in different frequency bands is still not fully understood and is explored further in Chapters 4 and 5 where more detail on the beta band can be found.

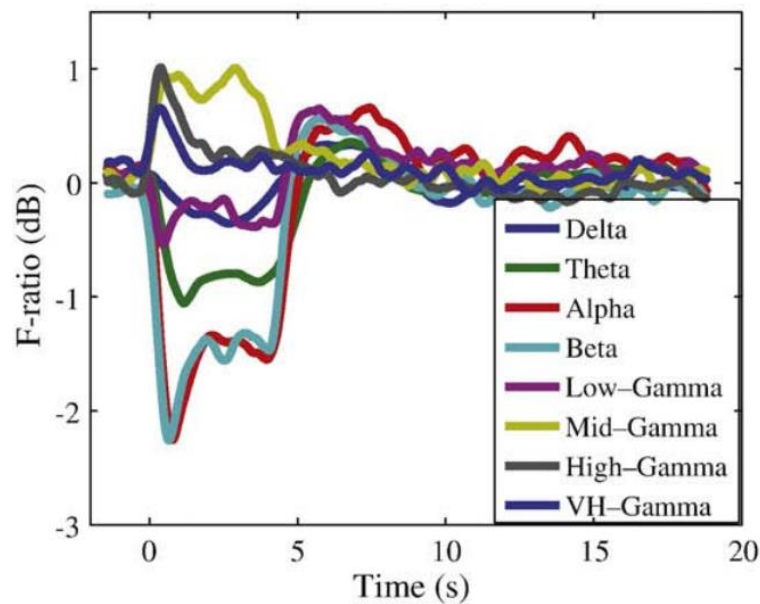


Figure 2.6. MEG virtual electrode time courses from the visual cortex for all frequency bands during a visual experiment. The visual stimulus occurred between 0 and 4 s. Taken from (Zumer et al., 2010).

2.3 Detection of MEG signals

Neuromagnetic fields are a billion times smaller than the Earth's magnetic field, making them difficult to detect. In fact, they are one hundred times smaller than the magnetic fields produced from the heart. In 1968, measurements of the brain's magnetic field were first performed (Cohen, 1968) using a single million-turn coil in a magnetically shielded room. Soon this was improved upon using a superconducting magnetometer (Cohen, 1972) with much higher sensitivity, called a superconducting quantum interference device (SQUID). Since 1972, technology has advanced to allow up to 300 SQUIDs to be used at once. SQUIDs are based on a quantum phenomenon of superconductivity which will be explained briefly in the following.

2.3.1 Superconductivity

When temperature is reduced below a certain transition temperature, metals can conduct electricity without any resistance. This is known as superconductivity. The electrons in the lattice of the metal become attracted to one another, and form pairs, known as Cooper pairs. A single electron is a Fermi particle, whereas a Cooper pair is a Bose particle. Therefore, the Fermi Exclusion principle which states that no two electrons can exist in the same state, no longer applies. Instead, as bosons, any number of electrons can exist in the same state. This is what happens in superconductivity: all the electrons are in the same state and can be described by the same wavefunction so there is no electrical resistance. As a consequence of no resistance, a current induced in a superconductor can persist without dissipating. However, this typically only applies at very low temperatures, as the thermal energy required to break the bond between the Cooper pairs is very small (on the order of 10^{-3} eV).

2.3.2 Josephson Junctions

An interesting phenomenon in superconductivity was discovered in 1962, when Josephson considered what would happen if two pieces of superconductor were connected by a weak, non-superconducting link. This is now known as a Josephson junction (Josephson, 1962). When two pieces of superconductor are joined by a weak link, such as an oxide barrier, which is sufficiently thin that the wavefunctions on either side couple, electrons in Cooper pairs can cross the gap in a quantum mechanical tunnelling process. If there were no gap between the superconductors, the wavefunctions of the electrons would be the same. If there were a large gap, the wavefunctions would be completely unrelated. Instead, the weak link causes the wavefunctions on either side of the gap to be coupled. Fundamentally, the tunnelling current I across the gap is dependent on the phase difference between the two superconductors,

$$I = I_0 \sin \delta \quad (1)$$

where $\delta = \theta_2 - \theta_1$, the difference in phase of the two wavefunctions at the junction, and I_0 is a characteristic of the particular junction.

An even more interesting effect occurs when two Josephson junctions are present in a superconducting ring (Figure 2.7). In this case, the currents interfere, caused by a difference in phase of the currents on the different paths around the ring. This is because

the phase difference of the wavefunctions must be the same no matter which way around the loop the electrons travel. The change in phase travelling around the loop through junction A (orange line, Figure 2.7), must be equal to the change in phase travelling around the loop through junction B (blue line, Figure 2.7). Therefore the change in phase can be equated, which gives

$$\delta_b - \delta_a = \frac{2q}{\hbar} \oint_{Loop} \mathbf{A} \cdot d\mathbf{s} \quad (2)$$

showing that the difference in phase equals the line integral over the whole superconducting loop, where \hbar is the reduced Planck's constant, \mathbf{A} is the vector potential and q is the charge on an electron. The line integral around the loop is the magnetic flux, Φ , through the loop. Therefore,

$$\delta_b - \delta_a = \frac{2q}{\hbar} \Phi. \quad (3)$$

This results in the difference in phase being proportional to the magnetic flux. To find the current of the loop, the total current, I , will be given by the sum of the currents through each junction. Using equation 1,

$$I_{total} = I_0 \sin \delta_a + I_0 \sin \delta_b. \quad (4)$$

Let $\delta_a = \delta_0 + \frac{2q}{\hbar} \Phi$ and $\delta_b = \delta_0 - \frac{2q}{\hbar} \Phi$, and using a trigonometric identity, this gives

$$I = 2I_0 \sin \delta_0 \cos \frac{q}{\hbar} \Phi. \quad (5)$$

For a maximum,

$$I_{max} = 2I_0 \left| \cos \frac{q}{\hbar} \Phi \right| \quad (6)$$

with maxima at $\Phi = n \frac{\pi \hbar}{q}$ where n is an integer. From equation 5, it can be seen that current depends in an oscillatory way on the flux inside the loop. As the period of the oscillation is so small, the current is extremely sensitive to tiny changes in magnetic flux. Therefore a pair of Josephson junctions can be used as a sensitive magnetometer to measure magnetic fields with great precision. This is the basis for a DC SQUID used in MEG.

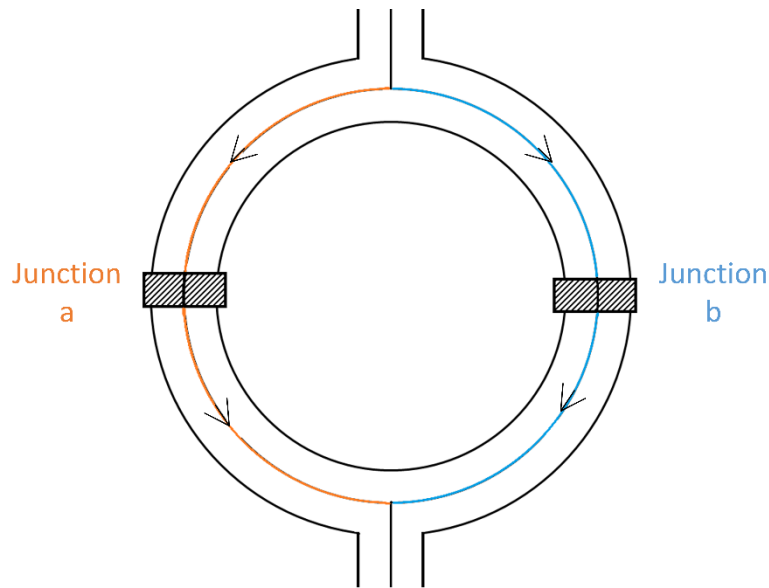


Figure 2.7. Two Josephson junctions, *a* and *b*, in a superconducting ring. The currents through the two junctions interfere, resulting in a total current which is dependent on magnetic flux, enabling its use as a magnetometer.

2.3.3 DC SQUID

This superconducting ring with two Josephson junctions is what is used in a DC SQUID. An example of the circuit diagram for a DC SQUID is given in Figure 2.8B. The SQUID is inductively coupled to a flux transformer. Flux transformers consist of a superconducting pickup coil which is placed close to the head, and a coupling coil which is inductively coupled to the SQUID. Time varying neuromagnetic fields induce currents in the superconducting pickup coil. Since the flux transformer is connected to the SQUID, and a bias current, I_{DC} , has been applied to the SQUID, the change in current will cause a change in flux through the SQUID. The SQUID flux voltage transfer function is a periodic sinusoid (Figure 2.8A). For greatest sensitivity in changes in magnetic flux, the SQUID is operated in the region where the function is steepest, where $\frac{dV}{d\Phi}$ is maximum, and the curve is approximately linear (Figure 2.8A). Therefore to ensure this holds, the SQUID is operated in a feedback loop, where the electronics apply a feedback current which counters the change in flux, to keep the flux through the SQUID constant. This applied voltage by the feedback circuit is the measured output of the SQUID.

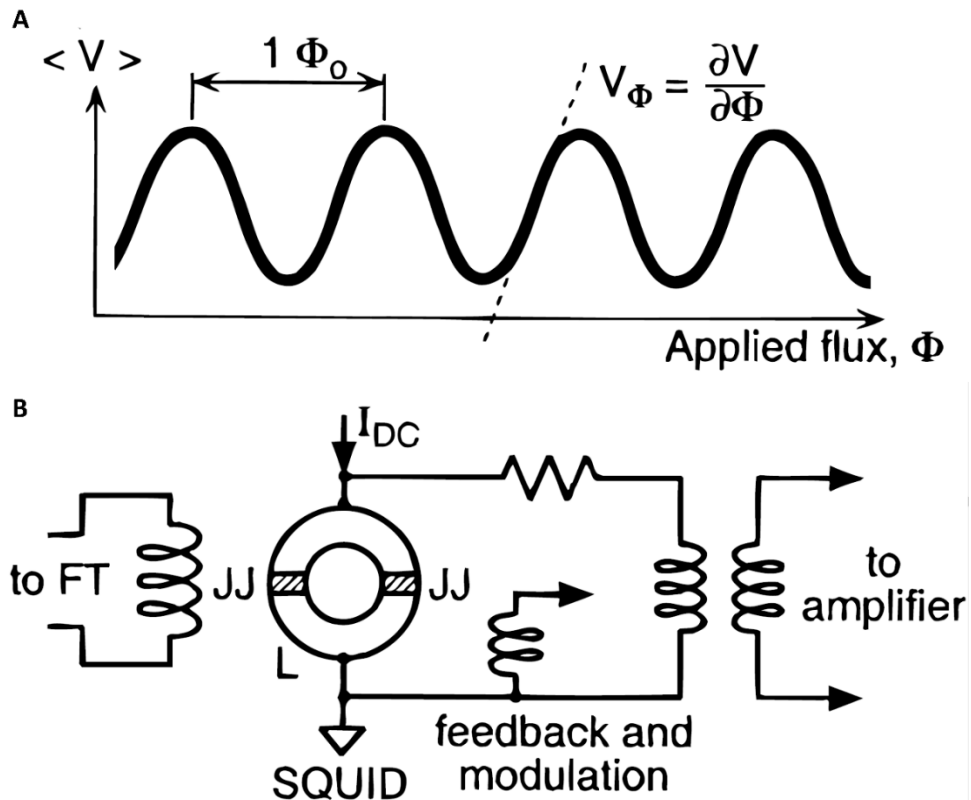


Figure 2.8. (A) Voltage as a function of flux. The DC SQUID is operated where the curve is approximately linear. (B) Circuit diagram of a DC SQUID. Pickup coil on the left picks up neuromagnetic fields, which is inductively coupled to the SQUID. This changes flux through the Josephson junctions, so a feedback current is applied to keep the flux through the SQUID the same and ensure the SQUID is operated on the linear part of the curve. Adapted from Vrba and Robinson (Vrba & Robinson, 2001).

2.3.4 Noise Reduction

Although SQUIDs are sensitive enough to measure neuromagnetic fields, the Earth's magnetic field is still orders of magnitude larger than the neuromagnetic fields, and external magnetic noise – such as electronics in the laboratory, moving magnetic objects (e.g. cars) and biomagnetic fields of no interest (e.g. magnetocardiogram) – can obscure the signal from the head. Hence, SQUIDs need to be used in conjunction with external noise reduction. The most straightforward approach to noise reduction is shielding using a magnetically shielded room. This is accomplished by eddy currents in a thick layer of high conductivity, high permeability metal (Zimmerman 1977), such as μ -metals which are nickel-iron alloys. Whilst magnetically shielded rooms remove most of Earth's magnetic field and sources of electrical equipment, this still leaves noise which is orders of magnitude higher than the neuromagnetic fields of interest.

To further isolate the neuromagnetic fields from the head, gradiometers are used. The CTF system uses axial gradiometers, shown in Figure 2.9. Gradiometers measure magnetic field gradient instead of magnetic field strength. The gradiometer is made of two loops of wire wound in opposite directions, separated by a short baseline distance, b . Since they are wound in opposition, the induced currents from a homogenous magnetic field will cancel out, and the net current will measure field gradient. As magnetic field strength follows an inverse square law, gradiometers are effective at measuring magnetic fields from nearby sources, such as the head, which the gradiometers are placed close to, whereas fields from distant noise sources are cancelled out (Figure 2.9).

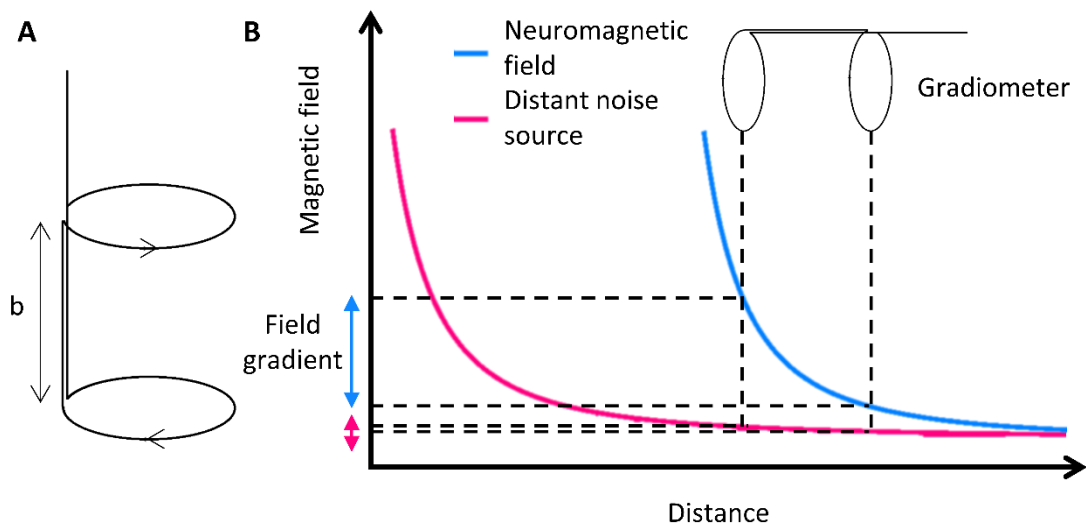


Figure 2.9. (A) Schematic of an axial gradiometer. Since the loops are oppositely wound, induced currents from fields which are the same at both loops will cancel out, whereas for a nearby source (the head) the field gradient will be large. (B) Field gradient measured from an axial gradiometer of a distant noise source (pink) and neuromagnetic field (blue) which is closer to the gradiometer. Since the noise source is far away, the gradient between the two loops is small, whereas for the nearby brain source, the gradient is large.

Using hardware gradiometers reduces a lot of environmental noise, but is usually not sufficient. Additional hardware gradiometers can be used, but become impractically long and are expensive to build (Hämäläinen et al., 1993). Instead, on the CTF system used in this thesis, higher order gradiometers can be synthesised using software. Second and third order gradiometers can be made electronically from first order gradiometers, used in conjunction with reference sensors. Reference sensors are positioned far away from the subject's head in order to detect distant noise sources. The magnetic fields detected at these reference sensors is expanded into a Taylor series about the primary sensor location. Using this, second and third order gradiometers can be synthetically

produced (Vrba & Robinson, 2001). These substantially improve the signal to noise of MEG recordings, particularly at low frequencies, enabling extra-cranial magnetic fields to be measured.

2.3.5 MEG System

A diagram of a MEG system is given in Figure 2.10. As mentioned in the previous section, the MEG system is housed inside a μ -metal magnetically shielded room. The MEG system comprises SQUIDs and flux transformers kept in a dewar of liquid helium to stay at superconducting temperature. The dewar is contained inside a movable gantry to allow horizontal or vertical positions. The subject is positioned on an adjustable chair which can be pulled out into a bed for supine scans. In this thesis, supine scanning was utilised to allow direct comparison to fMRI which is performed supine, as evidence has suggested body position can influence brain activity (Thibault et al., 2014). The subject is provided with head padding to minimise head movement during the scan to aid localisation. Measurements from the SQUIDs are digitised by an electronics rack and sent to an acquisition computer. A stimulus computer provides visual stimuli which are back-projected onto a screen inside the shielded room from a projector which is situated outside the shielded room to reduce interference. The acquisition and stimulus computer are connected via a parallel port so that temporal markers of stimulus occurrence can be placed in the MEG data for synchronicity and to aid post-processing.

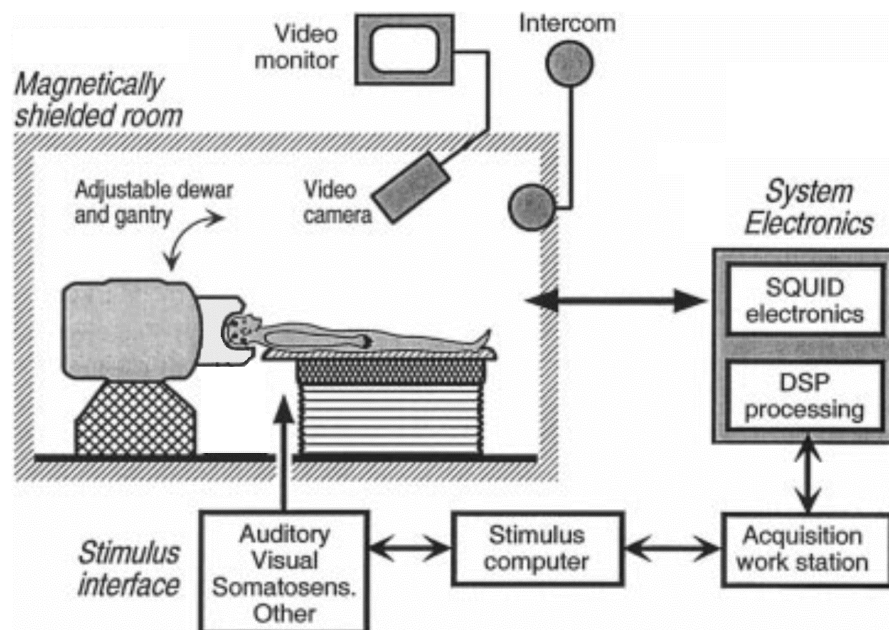


Figure 2.10. Diagram of a MEG system. Adapted from Vrba and Robinson (Vrba & Robinson, 2001).

Another important component of a MEG experiment is localising the head within the MEG scanner. This is achieved by attaching coils to the participant at three locations on the head (the nasion, left and right preauricular locations) to determine the position of the head in relation to the MEG. During the experiment, the coils are energised to localise the position of the coils within the scanner and track head movement during the experiment. The location of these coils is then registered relative to the subject's head geometry at the end of the scan session using a 3D digitiser. The 3D digitiser system (Polhemus, Colchester, VT, USA) uses a transmitter placed behind the subject and a receiver attached to the subject's head, which are able to locate the position of a stylus. The stylus is used to determine the location of the three coils relative to the surface of the subject's head, and to create a 3D representation of the surface of the head by moving the stylus over the head (Figure 2.11A). This surface is then matched to an anatomical image acquired using an MPRAGE sequence on either 3 T or 7 T MRI (Figure 2.11B). The scalp surface is extracted from the MRI image and is matched to the digitised head in an iterative process to find the best match. The position of the 3 coils are then known relative to the anatomy of the subject and also relative to the sensors in the MEG helmet (Figure 2.11B). This enables data acquired in the MEG scanner to be coregistered to the subject's brain anatomy.

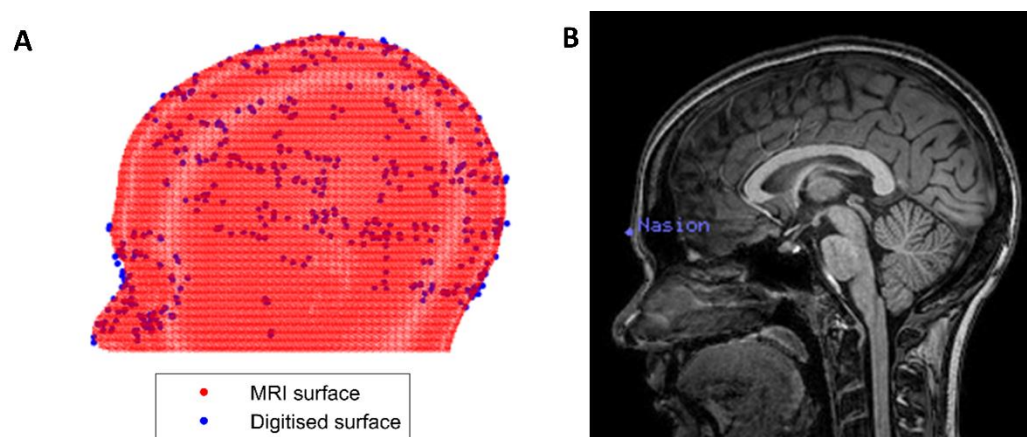


Figure 2.11. (A) Digitised surface points (blue) matched to head surface (red) extracted from anatomical MRI. (B) Nasion head coil location from the MEG scan can now be accurately matched to anatomical MRI.

2.3.6 Source Reconstruction

Once the MEG data have been collected, it is useful to localise the sources of the measured magnetic fields in the head. Not only does this enable investigation of the location of brain activity in functionally specific brain regions, but it can reduce

potential issues of field spread (since many sensors will detect the field from a single source) and reduce interference from noise sources. In order to project data into source space, two problems need to be solved: the forward problem and the inverse problem.

2.3.7 The Forward Problem

The forward problem is: given a known current distribution inside the brain, can the resulting electromagnetic field distribution outside the head be calculated? This problem is solvable, as the magnetic field outside the head can be calculated with Maxwell's equations, albeit with several assumptions. In this example, the head is assumed to be a single sphere with homogeneous conductivity. Secondly, the magnetic fields resulting from synchronised postsynaptic currents is assumed to resemble the field from a single current dipole at a distance. This is a reasonable assumption assuming the volume of brain activated is small.

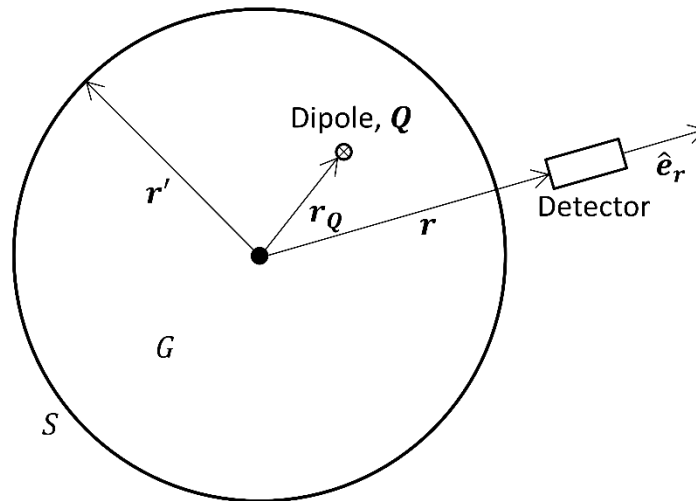


Figure 2.12. Geometry of a single spherical conductor, G , bounded by surface, S , with a dipole Q at location r_Q . A detector is at location r .

The magnetic field, B , outside a conductor (the head), G , with homogeneous conductivity is given by the Biot-Savart law,

$$\mathbf{B}(\mathbf{r}) = \frac{\mu_0}{4\pi} \int_G \frac{\mathbf{J}(\mathbf{r}') \times \mathbf{R}}{|\mathbf{R}|^3} dv' \quad (7)$$

where μ_0 is the permeability of free space, \mathbf{J} is the total current density contained in the volume, $\mathbf{R} = \mathbf{r} - \mathbf{r}'$ where \mathbf{r}' represents a location inside the head and \mathbf{r} represents a location outside the head (see Figure 2.12). For now, it is assumed the current is only due to the primary current, as it can be shown that the volume currents are zero for a radial field (Geselowitz, 1970). Therefore, assuming the current source is a single

dipole of strength Q , at location \mathbf{r}_Q , produced by primary currents of postsynaptic events, the current density, \mathbf{J}_P , can be expressed as

$$\mathbf{J}_P(\mathbf{r}') = Q\delta(\mathbf{r}' - \mathbf{r}_Q) \quad (8)$$

where δ is the Dirac delta function. This means that $\mathbf{J}_P = 0$ at every location other than \mathbf{r}_Q . It is also assumed that the volume is enclosed by a spherical surface and that the detector is oriented such that it only senses the radial component of the magnetic field, therefore the magnetic field only needs to be considered in the radial direction:

$$B_r(\mathbf{r}) = \frac{\mu_0}{4\pi} \int \frac{\mathbf{J}_P(\mathbf{r}') \times \mathbf{R}}{|\mathbf{R}|^3} \cdot \hat{\mathbf{e}}_r dv' \quad (9)$$

where $\hat{\mathbf{e}}_r$ is the unit vector in the radial direction. Substituting equation 8, this can be simplified to,

$$B_r(\mathbf{r}) = \frac{\mu_0}{4\pi} Q(\mathbf{r}_Q) \times \frac{\mathbf{r} - \mathbf{r}_Q}{|\mathbf{r} - \mathbf{r}_Q|^3} \cdot \hat{\mathbf{e}}_r. \quad (10)$$

Since $[\mathbf{Q}(\mathbf{r}_Q) \times \mathbf{r}] \cdot \hat{\mathbf{e}}_r = 0$,

$$B_r(\mathbf{r}) = -\frac{\mu_0 (Q \times r_Q)}{4\pi |r - r_Q|^3} \cdot \mathbf{e}_r. \quad (11)$$

To generate an expression for the magnetic field including non-radial components, consider that outside of the conductor, $\mathbf{J} = 0$, therefore from the quasistatic approximation of Maxwell's equation ($\nabla \times \mathbf{B} = \mu_0 \mathbf{J}$), $\nabla \times \mathbf{B} = 0$. Therefore, the magnetic field outside the conductor can be described as a scalar potential U :

$$\mathbf{B}(\mathbf{r}) = -\mu_0 \nabla U(\mathbf{r}). \quad (12)$$

To find an expression for U , consider a line integral of ∇U over $\mathbf{r} + t\mathbf{e}_r$, between $0 \leq t \leq \infty$,

$$\begin{aligned} U(\mathbf{r}) &= \int_0^\infty \nabla U(\mathbf{r} + t\mathbf{e}_r) \cdot \mathbf{e}_r dt \\ &= \frac{1}{\mu_0} \int_0^\infty B_r(\mathbf{r} + t\mathbf{e}_r) dt \\ &= \frac{1}{\mu_0} \int_0^\infty \mathbf{B}_0(\mathbf{r} + t\mathbf{e}_r) \cdot \mathbf{e}_r dt \\ &= \frac{1}{4\pi} Q \times (\mathbf{r} - \mathbf{r}_Q) \cdot \mathbf{e}_r \int_0^\infty \frac{dt}{|\mathbf{r} + t\mathbf{e}_r - \mathbf{r}_Q|^3}. \end{aligned} \quad (13)$$

Solving this integral gives

$$U(\mathbf{r}) = -\frac{1}{4\pi} \frac{\mathbf{Q} \times \mathbf{r}_Q \cdot \mathbf{r}}{F} \quad (14)$$

where

$$F = a(ra + r^2 - \mathbf{r}_Q \cdot \mathbf{r}) \quad (15)$$

and where $\mathbf{a} = \mathbf{r} - \mathbf{r}_Q$, $a = |\mathbf{a}|$ and $r = |\mathbf{r}|$.

Substituting this expression for $U(\mathbf{r})$ into equation 12, the magnetic field outside the conductor is given by

$$\mathbf{B}(\mathbf{r}) = \frac{\mu_0}{4\pi F^2} (F\mathbf{Q} \times \mathbf{r}_Q - \mathbf{Q} \times \mathbf{r}_Q \cdot \mathbf{r} \nabla F) \quad (16)$$

where $\nabla F = (r^{-1}a^2 + a^{-1}\mathbf{a} \cdot \mathbf{r} + 2a + 2r)\mathbf{r} - (a + 2r + a^{-1}\mathbf{a} \cdot \mathbf{r})\mathbf{r}_Q$. Equation 16 is known as the Sarvas equation (Sarvas, 1987) and is the general solution to the single sphere model. It is important to note that this equation now includes the contribution from the volume currents, since non-radial components of \mathbf{B} are considered. For a radial dipole, the magnetic field outside the head will be zero from Equation 16. Therefore, MEG is only sensitive to dipoles oriented tangentially. Fortunately, there are a large (roughly 70% (Hillebrand & Barnes, 2002)) number of postsynaptic potentials in cortical sulci which are oriented tangentially and can be detected.

2.3.8 Multiple Sphere Model

The solution in equation 11 is based on the assumption of a spherical conductor. Evidently, the head does not have spherical geometry as areas such as the frontal lobe deviate from a single sphere geometry (Hamalainen & Sarvas, 1989). Whilst the spherical head model is mostly reasonable, alternatives to the single sphere head model exist, such as the multiple spheres model (Huang et al., 1999) which was the model used in this thesis. The multiple spheres model was developed in 1999, whereby the head is modelled as a series of overlapping spheres instead of a single sphere (Huang et al., 1999). In the multiple spheres model, a sphere is fit for each sensor (see Figure 2.13) and the forward model is solved using the sphere assigned to that sensor. This has the benefit that the forward model for a sphere is simple to solve, so the forward model can be solved rapidly, and yet the head shape is more realistic than a single sphere. The multiple sphere model was found to have similar accuracy to other alternative models such as the boundary element model (BEM) (Mosher et al., 1999) with less

computational cost. However, it is important to note that more recent studies (Stenroos et al., 2014) have shown BEMs to be more accurate than multiple sphere models since computational power has increased rapidly since the 90s. Whilst BEMs, which require estimating the conductivity profile of the head, offer a large benefit to EEG, it could be argued that the improvements in MEG will be small since MEG is independent of the conductivity profile of the head.

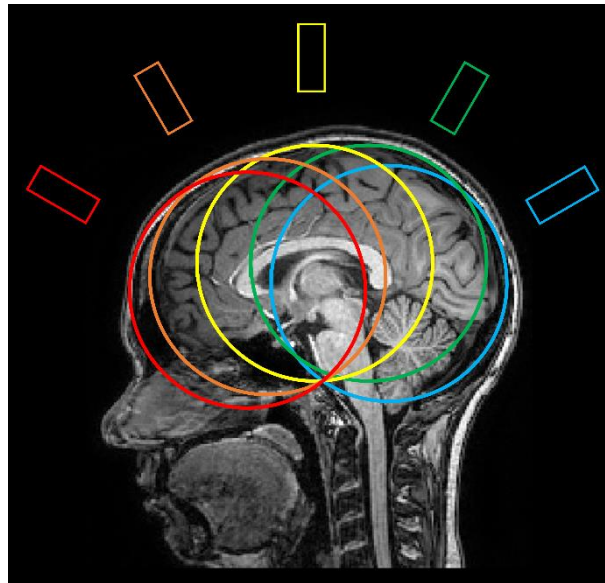


Figure 2.13. Schematic showing multiple spheres model. Each sphere is fit individually to each sensor, giving a more realistic head shape, whilst the forward model for a sphere is still simple to solve.

2.3.9 The Inverse Problem

Using the forward solution, the magnetic field of a dipole in the brain can be calculated outside the head. In MEG, the aim is then to localise sources inside the head given measured data. This is the inverse problem: given a measured magnetic field distribution outside the head, can we reconstruct the underlying current distribution inside the brain? The inverse problem is mathematically ill-posed as a measured field could result from an infinite number of current distributions inside the head due to field cancellation. Not only this, but for the inverse solution used in this thesis, many more sources are attempted to be reconstructed than there are sensors. However, the forward solution helps to constrain the number of possible inverse solutions and the inverse problem can be optimised to find the best solution, based on a few assumptions.

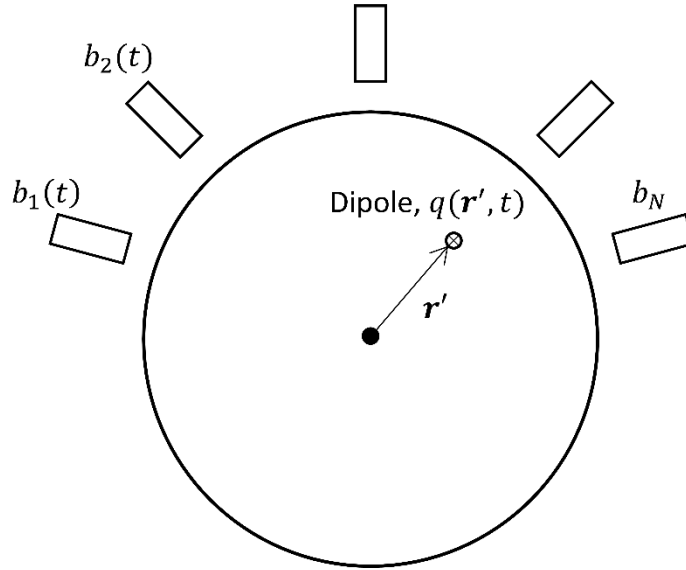


Figure 2.14. Geometry of a current dipole, $q(\mathbf{r}', t)$ at location \mathbf{r}' and the resultant magnetic fields, $b(t)$ measured at each of the N sensors.

The measured magnetic fields outside the head will be a superposition of the fields generated from many current sources inside the head. As shown in Figure 2.14, considering the head as a spherical conductor, V , the radial component of the magnetic field, $b_i(t)$, measured by a sensor ($i = 1, 2, \dots, N$, where N is the total number of sensors), will be the integral over the volume of all the sources:

$$b_i(t) = \int_V \mathbf{L}(\mathbf{r}') q(\mathbf{r}', t) dV \quad (17)$$

where $q(\mathbf{r}', t)$ is a current dipole at location \mathbf{r}' and time t . $\mathbf{L}(\mathbf{r}')$ is the lead field, the magnetic field that would be induced at location \mathbf{r} by a current dipole of unit amplitude at location \mathbf{r}' . In reality, the volume will be discretised into a set of M cubic voxels, therefore the integral tends to a sum over voxels, where M is the total number of voxels:

$$b_i(t) = \sum_{m=1}^M \mathbf{L}(\mathbf{r}'_m) q(\mathbf{r}'_m, t). \quad (18)$$

The lead fields can be described as an $N \times M$ matrix, where N is the number of sensor channels and M is the number of voxels. Therefore equation 18 can be written in matrix form,

$$\begin{bmatrix} b_1(t) \\ \vdots \\ b_N(t) \end{bmatrix} = \begin{bmatrix} \mathbf{l}_{1,1} & \cdots & \mathbf{l}_{1,M} \\ \vdots & \ddots & \vdots \\ \mathbf{l}_{N,1} & \cdots & \mathbf{l}_{N,M} \end{bmatrix} \begin{bmatrix} q_1(t) \\ \vdots \\ q_M(t) \end{bmatrix} \quad (19)$$

$$\mathbf{B}(t) = \mathbf{L} \mathbf{q}(t). \quad (20)$$

The MEG measurements, b_i , are a linear projection of the dipole time courses through the lead fields. To get to the underlying current sources, the equation needs to be inverted to find \mathbf{q} . Unfortunately, \mathbf{L} cannot be inverted simply as it is non-square and singular. Therefore some sort of optimisation must be used to find \mathbf{q} .

2.3.10 Beamforming

Beamforming is one possible solution to this problem. Beamforming is a spatial filtering technique where the dipole strength, $\mathbf{q}(\mathbf{r}', t)$, is given by a weighted sum of the sensor measurements at each of the sensor locations. Mathematically,

$$\hat{\mathbf{q}}(\mathbf{r}', t) = w_1(\mathbf{r}')b_1(t) + w_2(\mathbf{r}')b_2(t) + \dots + w_N(\mathbf{r}')b_N(t) \quad (21)$$

Or,

$$\hat{\mathbf{q}}(\mathbf{r}', t) = \mathbf{w}^T \mathbf{b}(t) \quad (22)$$

where $\hat{\mathbf{q}}(\mathbf{r}', t)$ is the reconstructed estimate of $\mathbf{q}(t)$, $w_1 \dots w_N$ are the weights for N sensors, and \mathbf{b} is the measured magnetic field at the sensor. For a single voxel location, the time course of current is reconstructed, and subsequently applied to all other voxels.

The accuracy of the reconstruction depends on how the weights are chosen. In beamforming, the weights are chosen such that the overall power is minimised, with the linear constraint that power originating from the location of interest remains. In this way, the signal from a specific location is estimated and activity from locations which are not of interest are attenuated. Mathematically this can be written (Van Veen et al., 1997),

$$\min_{\mathbf{w}(\mathbf{r}')} \langle \hat{q}^2(\mathbf{r}', t) \rangle \text{ subject to } \mathbf{w}^T(\mathbf{r}')\mathbf{L}(\mathbf{r}') = 1. \quad (23)$$

where the estimated power is the expectation value of the squared signal. This linear constraint $\mathbf{w}^T(\mathbf{r}')\mathbf{L}(\mathbf{r}') = 1$ originates from the definition of the lead field. Substituting equation 22, the expectation value of the dipole magnitude is given by,

$$\begin{aligned} \langle \hat{q}^2(\mathbf{r}', t) \rangle &= \langle (\mathbf{w}^T(\mathbf{r}')\mathbf{B}(t))(\mathbf{w}^T(\mathbf{r}')\mathbf{B}(t))^T \rangle \\ &= \langle \mathbf{w}^T(\mathbf{r}')\mathbf{B}(t) \mathbf{B}^T(t)\mathbf{w}(\mathbf{r}') \rangle \\ &= \mathbf{w}^T(\mathbf{r}')\mathbf{C}\mathbf{w}(\mathbf{r}') \end{aligned} \quad (24)$$

where $\mathbf{C} = \langle \mathbf{B}(t)\mathbf{B}(t)^T \rangle$ is the $N \times N$ covariance matrix which represents the data covariance over a time-frequency window of interest. This is usually chosen to span the entire experiment as increasing the amount of data increases the accuracy of the calculation of the covariance matrix (Brookes et al., 2008). Therefore the beamformer can be written as,

$$\min_{\mathbf{w}(\mathbf{r}')} [\mathbf{w}^T(\mathbf{r}')\mathbf{C}\mathbf{w}(\mathbf{r}')] \text{ subject to } \mathbf{w}^T(\mathbf{r}')\mathbf{L}(\mathbf{r}') = 1. \quad (25)$$

The solution to this can be found analytically (Van Veen et al., 1997), where the weights are given by,

$$\mathbf{w}^T(\mathbf{r}') = \frac{\mathbf{L}^T(\mathbf{r}')\mathbf{C}^{-1}}{\mathbf{L}^T(\mathbf{r}')\mathbf{C}^{-1}\mathbf{L}(\mathbf{r}')}. \quad (26)$$

This equation should be normalised to prevent a bias towards the centre of the brain. The weights are corrected by dividing the weights by the norm of itself,

$$\mathbf{w}_{norm}(\mathbf{r}') = \frac{\mathbf{w}(\mathbf{r}')}{\sqrt{\mathbf{w}(\mathbf{r}')\mathbf{w}^T(\mathbf{r}')}} \quad (27)$$

where

$$\begin{aligned} \sqrt{\mathbf{w}(\mathbf{r}')\mathbf{w}^T(\mathbf{r}')} &= \sqrt{\left(\frac{\mathbf{L}^T(\mathbf{r}')\mathbf{C}^{-1}}{\mathbf{L}^T(\mathbf{r}')\mathbf{C}^{-1}\mathbf{L}(\mathbf{r}')}\right) \frac{\mathbf{C}^{-1}\mathbf{L}(\mathbf{r}')}{\mathbf{L}^T(\mathbf{r}')\mathbf{C}^{-1}\mathbf{L}(\mathbf{r}')}} \\ &= \frac{\sqrt{\mathbf{L}^T(\mathbf{r}')\mathbf{C}^{-2}\mathbf{L}(\mathbf{r}')}}{\mathbf{L}^T(\mathbf{r}')\mathbf{C}^{-1}\mathbf{L}(\mathbf{r}')}. \end{aligned} \quad (28)$$

Therefore,

$$\mathbf{w}_{norm}(\mathbf{r}') = \frac{\mathbf{L}^T(\mathbf{r}')\mathbf{C}^{-1}}{\sqrt{\mathbf{L}^T(\mathbf{r}')\mathbf{C}^{-2}\mathbf{L}(\mathbf{r}')}}. \quad (29)$$

So far, the orientation of the source has not been considered, which needs to be correctly estimated. Since there is no radial contribution to MEG, the source could exist in any orientation on the tangential plane. Therefore, all possible orientations over 180° in the tangential plane are modelled, and the orientation with the highest signal to noise ratio is chosen as the direction of the source.

The weights can then be calculated over the whole brain. In the case of task data, rather than calculating the absolute power of a source, instead the power in a time window during the task (active window) is compared relative to a control window during rest. In this case, the covariance is measured during an active window, \mathbf{C}_{active} , (the window

of interest) and the control window, $\mathbf{C}_{control}$, ensuring that the control and active window are the same length (Brookes et al., 2008). Applying this to all voxels across the brain can build a pseudo-T-statistic image,

$$\mathcal{F} = \frac{\mathbf{w}^T(\mathbf{r}')\mathbf{C}_{active}\mathbf{w}(\mathbf{r}') - \mathbf{w}^T(\mathbf{r}')\mathbf{C}_{control}\mathbf{w}(\mathbf{r}')}{\mathbf{w}^T(\mathbf{r}')\Sigma\mathbf{w}(\mathbf{r}')} \quad (30)$$

where $\mathbf{w}^T(\mathbf{r}')\mathbf{C}_{active}\mathbf{w}(\mathbf{r}')$ is the power during the active window, similarly $\mathbf{w}^T(\mathbf{r}')\mathbf{C}_{control}\mathbf{w}(\mathbf{r}')$ is the power during the control window, and $\mathbf{w}^T(\mathbf{r}')\Sigma\mathbf{w}(\mathbf{r}')$ is estimated noise power. This process is used in Chapter 4.

2.3.11 Hilbert Transform

Once the source has been localised, time courses can be estimated from the location of the source. Stimulus induced responses are time locked to the stimulus but not phase locked, which means that when averaged over many trials the signal will be diminished. Therefore, the amplitude envelope of the signal is taken. This is usually performed with a Hilbert transform. The source reconstructed time course $\hat{q}(t)$ is a real signal. In order to measure the phase and amplitude of the signal, the signal needs to be converted into a complex signal $\hat{z}(t)$:

$$\hat{z}(t) = \hat{q}(t) + i\hat{y}(t) \quad (31)$$

where $\hat{y}(t)$ is the Hilbert transform of the real signal $\hat{q}(t)$.

The Hilbert transform is given by

$$\hat{y}(t) = h * \hat{q}(t) \quad (32)$$

$$\hat{y}(t) = P \left[\frac{1}{\pi} \int_{-\infty}^{\infty} \frac{\hat{q}(\tau)}{t - \tau} d\tau \right] \quad (33)$$

where P is the Cauchy principal value of the integral, h is the Hilbert transform kernel which is $\frac{1}{\pi t}$ and τ is a new label for the time coordinate. The Hilbert transform creates the analytic signal by convolving the signal with the Hilbert transform kernel. The signal envelope is then found by taking the absolute value of the Hilbert transform, an example is shown in Figure 2.15. Hilbert transforms are used in Chapter 4 and 5 to derive virtual electrode time courses, and are also used in Chapter 5 to investigate functional connectivity between brains which will be explained in Chapter 5.

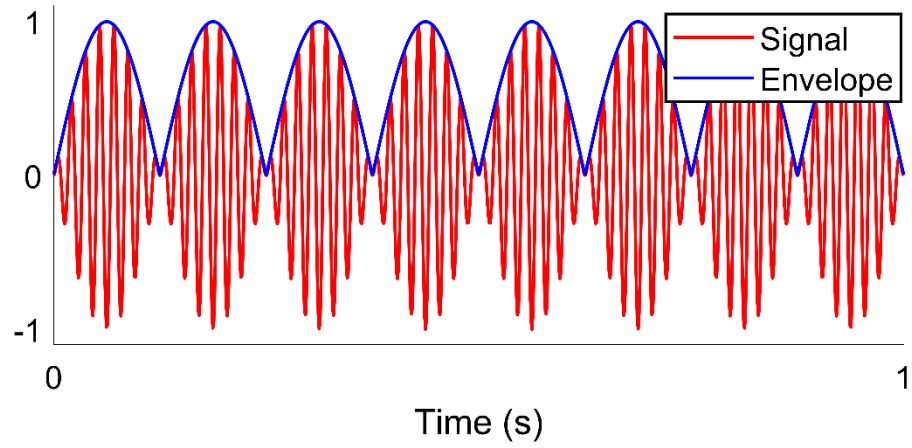


Figure 2.15. Demonstration of taking the Hilbert envelope (blue) of a sinusoidal signal (red).

2.4 References

- Bear, M., Connors, B., & Paradiso, M. A. (2020). *Neuroscience: Exploring the Brain, Enhanced Edition*. Burlington, UNITED STATES: Jones & Bartlett Learning, LLC.
- Berger, H. (1929). *Archiv für Psychiatrie und Nervenkrankheiten*, 87(1), 527-570.
- Boto, E., Holmes, N., Leggett, J., Roberts, G., Shah, V., Meyer, S. S., Muñoz, L. D., Mullinger, K. J., Tierney, T. M., & Bestmann, S. (2018). Moving magnetoencephalography towards real-world applications with a wearable system. *nature*, 555(7698), 657-661.
- Brookes, M. J., Vrba, J., Robinson, S. E., Stevenson, C. M., Peters, A. M., Barnes, G. R., Hillebrand, A., & Morris, P. G. (2008). Optimising experimental design for MEG beamformer imaging. *Neuroimage*, 39, 1788-1802.
- Cheyne, D. (2013). MEG studies of sensorimotor rhythms: A review. *Experimental Neurology*, 245, 37-39.
- Cohen, D. (1968). Magnetoencephalography: Evidence of Magnetic Fields Produced by Alpha-Rhythm Currents. *Science*, 161(3843), 784.
- Cohen, D. (1972). Magnetoencephalography: Detection of the Brain's Electrical Activity with a Superconducting Magnetometer. *Science*, 175(4022), 664.
- Fries, P. (2005). A mechanism for cognitive dynamics: neuronal communication through neuronal coherence. *Trends in Cognitive Sciences*, 9(10), 474-480.
- Geselowitz, D. (1970). On the magnetic field generated outside an inhomogeneous volume conductor by internal current sources. *IEEE Transactions on Magnetics*, 6(2), 346-347.
- Hämäläinen, M., Hari, R., Ilmoniemi, R. J., Knuutila, J., & Lounasmaa, O. V. (1993). Magnetoencephalography—theory, instrumentation, and applications to noninvasive studies of the working human brain. *Reviews of modern Physics*, 65(2), 413.
- Hamalainen, M. S., & Sarvas, J. (1989). Realistic conductivity geometry model of the human head for interpretation of neuromagnetic data. *IEEE TRANSACTIONS ON BIOMEDICAL ENGINEERING*, 36(2), 165-171.
- Hansen, P., Kringelbach, M., & Salmelin, R. (2010). *MEG: An introduction to methods*: Oxford university press.
- Hillebrand, A., & Barnes, G. (2002). A quantitative assessment of the sensitivity of whole-head MEG to activity in the adult human cortex. *Neuroimage*, 16(3), 638-650.
- Huang, M., Mosher, J. C., & Leahy, R. (1999). A sensor-weighted overlapping-sphere head model and exhaustive head model comparison for MEG. *Physics in Medicine & Biology*, 44(2), 423.
- Jaklevic, R. C., Lambe, J., Silver, A. H., & Mercereau, J. E. (1964). Quantum Interference Effects in Josephson Tunneling. *Physical Review Letters*, 12(7), 159-160.
- Jasper, H., & Penfield, W. (1949). Electroencephalograms in man: Effect of voluntary movement upon the electrical activity of the precentral gyrus. *Archiv für Psychiatrie und Zeitschrift Neurologie*, 183, 163-174.
- Josephson, B. (1962). Possible new effect in superconducting tunneling. *Phys. Lett.*, 1, 251-253.

- Mosher, J. C., Leahy, R. M., & Lewis, P. S. (1999). EEG and MEG: forward solutions for inverse methods. *IEEE TRANSACTIONS ON BIOMEDICAL ENGINEERING*, 46(3), 245-259.
- Murakami, S., & Okada, Y. (2006). Contributions of principal neocortical neurons to magnetoencephalography and electroencephalography signals. *The Journal of Physiology*, 575(3), 925-936.
- Neuper, C., & Pfurtscheller, G. (2001). Event-related dynamics of cortical rhythms: frequency-specific features and functional correlates. *International Journal of Psychophysiology*, 43, 41-58.
- Pfurtscheller, G., & Lopes da Silva, F. (1999). Event-related EEG/MEG synchronization and desynchronization: basic principles. *Clinical Neurophysiology*, 110, 1842-1857.
- Pfurtscheller, G., Stancak Jr, A., & Neuper, C. (1996). Event-related synchronization (ERS) in the alpha band - an electrophysiological correlate of cortical idling: A review *International Journal of Psychophysiology*, 24, 39-46.
- Ramón y Cajal, S. (1899). *Comparative study of the sensory areas of the human cortex*: Clark University.
- Sarvas, J. (1987). Basic mathematical and electromagnetic concepts of the biomagnetic inverse problem. *Physics in Medicine & Biology*, 32(1), 11.
- Stenroos, M., Hunold, A., & Haueisen, J. (2014). Comparison of three-shell and simplified volume conductor models in magnetoencephalography. *Neuroimage*, 94, 337-348.
- Thibault, R. T., Lifshitz, M., Jones, J. M., & Raz, A. (2014). Posture alters human resting-state. *Cortex*, 58, 199-205.
- Van Veen, B. D., & Buckley, K. M. (1988). Beamforming: A Versatile Approach to Spatial Filtering. *IEEE ASSP Magazine*, 5(2), 4-24.
- Van Veen, B. D., Van Drongelen, W., Yuchtman, M., & Suzuki, A. (1997). Localization of Brain Electrical Activity via Linearly Constrained Minimum Variance Spatial Filtering. *IEEE TRANSACTIONS ON BIOMEDICAL ENGINEERING*, 44(9), 867-880.
- Vrba, J., & Robinson, S. E. (2001). Signal processing in magnetoencephalography. *Methods*, 25(2), 249-271.
- Zumer, J. M., Brookes, M. J., Stevenson, C. M., Francis, S. T., & Morris, P. G. (2010). Relating BOLD fMRI and neural oscillations through convolution and optimal linear weighting. *NeuroImage*, 49, 1479-1489.

CHAPTER 3

3 Magnetic Resonance Imaging

MRI (magnetic resonance imaging) is a non-invasive technique that measures signals from precessing nuclei, typically protons, in a magnetic field. MRI has the ability to build high spatial resolution images throughout the whole body, and as the MR signal depends on tissues properties, MRI can be used clinically in diagnostic imaging. Not only can MRI give static images of tissue contrast with great detail, but MRI can also map dynamic changes in function, including in the brain, where MRI is used widely in neuroimaging for functional MRI (fMRI). Most importantly, MRI can produce images without the use of ionising radiation, unlike PET and CT.

Developments in MRI have led to a shift toward higher field strength scanners, where increased signal allows the collection of data at higher spatial resolution. The first 7 T scanner in the UK was installed at the Sir Peter Mansfield Imaging Centre in 2005, and at the time of writing there are 89 ultra-high field (UHF, ≥ 7 T) scanners worldwide (Huber, 2020). The increase in field strength, whilst providing many benefits, also poses many new challenges.

The origin of the MRI signal is based on the phenomenon of nuclear magnetic resonance (NMR), which will be described in this chapter. Localisation of NMR signals from nuclei is made possible using magnetic field gradients. Further, the process by which MRI can be used to measure functional changes in the human brain, functional magnetic resonance imaging (fMRI), is described along with the pulse sequences which are used in later experimental chapters of this thesis, including techniques for accelerating MRI acquisition.

3.1 Nuclear Magnetic Resonance

NMR (nuclear magnetic resonance) was first demonstrated in 1938 by Rabi (Rabi et al., 1938), and further developed by Bloch (Bloch, 1946) and Purcell (Purcell et al., 1946) in 1946. The theoretical explanation of NMR is founded on the properties of the nucleus, in particular, the fundamental property known as spin. Neutrons and protons have an intrinsic angular momentum called spin, where the total spin angular momentum of a nucleus is given by $I\hbar$, where I is the spin quantum number and \hbar is

the reduced Planck's constant. I can take integer or half-integer values, depending on the number of neutrons and protons in the nucleus. Only nuclei with $I \neq 0$ can exhibit NMR. For an even number of protons and neutrons, $I = 0$. If both the number of neutrons and the number of protons are odd, the nucleus will have integer I . If the nucleus has an odd number of neutrons or an odd number of protons, the nucleus will have half-integer spin. The hydrogen nucleus has spin $\frac{1}{2}$ and is the most common nucleus with net spin in the human body, as the body is on average 60% water (Institute of Medicine Food and Nutrition Board, 2004). Therefore, the hydrogen nucleus is commonly studied with MRI and is the nucleus studied in this thesis. Whilst based on quantum mechanical properties of the nucleus - spin - NMR can also be explained in terms of classical mechanics, which is the approach taken in this chapter.

3.1.1 Precession

A proton (hydrogen nucleus) with spin $\frac{1}{2}$ has a corresponding magnetic moment, $\boldsymbol{\mu}$,

$$\boldsymbol{\mu} = \gamma \boldsymbol{J} \quad (1)$$

where γ is the gyromagnetic ratio, specific for a particular nucleus, and \boldsymbol{J} is the spin angular momentum vector. For a ^1H nucleus, $\gamma = 42.58 \text{ MHz T}^{-1}$ (Hennel et al., 1993). When a magnetic moment $\boldsymbol{\mu}$ is placed in an external magnetic field, \boldsymbol{B} , the magnetic moment experiences a torque which attempts to align $\boldsymbol{\mu}$ with the magnetic field. Torque is defined as the rate of change of angular momentum and is given by

$$\frac{d\boldsymbol{J}}{dt} = \boldsymbol{\mu} \times \boldsymbol{B}. \quad (2)$$

Substituting from Equation 1 gives

$$\frac{d\boldsymbol{\mu}}{dt} = \gamma \boldsymbol{\mu} \times \boldsymbol{B}. \quad (3)$$

Equation 3 describes the equation of motion of a magnetic moment in a magnetic field. The rate of change of $\boldsymbol{\mu}$ is perpendicular to $\boldsymbol{\mu}$, resulting in the precession of $\boldsymbol{\mu}$ about the magnetic field axis. The angular frequency of this precession is given by the Larmor equation,

$$\omega = \gamma B_0 \quad (4)$$

where B_0 is the magnetic field strength and ω is the Larmor frequency. The quantisation of angular momentum results in a splitting of energy levels associated with the magnetic moments in a magnetic field, known as the Zeeman effect. For ^1H , angular momentum

can take two possible values, $\pm \frac{\hbar}{2}$. This gives rise to two distinct energy states for a hydrogen nucleus in a magnetic field, one high (E_+) and one low (E_-):

$$E_{\pm} = \pm \frac{\gamma \hbar B_0}{2}. \quad (5)$$

At thermal equilibrium, the spins will be distributed between these two energy states in accordance with Boltzmann statistics,

$$\frac{N_-}{N_+} = e^{-\frac{\gamma \hbar B_0}{k_B T}}, \quad (6)$$

where N_- is the number of spins occupying the low energy state and N_+ is the number of spins occupying the high energy state, k_B is the Boltzmann constant and T is the absolute temperature of the sample. The population difference between the two states results in a net magnetisation, M_0 , in the direction of the applied field, which is the sum of all the magnetic moments in the sample. M_0 is given by

$$M_0 = \frac{N(\gamma \hbar)^2 B_0}{4k_b T}. \quad (7)$$

This net magnetisation is the basis of the NMR signal. A stronger magnetic field, B_0 , a lower temperature, T , and a higher gyromagnetic ratio, γ , will all result in a larger net magnetisation, M_0 , and hence a larger NMR signal.

3.1.2 Relaxation

To detect an NMR signal, the nuclei must be perturbed from equilibrium along the z -axis by applying a magnetic field, B_1 . This magnetic field must be applied at an energy equal to the energy difference between the two spin states in order to allow transitions of the nuclei between the energy states (Equation 5). In order to do this, an oscillating B_1 field is applied at the Larmor frequency orthogonal to the net equilibrium magnetisation. For a 7 T magnetic field, the Larmor frequency is 298 MHz, which is in the radio frequency range and hence the applied B_1 field is often called the RF pulse. Initially, the net magnetisation, M_0 , is aligned with B_0 (along the z -axis). The applied RF pulse acts to tip M_0 away from B_0 into the transverse plane. The duration for which the RF pulse is applied, τ , and its amplitude, B_1 , determines the angle through which the net magnetisation is tipped (flip angle $\alpha = \gamma B_1 \tau$). A 90° RF pulse has two resultant effects: it equalises the population difference between the two spin states, and causes the spins to come into phase with each other thus the magnetisation is tipped from the

z-axis into the xy-plane, generating a transverse magnetisation signal. After the RF pulse is switched off, the spins will precess about B_0 at the Larmor frequency (Equation 4). The precession of the magnetisation will induce an oscillating electromotive force (emf) in a pickup coil, which is the detected NMR signal. This observed signal is known as a free induction decay (FID) as it decays with an exponential envelope.

Once the magnetisation has been perturbed from equilibrium, over time the longitudinal and transverse magnetisation will return back to Boltzmann equilibrium via two independent processes: longitudinal relaxation (T_1) acts to return spins parallel to B_0 to equilibrium (i.e. returning to a Boltzmann distribution and thus M_0), and transverse relaxation (T_2 and T_2^*) acts to return the transverse magnetisation perpendicular to B_0 back to zero. These two mechanisms are characterised by the longitudinal and transverse relaxation time constants, T_1 and T_2 respectively, and are described by the Bloch equation:

$$\frac{d\mathbf{M}}{dt} = \gamma(\mathbf{M} \times \mathbf{B}) - \frac{(M_z - M_0)\mathbf{k}}{T_1} - \frac{M_z\mathbf{i} + M_y\mathbf{j}}{T_2}. \quad (8)$$

3.1.2.1 Longitudinal Relaxation

Longitudinal recovery is the process by which spins return back to their equilibrium population difference, and the magnetisation along the z-axis (M_z) returns to the equilibrium magnetisation (M_0). This process is governed by the time constant T_1 which is known as the spin-lattice relaxation time. Longitudinal recovery depends on the transfer of energy between the spins and the lattice. The return to equilibrium arises due to the fact that molecules undergo Brownian motion, creating randomly fluctuating magnetic fields which interact with other spins and cause transitions between spin states. This motion has an associated time constant termed the correlation time. Transitions are more efficient the more closely matched the molecular motion is to the Larmor frequency. In highly mobile liquids such as water, molecules can move freely and so have very small correlation times, which are far from the Larmor frequency, so relaxation is inefficient leading to long T_1 values. In viscous liquids and solids, mobility of molecules is reduced, resulting in a correlation time that more closely matches the inverse of the Larmor frequency, resulting in a shorter T_1 . Since temperature affects the rate of Brownian motion, temperature also affects T_1 . The equation for the recovery of longitudinal magnetisation is determined by solving the Bloch equation (Equation 8) (Bloch, 1946). The longitudinal magnetisation, M_z , as a function of time is given by,

$$M_z(t) = M_0 \left(1 - e^{-\frac{t}{T_1}} \right) + M_z(0) e^{-\frac{t}{T_1}} \quad (9)$$

where M_0 is the equilibrium magnetisation.

Following a 90° RF pulse, the magnetisation M_0 , which is initially aligned along the z -axis, will be tipped into the xy -plane resulting in M_z at time zero being given by $M_z(0) = 0$. $M_z(t)$ will then recover to its equilibrium value via Equation 9, and return to equilibrium in a time approximately five times T_1 .

Following a 180° inversion pulse, the longitudinal magnetisation will be flipped along the $-z$ -axis and will recover from $-M_0$ to M_0 . At a later time TI (the inversion time), a 90° pulse can be applied to tip the magnetisation that has recovered at that given time into the transverse plane. This 90° pulse will result in an FID with initial amplitude proportional to the amount of longitudinal magnetisation. This is known as an inversion recovery sequence, and the recovery following an inversion pulse in different tissue types in the brain is shown Figure 3.1. The amount of signal is related to the amount of recovery that occurs, which generates a T_1 weighted image. For each tissue type, there will be a particular value of TI where the longitudinal magnetisation is zero, which is known as the null point, where there is no signal. The concept of an inversion recovery is used in Chapter 6 in the VASO sequence to null the signal from blood.

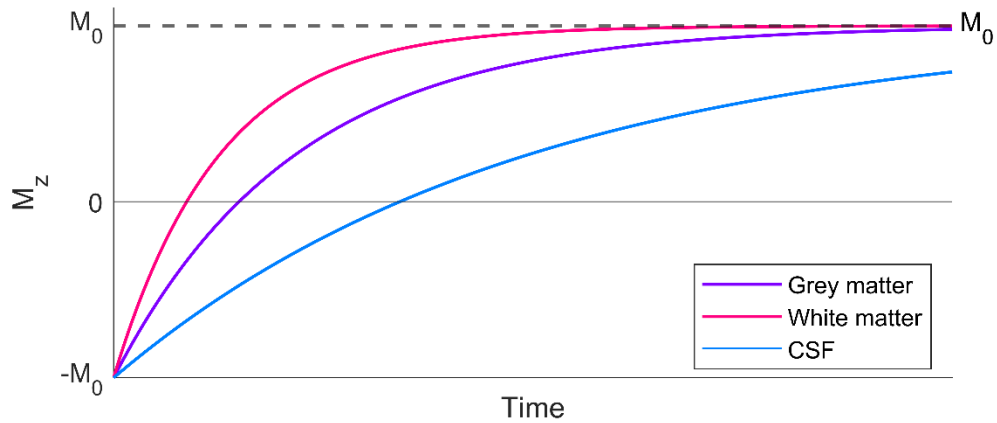


Figure 3.1. An inversion recovery sequence showing longitudinal (T_1) recovery following a 180° inversion pulse for grey matter (purple), white matter (pink) and CSF (blue).

Different tissues have different T_1 values, therefore by changing the time at which the signal is acquired (TI), different contrasts can be created. At 7 T, grey matter T_1 is approximately 1940 ms, white matter 1130 ms (Wright et al., 2008) and CSF 4425 ms (Rooney et al., 2007) and hence at a time less than T_1 of CSF, white matter signal will have recovered the most, appearing brightest, and CSF will appear dark, resulting in a

T_1 weighted image. This is the contrast used in many structural brain images such as MPRAGE (see section 3.5.1).

3.1.2.2 Transverse Relaxation

Transverse relaxation is the process via which spins which were initially coherent after a 90° pulse move out of phase with each other, i.e. the transverse magnetisation, M_{xy} , returns to zero. Transverse relaxation is governed by the time constant T_2 which is known as the spin-spin relaxation time as it depends on dephasing of spins. T_2 is due to magnetic interactions between neighbouring spins causing the magnetisation to dephase, and reducing the transverse magnetisation. T_2 is an irreversible loss of magnetisation; once the spins have dephased they cannot be brought back into phase. Additional dephasing will occur due to inhomogeneities in the magnetic field which results in variations in Larmor frequency, causing the spins to get out of phase with each other. However, the dephasing due to static inhomogeneities can be rephased. The combination of both fluctuating intrinsic T_2 dephasing and dephasing due to static field inhomogeneities, T_2' , is known as T_2^* , which is given by,

$$\frac{1}{T_2^*} = \frac{1}{T_2} + \frac{1}{T_2'}. \quad (10)$$

The rate of change of magnetisation is described by the Bloch equations, which can be solved to generate an equation for the recovery of transverse magnetisation, M_{xy} , for T_2 effects:

$$M_{xy}(t) = M_0 e^{-\frac{t}{T_2}}. \quad (11)$$

As illustrated in Figure 3.2, after a 90° RF pulse, all the spins are in phase. Over time, the spins dephase over the transverse plane as each precesses at a slightly different rate. However, if a 180° refocussing pulse is applied at time $TE/2$, the spins will be flipped, and any acquired positive phase is flipped and vice versa. The vectors will then precess at the same rate as before, due to the same inhomogeneities, and go back into phase producing an echo at time TE . However, loss of phase due to T_2 effects cannot be refocussed, as the dephasing is due to randomly fluctuating fields which cannot be exactly rephased, so the echo will be smaller in amplitude than the initial signal (Figure 3.2A). The time at which the echo is created is TE , the echo time, with the 180° RF pulse applied at $TE/2$. If $TE \sim T_2$, this results in a T_2 weighted image. Common values of T_2 at 7 T are 55 ms for grey matter and 46 ms for white matter (Yacoub et al., 2001).

Due to magnetic field susceptibility effects, T_2^* decreases with increasing magnetic field strength. T_2^* at 7 T is on the order of 33 ms for grey matter and 27 ms for white matter (Peters et al., 2007), but will also be dependent on the scanner.

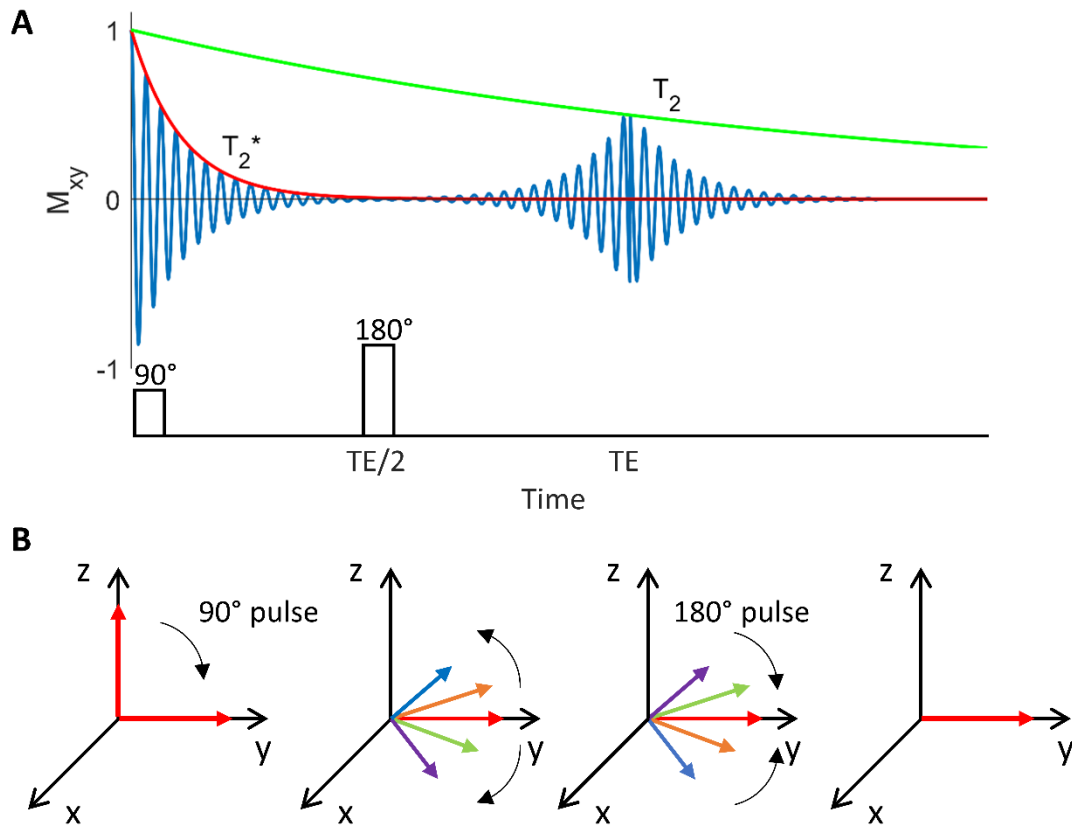


Figure 3.2. (A) Spin echo following a 90° pulse and a 180° pulse at time $TE/2$ which produces an echo at time TE . The echo is reduced in height by T_2 and decays exponentially with T_2^* . (B) Showing magnetisation during a spin echo. A 90° pulse is used to tip the magnetisation into the xy plane. The spins dephase and spread out across the xy plane as different spins experience slightly different precession rates. A 180° pulse is applied which flips the spins and the spins refocus to form an echo.

3.2 Magnetic Resonance Imaging (MRI)

The next requirement in MRI is to spatially encode the measured NMR signal to produce an image where each pixel is a representation of the magnetisation at a given location. This can be done using magnetic field gradients which spatially encode the magnetisation. This was first proposed in 1973 by Mansfield (Mansfield & Grannell, 1973) and Lauterbur (Lauterbur, 1973). An image represents the magnetisation at that point in time. Since magnetisation is transient, MRI can be used to image dynamic processes. This requires fast imaging techniques, which were made possible with the development of echo planar imaging (EPI) in 1977 (Mansfield, 1977).

3.2.1 Magnetic Field Gradients

Magnetic field gradients are used to spatially encode magnetisation. Gradients cause magnetisation at different spatial locations to precess at different frequencies (Equation 4). Magnetic field gradients (G) can be applied along any direction ($i = x, y, \text{ or } z$),

$$G_i = \frac{dB_z}{di}. \quad (12)$$

These gradients act to change the local magnetic field at a position r , causing a change in the Larmor frequency with spatial location,

$$\omega(r) = \gamma(B_0 + G_r r). \quad (13)$$

Therefore frequency is now a function of position, which can be used to localise signals and build up a 3D image. This signal in the time domain can be converted into a magnetisation distribution in the spatial domain using a Fourier transform. The concept of k-space, which is in the spatial frequency domain, is a helpful tool where the images are considered to be acquired before being transformed into Cartesian coordinates. MR images are acquired by navigating through k-space by altering gradient parameters in time. Commonly, k-space is sampled line by line in the read direction.

3.2.1.1 Slice Selection

Rather than excite the whole head, it is possible to apply the magnetic field gradients so that only a thin slab of spins are excited to generate a slice. In the presence of a magnetic field gradient, applied along the z -axis, the Larmor frequency will vary linearly in the direction of z . An RF pulse can be applied over a narrow bandwidth of frequencies so that only spins with those frequencies are excited (Figure 3.3). The position of the spins excited can be modulated by changing the carrier frequency of the RF pulse. In order to excite a thin rectangular slab in space, a sinc pulse is used in frequency space, since the Fourier transform of sinc function is a rectangular window. The thickness of the slice (Δz) selected will depend on the amplitude of the gradient, G_z , or the bandwidth, $\Delta\omega$ of the RF pulses,

$$\Delta z = \frac{\Delta\omega}{\gamma G_z}. \quad (14)$$

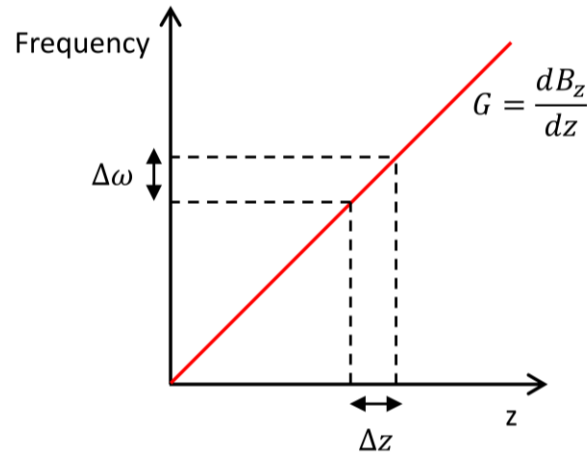


Figure 3.3. Magnetic field gradient $\frac{dB_z}{dz}$ applied along the z -axis results in the variation of frequency along the z -axis. Therefore a narrow range of frequencies ($\Delta\omega$) can be excited to select a narrow range in space (Δz), a slice.

3.2.1.2 Frequency Encoding

After slice selection, additional gradients can be applied to spatially encode information in the selected 2D slice. Frequency encoding uses the same concept as slice selection, whereby a linear magnetic field gradient is used to generate a Larmor frequency that varies linearly across the sample. The spins in a slice have already been selected using a gradient along the z -axis during the RF pulse, so to achieve further localisation another gradient is applied along the x -axis during the readout. This gradient results in a variation of precessional frequency of the selected spins. A Fourier transform of this signal then provides information about the spin density along one dimension.

3.2.1.3 Phase Encoding

To encode in a third dimension, y , a further magnetic field gradient along the y -axis can be applied. Again, this uses the same concept as before, except rather than a linear variation of frequency with space, now the phase of the magnetisation is linearly varied along the y -axis. A y -gradient is applied before the frequency encoding for a short period of time to induce a specific phase. Therefore each line of k -space corresponds to a different combination of phase and frequency. A further phase encoding gradient can be applied in the third dimension (slice select dimension (i.e. z -axis in the example above)) to produce a 3D image. The benefits of 3D images are explored in Section 3.4.2 and used in Chapter 6.

3.3 MRI System

An MRI scanner comprises the magnet, shims, gradient coils and RF coils. The MRI scanner used in this thesis was the Philips 7 T Achieva at the Sir Peter Mansfield Imaging Centre, University Of Nottingham, UK.

An MRI scanner requires a strong, homogeneous B_0 magnetic field. The magnet requires a high magnetic field strength (of the order 100 000 times larger than Earth's magnetic field), and also needs to be spatially uniform and temporally stable to produce undistorted images. Most magnets for MRI are made using superconducting electromagnets where magnetic fields are generated by currents flowing through wires. Large magnetic fields can be created from solenoids, where the field is proportional to the number of turns per unit length and the current through the coil. This can be done using superconducting wires with no resistance, so there is no heat dissipation. Below a certain threshold, superconducting materials have no resistance, dependent on temperature, current density and the field. Therefore, the magnet is kept in liquid helium to keep it superconducting. The magnetic field outside the scanner, termed the fringe field, needs to be reduced as it has the potential to cause harm (to people with pacemakers for example). This reduction is achieved by shielding the 7 T scanner room with iron, for the SPMIC scanner this consists on the order of 300 tonnes of iron.

Within the magnet are the shim coils. Shims are used to cancel out inhomogeneity in the main magnetic field. Shims can be passive, in the form of magnetic material (typically steel) permanently in the scanner to overcome major inhomogeneity in the magnet. Alternatively shims can be active, where currents are generated through coils to create weak spatially varying magnetic fields. This helps to overcome inhomogeneity caused by the field distortions arising from placing a human body in the scanner.

Within the magnet bore are the gradient coils. Gradient coils consist of three coils to generate the magnetic field gradients required to make the MR image (see Section 3.2.1). By rapidly varying the large current through the gradient coils in time, an image can be formed. It is this variation of current through these coils which generates the acoustic noise experienced during an MRI scan.

Radio frequency (RF) coils are used for both exciting and receiving the signal. As the detected RF signals are small, the magnet needs to be placed in a screened room to prevent external RF being picked up. Generally the transmit coil and receive coil are

two separate coils, with the transmit coil able to generate a uniform field over a large region and the receive coil optimised to be able to detect much smaller RF signals. The receive coil should be placed as close as possible to the part of the body being imaged. In this thesis, all data were acquired using a head-only transmit coil and 32-channel receive coil (Nova Medical).

3.4 Imaging Techniques

The focus of this thesis is to collect images rapidly to assess dynamic changes in the brain. This section will outline sequences to do this and summarise the structural images used. The sequence of RF pulses used to generate a specific image is called a pulse sequence. A pulse sequence consists of variable sequence parameters such as the repetition time, TR, which is the length of time between repeating the pulse sequence and the echo time, TE. These can be altered to produce different image contrasts.

3.4.1 2D Gradient Echo Planar Imaging

Using the techniques described in Section 3.2, a pulse sequence would need to be repeated for each phase encoding step in order to collect data to completely sample k – space and generate a 2D image. This would result in a long imaging time, depending on the number of phase encoding steps and the TR. One way to speed up the acquisition of an image is to acquire data corresponding to more than one phase encoding step for each excitation pulse. This is what is done in echo planar imaging, or EPI (Mansfield, 1977). In EPI, all phase encoding steps are collected after a single RF excitation pulse, meaning an entire image can be acquired from one RF pulse. This is achieved using rapidly switching gradients in the read direction to create multiple gradient echoes, therefore EPI requires very strong gradients and is intensive on the scanner hardware (Section 3.3). Since the whole of k -space is sampled after a single RF pulse, EPI has high temporal resolution which makes it an excellent tool for studying dynamic processes such as the brain's response to stimuli and is commonly used in fMRI (see fMRI Section 3.6) and is used in this thesis in Chapter 7.

The pulse sequence for a gradient echo EPI sequence is shown in Figure 3.4. Firstly, an RF excitation pulse is applied along with a slice selection gradient. This is shown for a 90° RF pulse, but is typically chosen to be the Ernst angle (see below). After this, two gradients, G_{read} and G_{phase} are used to move from the centre to the edge of k -space. Following this, the frequency encoding gradient is used to sample a line of k -space.

After a line is acquired, a small phase encoding gradient (blip) is used to step to a new line of k-space. The frequency encoding gradient is then reversed and a new line of k-space is acquired. This sequence is repeated and alternating lines of k-space are acquired until all of k-space has been acquired. The repeated reversals of the gradients acts to dephase and rephase the transverse magnetisation which generates an echo. The lines of k-space must be collected before the magnetisation decays away, which makes EPI T_2^* dependent.

When the whole of k-space is acquired after one RF pulse, the sequence is referred to as single shot EPI. EPI can also be performed in a multi-shot sequence, where multiple excitation pulses are used to acquire each portion of k-space data. The benefit of this is that image distortion can be reduced and higher resolution can be achieved, however, the images take longer to acquire (increases by the number of multi-shots used). Spatial image distortion can be a problem in EPI, as EPI has a low bandwidth in the phase encoding direction. If there is a small deviation in precessional frequency there can be a mislocalisation of information in the phase encode direction causing geometric distortions. This is worse at air-tissue interfaces and increased at higher field strength where B_0 inhomogeneities are often more severe.

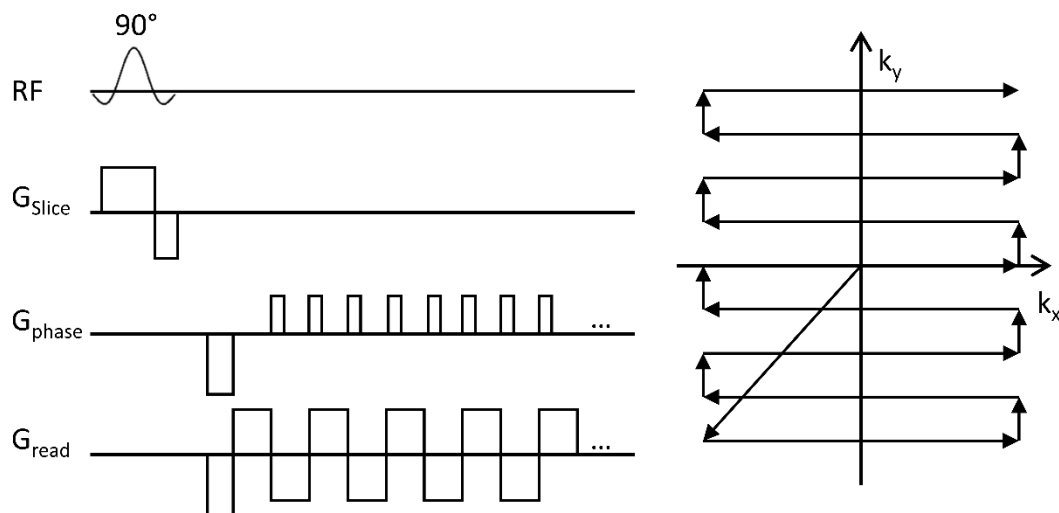


Figure 3.4. 2D gradient EPI pulse sequence diagram. The RF pulse tips the magnetisation into the transverse plane to excite a 2D slice. A coincident slice selective gradient is used to excite a thin slice. Gradients are rapidly switched along the read direction and a phase encoding gradient is used to step lines across k-space and generate an echo train from a single FID.

3.4.2 3D Gradient Echo Planar Imaging

With 2D EPI, one slice is acquired at a time, with the sequence repeated to collect multiple slices of a 2D image. This means the time to acquire the volume of interest is

directly proportional to number of slices. An alternative is to image a 3D volume (Poser et al., 2010). In 3D imaging, instead of exciting a slice, a thick slab is excited with the RF pulse. Spatial information in the third (z) dimension (slice select direction) is encoded using a second phase encoding in z (in addition to that in y). The same slab is repeatedly excited and data are collected for a k_x - k_y plane in increments of k_z (Figure 3.5). Since the same slab is excited each time, the signal from each voxel contributes to every measurement resulting in 3D EPI having a higher signal to noise ratio (SNR) than 2D EPI. Because of this increase in SNR, 3D EPI can be used to achieve higher spatial resolution whilst maintaining sufficient SNR. An example of a 3D EPI image, used in Chapter 6, is given in Figure 3.6. Another benefit is that parallel imaging (discussed below, Section 3.4.3) can be applied in both of the two phase encode directions which will reduce scan time. However, the acquisition time is usually longer than 2D EPI and therefore 3D sequences are also thought to be more affected by physiological noise than 2D (Poser et al., 2010; Van der Zwaag et al., 2012). Also, there is less time for the signal to recover from a voxel before it is excited again, which reduces the steady state signal. Because of this, the flip angle used is typically lower than 90° . The optimum flip angle to give the highest signal is found from the Ernst angle (Equation 15), which is dependent on the TR and T_1 . At lower TRs, the signal does not have time to fully recover between inversions when using a 90° pulse. Therefore, flip angles lower than 90° are used to maximise the signal for a given TR, as less recovery time is required. The optimum angle is defined by the Ernst angle (Ernst & Anderson, 1966), α_E ,

$$\alpha_E = \cos^{-1}(e^{-TR/T_1}). \quad (15)$$

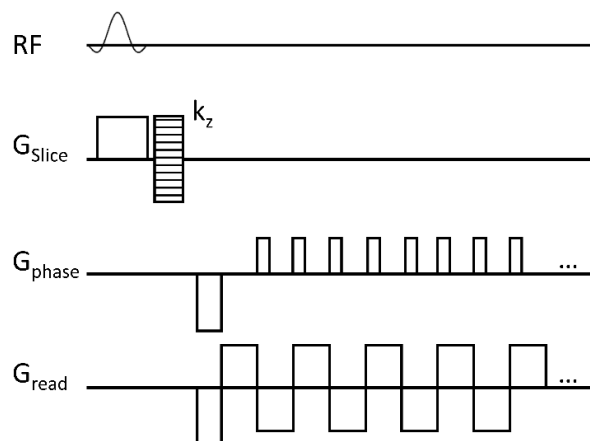


Figure 3.5. 3D EPI pulse sequence diagram. The RF pulse (typically low flip angle) tips the magnetisation into the transverse plane. A slab is repeatedly excited with varying increments of k_z . Gradients are rapidly switched along the read and phase encoding directions to acquire the whole of k -space from a single FID.

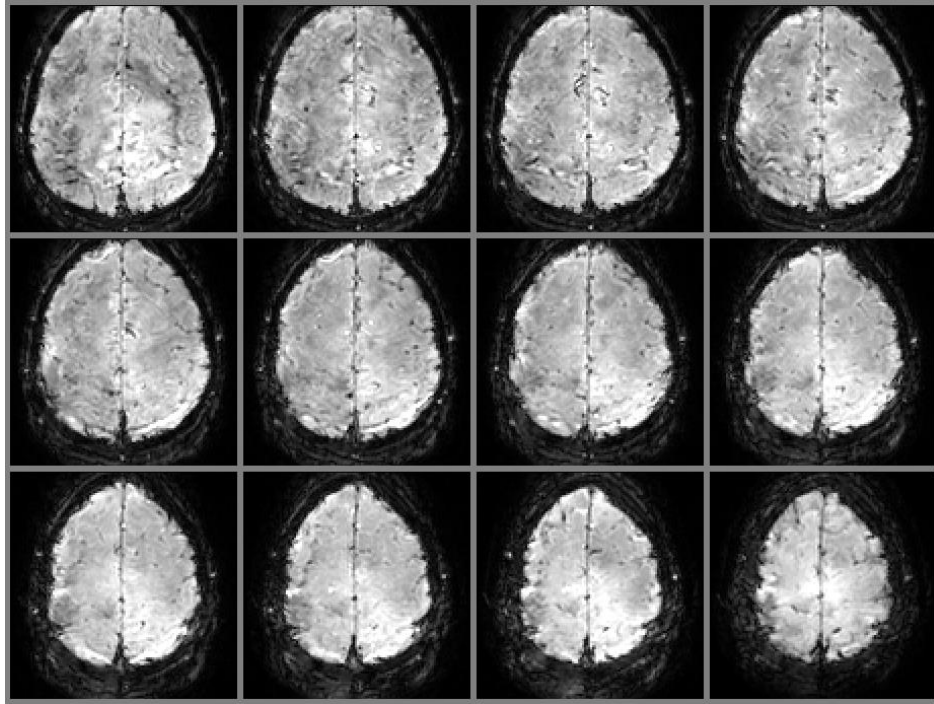


Figure 3.6. Example of a 3D EPI image with 12 slices with 1.5 mm isotropic resolution and SENSE 2.5 x 1 as used in Chapter 6.

3.4.3 Accelerated Imaging

One possible way to speed up imaging is to sample fewer lines of k-space. Although this would usually reduce field of view or increase blurring, k-space has phase-conjugate symmetry so only half of k-space needs to be sampled, and the other half can be reconstructed. This is called ‘half-scan’ on a Philips scanner console. This approach only works if the centre of k-space is aligned with the centre of the echo, therefore in reality more than half of k-space is sampled, commonly 75%. Whilst this reduces acquisition time, it always comes with a drop in SNR as less data points are acquired (Feinberg et al., 1986). Halfscan can be used with 2D and 3D EPI acquisitions.

Another method to reduce the image acquisition time is parallel imaging. The term parallel imaging refers to the use of multiple receive coils at once to spatially encode based on the RF receive coil sensitivity. The induced voltage at a RF receive coil from a source depends on the position of the coil in relation to the source. This means each receive coil will measure a slightly different signal, with receive coils closer to the source measuring a stronger signal (see Figure 3.7). Therefore, extra information about the source is available from the coil sensitivities. By using this information about spatial location, less phase encode steps are needed which reduces acquisition time. Reducing the sampling of k-space reduces the field of view causing aliasing. An aliased image is

created for each coil. The full image is then created by separating the aliased image based on weightings of the coil sensitivities and a matrix inversion. The full image can then be reconstructed from the coil sensitivities.

The version of parallel imaging used on Philips scanners is called SENSE (sensitivity encoding in the image domain) (Pruessmann et al., 1999). In SENSE, firstly the coil sensitivity maps from each receive coil must be generated to provide the weightings. This is usually done at the start of the scan session. Then the reduced k-space data are acquired in parallel at each receive coil. Using this information, the full image can then be reconstructed by unfolding the aliased images via matrix inversion. For example, a SENSE factor of 2 results in k-space being under sampled by a factor of 2. An issue with this technique is that it comes with a reduction in SNR as the amount of k-space that is sampled has been reduced. However in EPI, especially at high field where T_2^* is lower, the benefit of being able to sample k-space faster means that less T_2^* decay occurs, so the gain in signal outweighs the loss in SNR of using SENSE. Also, the shorter acquisition time reduces image distortions. SENSE can be used in both 2D and 3D EPI, with the advantage that in 3D EPI SENSE acceleration can be applied along both of the phase encode directions.

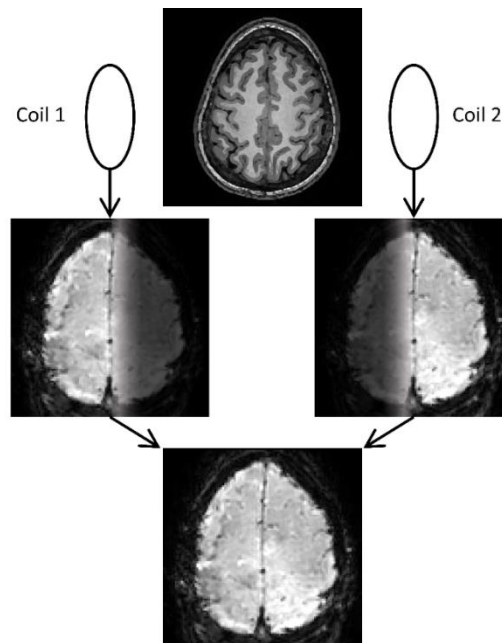


Figure 3.7. A simple example of SENSE for two receive coils. Images are acquired from each coil, each with different coil sensitivity. Coil sensitivity maps are used to reconstruct the full image based on the weightings of the sensitivities.

So far, the fast imaging techniques introduced have reduced acquisition time of a volume of images through reduction in k-space sampling. Yet, for a 2D acquisition, each slice still has to be selected one at a time which is time-consuming. Simultaneous multi-slice (SMS or multiband (MB)) imaging, instead, allows multiple slices to be excited at the same time, significantly reducing the repetition time, up to ten times has been demonstrated (Feinberg & Setsompop, 2013), though typically a factor of 3 or 4 is used. Larkman et al. first demonstrated simultaneous multi-slice imaging in the human leg (Larkman et al., 2001). The method works by introducing a frequency offset into the RF pulse, to simultaneously excite multiple 2D slice planes. The signal measured at a coil will be a linear combination of the signal from each slice, weighted by the coil sensitivities. The simultaneously excited 2D slices can then be separated by using the coil sensitivities. One major advantage of this technique is that there is no undersampling of k-space so SNR is not reduced in this way. However, there are losses in SNR due to a coil geometry factor (known as g-factor) which results in spatially varying noise enhancement (Moeller et al., 2010). Multiband imaging is often used in conjunction with SENSE, as utilised in Chapter 7. However, care must be taken not to increase both SENSE and MB factor to unacceptable levels where the SNR becomes too low.

3.5 Structural Imaging

Throughout this thesis structural images are required for coregistration of MEG data and anatomical references in fMRI chapters. In the following sections the structural images implemented are described.

3.5.1 Magnetisation Prepared Rapid Gradient Echo (MPRAGE)

Magnetisation prepared rapid gradient echo, or MPRAGE (Mugler & Brookeman, 1990), is a T_1 -weighted gradient echo sequence which can produce high spatial resolution 3D images with good contrast between grey and white matter (see Figure 3.8). MPRAGE is used widely in neuroimaging to produce anatomical images - in this thesis it is used in both MEG and fMRI work as an anatomical reference image. The sequence comprises an initial 180° pulse to invert the magnetisation followed by a delay to achieve T_1 weighting – this is the magnetisation preparation period. Following this, there is a rapid gradient echo sequence to sample the prepared magnetisation. Finally, there is a recovery period after the acquisition. By doing the magnetisation preparation

as a separate step, the acquisition is faster compared to a steady-state acquisition scheme with the same contrast (Mugler & Brookeman, 1990).



Figure 3.8. Example of a sagittal slice of an MPRAGE image used in Chapter 4 and Chapter 5 as a MEG anatomical image with 1 mm isotropic resolution.

3.5.2 Phase Sensitive Inversion Recovery (PSIR)

Phase sensitive inversion recovery (PSIR) is another anatomical image sequence used in this thesis in Chapters 6 and 7, which was used to create grey (GM) and white matter (WM) maps. PSIR (Hou et al., 2005) is an inversion recovery technique where the inversion time is chosen to give signal equal in magnitude from grey matter and white matter, in between the two null points. Phase correction is then used to retrieve the sign of the magnetisation from this image. In this thesis, an adapted PSIR protocol (Mougin et al., 2016) was used which combines PSIR with MP2RAGE (Marques et al., 2010). The inversion recovery image at TI_1 (the first inversion time) is interleaved with a recovered image acquired at TI_2 (second inversion time) after the WM, GM and CSF null points. The phase of the second image is used to restore the sign of the first image and the magnitude is used to correct the bias field (Van de Moortele et al., 2009). The benefits of this version is increased contrast-to-noise ratio (CNR) between GM and WM, and the ability to acquire high resolution data (0.7 mm at 7 T) in 3 directions in a reasonable acquisition time (e.g. 6 minutes). An example PSIR image is shown in Figure 3.9.

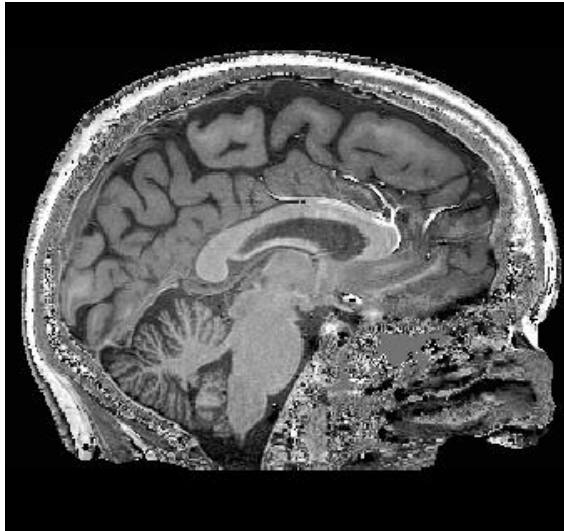


Figure 3.9. Example of a 7 T PSIR image with 0.7 mm isotropic resolution used in Chapter 6, for the same subject as Figure 3.8.

3.5.3 Fast Low Angle Shot (FLASH)

The fast low angle shot pulse sequence (FLASH) (Haase et al., 1986) is a gradient echo sequence which uses a low flip angle and short TR so that the sequence can be rapidly repeated, therefore FLASH is a very fast imaging technique. FLASH can be T_1 or T_2^* weighted depending on the TE and the flip angle. A longer TE maximises T_2^* weighting and a long TR and low flip angle minimises any T_1 dependence. In Chapter 6, a T_2^* weighted FLASH sequence was used to be sensitive to magnetic susceptibility changes around veins, so that a vein mask could be produced to aid fMRI analysis. For example, in Figure 3.10, veins appear dark in the FLASH image.

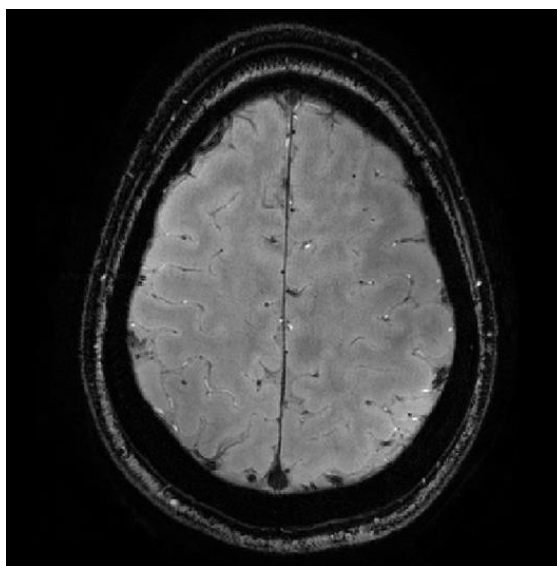


Figure 3.10. Example of a T_2^ weighted FLASH image with $TE = 11.4$ ms, resolution $0.5 \times 0.5 \times 1.5$ mm.*

3.6 Functional Magnetic Resonance Imaging (fMRI)

Having described the process by which an MR signal is produced and detected, this section details the basis of functional MRI (fMRI). fMRI is widely used to measure human brain function, and has become perhaps the most popular technique in neuroimaging since it was first performed in 1992 (Bandettini et al., 1992; Kwong et al., 1992; Ogawa et al., 1992). Commonly, fMRI is based on the blood oxygen level dependent (BOLD) contrast due to changes in the concentration of deoxyhaemoglobin in the blood. Other non-BOLD mechanisms can be used to study functional activity, such as arterial spin labelling (ASL) which is commonly based on changes in cerebral blood flow (CBF), and vascular space occupancy (VASO) which measures changes in cerebral blood volume (CBV). These methods are discussed further in Chapter 6.

The BOLD contrast was first demonstrated in 1990 (Ogawa et al., 1990). The BOLD response in the brain is due to the combination of the paramagnetic nature of deoxygenated blood, and the brain's response to a stimulus resulting in a large overshoot of cerebral blood flow. Changes in neural activity result in a mixture of changes in CBF, CBV and cerebral metabolic rate of oxygen consumption (CMRO₂) hence the BOLD signal is an indirect measure of neural activity. These vascular changes are slow and therefore fMRI has poor temporal resolution compared to MEG. On the other hand, fMRI has excellent spatial resolution, capable of resolving sub-millimetre activation.

3.6.1 Origin of fMRI Signal

3.6.1.1 Physiology

As described in Chapter 2, neuronal activity results in currents across the cell membrane which create fluctuation in electric potentials – extracellular potentials. These can be characterised into low and high frequency components. Local field potentials (LFPs) are low frequency components reflecting synaptic activity, whereas high frequency activity called multi-unit activity (MUA) represents spiking (Logothetis, 2002). BOLD fMRI has been shown to correlate with LFPs corresponding to neural input, rather than spiking activity which represents neural output (Goense & Logothetis, 2008).

Neuronal activity requires glucose and oxygen for metabolism which is supplied via blood flow. The brain is one of the most energetic organs in the body, yet it has no store

of oxygen, meaning it needs a constant delivery of blood. As a result, the brain receives around 15% of the body's total cardiac output, making it one of the most heavily perfused organs in the body. The grey matter, where the cell bodies are, receives more blood supply than the white matter. This is achieved by large arteries (red vessels in Figure 3.11) to provide oxygen-rich blood which branch into arterioles in grey matter, which further divide into capillaries where exchange of nutrients between blood and tissue occurs. Blood then returns back towards the heart via venules into larger pial veins on the cortical surface (Duvernoy et al., 1981), see black vessels in Figure 3.11. Upon neural activity, muscles surrounding the arterioles and capillaries dilate to increase blood flow, to increase the delivery of glucose and oxygen. CBF is defined as the rate of delivery of arterial blood to the capillary bed. Cerebral blood volume (CBV) is the fraction of tissue volume occupied by blood vessels and it can be subdivided into arterial (aCBV), capillary and venous volumes (vCBV).

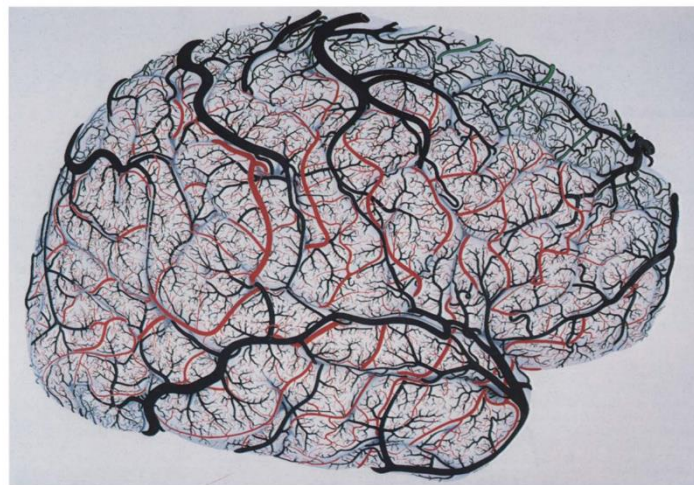


Figure 3.11. Drawing of cortical vasculature of the human brain. Arteries are shown in red and veins are shown in black. Shows large pial vessels on the cortical surface, which branch into smaller diameter arterioles and venules. Taken from Duvernoy et al. (Duvernoy et al., 1981).

3.6.1.2 BOLD Contrast

When a region of the brain is active, there will be an increase in $CMRO_2$ in that area. Oxygen is delivered to the area via oxyhaemoglobin in the blood. Oxyhaemoglobin is diamagnetic, yet when oxyhaemoglobin loses oxygen it becomes deoxyhaemoglobin which is paramagnetic. Deoxyhaemoglobin creates local magnetic field distortions in and around blood vessels, which will cause local spins to precess at different frequencies causing more dephasing and shortening T_2^* . Following neural activity,

CBF and CBV increase to provide oxygen. The increase in flow is considerably higher than the consumption of oxygen (Figure 3.12B). This means there is a local decrease in the concentration of deoxyhaemoglobin, increasing the local MR signal, giving rise to the BOLD signal.

The BOLD signal increases with increasing field strength. At higher magnetic field, there will be larger magnetisation present due to Boltzmann statistics (see Equation 6), leading to increased signal. Susceptibility effects are increased at higher field strength, and since BOLD is due to susceptibility effects of deoxyhaemoglobin, BOLD contrast also increases (van der Zwaag et al., 2009). However, the increased susceptibility effects will shorten the time in which data can be collected due to decreasing T_2 and T_2^* at higher field (see Section 3.6.2.1).

The change in MR signal over time after a stimulus is known as the BOLD haemodynamic response function (HRF), as shown in Figure 3.12. The BOLD response consists of the primary response and the post-stimulus undershoot which can take up to a minute to return to baseline (Frahm et al., 1996). Some models also include an initial dip in BOLD signal before the primary response, however this has not been observed consistently across studies (Buxton, 2001). The positive primary response is an increase in MR signal relative to baseline beginning at the start of stimulation, which reaches its peak around typically 6 s after stimulus onset. This lag in the peak of the response from the start of the stimulus is often referred to as haemodynamic lag. The peak in signal corresponds to an oversupply of oxygenated blood, as the concentration of deoxyhaemoglobin decreases. Following the primary response, the BOLD signal then undershoots below baseline before returning to baseline. The BOLD signal is measured as a percentage change from baseline. The origin of the post-stimulus undershoot is the subject of much debate and is discussed and investigated in more detail in Chapter 6. One widely acknowledged theory is the Balloon model where vasculature causes the slow return of blood volume (Lu et al., 2004) (Buxton et al., 1998). However, other theories such as elevated $CMRO_2$ suggest the undershoot is a metabolic phenomenon, whilst another theory of decreased CBF suggests a neuronal origin (Uludağ et al., 2004).

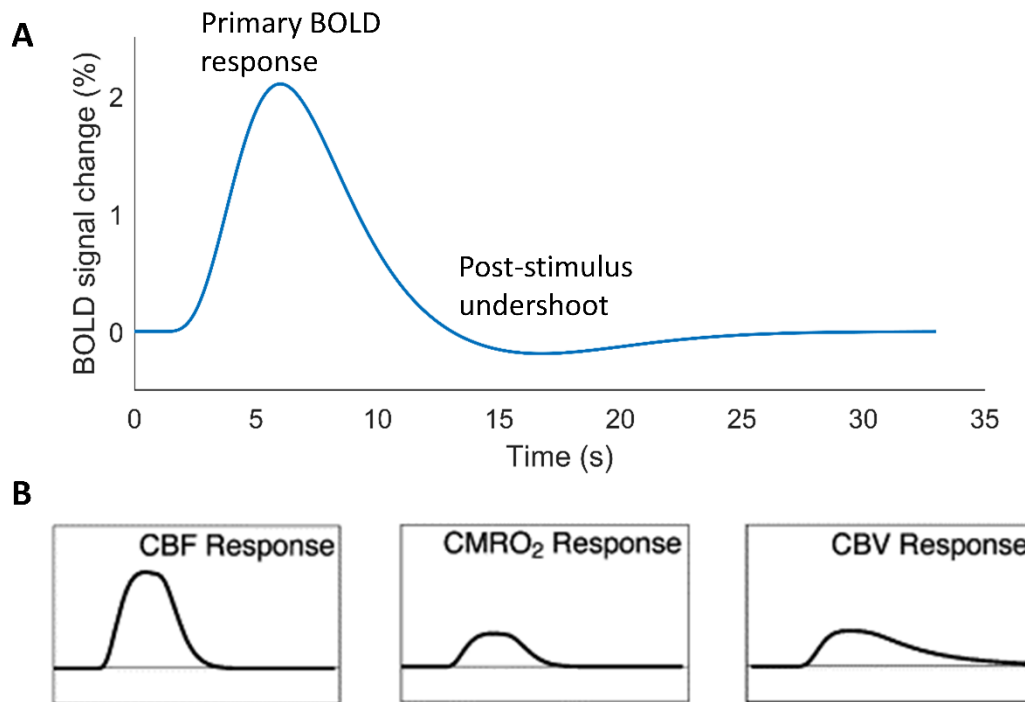


Figure 3.12. (A) BOLD haemodynamic response function to a short stimulus at time 0 s. The BOLD signal rises to a peak at 6 s from stimulus onset and undershoots before returning to baseline. (B) Classical view of CBF, CMRO₂ and CBV responses during the BOLD response, adapted from Buxton et al. (Buxton et al., 2004). CBF increases more than CMRO₂ during the primary response, causing a decrease in deoxyhaemoglobin and increased BOLD signal. During the post-stimulus undershoot, CBV remains elevated while CBF and CMRO₂ return to baseline, resulting in a negative BOLD signal termed the post-stimulus undershoot.

3.6.2 Detection of the fMRI Response

3.6.2.1 Data Acquisition

To measure the BOLD signal, the pulse sequence needs to be sensitive to T_2^* changes. The greatest BOLD signal occurs for an echo time which matches T_2^* of grey matter. The data acquisition also needs to be fast to capture dynamic changes in the brain, and have the spatial resolution and coverage to cover the region of interest with sufficient detail. There is a trade-off between higher spatial resolution and SNR, as the smaller the volume that is imaged (i.e. each voxel of the image), the fewer nuclei there will be within that volume, thus reducing the signal which can be measured. Generally the spatial resolution is selected to be the minimum resolution to resolve the region of interest (ROI). As explained in Section 3.4.1, gradient echo EPI is T_2^* -weighted and is a fast sequence, therefore it is commonly used in fMRI.

In order to assess the quality of fMRI data, it is necessary to measure the image stability over time, as fMRI is primarily concerned with fluctuations in time. Temporal SNR

(tSNR) is the metric typically used to determine the image quality over time, where the mean signal from each voxel over a given time is calculated and divided by the variation in the signal of that voxel over time:

$$tSNR = \frac{\textit{mean signal of time series}}{\textit{standard deviation of time series}} \quad (16)$$

This measure is used in chapter 6 and 7.

3.6.2.2 Data Analysis: General Linear Model

Once an fMRI time series has been acquired, data are analysed to produce maps of activation from which time courses of the response can be extracted. However, the signal change measured in fMRI is of the order of a few percent (dependent on the field strength and stimulus) and it can be a challenge to separate the signal related to underlying neuronal activity from the noise. This is particularly challenging as noise can vary across the image, making it more difficult to eliminate. The signal will also contain contributions from thermal noise and physiological noise, such as respiration and cardiac noise. Physiological noise increases at higher field strength (Triantafyllou et al., 2005) but can be corrected using methods such as RETROICOR (retrospective correction of physiological motion effects in the image domain) (Glover et al., 2000). RETROICOR is applied in post-processing and works by assuming the time course consists of the signal plus noise from cardiac and respiratory traces, using the phase of the cardiac and respiratory trace to calculate and remove the noise. Respiration can be recorded during the scan using bellows, and the cardiac trace is measured using a peripheral pulse unit attached to the index finger.

One way to solve the problem of separating signal from noise when a task is performed is to use a general linear model (GLM). This models the data as a linear combination of various models (called regressors). The contribution to the variance of the fMRI time course of a single voxel from each regressor is assessed, and given a weighting depending on its contribution, which gives the overall best fit to the data. The group of regressors is called a design matrix. The model of the task is derived by predicting the shape of the BOLD response to the stimulus. The model is created by modelling the stimulus as a boxcar which is 1 when the stimulus is on and 0 when it is off, which is then convolved with a standard HRF (Figure 3.12). The shape of the time course is

specified but the amplitude is unknown. The voxel time courses, Y , are considered to be a sum of the regressors multiplied by a weighted factor, β , known as beta weights, plus noise, e , which can be described by the matrix equation,

$$Y = X\beta + e \quad (17)$$

where Y is the data vector, X is the matrix of model functions (or regressors) also known as the design matrix, β is the amplitude weighting (beta weight) vector and e is the noise vector. The analysis aims to find the values of the weights which best explains the signal variation. A large positive beta weight suggests the measured voxel time course is well explained by the regressor. This analysis is performed over all voxels to find voxels which match the modelled response and are therefore considered to be activated by the task.

Statistical analysis is then performed to test the significance of the active voxels. Since there are thousands of voxels in an fMRI dataset, testing each voxel will result in a multiple comparisons problem. Applying an uncorrected p-value of $p < 0.05$ will result in a large number of false positives – if there are 10 000 voxels, 500 voxels will appear active when they are not truly active. Therefore, p-values are usually corrected to overcome this issue. The familywise error rate (FWE) is the probability of a false positive occurring. A Bonferroni correction is performed where the p-value is divided by the number of tests being performed in all voxels. However, for the large number of tests performed in fMRI, Bonferroni correction can be too strict and remove true positives as well as false positives. An alternative method is false discovery rate (FDR) correction (Benjamini & Hochberg, 1995), where rather than controlling false positives in the entire image, only false positives among the voxels which produce a significant result are controlled. This correction method means that the number of false positives is related to the number of active voxels, such that if there is little activity the correction is strict, but it is more conservative for large active regions (Genovese et al., 2002).

Once maps of significant activation are produced, the time course can be investigated in the active voxels. These are usually created by comparing the signal during the task to a baseline period either at the start of the scan session or at the end of each trial, and converted into a percentage signal. These methods are used in Chapters 6 and 7.

3.7 References

- Bandettini, P. A., Wong, E. C., Hinks, R. S., Tikofsky, R. S., & Hyde, J. S. (1992). Time course EPI of human brain function during task activation. *Magnetic Resonance in Medicine*, 25(2), 390-397.
- Benjamini, Y., & Hochberg, Y. (1995). Controlling the false discovery rate: a practical and powerful approach to multiple testing. *Journal of the Royal statistical society: series B (Methodological)*, 57(1), 289-300.
- Bloch, F. (1946). Nuclear induction. *Physical review*, 70(7-8), 460.
- Buxton, R. B. (2001). The elusive initial dip. *Neuroimage*, 13(6 Pt 1), 953-958.
- Buxton, R. B., Uludağ, K., Dubowitz, D. J., & Liu, T. T. (2004). Modeling the hemodynamic response to brain activation. *Neuroimage*, 23, S220-S233.
- Buxton, R. B., Wong, E. C., & Frank, L. R. (1998). Dynamics of blood flow and oxygenation changes during brain activation: The balloon model. *Magnetic Resonance in Medicine*, 39(6), 855-864.
- Duvernoy, H. M., Delon, S., & Vannson, J. L. (1981). Cortical blood vessels of the human brain. *Brain Research Bulletin*, 7(5), 519-579.
- Ernst, R. R., & Anderson, W. A. (1966). Application of Fourier transform spectroscopy to magnetic resonance. *Review of Scientific Instruments*, 37(1), 93-102.
- Feinberg, D. A., Hale, J. D., Watts, J. C., Kaufman, L., & Mark, A. (1986). Halving MR imaging time by conjugation: demonstration at 3.5 kG. *Radiology*, 161(2), 527-531.
- Feinberg, D. A., & Setsompop, K. (2013). Ultra-fast MRI of the human brain with simultaneous multi-slice imaging. *Journal of Magnetic Resonance*, 229, 90-100.
- Frahm, J., Krüger, G., Merboldt, K. D., & Kleinschmidt, A. (1996). Dynamic uncoupling and recoupling of perfusion and oxidative metabolism during focal brain activation in man. *Magnetic Resonance in Medicine*, 35(2), 143-148.
- Genovese, C. R., Lazar, N. A., & Nichols, T. (2002). Thresholding of Statistical Maps in Functional Neuroimaging Using the False Discovery Rate. *Neuroimage*, 15(4), 870-878.
- Glover, G. H., Li, T.-Q., & Ress, D. (2000). Image-based method for retrospective correction of physiological motion effects in fMRI: RETROICOR. *Magnetic Resonance in Medicine*, 44(1), 162-167.
- Goense, J. B. M., & Logothetis, N. K. (2008). Neurophysiology of the BOLD fMRI Signal in Awake Monkeys. *Current Biology*, 18(9), 631-640.
- Haase, A., Frahm, J., Matthaei, D., Hancike, W., & Merboldt, K. D. (1986). FLASH imaging. Rapid NMR imaging using low flip-angle pulses. *Journal of Magnetic Resonance (1969)*, 67(2), 258-266.
- Hennel, J. W., Klinowski, J., & Haeberlen, U. (1993). *Fundamentals of nuclear magnetic resonance*: Longman Scientific & Technical Essex.
- Hou, P., Hasan, K. M., Sitton, C. W., Wolinsky, J. S., & Narayana, P. A. (2005). Phase-Sensitive T1 Inversion Recovery Imaging: A Time-Efficient Interleaved Technique for Improved Tissue Contrast in Neuroimaging. *American Journal of Neuroradiology*, 26(6), 1432.
- Huber, L. (2020). Map of Ultra-High Field MRI scanners worldwide. Retrieved from <https://www.google.com/maps/d/u/0/viewer?mid=1dXG84OZIAOxjsqh3x2tGzWL1bNU>
- Institute of Medicine Food and Nutrition Board. (2004). *Dietary reference intakes for water, potassium, sodium, chloride, and sulfate. Panel on Dietary Reference*

- Intakes for Electrolytes and Water, Standing Committee on the Scientific Evaluation of Dietary Reference Intakes, Food and Nutrition Board.* Washington, D.C.: Washington, D.C. : National Academies Press.
- Kwong, K. K., Belliveau, J. W., Chesler, D. A., Goldberg, I. E., Weisskoff, R. M., Poncelet, B. P., Kennedy, D. N., Hoppel, B. E., Cohen, M. S., & Turner, R. (1992). Dynamic magnetic resonance imaging of human brain activity during primary sensory stimulation. *Proceedings of the National Academy of Sciences*, 89(12), 5675.
- Larkman, D. J., Hajnal, J. V., Herlihy, A. H., Coutts, G. A., Young, I. R., & Ehnholm, G. (2001). Use of multicoil arrays for separation of signal from multiple slices simultaneously excited. *Journal of Magnetic Resonance Imaging*, 13(2), 313-317.
- Lauterbur, P. C. (1973). Image formation by induced local interactions: examples employing nuclear magnetic resonance. *nature*, 242(5394), 190-191.
- Logothetis, N. K. (2002). The neural basis of the blood–oxygen–level–dependent functional magnetic resonance imaging signal. *Philosophical Transactions of the Royal Society of London. Series B: Biological Sciences*, 357(1424), 1003-1037.
- Lu, H., Golay, X., Pekar, J. J., & van Zijl, P. C. M. (2004). Sustained Poststimulus Elevation in Cerebral Oxygen Utilization after Vascular Recovery. *Journal of Cerebral Blood Flow & Metabolism*, 24(7), 764-770.
- Mansfield, P. (1977). Multi-planar image formation using NMR spin echoes. *Journal of Physics C: solid state physics*, 10(3), L55.
- Mansfield, P., & Grannell, P. K. (1973). NMR'diffraction'in solids? *Journal of Physics C: solid state physics*, 6(22), L422.
- Marques, J. P., Kober, T., Krueger, G., van der Zwaag, W., Van de Moortele, P.-F., & Gruetter, R. (2010). MP2RAGE, a self bias-field corrected sequence for improved segmentation and T1-mapping at high field. *Neuroimage*, 49(2), 1271-1281.
- Moeller, S., Yacoub, E., Olman, C. A., Auerbach, E., Strupp, J., Harel, N., & Ugurbil, K. (2010). Multiband multislice GE-EPI at 7 tesla, with 16-fold acceleration using partial parallel imaging with application to high spatial and temporal whole-brain fMRI. *Magnetic Resonance in Medicine*, 63(5), 1144-1153.
- Mougin, O., Abdel-Fahim, R., Dineen, R., Pitiot, A., Evangelou, N., & Gowland, P. (2016). Imaging gray matter with concomitant null point imaging from the phase sensitive inversion recovery sequence. *Magnetic Resonance in Medicine*, 76(5), 1512-1516.
- Mugler, J. P., & Brookeman, J. R. (1990). Three-dimensional magnetization-prepared rapid gradient-echo imaging (3D MP RAGE). *Magnetic Resonance in Medicine*, 15(1), 152-157.
- Ogawa, S., Lee, T.-M., Kay, A. R., & Tank, D. W. (1990). Brain magnetic resonance imaging with contrast dependent on blood oxygenation. *Proceedings of the National Academy of Sciences*, 87(24), 9868-9872.
- Ogawa, S., Tank, D. W., Menon, R., Ellermann, J. M., Kim, S. G., Merkle, H., & Ugurbil, K. (1992). Intrinsic signal changes accompanying sensory stimulation: functional brain mapping with magnetic resonance imaging. *Proceedings of the National Academy of Sciences*, 89(13), 5951.
- Peters, A. M., Brookes, M. J., Hoogenraad, F. G., Gowland, P. A., Francis, S. T., Morris, P. G., & Bowtell, R. (2007). T2* measurements in human brain at 1.5, 3 and 7 T. *Magnetic Resonance Imaging*, 25(6), 748-753.

- Poser, B. A., Koopmans, P. J., Witzel, T., Wald, L. L., & Barth, M. (2010). Three dimensional echo-planar imaging at 7 Tesla. *Neuroimage*, *51*(1), 261-266.
- Pruessmann, K. P., Weiger, M., Scheidegger, M. B., & Boesiger, P. (1999). SENSE: sensitivity encoding for fast MRI. *Magnetic Resonance in Medicine: An Official Journal of the International Society for Magnetic Resonance in Medicine*, *42*(5), 952-962.
- Purcell, E. M., Torrey, H. C., & Pound, R. V. (1946). Resonance absorption by nuclear magnetic moments in a solid. *Physical review*, *69*(1-2), 37.
- Rabi, I. I., Zacharias, J. R., Millman, S., & Kusch, P. (1938). A New Method of Measuring Nuclear Magnetic Moment. *Physical review*, *53*(4), 318-318.
- Rooney, W. D., Johnson, G., Li, X., Cohen, E. R., Kim, S.-G., Ugurbil, K., & Springer Jr, C. S. (2007). Magnetic field and tissue dependencies of human brain longitudinal 1H₂O relaxation in vivo. *Magnetic Resonance in Medicine*, *57*(2), 308-318.
- Triantafyllou, C., Hoge, R. D., Krueger, G., Wiggins, C. J., Potthast, A., Wiggins, G. C., & Wald, L. L. (2005). Comparison of physiological noise at 1.5 T, 3 T and 7 T and optimization of fMRI acquisition parameters. *Neuroimage*, *26*(1), 243-250.
- Uludağ, K., Dubowitz, D. J., Yoder, E. J., Restom, K., Liu, T. T., & Buxton, R. B. (2004). Coupling of cerebral blood flow and oxygen consumption during physiological activation and deactivation measured with fMRI. *Neuroimage*, *23*(1), 148-155.
- Van de Moortele, P.-F., Auerbach, E. J., Olman, C., Yacoub, E., Ugurbil, K., & Moeller, S. (2009). T1 weighted brain images at 7 Tesla unbiased for Proton Density, T2* contrast and RF coil receive B1 sensitivity with simultaneous vessel visualization. *Neuroimage*, *46*(2), 432-446.
- van der Zwaag, W., Francis, S., Head, K., Peters, A., Gowland, P., Morris, P., & Bowtell, R. (2009). fMRI at 1.5, 3 and 7 T: Characterising BOLD signal changes. *Neuroimage*, *47*(4), 1425-1434.
- Van der Zwaag, W., Marques, J., Kober, T., Glover, G., Gruetter, R., & Krueger, G. (2012). Temporal SNR characteristics in segmented 3D-EPI at 7T. *Magnetic Resonance in Medicine*, *67*(2), 344-352.
- Wright, P., Mougín, O., Totman, J., Peters, A., Brookes, M., Coxon, R., Morris, P., Clemence, M., Francis, S., & Bowtell, R. (2008). Water proton T₁ measurements in brain tissue at 7, 3, and 1.5 T using IR-EPI, IR-TSE, and MPRAGE: results and optimization. *Magnetic Resonance Materials in Physics, Biology and Medicine*, *21*(1-2), 121.
- Yacoub, E., Shmuel, A., Pfeuffer, J., Van De Moortele, P.-F., Adriany, G., Andersen, P., Vaughan, J. T., Merkle, H., Ugurbil, K., & Hu, X. (2001). Imaging brain function in humans at 7 Tesla. *Magnetic Resonance in Medicine*, *45*(4), 588-594.

CHAPTER 4

4 Post-stimulus Oscillatory MEG Responses

4.1 Abstract

Modulation of beta-band neural oscillations during and following movement is a robust marker of brain function. In particular, the post-movement beta rebound (PMBR), which occurs on movement cessation, has been related to inhibition in the healthy brain, and is perturbed in disease. However, to realise the potential of the PMBR as an indicator of brain function, its modulation by task parameters must be characterised and its functional role determined. In this chapter, MEG was used to image brain electrophysiology during and after a grip-force task, with the aim to characterise how task duration, in the form of an isometric contraction, modulates beta responses. Fourteen participants exerted a 30% maximum voluntary grip-force for 2, 5 and 10 s. The results showed that the amplitude of the PMBR is systematically modulated by task duration, with increasing duration significantly reducing PMBR amplitude and increasing its time-to-peak. The time at which the PMBR returned to baseline was unchanged by task duration. No variation in the amplitude of the movement related beta decrease (MRBD) with task duration was observed. The results add to the emerging picture that, in the case of a carefully controlled paradigm, beta modulation can be systematically controlled by task parameters. These findings will support design of clinically relevant paradigms and analysis pipelines in future use of the PMBR as a marker of neuropathology.

The work in this chapter formed a considerable component of the published paper: ‘Post-stimulus responses are modulated by task duration’, DO Pakenham et al, *NeuroImage* 2020. It has also been presented at Biomag 2020 in Philadelphia.

4.2 Introduction

As described in Chapter 2, the amplitude of neural oscillations can be modulated by a task. Motor tasks typically generate electrophysiological responses in the beta (15 – 30 Hz) frequency band (Jurkiewicz et al., 2006). Such responses comprise a decrease in amplitude during movement - the movement related beta decrease (MRBD) - followed by an increase in amplitude above baseline on movement cessation - the post-movement beta rebound (PMBR). These phenomena are well documented (Cheyne, 2013; Kilavik et al., 2013; Pfurtscheller & Lopes da Silva, 1999), yet a full understanding of how they are modulated by stimulus parameters and their functional roles is lacking. Whilst similar characteristics are seen in the alpha band (commonly referred to as mu when observed in central regions), and movement can induce an increase in power in the gamma band, there has been a greater focus on beta band activity when studying the motor cortex as modulations are more pronounced in MEG, hence this chapter will be primarily concerned with characterising beta band activity.

The MRBD is not only observed during movement but also during motor planning (Tzagarakis et al., 2010) and imagining movements (Pfurtscheller et al., 2005; Schnitzler et al., 1997) (albeit at lower amplitude). Previous work has shown that the MRBD amplitude, duration and onset time is modulated by task parameters such as certainty of movement or number of movement options. For example, Tzagarakis and colleagues (Tzagarakis et al., 2010) showed that during movement preparation (i.e. prior to actual movement onset), the drop in beta oscillatory amplitude was significantly greater in a case where the direction of movement was certain, than a case where the direction of movement was uncertain. However, during movement itself, the MRBD has been shown to be relatively unaffected by parameters such as force output, rate of force development (Fry et al., 2016), or speed of force development (Stancak Jr & Pfurtscheller, 1995, 1996). This has led to a hypothesis that the MRBD relates to movement planning and execution, but not to measurable changes in peripheral output.

The PMBR has also been shown to be modulated by a number of task parameters. Stevenson et al. (2011) measured MEG responses to finger abductions performed for a range of durations (1, 2, 4 and 6 s) and found an increase in the total PMBR with increased task duration, which plateaued after stimulus durations of 4 s. Another study (Parkes et al., 2006) showed that the rate of finger extensions affects PMBR, with faster

movements resulting in a higher amplitude. The PMBR has been found to be larger for incorrect compared to correct button presses (Koelewijn et al., 2008). Whilst Heinrichs-Graham and colleagues (2017) showed the PMBR is stronger for cues to terminate movement at 2 s compared to at 2.5 s. It is therefore evident that the PMBR can be modulated by a number of movement parameters.

Variation between cohorts in PMBR have also been seen. A number of studies have shown modulation of PMBR across subjects; for example, Gaetz et al. (2010) found that the PMBR is significantly reduced in children and diminished in adolescents compared to adults. Vakhtin et al. (2015) showed similar findings and suggested that the PMBR is modulated by age in a predictable manner in adolescents. Perhaps most importantly, the PMBR is modulated by disease, opening the potential for its use as a clinical tool. For example, Robson et al. (Robson et al., 2016) showed that patients with schizophrenia have a smaller PMBR compared to healthy controls, and the amplitude of the response decreases with increasing symptom severity. In a study of autism, the PMBR was found to be reduced when patients were observing hand movements compared with healthy controls (Honaga et al., 2010). In a study of stroke patients, Parkkonen et al. (2017) found the PMBR was decreased bilaterally (i.e. independent of affected side) in patients during passive finger movements compared with controls, perhaps providing some indication regarding the functional role and origin of this response. Other studies have shown modulation in the timing rather than amplitude of the response. Barratt et al. (2017) found patients with multiple sclerosis had delayed PMBR compared to healthy controls. Proudfoot et al. (2017) showed a delayed PMBR and larger MRBD during movement execution in patients with amyotrophic lateral sclerosis. Together, these results suggest that the PMBR is functionally important, and the generation of a better understanding of its role may lead to its use as a predictor of a number of disorders.

The fact that the MRBD and PMBR differ in their response to stimulus parameters, individual differences and disease suggests that they also have different neuronal generators (Parkkonen et al., 2015). This is supported by a number of studies showing that the generator of the PMBR is anterior in the brain compared to the MRBD (Fry et al., 2016; Jurkiewicz et al., 2006; Salmelin et al., 1995; Stancak Jr & Pfurtscheller, 1995). The MRBD has been described as a “cortical gate” to facilitate local processing in sensory and motor cortex (Fry et al., 2016; Stevenson et al., 2011), whereas the

PMBR might provide active inhibition of motor cortex (Pfurtscheller et al., 1996; Stevenson et al., 2011). This latter hypothesis is supported by a measurable relationship between the concentration of gamma-aminobutyric acid (GABA) and the PMBR (Cheng et al., 2017; Gaetz et al., 2011; Hall et al., 2011; Muthukumaraswamy et al., 2013). It has further been suggested that whilst the MRBD might represent local processing, the PMBR is likely to relate to long range integrative processes over distributed networks (Tewarie et al., 2018). This also agrees with resting state studies showing that long range networks are mediated by beta band oscillations (Hipp et al., 2012). It is therefore tempting to suggest that the PMBR is representative of top-down inhibitory control of the primary motor region, by a wider sensorimotor and premotor network.

Whilst beta band activity is integral to motor function, beta band activity does not occur in isolation and modulations in other frequency bands, such as alpha and gamma bands for a simple motor task have also been observed previously. Movement-related gamma is commonly reported in the 60 – 90 Hz frequency range in the contralateral primary motor region (Wiesman et al., 2020). Studies of motor gamma have shown brief bursts of gamma activity on movement execution for simple finger movement tasks, i.e. a gamma event related synchronization (ERS) (Cheyne et al., 2008; Gaetz et al., 2010). Muthukumaraswamy and colleagues showed that gamma activity was modulated by the type of movement performed, as gamma activity was not present in a passive task but was observed in an active contraction, suggesting gamma plays a role in information encoding rather than simply muscle contraction (Muthukumaraswamy, 2010). Gamma band activity is thought to serve many different functions and is fundamental to information processing (Fries, 2009), representing top-down processes (Donner et al., 2009) but its role in motor function is still not entirely clear. Alpha band activity in the sensorimotor area is thought to be tightly linked to beta band activity in the motor cortex, and follows the similar desynchronization (termed event related desynchronization, ERD) and rebound pattern (event related synchronization, ERS) observed in the beta band (Salenius et al., 1997). The mu rhythm can be modulated by attention (Anderson & Ding, 2011; Jones et al., 2010) and is thought to represent a sensory gating mechanism (Jones et al., 2010).

Before understanding the functional role of neural oscillations in the motor cortex, it is necessary that they are consistently and correctly characterised. Understanding how the

PMBR is affected by task parameters is important to reduce variance within cohorts and better disassociate disease types from variation due to the way a task is performed. However, the characterisation of PMBR variation with task parameters remains poorly documented. For example, precise movement parameters (i.e. rate, force of movement etc.) are rarely recorded and although Pfurtscheller et al. argued in 1999 that it was necessary to leave 10 s between movements to allow the PMBR to return to a true baseline (Pfurtscheller & Lopes da Silva, 1999), this has rarely been adhered to.

As such, investigations of PMBR have used relatively short periods of rest between tasks with these rest periods varying between studies. Commonly, the inter-stimulus-interval is between 1 and 6 s, with some of this time window used to define a “baseline” from which MRBD and PMBR are quantified (Gaetz et al., 2010; Heinrichs-Graham et al., 2017; Koelewijn et al., 2008; Parkes et al., 2006; Stevenson et al., 2011). If task parameters and/or disease states modulate the duration or amplitude of the PMBR, then it is likely that such a task design will lead to incorrect definition of the baseline, and consequently spurious quantification of the MRBD and PMBR.

The importance of long baseline periods was highlighted in recent work by Fry and colleagues (2016) who carefully controlled force levels during a wrist flexion task. Here, force was held at 5%, 15%, 35% and 60% of each subject’s maximum voluntary force (MVF) for 3 s, with rest periods extending to 25 s. The study found that PMBR amplitude increases with increasing force output, whilst MRBD was unchanged. The authors also explored changing the rate of force development (RFD), with participants required to reach 65% MVF in either 6.25 s, 2.25 s or 0.75 s, with a minimum rest period of 25 s between contractions. The study showed that a greater RFD resulted in a higher amplitude and shorter duration PMBR. Importantly, the duration of the PMBR was shown to vary systematically between 4 s and 7.5 s; this metric was only possible due to the long inter-stimulus interval (baseline was defined to be at least 16.8 s after stimulus onset). In contrast, many other studies have recorded the PMBR as lasting about 2 s after movement offset (Gaetz et al., 2010; Heinrichs-Graham et al., 2017; Jurkiewicz et al., 2006; Kilavik et al., 2013; Parkes et al., 2006). Heinrichs-Graham et al. (2017) defined baseline a maximum of 3.85 s after stimulus offset of the previous trial, which will likely cause a premature end to the PMBR. This clearly demonstrates the problem related to baseline definition, implying studies using shorter inter-stimulus

intervals may not measure a true baseline which will have detrimental effects on the interpretation of modulations in MRBD or PMBR.

Fry et al. (2016) provide a basis for more precise characterisation of movement related beta responses via careful control and characterisation of motor output. However, the complexity of the RFD task they employed (in which task force and duration varied) means that it is unclear which stimulus parameter drove the measured changes in PMBR. Heinrichs-Graham et al. (2017) concluded that future work should investigate the relationship between MRBD duration and PMBR amplitude using carefully controlled motor output. These arguments show the increasing importance of developing a new generation of well controlled motor tasks with long inter-stimulus intervals for use in electrophysiology investigations.

Here, in this Chapter, a well-controlled motor task is used to fully parameterise the changes in beta band oscillations with task duration. In particular, the aim is to understand how task duration affects amplitude and duration of post-stimulus responses, and their relationship to the MRBD during stimulation.

4.3 Methods

4.3.1 Subjects

Fifteen healthy volunteers (10 female, aged 27 ± 3 (mean \pm SD) years) took part in this study, which was approved by the University of Nottingham Medical School Research Ethics Committee. All volunteers gave written, informed consent and self-reported as being right-handed.

4.3.2 Motor Paradigm

Maximum voluntary force (MVF) was determined for each subject prior to the start of the experiment. Subjects were encouraged to exert their maximum force, with verbal encouragement provided, using a grip-force bar (Current Designs, Philadelphia, USA) for a period of 1-2 s, with two repeats separated by ~ 15 s. The MVF was taken as the peak maximum force averaged over a 200 ms epoch achieved in either repeat, compared with the baseline reading of the force bar (mean over 400 ms at the end of the recording). A target force for the main study was then set at 30% of the subject's MVF.

Subjects lay supine with their head resting in the MEG helmet and held a grip-force bar in their right hand (Figure 4.1A). Subjects applied a force to the bar when visually cued. The visual stimulus comprised a target profile of the required force output, which appeared 2 s before the stimulus period onset. During the stimulus period, subjects were instructed to squeeze the grip-force bar to match the target profile at 30% MVF for periods of either 2, 5 or 10 s. The force output was measured directly and overlaid onto the target profile in real-time, to provide visual feedback (see Figure 4.1B). The target profile remained on the screen 0.5 s after the end of the stimulus. A fixation cross was then presented on the centre of the screen for 27.5 s, giving a 30 s rest period between contractions ensuring sufficient time for the post-stimulus response to end. During the rest period, subjects relaxed their hand and refrained from movement. Complete relaxation of the hand was made possible by use of a fingerless glove attached to the grip-force bar; this was worn on the right hand, enabling subjects to release their grip without dropping the bar (Figure 4.1A). All stimulus presentation, as well as the recording of outputs from the grip-force bar, was implemented using in-house software written using the Psychophysics Toolbox (Brainard, 1997) in MATLAB (MathWorks, Massachusetts, USA). Subjects were instructed to lie as still as possible and only move

the hand needed to perform the task. Only monitoring of movement of the hand and forearm performing the task was carried out.

Within one experimental run, 15 trials of each of the three stimulus durations were presented in a pseudo-random order, providing a total of 45 trials per run. Two runs were acquired per subject, each lasting ~27 minutes, with a ~15-minute break between runs. Before and after each run, subjects attempted to reach two, 3-s-long target profiles of 100% MVF with a 30 s rest period between, akin to that used in Fry et al. (Fry et al., 2017) to assess fatigue within and between runs. A schematic overview of the experiment is shown in Figure 4.1C.

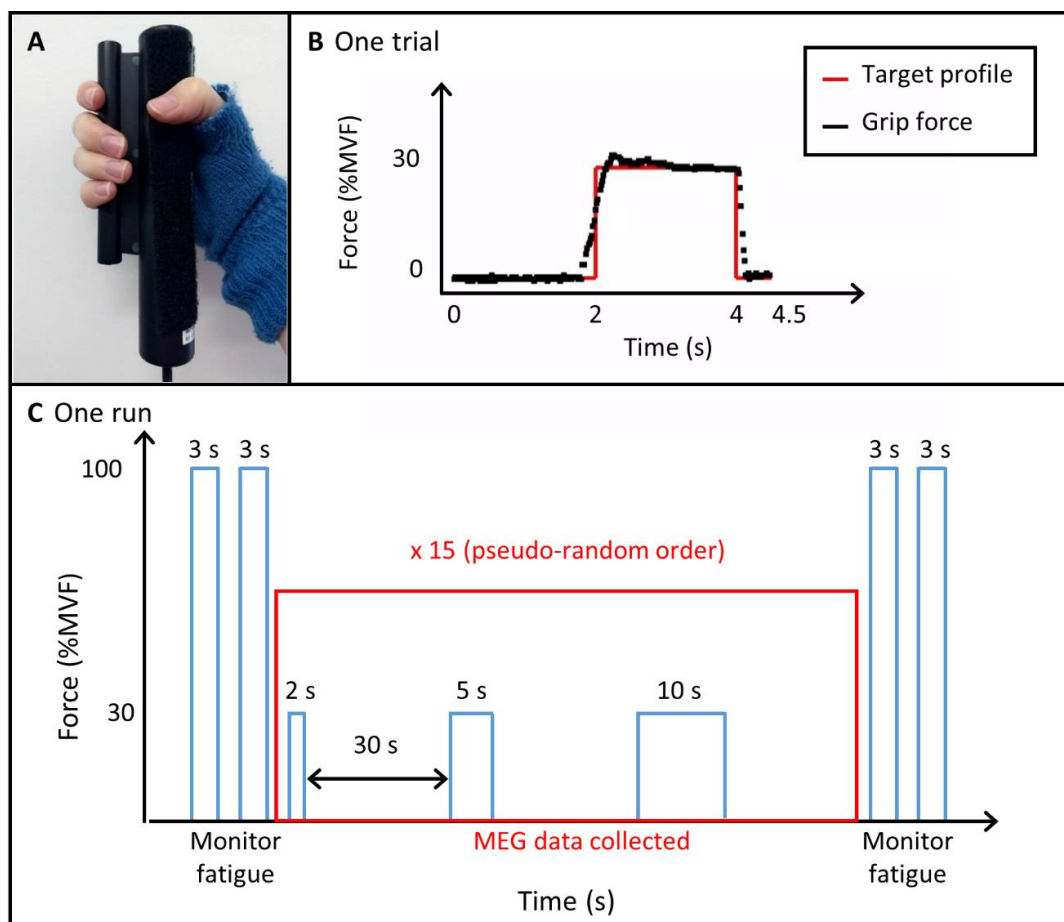


Figure 4.1. Overview of the experiment. (A) The grip-force bar (Current Designs, Philadelphia, USA) attached to a fingerless glove to allow relaxation of the hand. (B) Example single trial. The target force profile is shown (red) with real-time force output from a single trial overlaid (black). The visual stimulus appeared 2 s before the force output period, which was sustained for 2, 5 or 10 s [shown here for 2 s]. The profile remained on the screen for a further 0.5 s after the end of the force output period and was followed by a fixation cross for 27.5 s. (C) Schematic diagram of one run. Single trials were repeated 15 times for each duration in a pseudo-random order, totalling 45 trials within one run. This was followed by a second run after an approximately 15-minute break. Two 3 s target profiles of 100% MVF were presented before and after each run to monitor fatigue.

4.3.3 Data Acquisition

Surface Ag/AgCl electrodes (EasyCap GmbH, Germany) to measure electromyography (EMG) were attached to the subject's right arm, in order to quantify the time at which the subject gripped the bar, as well as to monitor any extra, unwanted movements of the hand during the rest periods. Electrode pairs were positioned in a bipolar configuration over the forearm extensor bundle (channel 1) and forearm flexor bundle (channel 2) muscle groups. EMG data were acquired using an ExG amplifier (Brain Products GmbH, Germany) and BrainVision recorder (v 1.1), with a sampling rate of 1000 Hz and frequency range of 0.016 – 250 Hz (with 30 dB roll-off at high frequencies). A marker was inserted at the start of the experiment to temporally synchronise with the MEG data.

MEG data were recorded using a 275-channel CTF MEG system (MISL, Coquitlam, BC) in synthetic 3rd order gradiometer configuration at a sampling rate of 600 Hz. Head localisation coils were attached to the subject at the nasion and preauricular points as fiducial markers. To coregister brain anatomy with the MEG sensor geometry, a digitised head shape was created using a 3D digitiser (Polhemus, Colchester, VT, USA) relative to the head localisation coils. T₁-weighted anatomical images were acquired using a 1 mm isotropic MPRAGE sequence on either a 3 T or 7 T Philips Achieva MR scanner. Coregistration was achieved by matching the digitised head surface with the head surface from the anatomical MRI using an iterative closest point algorithm.

4.3.4 Pre-processing

4.3.4.1 EMG

EMG data were downsampled to 600 Hz to match the MEG data sampling rate. An in-house MATLAB programme was developed to determine the exact time of the start and end of the individual grip contractions. For this, EMG data were filtered from 1 to 150 Hz and rectified. The standard deviation in baseline EMG activity was determined in a time window 13 to 23 s after the visual cue for contraction offset from all contractions, independently for each EMG channel and subject. This baseline period was used to determine a noise threshold which was defined as three times the standard deviation of the baseline (Cheyne et al., 2008; Muthukumaraswamy, 2010). Subsequently, the onset of contraction was defined as the first time point, in a 0.5 s window either side of the visual cue, when the signal was greater than the noise threshold. If the contraction did

not start in this time, the trial was discarded. Similarly, contraction offset was determined as the last time point, in a time window 0.5 s either side of the cue to end contraction, when the signal was greater than the noise threshold. Trials were also discarded if any extra movements occurred during the rest period, detected in both EMG channels.

4.3.4.2 MEG

MEG data were bandpass filtered from 1 to 150 Hz then visually inspected to remove any trials and channels which contained excessive interference (e.g. due to SQUID resets or excessive muscle activity) using DataEditor (CTF MEG, Canada). This resulted in the removal of, on average, 3 ± 2 trials (range 0 – 9) out of 15 trials per run, per condition. In addition, markers were added to the MEG data at the times of the contraction start and end, based on the EMG data. The MEG data were then segmented in two ways:

- 1) To investigate the MRBD, the start of an epoch was defined as 3 s before the contraction onset (to ensure all preparatory effects were included).
- 2) To investigate the PMBR, the data were segmented according to contraction offset. In this case, the start of an epoch was defined as 5 s, 8 s and 13 s before contraction offset. The trials were then segmented into 31, 34 and 39 second epochs (in relation to the cued contraction durations of 2, 5 and 10 s respectively). The epoch lengths were chosen to allow for discrepancies between cued and actual contraction periods.

Following filtering, artefact removal and segmentation, these data were processed using a beamformer spatial filter (see below).

4.3.5 Post-processing

4.3.5.1 Grip-force and EMG

Mean grip-force during each contraction was determined, with the first and last 0.5 s excluded so that only steady force output was captured. Force output was calculated as a percentage of the subject's MVF. The mean rectified EMG signal from each muscle group (forearm extensors and flexors) was determined for each grip contraction (again excluding the first and last 0.5 s of each trial). Separately for the force output and EMG measures, paired Student's T-tests were used to assess whether any difference in force

output/EMG signal occurred in the different runs of the experiment, and a repeated measures ANOVA (RM ANOVA) was used to assess whether there was a systematic difference in force output/EMG signal between durations of the task.

The 100% MVF contractions were analysed in post-processing to determine if there had been an effect of fatigue. To do this, the peak force over a 200 ms epoch during the 100% MVF contractions was compared to the subject's MVF which had been determined at the start of the experiment. Paired Student's T-tests were used to determine if there were any significant differences in %MVF before and after a run.

4.3.5.2 Source Localisation

Pre-processed MEG data were analysed using a scalar Linearly Constrained Minimum Variance (LCMV) beamformer (Robinson & Vrba, 1998; Van Veen & Buckley, 1988; Van Veen et al., 1997) with a local spheres forward model (see Chapter 2). Pre-processed MEG data were further filtered to the beta band (15 – 30 Hz), and active and control windows contrasted to determine the spatial signature of task induced beta modulation in the brain. To localise the MRBD, the active window was defined from contraction onset to the cued duration of the contraction (i.e. 2 s, 5 s or 10 s). The control window was defined to start 24 s after contraction onset with a length matching the active window (i.e. terminating at 26, 29 or 34 s). To localise the PMBR, the active window was defined as an 8 s window starting from contraction offset (Fry et al., 2016). The control window was 16-24 s after contraction offset. Similarly, to investigate alpha (as both visual and motor alpha were investigated in this chapter, motor alpha is simply referred to as alpha rather than mu for ease) and gamma responses, MEG data were filtered to the alpha band (8 – 13 Hz) and gamma band (60 – 90 Hz).

The covariance matrices used to compute the weights for the beamformer were created by concatenating the (band filtered) data from the active and control windows for the 2, 5 and 10 s trials. Concatenation of data from different task durations was valid as it is expected that the neuronal sources of the PMBR or MRBD are the same for all task durations. This concatenation provided the maximum amount of data for the calculation of the covariance matrix thus increasing its accuracy (Brookes et al., 2008). Since evidence suggests the MRBD and PMBR are generated by different sources (Fry et al., 2016; Jurkiewicz et al., 2006), the responses were localised separately using the relevant concatenated active and control window data to calculate two sets of

covariance matrices and beamformer weights. Pseudo-t-statistical (\mathbb{F} -stat) images were produced to localise the MRBD and the PMBR by contrasting the relevant active and control windows. A single peak was identified for the MRBD and the PMBR for each subject over all task durations, to ensure source localisation was not biased to any one task duration. The peak of the activity in the left sensorimotor cortex was found for each subject and used to extract time frequency spectrograms (TFSs) at these locations for each subject with maximum signal to noise (see Section 4.3.5.3 below).

In order to compare the spatial locations of the MRBD and PMBR, the \mathbb{F} -stat maps were transformed from subject space into MNI space using FLIRT (FSL) (Jenkinson et al., 2002; Jenkinson & Smith, 2001). For each subject, MNI coordinates of the peak location in left sensorimotor cortex of the MRBD and PMBR were recorded. Paired Student's t-tests were used to separately identify changes in peak locations in the x (left/right), y (anterior/posterior) and z (superior/inferior) direction between the MRBD and PMBR. Group average \mathbb{F} -stat maps were produced for the PMBR and MRBD by averaging across subjects.

Additional analysis was performed to investigate alpha and gamma responses. Alpha and gamma filtered data were beamformed separately with weights formed for each frequency band individually. \mathbb{F} -stat images were calculated for the alpha ERD, using the same timings as the beta MRBD, and alpha ERS, using the same timings as the PMBR. For the gamma ERS during the task, the same timings as the MRBD were used. Again, as for the beta band, the peak of the activity in the left (contralateral) sensorimotor cortex was found for each subject for each of these additional contrasts and used to extract time frequency spectrograms (TFSs) at these locations for each subject with maximum signal to noise. For alpha, the peak of the activity in the visual cortex was also found (see Appendix B).

4.3.5.3 Time Frequency Spectrograms (TFSs)

TFSs were generated with the MEG data filtered into a broader 1 – 150 Hz band (to capture the broad band response) and all data were used to create the covariance matrix. The derived beamformer weights were multiplied by the MEG sensor data to provide estimates of the electrical signal at the identified locations. TFSs were created by frequency filtering these time courses into 31 overlapping frequency bands, with a Hilbert transform used to calculate the envelope of activity within each band (see

Chapter 2). Envelope time courses were averaged over all trials of the same duration (i.e. 2, 5 or 10 s), baseline corrected (baseline was defined as 2 – 10 s prior to the end of the trial) by subtracting baseline for each band, normalised by dividing by baseline measures (providing a measure of relative amplitude for each subject) and then concatenating in frequency. Resultant TFSs were then averaged over subjects.

4.3.5.4 Quantification of the MRBD and PMBR

In order to quantify the size of the MRBD and PMBR, a curve fitting routine was employed. The beamformer derived time courses were filtered into the beta band (15 – 30 Hz) and Hilbert transformed to provide the amplitude envelope of beta oscillations. Amplitudes were baseline corrected and averaged over trials, with the absolute measure of beta amplitude (as distinct from percent change from baseline) maintained. Time courses were averaged over subjects and the standard error over subjects computed.

A Weibull curve was fitted to the rebound period (Barratt et al., 2017; Liddle et al., 2016), given by

$$f(t) = \frac{b}{a} \left(\frac{t}{a}\right)^{b-1} e^{-\left(\frac{t}{a}\right)^b}, \quad (1)$$

where a is the scale and b is the shape parameter. A general linear model was used to fit the Weibull curve to the PMBR (defined as the first time point when the beta time course amplitude returned to 0 nAm after the MRBD); the scale and shape parameters were iterated to find the best curve fit to the data (minimised sum of squared residuals). These fits were performed for each subject and task duration individually, allowing estimation of the peak PMBR amplitude, time-to-peak, and time the PMBR returned to baseline (defined as when the gradient of the Weibull curve fit was less than 0.0001). Once the best fit to the rebound had been computed, a trapezoid was fitted to the MRBD, using a similar procedure. The time of the vertices of the trapezium were allowed to vary along with the height of the trapezium. The lateral arms of the trapezium were fitted to the downward and upward slopes of the MRBD whilst the base was fitted to the constant MRBD during the movement. Once the best fit was found, the time between the two vertices of the base determined the duration of the MRBD whilst the height of the trapezium determined the amplitude of the MRBD. A RM ANOVA was used to determine if there was a significant effect of stimulus duration on each parameter. A Weibull curve was also fit to the gamma results for use in Chapter 6.

4.4 Results

From initial assessment of the EMG data, one subject was removed from further analysis due to movement of the hand during the rest periods (EMG data showed hand movement in just under half the trials). Results are therefore reported for the remaining 14 subjects. Following removal of the bad trials, 13 ± 2 , 13 ± 2 , 12 ± 3 trials out of 15 (average and standard deviation across all subjects and runs) remained for the 2, 5 and 10 s durations respectively.

4.4.1 Grip-force and EMG data

The mean force output (across subjects and durations \pm standard deviation) was $29.5 \pm 0.8\%$ MVF during run 1 and $29.8 \pm 0.6\%$ MVF during run 2, a significant difference ($p=0.02$, paired t-test). The EMG amplitudes for runs 1 and 2 were $334 \pm 175 \mu\text{V}$ and $306 \pm 128 \mu\text{V}$ respectively on channel 1 (forearm extensor bundle) and $194 \pm 75 \mu\text{V}$ and $181 \pm 59 \mu\text{V}$, on channel 2 (forearm flexor bundle). These values were not statistically different ($p>0.05$, paired t-test). The high similarity of the force output and EMG responses across runs, combined with the fact the same number of trials were performed in each run allowed data to be grouped across runs for each subject for the grip-force duration of 2, 5 and 10 s.

Single subject time courses of the mean force output and mean EMG responses are shown in Figure 4.2A-C. Force data show the high overall performance of the subjects in the task, reaching the 30% MVF and maintaining it for the different durations as required. The EMG traces also indicate neuromuscular activation to perform the task remained the same for the different durations (Figure 4.2B and C). The mean force output and mean EMG amplitude across all subjects is shown in Figure 4.2D-F. A significant difference between the three durations ($p=0.04$, RM ANOVA) was found between the force outputs however, this was not seen in the EMG data for either channel. As the mean force output differences were so small ($29.8 \pm 0.7\%$, $29.4 \pm 0.7\%$ and $29.5 \pm 0.3\%$ for 2, 5 and 10 s grip durations respectively) and no changes in EMG were observed, overall the performance for all three durations was considered to be similar.

The 100% MVFs before and after each run were analysed to assess fatigue during the experiment. Mean force outputs before and after run 1 were $96 \pm 12\%$ MVF and $89 \pm 12\%$ MVF, respectively whilst they were $87 \pm 14\%$ MVF and $83 \pm 15\%$ MVF before and

after run 2, respectively. Comparing 100% MVF responses no significant differences (paired t-tests, Bonferroni corrected) were seen before and after the task for either run, or when comparing the before or after task 100% MVF measures for each run.

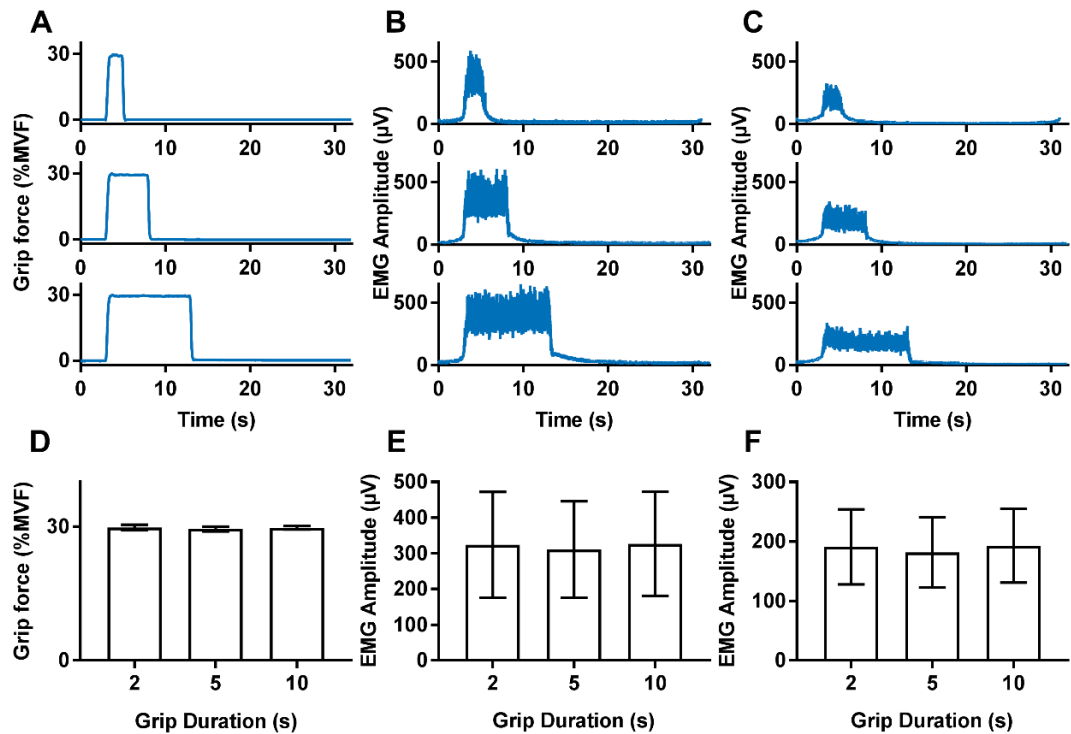


Figure 4.2. Behavioural results. (A-C) Example of output for one subject of (A) grip-force, (B) forearm extensor bundle EMG trace, (C) forearm flexor bundle EMG trace. (D-F) Average 2, 5 and 10 s responses across subjects and runs for (D) grip-force, (E) EMG amplitude in the forearm extensor bundle, (F) EMG amplitude in the forearm flexor bundle.

4.4.2 Beta Responses

Contralateral MRBD, localised to the sensorimotor cortex, was found for all subjects, and contralateral PMBR, also localised to sensorimotor cortex, was found in 13 out of 14 subjects. Figure 4.3A and Figure 4.4A show example T -stat maps for an individual subject for a single run for the PMBR and MRBD, respectively.

Time-frequency spectrograms for the PMBR, averaged across trials, runs and subjects are shown in Figure 4.3B, where time zero indicates contraction offset, determined from the EMG trace. As expected, an increase in beta amplitude (the PMBR) was observed after contraction offset for all three durations, which appears to increase in magnitude as the gripping period decreases (Figure 4.3B, red). A slight increase in alpha amplitude was also observed during the PMBR period at the PMBR location, although this effect was weaker.

Figure 4.3C shows the time courses of the beta band amplitude for each task duration averaged over all subjects and runs. Again, it is evident that the PMBR is modulated by task duration, with shorter contractions (red) showing higher amplitude compared to longer contractions (blue). Interrogating the PMBR using the Weibull fit showed a significant decrease ($p=0.018$, RM ANOVA corrected for multiple comparisons (Benjamini-Hochberg)) in the peak amplitude with increasing contraction duration (Figure 4.3D), and a significant increase ($p = 0.017$, RM ANOVA) in the time-to-peak of the PMBR (Figure 4.3E). No difference ($p=0.55$, RM ANOVA) in the time to return to baseline of the PMBR was found between contraction durations (Figure 4.3F). The average time to return to baseline was 9 ± 3 s across all subjects and durations. The integral of the PMBR, which combines these effects, showed a significant reduction ($p=0.001$, RM ANOVA) with increasing task duration.

Figure 4.4 shows results for the MRBD, here time zero represents contraction onset, as determined from the EMG traces. As expected, the TFS revealed a distinct beta (and alpha) band decrease during the grip contraction, with the effect in the alpha band more pronounced than during the rebound period. Furthermore, an increase in gamma band activity (~60-90 Hz) was seen on contraction onset and offset at the MRBD location. Figure 4.4B&C show that the MRBD is sustained for the duration of the task, and the MRBD consistently began approximately 2 s before the onset of contraction, when the visual presentation appeared. The amplitude of the MRBD during the contraction was consistent across task durations, reflected by no significant difference ($p=0.767$, RM ANOVA) in MRBD amplitude calculated from the trapezoid fit parameters (Figure 4.4D). As expected, the integral of the trapezoid increased linearly with duration (Figure 4.4E), reflecting the increase in duration of the MRBD with task duration.

Figure 4.5 shows the average T -stat map for the MRBD and PMBR over all subjects, normalised to the MNI brain. The location of the PMBR peak response across all subjects was (-36, -10, 62) mm (MNI coordinates (x, y, z)) while the MRBD peak was at (-40, -20, 58) mm. According to the probabilistic Harvard-Oxford Cortical Structural Atlas (i.e. the fsl “atlasquery” tool) the most likely cortical region relating to the average peak MNI coordinate of the PMBR was precentral gyrus (43%), whilst the peak of the MRBD was split between precentral gyrus (36%) and postcentral gyrus (18%). Whilst there was considerable spatial overlap of the PMBR and MRBD responses, the peak

location of the PMBR was significantly more anterior ($p < 0.05$, paired samples t-test) and more medial compared with the MRBD when considered over all subjects.

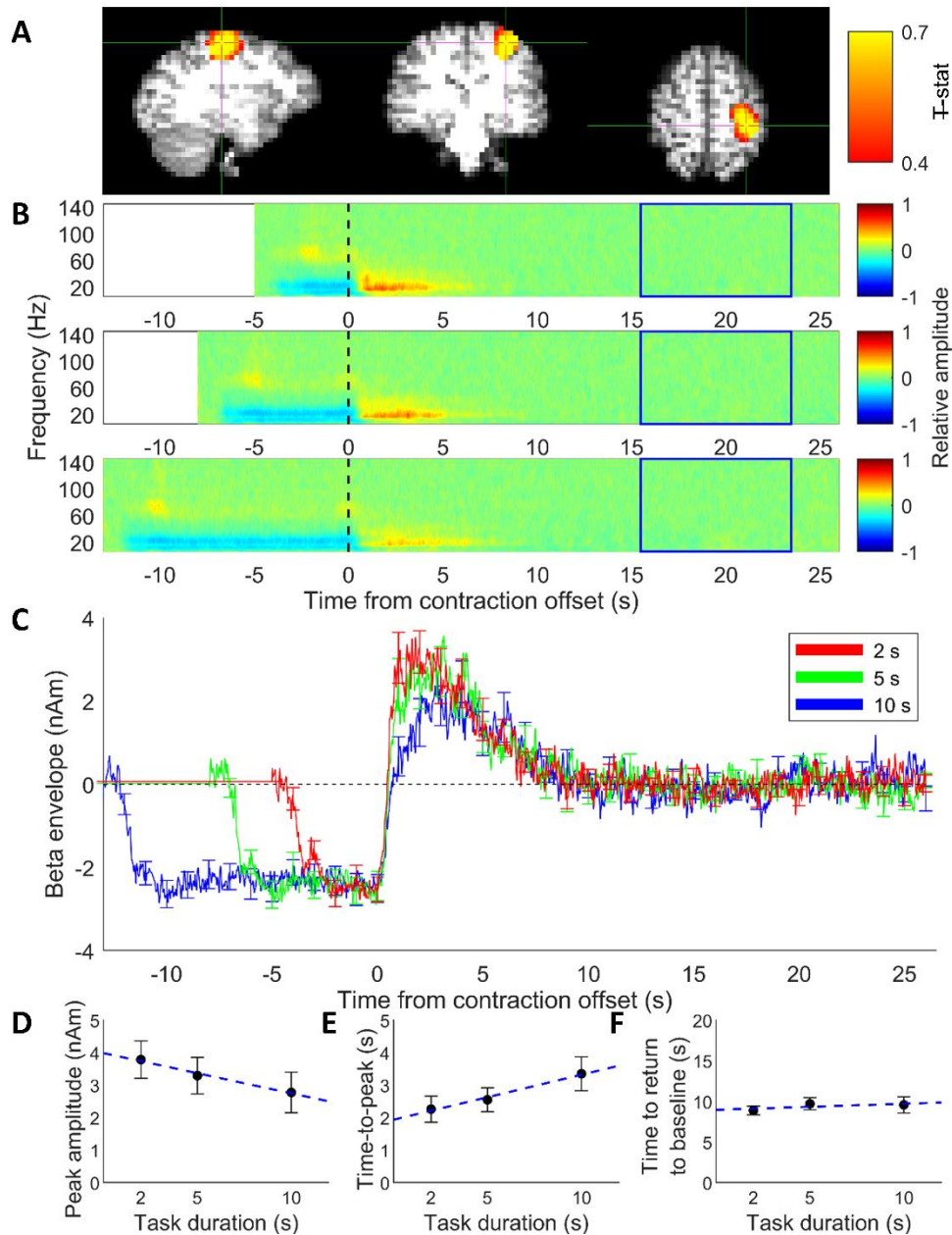


Figure 4.3 (A) Pseudo-*t*-statistical map showing the PMBR localised to motor cortex for one run of a single representative subject (radiological view). (B) Average TFSs extracted from individual subject PMBR location for the three contraction durations, 2, 5 and 10 s (top to bottom) where baseline was 16-24 s (blue box). Time zero is cessation of the contraction. (C) Average time courses of beta band amplitude for the three task durations from the peak location of the PMBR across 14 subjects. Responses are aligned to contraction offset (time = 0 s). Red line shows the response to 2 s task duration, green line = 5 s task duration and blue line = 10 s task duration. Error bars show the standard error across subjects. (D–F) Measures from Weibull curves fitted to the PMBR showing effects of task duration. All times reported on y-axes are measured relative to contraction offset. (D) The amplitude of the PMBR peak (*R*-square 0.98), (E) the time at which peak of PMBR occurs (*R*-square 0.92) and (F) the time taken for rebound to return to baseline (*R*-square 0.01). Error bars show the standard error. Blue dashed line shows linear fit of the data.

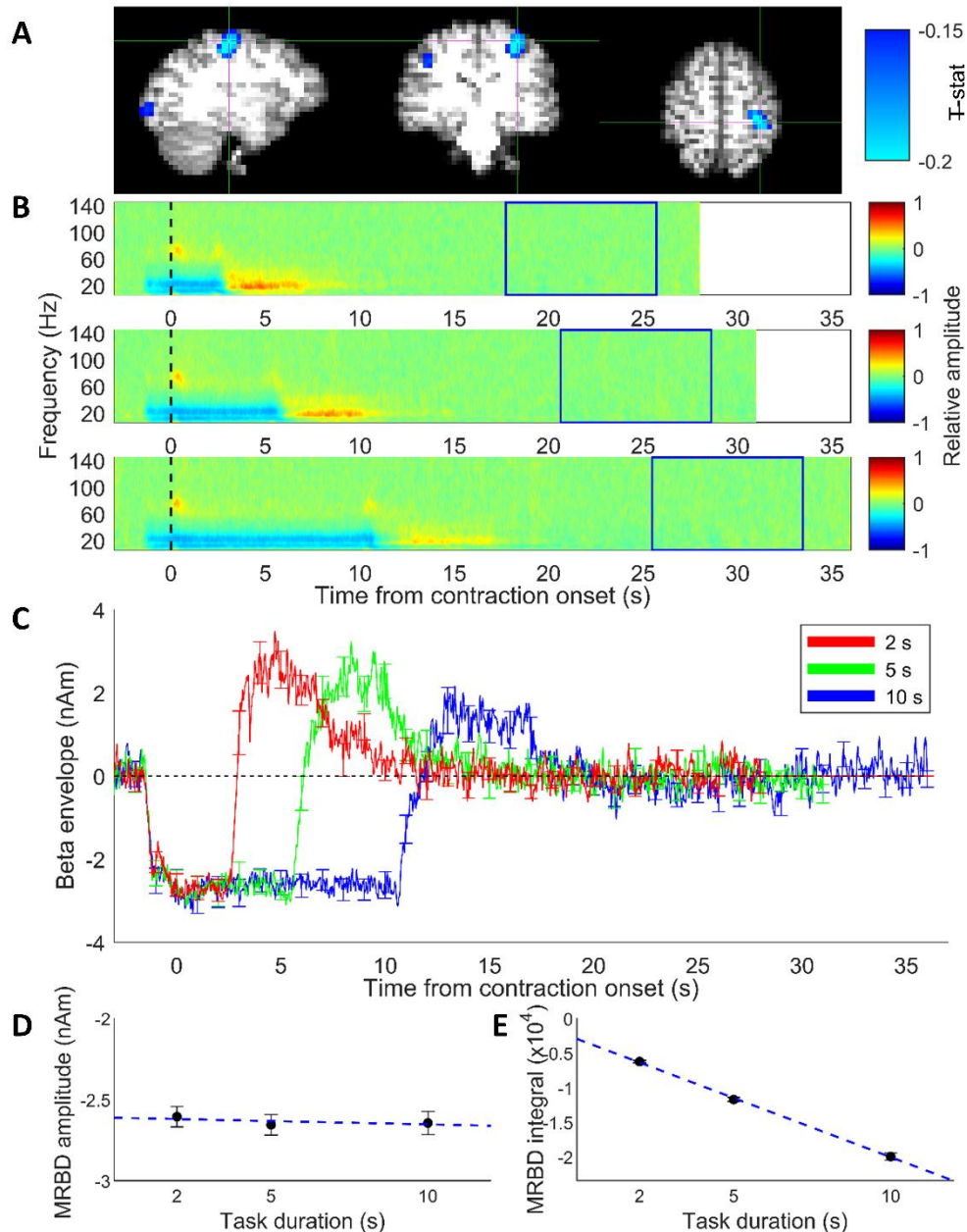


Figure 4.4 (A) Pseudo-t-statistical map showing MRBD localised to motor cortex for one run of a single representative subject (radiological view). (B) Average TFSs extracted from individual subject MRBD location for the three contraction durations. Spectrograms show the relative change in power for each frequency band where baseline was 2-10 s prior to the end of the trial (blue box). Time zero is contraction onset. (C) Average time courses of beta band amplitude for the three task durations from the peak location of the MRBD across 14 subjects. Responses are aligned to contraction onset (time = 0 s). Red line shows the responses to 2 s task duration, green line response to the 5 s task duration and blue line to the 10 s task duration. Error bars show the standard error across subjects. (D-E) Measures from a trapezoid fitted to the MRBD showing effects of task duration. (D) Amplitude of MRBD and (E) integral of MRBD plotted against task duration. Error bars show the standard deviation across subjects. Blue dashed line shows linear fit of the data.

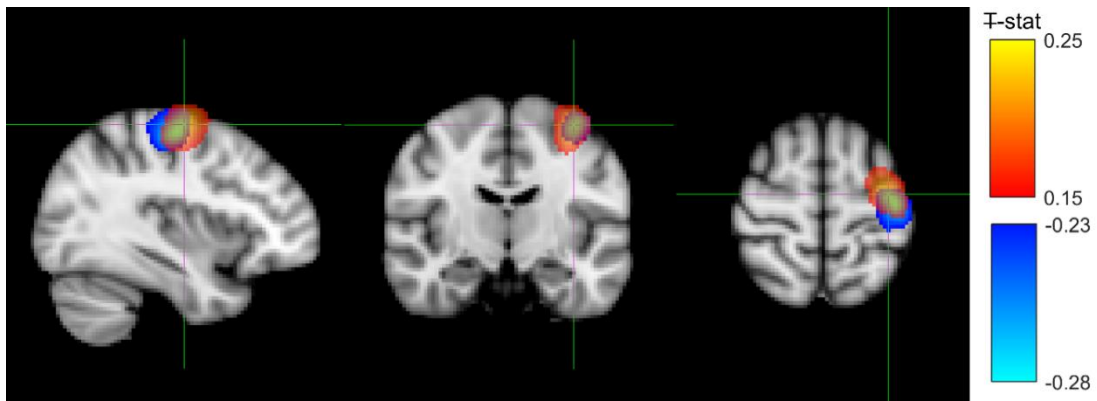


Figure 4.5. Pseudo-*t*-statistical map of the group average location of the MRBD (blue, peak (-40, -20, 58) mm) overlaid with the PMBR (red, peak (-36, -12, 62) mm) with the cross hairs at the PMBR peak (radiological view). *T*-stat maps were created in individual subject space before normalising to MNI space and averaging over subjects.

4.4.3 Alpha Responses

The time frequency spectrograms in Figure 4.3 and Figure 4.4 showed changes in oscillatory activity outside of the beta band, namely in the alpha and gamma bands. Therefore the alpha and gamma responses were interrogated separately. The broadband frequency time courses were extracted from the peak of the alpha event related synchronization (ERS) for each subject, to investigate post-stimulus effects (akin to the PMBR), and from the peak of the alpha event related desynchronization (ERD) to investigate effects in this frequency band during the task (akin to the MRBD). For two of the subjects, an alpha ERS could not be source localised and therefore in these subjects the peak of the alpha ERD was taken as the alpha location for all time course extraction. Resultant TFS and alpha power time courses are shown in Figure 4.6 and Figure 4.7. Both alpha ERD and MRBD responses show very similar behaviour with no clear effect of task duration on the amplitude (Figure 4.7 and Figure 4.4) of the response during the task. In addition, the alpha ERD also begins during the preparation phase, rather than on contraction onset. In contrast, the alpha ERS after the contraction had ceased was much smaller and less distinct than the PMBR (Figure 4.6 compared with Figure 4.3). Whilst the signal to noise prevents any detailed analyses of this response, it appears that the alpha ERS is modulated with task duration in a similar manner to the PMBR with the shortest task duration (2 s) resulting in the largest alpha ERS (Figure 4.7B&C). Therefore, it appears that the alpha response to the task has the same characteristics, but weaker in the sensorimotor cortex, as that of the beta response. Visual alpha effects were also investigated which are shown in Appendix B.

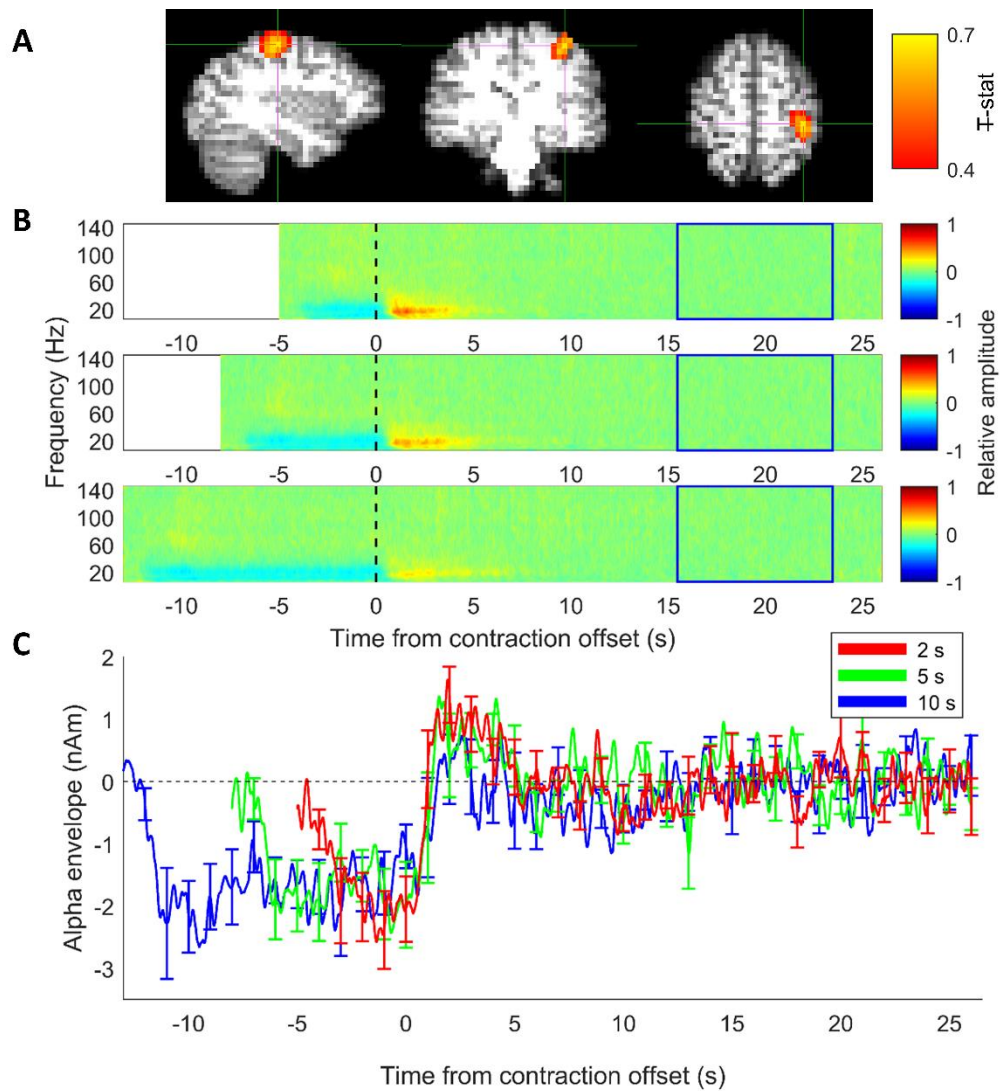


Figure 4.6. Alpha ERS response. (A) Location of maximum power change during the event related synchronization in alpha band in a single representative subject (same subject as for beta, Figure 4.3). (B) Time frequency spectrogram averaged over all subjects. Top panel is the response from the 2 s stimulus, middle 5 s, bottom 10 s. (C) Subject average alpha envelope time course from peak location of power change in motor cortex. Red is 2 s, green is 5 s and blue is 10 s task duration. Aligned at time = 0 s at contraction offset.

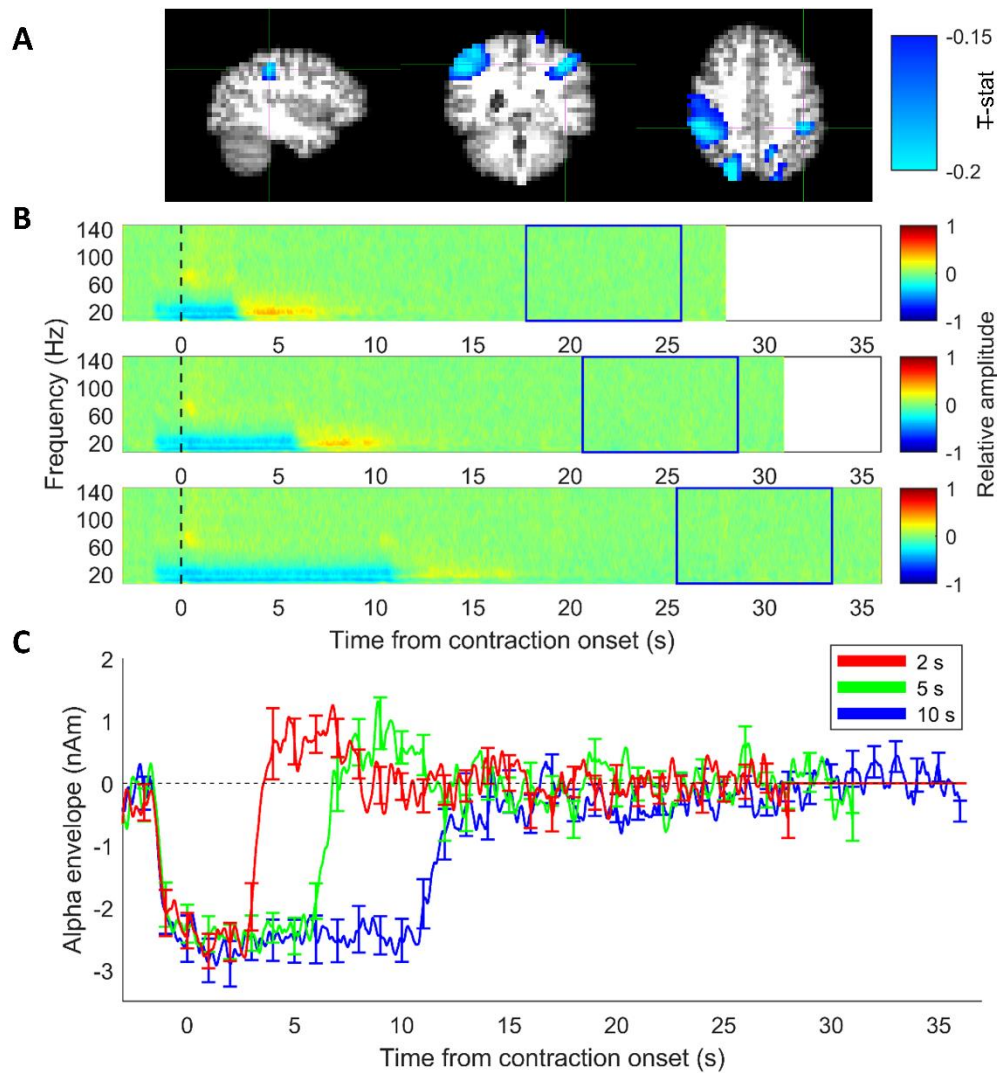


Figure 4.7. Alpha ERD. (A) Location of maximum power change during the task in the alpha band in a single representative subject (same subject as for beta, Figure 4.4). (B) Subject average TFS where time = 0 s is contraction onset. Top panel is the response from the 2 s stimulus, middle 5 s, bottom 10 s. (C) Subject average alpha envelopes from the peak location of alpha ERD. Red is 2 s, green is 5 s and blue is 10 s task duration.

4.4.4 Gamma Responses

Gamma band responses were observed between 60 and 90 Hz from the beta peak locations during the task (see Figure 4.4B). Therefore, gamma ERS was source localised only during the task for each subject and broadband frequency time courses were extracted. The results are shown in Figure 4.8. As expected, the amplitude of the gamma response was far smaller than that of the alpha or beta response. The response was not sustained throughout the stimulation period but was strongest at contraction onset, with a gamma burst lasting approximately 1.5 s. There were also hints of a weak gamma response at contraction offset. For the 2 s task duration it appeared that these onset and offset gamma responses merged so gamma band activity appeared more

sustained throughout the task duration (Figure 4.8C). There was however, no sign of a gamma response in the post-movement period of primary interest in this study.

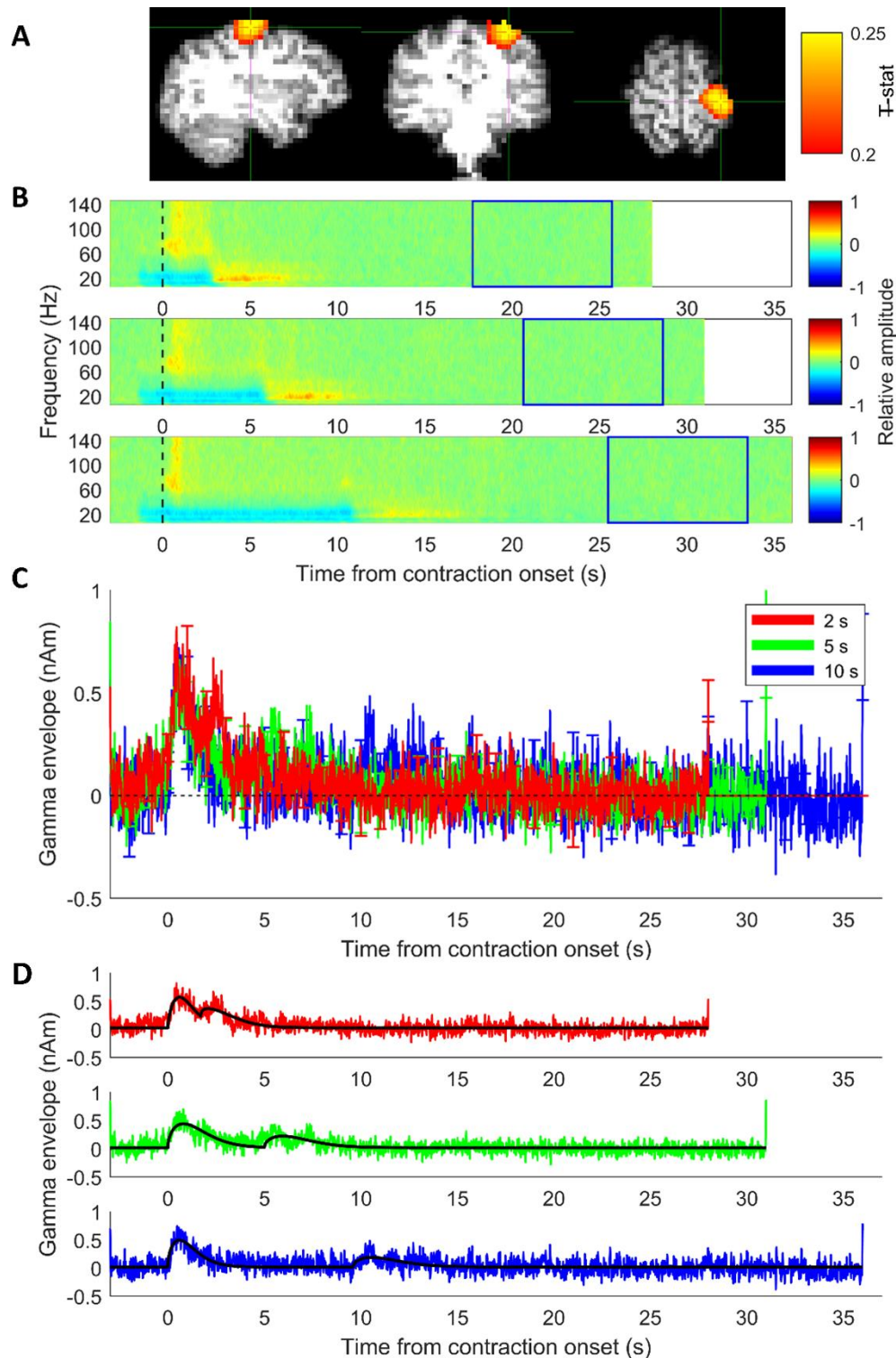


Figure 4.8. Gamma ERS. (A) F -stat map showing maximum power change in the gamma (60 – 90 Hz) band during the task. (B) Subject average TFS, where the blue box shows the baseline period. (C) Subject average gamma envelope taken from the peak of the F -stat map where red represents the response to the 2 s task duration, green 5 s and blue 10 s. (D) Gamma envelopes for 2 s (top, red), 5 s (middle, green) and 10 s (bottom, blue) with Weibull fit overlaid (black).

4.5 Discussion

Using a controlled grip-force task, the results from this chapter show that the amplitude of the PMBR is modulated by task duration (for an isometric contraction task), with increased amplitude associated with shorter contraction durations. This was accompanied by a shorter time-to-peak following contraction offset. It was also shown that the total duration of the PMBR was independent of task duration, returning to baseline approximately 9 s after contraction offset. The amplitude of the MRBD was unaffected by task duration. It was also shown, in agreement with previous studies, that the MRBD and PMBR localised to spatially neighbouring, but significantly different cortical locations. Motor alpha responses were found to mirror those of beta, whilst visual alpha showed no modulation of the rebound with task duration, unlike in motor cortex. Brief bursts of motor gamma were observed on movement onset and to a lesser extent movement offset.

Fry et al. (2016) showed that the amplitude of the PMBR, measured from the primary sensorimotor region, decreased and the duration of the response increased with increasing duration of contraction, when rate of force development (RFD) was modulated. This task was relatively complex as both force and duration were simultaneously varied, making it impossible to determine which aspect of the task resulted in the observed changes in PMBR. The authors proposed that it was the duration of the contraction that determined the duration of the PMBR. However here, using a task where only the duration of the contraction was varied, the results show that increasing task duration decreases the amplitude of the post-stimulus response and has no effect on PMBR longevity. Nevertheless, the modulation of PMBR amplitude with task duration observed agrees with Fry et al. (2016). These findings are also supported by those of Heinrichs-Graham et al. (2017) who showed that a longer stimulus duration resulted in a smaller PMBR. However, caution is needed when comparing these studies; in this study the altered PMBR is observed in the primary sensorimotor cortex, whereas in Heinrichs-Graham et al. the PMBR was reported in higher order brain areas as well as the somatosensory cortex, but not the motor cortex. This difference may be due to differences in task paradigm. In the study presented in this chapter, the subjects knew when contraction offset would occur (due to the visual cue), whereas the aim of Heinrichs-Graham et al. was to characterise the effect of not knowing when contraction

offset would occur. This may involve recruitment of cognitive networks which potentially gives rise to the spatial differences observed.

The fact that time-to-peak was lower, and amplitude higher for shorter durations suggests that the beta response on contraction offset is a direct response to the duration of the force output, rising more rapidly and to a higher amplitude for shorter task durations (Figure 4.3C). A possible explanation for this finding is linked to task difficulty. Anecdotally, subjects reported finding the task cognitively easier for the longer durations. This was because once the required 30% MVF had been reached and subjects had stabilized their grip it was not difficult to hold that force (as the task had been designed to prevent fatigue). This is supported by quantitative data; there was significantly ($p < 0.05$, paired Student's t-test) greater variation in force output recorded across trials for the 2 s task duration (mean over subjects of SD over trials = $1.0 \pm 0.5\%$ MVF) than the 10-s task duration (mean over subjects of SD over trials = $0.6 \pm 0.3\%$ MVF). Another suggestion the modulation may be linked to task difficulty is that no modulation was seen in the visual cortex (Appendix B), where ostensibly the task did not vary in difficulty between durations. Fry et al. (2016) argued that when muscle contraction force is increased, it is conceivable that the perceived task difficulty is increased as it is harder to reach the required force. Indeed their study reports an increase in mean absolute error (a measure of task accuracy) with target force. It is harder to hypothesize how task difficulty is changed by RFD but it is likely that the lower RFD trials were easier as, similar to the longer task durations in the current work, once the desired RFD had been found it could be continued until the end of the prescribed contraction. Again, the reported mean error values supported this suggestion, with smaller errors for lower RFD (Fry et al., 2016). This also agrees with the work from Heinrichs-Graham et al. (Heinrichs-Graham et al., 2017), which shows reduced PMBR amplitude for slow conditions, which would arguably be easier. Thus in all these cases it appears that the more challenging the task the greater the PMBR. Therefore the PMBR in primary sensory regions may be modulated by top-down feedback mechanisms associated with perceived task difficulty even in these relatively simple tasks.

As summarized in the introduction to this chapter, beta band responses have been associated with GABAergic inhibition (Cheng et al., 2017; Gaetz et al., 2011; Jensen et al., 2005; Kilavik et al., 2013; Muthukumaraswamy et al., 2013). In support of this,

in a previous study, Chen et al. (Chen et al., 1999) used transcranial magnetic stimulation (TMS) to explore the functional significance of the PMBR by probing excitability of the motor cortex to drive a muscle twitch in the hand at different lags following median nerve stimulation. They showed maximum cortical inhibition around 200 ms to 1000 ms post-stimulus; this timing is closely matched to that of the PMBR. Taking results presented here, it is likely that the peak inhibition is highest and fastest following completion of a task with a shortened duration; or perhaps more generally, peak inhibition is highest and fastest following more challenging motor outputs. One possible explanation for the increased PMBR is that increased PMBR is a result of increased top-down inhibition required to end the excitatory activity associated with the movement, with greater inhibition required for more cognitively demanding movements.

Interestingly, in the later stages of the response, the rate of decay of the PMBR appears to be the same (from 5 s after movement offset) regardless of task duration and amplitude/latency of the peak of the PMBR (Figure 4.3C&F). It appears that the PMBR of lower amplitude has a wider peak before returning to baseline such that all PMBR responses follow a highly similar trajectory in the later stages of the response, which is surprising. It is tempting to speculate that these later stages are related to fundamental processes such as rebalancing of ionic gradients through after-hyperpolarization currents (Fry et al., 2016; McCormick et al., 1993) which can elicit beta band responses (Kopell et al., 2000; Lu et al., 2004). It is interesting that a similar mechanism of rebalancing of ionic gradients has been proposed as a putative cause of the post-stimulus fMRI response (Lu et al., 2004) and post-stimulus responses across imaging modalities have been linked (Mullinger et al., 2017; Mullinger et al., 2013), see Chapter 6 for investigation of fMRI post-stimulus responses to this task. However, if ionic rebalancing is the driving mechanism of the later stages of the PMBR it is still challenging to explain why the same trajectory is followed regardless of the peak amplitude of the PMBR, and requires further investigation through modelling and invasive recording approaches.

The data presented here (Figure 4.3) suggest that the duration of the PMBR is longer than has been reported in recent studies (Gaetz et al., 2010; Heinrichs-Graham et al., 2017; Jurkiewicz et al., 2006; Kilavik et al., 2013; Parkes et al., 2006) and agrees with the observation of Fry et al. of a long (> 6 s) PMBR (Fry et al., 2016). However, it is

important to note that the present study, and Fry et al., involved long duration force outputs as distinct from short ballistic (transient) finger movements and so any comparisons should be treated with care. Nevertheless, it is possible that the short duration (1-3 s) of the PMBR which has commonly been reported is due to the baseline periods previously used, which typically begin less than 4 s after stimulus/task cessation (Gaetz et al., 2010; Heinrichs-Graham et al., 2017; Jurkiewicz et al., 2006; Kilavik et al., 2013; Parkes et al., 2006). Whilst long inter-stimulus intervals are often used in fMRI paradigm design due to the haemodynamic lag, it has generally been thought unnecessary for electrophysiology recordings. However, these short gaps between stimulus cessation and baseline window will artificially return the time course to baseline giving the impression of a shorter PMBR (and an MRBD that is increased in magnitude). For example, work by Stevenson and colleagues (Stevenson et al., 2011) found that the integral of the PMBR increased with increasing stimulus duration, but plateaued at durations above 4 s. This result disagrees with the results found here, and whilst this difference may be due to the motor task used (Stevenson et al. used a self-paced finger movement), it could be attributed to the baseline periods employed. Finger abductions were performed for different durations of 1, 2, 4 and 6 s, with trial length fixed at 12 s, such that for the 6 s stimulus there was 6 s rest period, with the final 2 s of this used as baseline. If the PMBR is as long as found here, it is possible this discrepancy in results is caused by the limited baseline. This raises an important methodological point which was explored further and is presented in Appendix A.

Similar results to the beta responses were found in the alpha band in motor cortex. Whilst the alpha results (Figure 4.6 and Figure 4.7) were less prominent, they showed the same trend of increased amplitude and decreased time to peak for the 2 s stimulus compared to 10 s stimulus. This shows the modulation of post-stimulus responses in the motor cortex to this motor task is not limited to the beta band. In contrast, in the visual cortex where alpha is an inherently more prominent rhythm, there appears to be no modulation in the amplitude or shape of the post-stimulus rebound despite the length of the visual stimulus (presentation of the target trace and visual feedback [Figure 4.1B]) varying with stimulus duration. It is difficult to draw insight from what this may mean as this was not a classic visual stimulus such as a flashing checkerboard, although there was visual feedback during this task. However, as discussed above this may be related to lack of modulation in the level of difficulty for the visual system by this task.

In the gamma band (investigated here between 60 to 90 Hz), an increase in activity was observed on movement onset and offset but was not sustained during the movement period. This transient gamma response is observed in the literature (Cheyne et al., 2008; Gaetz et al., 2010; Muthukumaraswamy, 2010; Wiesman et al., 2020), however most studies do not report a gamma response on movement offset. This could be due to the task used in this study where the bar is let go on movement offset, which is more active than stopping a finger movement for example, which is in agreement with the previous result that gamma is not observed for passive stimuli (Muthukumaraswamy, 2010). However, the possibility that the gamma responses observed are due to muscle artefact cannot be ruled out.

Finally, as expected from previous work (Fry et al., 2016; Stancak Jr & Pfurtscheller, 1995, 1996), the amplitude of the MRBD remained constant (Figure 4.4D) for all task durations and the integral of the MRBD scaled linearly with task duration (Figure 4.4E). These findings agree with the previously proposed hypothesis that, during movement, the MRBD acts as a cortical gate which is unaffected by measurable stimulus parameters such as force output (Fry et al., 2016; Stevenson et al., 2011). The fact that task duration modulates the PMBR and not the MRBD suggests that MRBD and PMBR are distinct responses. This is also reflected by the results from spatial localisation which found that the PMBR is located significantly more anterior in the motor strip whilst the MRBD is located more posterior in the somatosensory strip in agreement with previous studies (Fry et al., 2016; Jurkiewicz et al., 2006; Salmelin et al., 1995; Stancak Jr & Pfurtscheller, 1995). Interestingly, it was noticed that the PMBR appeared unilaterally, whereas the MRBD was bilateral in most subjects. Figure 4.4C shows that the MRBD began at exactly the same time prior to contraction onset, regardless of task duration. The MRBD commenced with the presentation of the visual cue, prior to the contraction. During this preparatory period the MRBD appears to have a slightly lower magnitude than during the contraction itself. This observation is in line with previous work showing that MRBD occurs during movement planning (Kilavik et al., 2013).

4.6 Conclusion

This chapter shows that, with increasing task duration, the amplitude of the PMBR drops and its time-to-peak increases. There was no effect on overall PMBR duration and no effect on MRBD. The work here adds weight to the argument that precise control

of task parameters enables systematic variation of the PMBR, and hence investigation of its functional role. With increasing evidence of abnormalities of the PMBR in disorders, this will become increasingly important if it is to realise its potential as an indicator of disease.

4.7 References

- Anderson, K. L., & Ding, M. (2011). Attentional modulation of the somatosensory mu rhythm. *Neuroscience*, *180*, 165-180.
- Barratt, E. L., Tewarie, P. K., Clarke, M. A., Hall, E. L., Gowland, P. A., Morris, P. G., Francis, S. T., Evangelou, N., & Brookes, M. J. (2017). Abnormal Task Driven Neural Oscillations in Multiple Sclerosis: A Visuomotor MEG Study. *Human Brain Mapping*, *38*(5), 2441-2453.
- Brainard, D. H. (1997). The Psychophysics Toolbox. *Spatial Vision*, *10*, 433-436.
- Brookes, M. J., Vrba, J., Robinson, S. E., Stevenson, C. M., Peters, A. M., Barnes, G. R., Hillebrand, A., & Morris, P. G. (2008). Optimising experimental design for MEG beamformer imaging. *Neuroimage*, *39*, 1788-1802.
- Chen, R., Corwell, B., & Hallett, M. (1999). Modulation of motor cortex excitability by median nerve and digit stimulation. *Experimental Brain Research*, *129*(1), 77-86.
- Cheng, C.-H., Tsai, S.-Y., Liu, C.-Y., & Niddam, D. M. (2017). Automatic inhibitory function in the human somatosensory and motor cortices: An MEG-MRS study. *Scientific Reports*, *7*(4234).
- Cheyne, D., Bells, S., Ferrari, P., Gaetz, W., & Bostan, A. C. (2008). Self-paced movements induce high-frequency gamma oscillations in primary motor cortex. *Neuroimage*, *42*(1), 332-342.
- Cheyne, D. O. (2013). MEG studies of sensorimotor rhythms: A review. *Experimental Neurology*, *245*, 27-39.
- Donner, T. H., Siegel, M., Fries, P., & Engel, A. K. (2009). Buildup of Choice-Predictive Activity in Human Motor Cortex during Perceptual Decision Making. *Current Biology*, *19*(18), 1581-1585.
- Fries, P. (2009). Neuronal Gamma-Band Synchronization as a Fundamental Process in Cortical Computation. *Annual Review of Neuroscience*, *32*(1), 209-224.
- Fry, A., Mullinger, K. J., O'Neill, G. C., Brookes, M. J., & Folland, J. P. (2017). The effect of physical fatigue on oscillatory dynamics of the sensorimotor cortex. *Acta Physiologica*, *220*(3), 370-381.
- Fry, A., Mullinger, K. J., O'Neill, G. C., Barratt, E. L., Morris, P. G., Bauer, M., Folland, J. P., & Brookes, M. J. (2016). Modulation of Post-Movement Beta Rebound by Contraction Force and Rate of Force Development. *Human Brain Mapping*, *37*, 2493-2511.
- Gaetz, W., Edgar, J. C., Wang, D. J., & Roberts, T. P. L. (2011). Relating MEG measured motor cortical oscillations to resting γ -Aminobutyric acid (GABA) concentration. *Neuroimage*, *55*, 616-621.
- Gaetz, W., MacDonald, M., Cheyne, D., & Snead, O. C. (2010). Neuromagnetic imaging of movement-related cortical oscillations in children and adults: Age predicts post-movement beta rebound. *Neuroimage*, *51*, 792-807.
- Hall, S. D., Stanford, I. M., Yamawaki, N., McAllister, C. J., Rönqvist, K. C., Woodhall, G. L., & Furlong, P. L. (2011). The role of GABAergic modulation in motor function related neuronal network activity. *Neuroimage*, *56*, 1506-1510.
- Heinrichs-Graham, E., Kurz, M. J., Gehringer, J. E., & Wilson, T. W. (2017). The functional role of post-movement beta oscillations in motor termination. *Brain Structure and Function*, *222*(7), 3075-3086.

- Hipp, J. F., Hawellek, D. J., Corbetta, M., Siegel, M., & Engel, A. K. (2012). Large-scale cortical correlation structure of spontaneous oscillatory activity. *Nature Neuroscience*, *15*, 884.
- Honaga, E., Ishii, R., Kurimoto, R., Canuet, L., Ikezawa, K., Takahashi, H., Nakahachi, T., Iwase, M., Mizuta, I., Yoshimine, T., & Takeda, M. (2010). Post-movement beta rebound abnormality as indicator of mirror neuron system dysfunction in autistic spectrum disorder: An MEG study. *Neuroscience Letters*, *478*(3), 141-145.
- Jenkinson, M., Bannister, P., Brady, M., & Smith, S. (2002). Improved Optimization for the Robust and Accurate Linear Registration and Motion Correction of Brain Images. *Neuroimage*, *17*(2), 825-841.
- Jenkinson, M., & Smith, S. (2001). A global optimisation method for robust affine registration of brain images. *Medical Image Analysis*, *5*(2), 143-156.
- Jensen, O., Goel, P., Kopell, N., Pohja, M., Hari, R., & Ermentrout, B. (2005). On the human sensorimotor-cortex beta rhythm: Sources and modeling. *Neuroimage*, *26*(2), 347-355.
- Jones, S. R., Kerr, C. E., Wan, Q., Pritchett, D. L., Hämäläinen, M., & Moore, C. I. (2010). Cued Spatial Attention Drives Functionally Relevant Modulation of the Mu Rhythm in Primary Somatosensory Cortex. *The Journal of Neuroscience*, *30*(41), 13760.
- Jurkiewicz, M. T., Gaetz, W. C., Bostan, A. C., & Cheyne, D. (2006). Post-movement beta rebound is generated in motor cortex: evidence from neuromagnetic recordings. *Neuroimage*, *32*(3), 1281-1289.
- Kilavik, B. E., Zaepffel, M., Brovelli, A., MacKay, W. A., & Riehle, A. (2013). The ups and downs of beta oscillations in sensorimotor cortex. *Experimental Neurology*, *245*, 15-26.
- Koelewijn, T., van Schie, H. T., Bekkering, H., Oostenveld, R., & Jensen, O. (2008). Motor-cortical beta oscillations are modulated by correctness of observed action. *Neuroimage*, *40*, 767-775.
- Kopell, N., Ermentrout, G. B., Whittington, M. A., & Traub, R. D. (2000). Gamma rhythms and beta rhythms have different synchronization properties. *Proceedings of the National Academy of Sciences*, *97*(4), 1867-1872.
- Liddle, E. B., Price, D., Palaniyappan, L., Brookes, M. J., Robson, S. E., Hall, E. L., Morris, P. G., & Liddle, P. F. (2016). Abnormal Salience Signaling in Schizophrenia: The Role of Integrative Beta Oscillations. *Human Brain Mapping*, *37*, 1361-1374.
- Lu, H., Golay, X., Pekar, J. J., & van Zijl, P. C. M. (2004). Sustained Poststimulus Elevation in Cerebral Oxygen Utilization after Vascular Recovery. *Journal of Cerebral Blood Flow & Metabolism*, *24*(7), 764-770.
- McCormick, D. A., Wang, Z., & Huguenard, J. (1993). Neurotransmitter Control of Neocortical Neuronal Activity and Excitability. *Cerebral Cortex*, *3*(5), 387-398.
- Mullinger, K. J., Cherukara, M. T., Buxton, R. B., Francis, S. T., & Mayhew, S. D. (2017). Post-stimulus fMRI and EEG responses: Evidence for a neuronal origin hypothesised to be inhibitory. *Neuroimage*, *157*, 388-399.
- Mullinger, K. J., Mayhew, S. D., Bagshaw, A. P., Bowtell, R., & Francis, S. T. (2013). Poststimulus undershoots in cerebral blood flow and BOLD fMRI responses are modulated by poststimulus neuronal activity. *Proceedings of the National Academy of Sciences*, *110*(33), 13636-13641.
- Muthukumaraswamy, S. D. (2010). Functional Properties of Human Primary Motor Cortex Gamma Oscillations. *Journal of Neurophysiology*, *104*(5), 2873-2885.

- Muthukumaraswamy, S. D., Myers, J. F. M., Wilson, S. J., Nutt, D. J., Lingford-Hughes, A., Singh, K. D., & Hamandi, K. (2013). The effects of elevated endogenous GABA levels on movement-related network oscillations. *Neuroimage*, *66*, 36-41.
- Parkes, L. M., Bastiaansen, M. C., & Norris, D. G. (2006). Combining EEG and fMRI to investigate the post-movement beta rebound. *Neuroimage*, *29*(3), 685-696.
- Parkkonen, E., Laaksonen, K., Piitulainen, H., Parkkonen, L., & Forss, N. (2015). Modulation of the ~20 - Hz motor - cortex rhythm to passive movement and tactile stimulation. *Brain and Behavior*, *5*(5), e00328.
- Parkkonen, E., Laaksonen, K., Piitulainen, H., Pekkola, J., Parkkonen, L., Tatlisumak, T., & Forss, N. (2017). Strength of ~20-Hz Rebound and Motor Recovery After Stroke. *Neurorehabilitation and Neural Repair*, *31*(5), 475-486.
- Pfurtscheller, G., & Lopes da Silva, F. (1999). Event-related EEG/MEG synchronization and desynchronization: basic principles. *Clinical Neurophysiology*, *110*, 1842-1857.
- Pfurtscheller, G., Neuper, C., Brunner, C., & da Silva, F. L. (2005). Beta rebound after different types of motor imagery in man. *Neuroscience Letters*, *378*, 156-159.
- Pfurtscheller, G., Stancák, A., & Neuper, C. (1996). Post-movement beta synchronization. A correlate of an idling motor area? *Electroencephalography and Clinical Neurophysiology*, *98*(4), 281-293.
- Proudfoot, M., Rohenkohl, G., Quinn, A., Colclough, G. L., Wu, J., Talbot, K., Woolrich, M. W., Benatar, M., Nobre, A. C., & Turner, M. R. (2017). Altered Cortical Beta-Band Oscillations Reflect Motor System Degeneration in Amyotrophic Lateral Sclerosis. *Human Brain Mapping*, *38*, 237-254.
- Robinson, S. E., & Vrba, J. (1998). Functional neuroimaging by synthetic aperture magnetometry. *Recent Advances in Biomagnetism*, 302-305.
- Robson, S. E., Brookes, M. J., Hall, E. L., Palaniyappan, L., Kumar, J., Skelton, M., Christodoulou, N. G., Qureshi, A., Jan, F., Katshu, M. Z., Liddle, E. B., Liddle, P. F., & Morris, P. G. (2016). Abnormal visuomotor processing in schizophrenia. *Neuroimage Clin*, *12*, 869-878.
- Rossiter, H. E., Boudrias, M.-H., & Ward, N. S. (2014). Do movement-related beta oscillations change after stroke? *Journal of Neurophysiology*, *112*(9), 2053-2058.
- Salenius, S., Schnitzler, A., Salmelin, R., Jousmäki, V., & Hari, R. (1997). Modulation of human cortical rolandic rhythms during natural sensorimotor tasks. *Neuroimage*, *5*(3), 221-228.
- Salmelin, R., Hamalainen, M., Kajola, M., & Hari, R. (1995). Functional segregation of movement-related rhythmic activity in the human brain. *Neuroimage*, *2*, 237-243.
- Schnitzler, A., Salenius, S., Salmelin, R., Jousmaki, V., & Hari, R. (1997). Involvement of Primary Motor Cortex in Motor Imagery: A Neuromagnetic Study. *Neuroimage*, *6*, 201-208.
- Stancak Jr, A., & Pfurtscheller, G. (1995). Desynchronization and recovery of β rhythms during brisk and slow self-paced finger movements in man. *Neuroscience Letters*, *196*, 21-24.
- Stancak Jr, A., & Pfurtscheller, G. (1996). Event-related desynchronisation of central beta-rhythms during brisk and slow self-paced finger movements of dominant and nondominant hand. *Cognitive Brain Research*, *4*, 171-183.
- Stevenson, C. M., Brookes, M. J., & Morris, P. G. (2011). Beta-band correlates of the fMRI BOLD Response. *Human Brain Mapping*, *32*(2), 182-197.

- Tewarie, P., Hunt, B. A. E., O'Neill, G. C., Byrne, A., Aquino, K., Bauer, M., Mullinger, K. J., Coombes, S., & Brookes, M. J. (2018). Relationships Between Neuronal Oscillatory Amplitude and Dynamic Functional Connectivity. *Cerebral Cortex*, bhy136-bhy136.
- Tzagarakis, C., Ince, N. F., Leuthold, A. C., & Pellizzer, G. (2010). Beta-Band Activity during Motor Planning Reflects Response Uncertainty. *The Journal of Neuroscience*, 30(34), 11270-11277.
- Vakhtin, A. A., Kodituwakku, P. W., Garcia, C. M., & Tesche, C. D. (2015). Aberrant development of post-movement beta rebound in adolescents and young adults with fetal alcohol spectrum disorders. *NeuroImage: Clinical*, 9, 392-400.
- Van Veen, B. D., & Buckley, K. M. (1988). Beamforming: A Versatile Approach to Spatial Filtering. *IEEE ASSP Magazine*, 5(2), 4-24.
- Van Veen, B. D., Van Drongelen, W., Yuchtman, M., & Suzuki, A. (1997). Localization of Brain Electrical Activity via Linearly Constrained Minimum Variance Spatial Filtering. *IEEE TRANSACTIONS ON BIOMEDICAL ENGINEERING*, 44(9), 867-880.
- Wiesman, A. I., Koshy, S. M., Heinrichs-Graham, E., & Wilson, T. W. (2020). Beta and gamma oscillations index cognitive interference effects across a distributed motor network. *Neuroimage*, 213, 116747.

4.8 Appendices

A. Investigating Baseline

Realising the potential of the PMBR as a biomarker of disease requires its robust characterisation across multiple laboratories. This, in turn, would require standardisation of experimental paradigms. However, to date, the literature is inconsistent regarding how best to illicit a PMBR response. One important question is how long it takes for the PMBR to reach baseline following movement offset. The work presented in this Chapter (Figure 4.3 and Figure 4.4) in agreement with previous work (e.g. Fry et al. (2016)), shows that the PMBR can take up to 10 s to reach a true baseline value following stimulus offset; indeed this is consistent with advice from early studies (Pfurtscheller & Lopes da Silva, 1999) which recommended that a minimum of 10 s is left between trials. However, in recent years this advice is rarely adhered to, with experimenters opting for much shorter inter-stimulus-intervals (ISIs) in order to fit more trials into an experiment. Whilst direct comparisons between the present work and the vast literature on short ISI experiments, which typically employ ballistic finger movements rather than extended force outputs, should be treated with caution, it is possible that such short ISIs, with baselines taken at the end of each trial, could risk underestimation of the magnitude of the PMBR, and overestimation of the MRBD. Here, a simple experiment was performed to demonstrate this point.

Methods

Six subjects (3 female, aged 26 ± 1 (mean \pm SD) years) took part in a further grip-force experiment in which they were asked to apply force to a bar to match a target profile, as described above. Here, the duration of force output remained constant (at 5 s) across all trials, but the inter-stimulus interval (ISI) was varied between 5, 10 and 30 s, with 30 trials for each ISI resulting in a total trial duration of 10 s, 15 s and 35 s for the three different ISIs respectively. The different ISIs were distributed randomly throughout the experiment which lasted 30 minutes in total. Data were processed as described above using a scalar beamformer to determine the location in the brain of the maximum beta band change. Both a time frequency spectrum, and the Hilbert envelope of beta band oscillations, were extracted from this location, on a subject-by-subject basis, with results averaged over both trials and subjects. Importantly, baseline correction was performed in two ways: 1) Single baseline: the baseline was calculated in the 23 to 27

s window (relative to contraction offset) for the 35s ISI trials only, and all three conditions (ISIs) were baseline corrected to this same value. 2) Independent baselines: baselines were selected independently for the three trial types, using the 1 to 2 s window for the ISI of 5 s; the 4 to 7 s window for the ISI of 10 s and the 23 to 27 s window for the ISI of 30 s (all relative to contraction offset). These analyses resulted in three time-frequency-spectra and associated beta envelopes (one for each of the three separate ISIs) for the single value baseline correction, and a further three for the independent baseline correction.

Results and Discussion

Figure 4.9A shows the 3 time frequency spectra for each of the three ISIs, baseline corrected using a single value derived from the long ISI. Figure 4.9B shows the corresponding beta envelopes baseline corrected in the same way. Figure 4.9C and Figure 4.9D show the same plot, but in this cases baseline corrected using values derived from each ISI independently.

The results show that the beta band envelopes follow robust and well characterised profiles regardless of ISI; for the shorter ISIs, the rebound is simply curtailed by the onset of movement. In cases in which the baseline is measured independently for each ISI, it is clear that the “baseline” value is estimated during the PMBR, and this leads to an overestimation of the resting beta amplitude, a diminishing PMBR, and an increased (more negative) MRBD. It follows that short ISIs will likely lead to misrepresentation of the MRBD/PMBR and this could, potentially, mask subtle differences in the PMBR between, for example, experimental conditions or clinical populations. An example of this is provided by Rossiter et al. (Rossiter et al., 2014) where differences in MRBD were found between stroke patients and controls, but the ISI for the 3 s grip task was only between 3 and 7 s. Thus, it is impossible to determine, with a short ISI, what is driving the differences in the clinical population, especially if MRBD and PMBR do have different neuronal mechanisms.

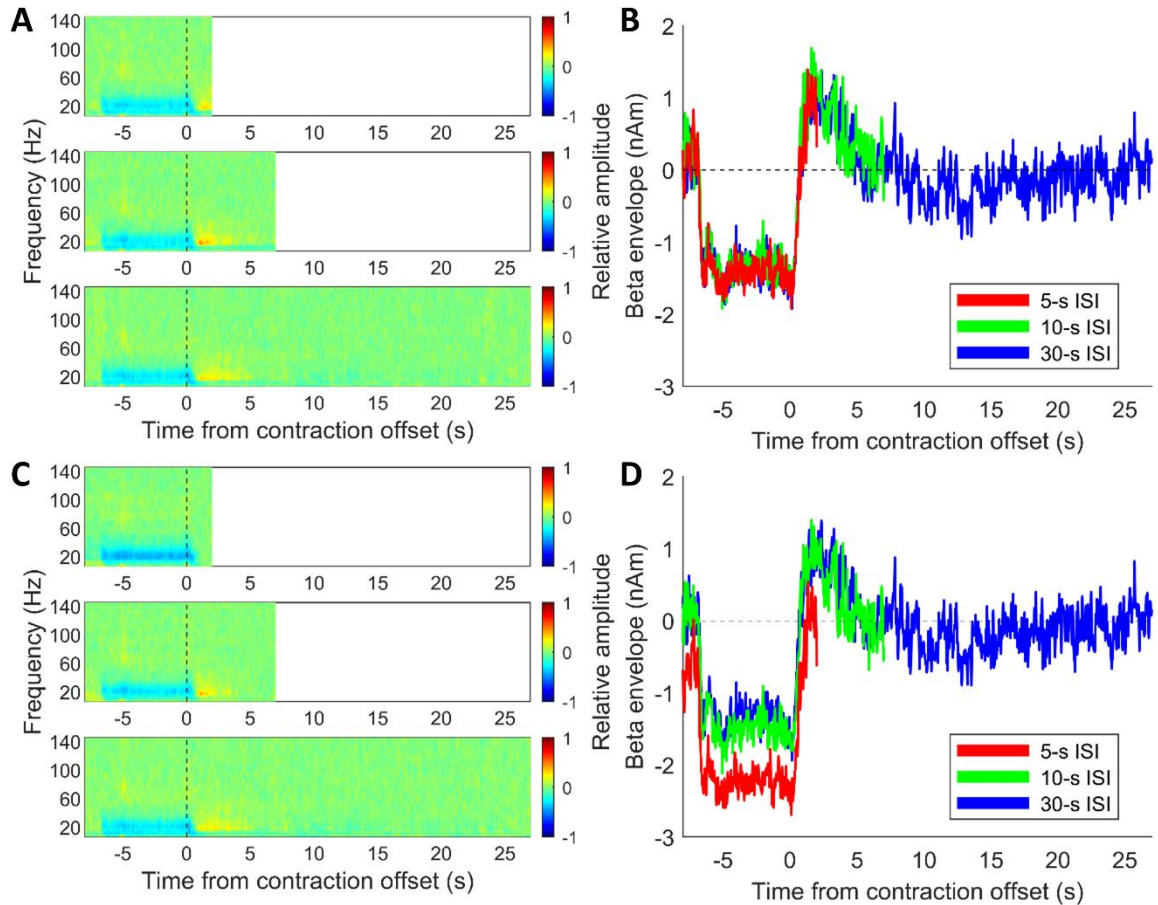


Figure 4.9. The effect of ISI on the PMBR and MRBD characterisation: (A) Trial averaged time frequency spectra and (B) beta band envelopes for three separate ISIs (5 s (red); 10 s (green); 30 s (blue)). Baselines were determined as a single value taken from the long ISI condition. (C&D) Equivalent to (A&B) but where baselines were determined independently from each ISI, i.e. 1 to 2 s for the 5 s ISI, 4 to 7 s for the 10 s ISI, 23 to 27 s for the 30 s ISI.

Conclusion

It is recommended that, in future experiments attempting to characterise the PMBR, sufficient time is left between trials to allow a true baseline measure to be derived, in order that robust PMBR characterisation is possible.

B. Visual Alpha

Figure 4.10 shows an example of the activation observed in the visual cortex during the rebound period. The peak of the activity was found and virtual electrodes extracted for each subject, the average of which is shown in Figure 4.10C. No difference between the three task durations is observed during the rebound. During the movement, a sustained decrease in alpha was observed in the visual cortex, as seen in Figure 4.11.

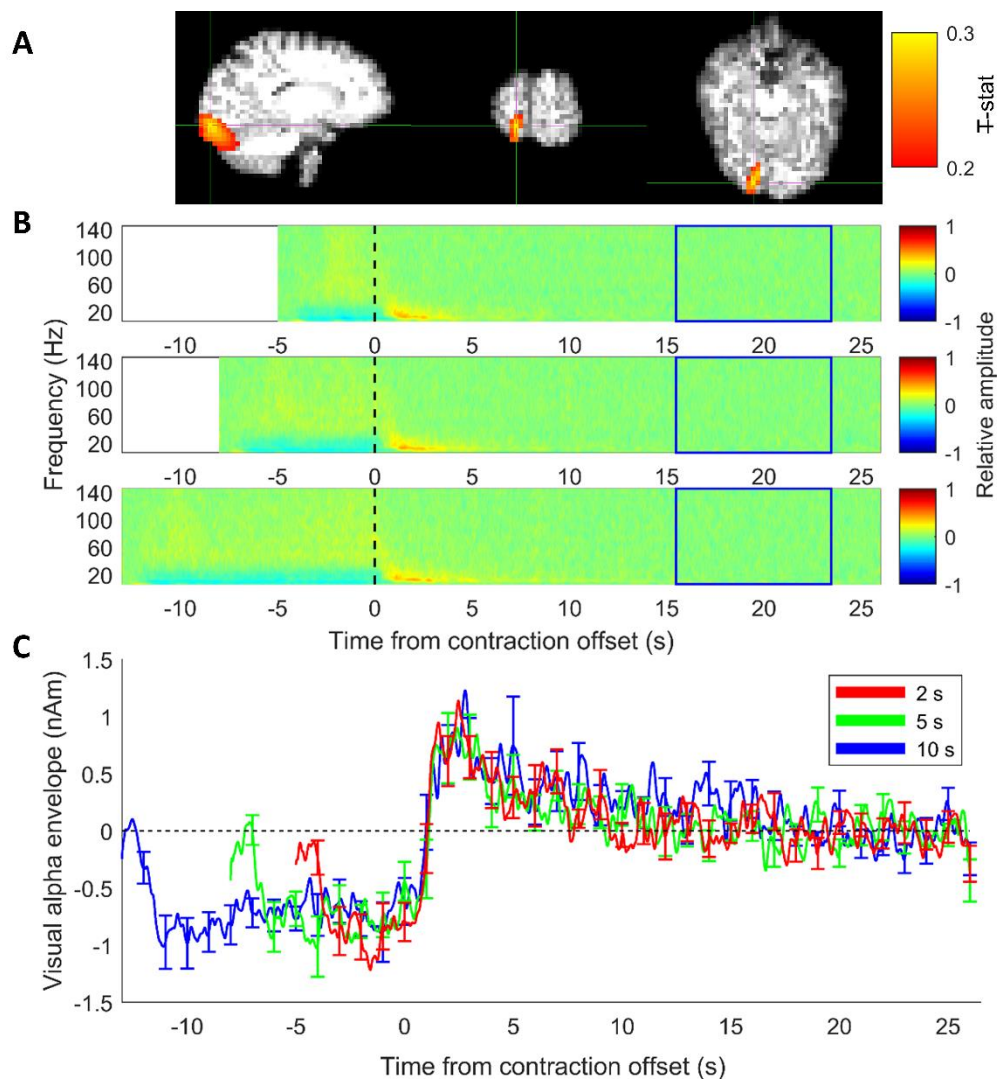


Figure 4.10 Visual alpha ERS. (A) Activation localised to the visual cortex during the rebound in the alpha band, shown for a single subject. (B) TFSs averaged over all subjects from individual locations of peak visual alpha activity. Top panel shows response to 2 s, middle 5 s, and the bottom panel shows 10 s task duration. (C) Time courses of visual alpha envelopes averaged over all subjects. Where red is 2 s task duration, green is 5 s task duration and blue is the 10 s task duration aligned to contraction offset. Error bars show standard error across subjects.

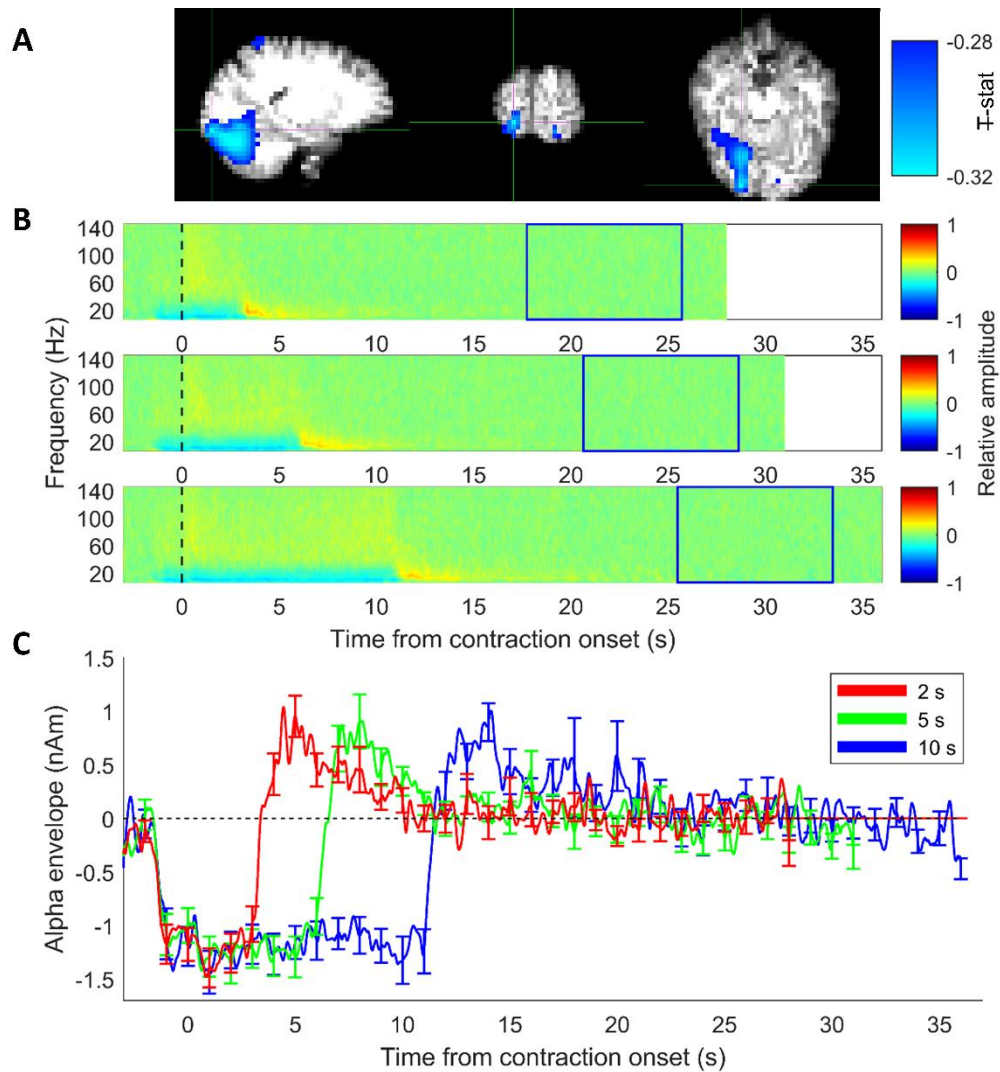


Figure 4.11 Visual alpha ERD. (A) Activation localised to the visual cortex during the movement in the alpha band, shown for a single subject. (B) TFSs averaged over all subjects from individual locations of peak visual alpha activity during the movement. Top panel shows response to 2 s, middle 5 s, and the bottom panel shows 10 s task duration. (C) Time courses of visual alpha envelopes averaged over all subjects. Where red is 2 s task duration, green is 5 s task duration and blue is the 10 s task duration aligned to contraction onset. Error bars show standard error across subjects.

CHAPTER 5

5 Exploring Transient Networks in Task-based MEG Data

5.1 Abstract

Whilst the PMBR is well observed in terms of a beta time course of trial averaged results, as characterised in the last chapter, this chapter aims to understand the formation and functional role of the PMBR beyond the classical picture. New analyses will be used to investigate what drives the rebound, using the rich temporal resolution of MEG to study brain networks on short time scales. Few studies have examined the temporal evolution of connectivity within and between brain networks throughout a task, which may provide important information as to the functional relevance of the PMBR. In this chapter, amplitude envelope correlation (AEC) was used to study network changes during a right-handed grip contraction task. Following this, a hidden Markov model (HMM) was used to identify the individual trial dynamics of a sensorimotor brain network. For AEC, correlations between beta band amplitude envelopes were measured in three time-windows: event related desynchronization (ERD), event related synchronization (ERS) and baseline. Significant differences between the three time-windows were found in beta band connectivity. The ERS time-window exhibited greatest overall functional connectivity, with the strongest effect in contralateral sensorimotor region. These data show clear changes in connectivity during different task stages. Inter-hemispheric connectivity in primary sensory regions breaks down during ERD and is re-established during the ERS, before returning to resting networks. The results from the HMM identified a bilateral sensorimotor network which was visited most frequently during the ERS. The rapidly evolving dynamics of this network demonstrated similar variation with task parameters to the ‘classical’ rebound, and show that the modulation of the PMBR can be well-described in terms of increased frequency of beta events on a millisecond timescale rather than modulation of beta amplitude during this time period, providing new information with regards to the formation of ‘classical’ responses. Together, these findings suggest the PMBR fulfils a role in re-establishing resting-state networks after disparate activity during a task.

This work was presented as a short talk and poster at MEGUK 2018, Derry/Londonderry entitled 'Dynamic Functional Connectivity During a Grip-force Task'; a poster at BIOMAG 2018 Philadelphia, 'Dynamic Functional Connectivity During a Grip-force Task'; and some of the work formed part of paper in NeuroImage, 'Post-stimulus beta response are modulated by task duration' Vol 206, 2020.

5.2 Introduction

The post movement beta rebound (PMBR), is robustly observed on stimulus offset. Whilst the aim of the last chapter was to characterise how the beta rebound varies with systematic modulation of task parameters, how the PMBR is formed and its functional role remains poorly understood, hindering its use as a metric of brain health. This chapter aims to understand what drives the beta rebound, using novel analysis methods applied to the motor task data collected in the previous chapter.

In the previous chapter it was hypothesised that the PMBR represents the integration of brain networks over a long range after a task. Recent advances in MEG allow the investigation of the temporal evolution of connectivity within and between brain networks (de Pasquale et al., 2010). Therefore, this hypothesis can be tested by measuring functional connectivity during the different stages of a task.

In 1995, Biswal (Biswal et al., 1995) showed with fMRI that so-called resting state activity – brain responses in the absence of a task – contained meaningful spatio-temporal structure. In other words, brain activity measured in spatially separated regions was found to be temporally correlated even in the absence of a task. This revealed spatial patterns of connected regions, termed resting state networks. These networks have since been thought to underlie core brain function and can be perturbed by disease (Stam et al., 2008). Functional connectivity is defined as statistical interdependencies between time courses of functional signals from two regions in the brain. Until around 2010, most studies investigated functional connectivity over long periods of time. Dynamic connectivity, on the other hand, is the study of functional connectivity in the brain which is non-stationary in time.

fMRI has been used to study functional connectivity for many years, with the last 10 years seeing a shift in neuroimaging towards investigation of dynamic connectivity (Chang & Glover, 2010). However, for fMRI, the minimum time window usable in dynamic connectivity is about 30 s due to haemodynamic lag, with most studies using a window of 30 – 60 s (Prete et al., 2017), which is not a short enough time scale to elucidate fast changes in the brain as there is not enough data to reliably estimate connectivity. MEG, on the other hand, is an excellent technique for investigating fast changes in brain activity as it has millisecond temporal resolution. However, it is only recently that the temporal dynamics of functional connectivity have been studied in

MEG (Baker et al., 2014; de Pasquale et al., 2010; Liu et al., 2010) due to a number of technical challenges which are explored in Section 5.3 below. Temporal connectivity dynamics will be extremely useful to understand the role of the PMBR and how it is formed. However, there is a relatively small body of literature that is concerned with functional connectivity during a task.

An example of a motor task studied with connectivity is Brovelli et al. (Brovelli et al., 2017). This research involved a visuomotor task, where finger movements were performed based on an associated number shown on screen. 500 ms sliding windows were used to investigate the high gamma band (60 – 150 Hz). A visuomotor network was found in the high gamma band associated with the movement. Connectivity of this network increased on stimulus presentation (movement planning) and peaked a second time after the movement which was said to represent dissolution of the network after the movement. They hypothesised that brain function is due to the interplay of many overlapping subnetworks rather than single brain regions. Nevertheless, this study did not explore the beta band or what happens in the post-movement period.

Another example investigating connectivity during a task is O’Neill et al. (O’Neill et al., 2017). In this paper, a self-paced button press task was used and connectivity was measured in the 13 – 30 Hz frequency band in 6 s sliding windows. A network centred on the right primary somatosensory cortex with strong connections between sensory and motor areas was found to modulate during the task. An increase in connectivity was observed, centred on the button press. The increase in connectivity began 3 s before the movement, and was sustained for about 6 s, which could be due to the windows used. However, there was no explicit exploration of the post-stimulus window. More recently, these data (O’Neill et al., 2017) were analysed further by Tewarie et al. using phase difference derivative (PDD) (Tewarie et al., 2018) which is a method to quantify the phase synchronous dynamics in time series data (Breakspear et al., 2004), and further explored using instantaneous amplitude correlation, wavelet coherence and PDD (Tewarie et al., 2019). A sensorimotor network was found to modulate during the task, showing an increase in connectivity during the PMBR. The authors suggest that this represents the PMBR acting as a mechanism to reintegrate isolated regions back into the sensorimotor network. Yet, a large proportion of functional connectivity studies have focused on resting state networks, with few studies investigating dynamic connectivity during a task. This indicates a need to study the connectivity and evolution

of networks during the PMBR. Functional connectivity during the PMBR will be explored further in this chapter using amplitude envelope correlation (AEC). A detailed explanation of amplitude envelope correlation is given in Section 5.3.

The PMBR is usually considered in the form of a beta envelope averaged over many trials (see Chapter 4), yet a recent body of work describes beta oscillations in terms of a “bursting” hypothesis (Little et al., 2018; Sherman et al., 2016). The premise is that, distinct from the view of an ongoing oscillation whose amplitude changes over time, beta oscillations are generated by short punctate events, or bursts, that are not necessarily time-locked over trials. The MRBD can be thought of as an absence of bursts, whilst the PMBR reflects an increased burst likelihood which, when averaged over trials, looks like a smooth increase in oscillatory amplitude (Little et al., 2018). The idea that electrophysiological data can be broken down into transient events is not new; it has been supported by a vast body of evidence that decomposes whole brain electrophysiological data, measured using EEG, into “microstates” (Koenig et al., 2005; Lehmann et al., 1998) that represent short (~100 ms) windows, in which the distribution of EEG power over the scalp remains stable. However, this field is still unfolding (van Ede et al., 2018), and to date the relationships between connectivity and classical metrics like the PMBR remain unclear.

To better understand the PMBR, it is imperative to understand what underlies these trial-averaged results and the brain regions recruited during this period compared with other task and rest periods. To fully understand the nature of transient brain networks, and their role in the PMBR, high temporal (millisecond) analysis methods are needed. One method that has recently been applied to MEG data are hidden Markov models (HMM) (Baker et al., 2014), which fully takes advantage of the excellent temporal resolution of MEG. The HMM is able to identify brain states which vary on 100 ms time scales. The benefits of using the HMM on task data are that the HMM is given no knowledge of the task timings and is a data driven approach, unlike other connectivity metrics where timings and time windows need to be specified. Novel methods, like the HMM, potentially offer a new means to understand the nature of the MRBD and the PMBR, and their perturbation in disease in the context of beta bursts and network dynamics.

Studies have identified states related to the PMBR during a task, for example Vidaurre et al. (Vidaurre et al., 2016) investigated a self-paced button press task and found an ERD and an ERS state associated with the button press using a 3-state HMM. Quinn et al. 2018 (Quinn et al., 2018) applied an HMM to a face perception task and revealed task-dependent HMM states which varied on millisecond time scales. These approaches show that HMMs have the power to reveal transient networks in brain activity which vary on very short time scales.

5.2.1 Aims and Objectives

In this chapter, to explore the relationship between the PMBR, connectivity and brain networks, two analysis methods (AEC and HMM) will be used to investigate the motor task data from the previous chapter. The aim of this work is to investigate the evolution of connectivity through the entire time series of the task to gain further insight into the functional role of the PMBR. This motor task is ideal for studying dynamic connectivity, as the long rest periods between stimuli provides sufficient data to act as ‘resting state’ to compare with different task periods.

The hypothesis is that during the motor task, connectivity will be localised to the contralateral motor cortex during the movement, with an increase in connectivity during the post-stimulus response between the motor region and all other brain areas as the brain integrates itself with resting state networks, as previously proposed in an EEG-fMRI study (Mullinger et al., 2013b). Further, it is hypothesised that the networks of functional connectivity are transient events but the sensorimotor network, which is re-established in the PMBR period, is visited more often during this period than any other period of time. These networks form and dissolve through “bursts” of concordant brain activity. These hypotheses will be tested by exploring the networks present during the PMBR compared with stimulation and baseline periods throughout the task, using AEC to investigate whether the connectivity between the contralateral motor cortex and the rest of the brain is modulated across three different time windows: a window during ERD, ERS and baseline. The second objective was to investigate whether a HMM could provide further information on how network connectivity evolves and ultimately understand the evolution of the PMBR in the context of brain network architecture.

5.3 Background Theory

5.3.1 Functional Connectivity

In MEG, when measuring neural oscillations, there are typically two ways of relating signals: measuring correlation between the amplitude envelope of band-limited oscillations, or the relationship between the phase of oscillations. See (O'Neill et al., 2015; O'Neill et al., 2018), and (Bastos & Schoffelen, 2016) for a review of connectivity analyses. Amplitude envelope connectivity tends to better match fMRI connectivity than phase-based connectivity (Brookes et al., 2011a; Tewarie et al., 2016a) and is one of the most reliable methods (Colclough et al., 2016). For example, de Pasquale (de Pasquale et al., 2010) uses MEG to study resting state networks. The authors show two well-characterised resting state networks: the dorsal attention network and the default mode network. After creating the MEG power time series, correlation was measured between a seed voxel and the rest of the brain voxel over the entire 5-min MEG time series. Many other studies have since confirmed that power envelope correlation in MEG agrees with resting state networks found in fMRI (Brookes et al., 2011a; Brookes et al., 2011b; Hipp et al., 2012; Hipp & Siegel, 2015; Liu et al., 2010).

Unlike the sluggish haemodynamic metric of brain activity in fMRI, MEG provides a direct measure of neuronal activity with excellent time resolution (see Chapter 2) allowing instantaneous connectivity metrics to be derived such as various phase metrics (coherence (Nunez et al., 1997), imaginary coherence (Nolte et al., 2004), phase locking value (Lachaux et al., 1999), phase lag index (Stam et al., 2007), phase difference derivative (Breakspear et al., 2004)) as well as cross-frequency correlations (Florin & Baillet, 2015). This allows the interrogation of dynamic connectivity. That is, connectivity representing functional networks that form and dissolve on sub-second time frames.

5.3.2 Dynamic Functional Connectivity

Following in the footsteps of fMRI (Sakoğlu et al., 2010), one simple way to measure dynamic functional connectivity in MEG is with a sliding window approach. This involves selection of a time window of fixed length in which the functional connectivity is assessed (in the same way as a stationary approach), then the window is shifted along (by a set number of points) and the connectivity is reassessed. The benefits of the sliding window are that most conventional static methods of measuring functional connectivity

still apply and do not need to be changed. However, the choice of window length is non-trivial. The window needs to be large enough to robustly measure connectivity, yet short enough to explore transient network features. Shorter windows mean there are less time points to measure and therefore less signal to noise ratio (SNR) and the measurements can become dominated by noise. If the window is too long, any effects from fast changes will be diluted.

Windows of varying length have been used through many different studies. In one of the first studies of dynamic connectivity in MEG, de Pasquale used a 10 s sliding window (de Pasquale et al., 2010). They showed fluctuations in the dorsal attention network on the order of minutes, and also found evidence for correlations existing on 10 – 20 s time scales, providing evidence for non-stationary MEG networks. The same group added to this work in 2016 (de Pasquale et al., 2016), by showing that multiple dynamic networks exist which interact with each other. They used the same 10 s sliding window and found three distinct networks: default mode (DMN), dorsal attention (DAN) and motor network. The DMN, DAN and motor network were shown to have strong cross-network interactions. They hypothesised that these dynamic networks are a property of the brain to increase the efficiency of communication.

Since the inception of sliding window analysis, the issue of window length choice has remained. The effect of window length on correlations was investigated by Brookes et al. (Brookes et al., 2011a) using varying time segment lengths of 0.5, 1, 4, 6 and 10 s to measure AEC between left and right motor cortex. For AEC, no significant correlations were measured using the 0.5 s window, with correlation values and significant correlations increasing with increasing time window length. This suggests longer time windows (10 s) are more reliable, however the results for 4, 6 and 10 s window were found to be similar.

5.3.3 Amplitude Envelope Correlation

Perhaps the simplest way to assess the relationship between two time courses is to measure the correlation of their amplitudes. This first requires the amplitude envelope of the oscillation, which is commonly calculated using a Hilbert transform (Chapter 2). Once the Hilbert envelope has been created, the correlation between two given envelopes can be calculated. This is done by simply taking the linear correlation coefficient between two time courses, usually the Pearson correlation coefficient. This

can take a value between +1 and -1, where 1 is positive correlation, 0 is no correlation and -1 is negative correlation. The Pearson correlation coefficient is the covariance of two variables divided by the product of their standard deviations. These correlations can be assessed across the brain and at a range of different frequencies to reveal regions of the brain connected with each other.

5.3.4 Leakage

Probably the most significant challenge when using MEG for connectivity analyses is signal leakage. Due to the ill-posed inverse problem, signals at spatially separate locations may not be independent, which can lead to wrongly inflated measures of connectivity between these regions, especially if these regions are spatially neighbouring. Therefore, this issue of signal leakage must be addressed before connectivity metrics of any type can be taken.

When two separate sources are beamformed, signals originating from one brain location can leak into the estimated signals from a separate brain region. The reason for this is explained mathematically here, also refer to Chapter 2 for further information on beamforming. Assuming two separate sources in the brain, \mathbf{q}_1 and \mathbf{q}_2 , the measured MEG data will be

$$\mathbf{m} = \mathbf{l}_1 \mathbf{q}_1 + \mathbf{l}_2 \mathbf{q}_2 + \boldsymbol{\epsilon} \quad (1)$$

where \mathbf{l}_1 and \mathbf{l}_2 represent the forward vectors for the sources and $\boldsymbol{\epsilon}$ is measurement noise. To reconstruct source \mathbf{q}_1 with a beamformer, \mathbf{q}_1 can be reconstructed as the beamformer weights multiplied by the MEG data:

$$\hat{\mathbf{q}}_1 = \mathbf{w}_1^T \mathbf{m}. \quad (2)$$

Substituting in the MEG data from equation 1,

$$\hat{\mathbf{q}}_1 = \mathbf{w}_1^T \mathbf{l}_1 \mathbf{q}_1 + \mathbf{w}_1^T \mathbf{l}_2 \mathbf{q}_2. \quad (3)$$

Since the beamformer is subject to the linear constraint $\mathbf{w}_1^T \mathbf{l}_1 = 1$,

$$\hat{\mathbf{q}}_1 = \mathbf{q}_1 + \mathbf{w}_1^T \mathbf{l}_2 \mathbf{q}_2. \quad (4)$$

Therefore \mathbf{q}_1 will be reconstructed with an additional term dependent on \mathbf{q}_2 , which will only be independent of \mathbf{q}_2 if $\mathbf{w}_1^T \mathbf{l}_2 = 0$, i.e. if the weights of \mathbf{q}_1 are orthogonal to the forward vector for \mathbf{q}_2 . This is a simplistic example with only two sources in the brain and assuming no noise. In reality, this needs to be simulated for varying number of dipoles and locations and sensor noise. O'Neill et al. (O'Neill et al., 2015) simulated

this and showed that leakage is greatest in sources close to each other, and still has large effects in sources 5 cm apart from each other. Sources need to be at least 6 cm apart for leakage to be less of a concern. They also showed that leakage is increased for regions with lower SNR, for example for sources deep in the brain. Therefore, to produce accurate connectivity results, leakage needs to be controlled.

Leakage results in overestimated connectivity between sources, where this correlation will have zero-phase-lag. Source leakage is linear, therefore leakage can be corrected by removing zero-lag correlations. In reality, there is expected to be a time lag in true connectivity, as signals take time to travel along nerve fibres in the brain. As a result, a way to reduce leakage is to remove all zero-phase-lag connectivity. In envelope connectivity, this can be done via linear regression. The linear projection of a voxel is removed using a general linear model. This has been done by pairwise comparison between voxels (Brookes et al., 2012; Hipp et al., 2012), where time courses are orthogonalised with respect to a seed voxel. This can be used when investigating a seed compared to the rest of the brain. In whole brain analysis, symmetric multivariate leakage correction can be used (Colclough et al., 2015), where all time courses from each region are made orthogonal to each other.

5.3.5 HMM Theory

Sliding window approaches are limited as the window length needs to be defined a priori, and perhaps varies over the length of an experiment. Higher temporal resolution connectivity metrics and shorter sliding windows are available, however this often means less data are being used, resulting in lower SNR. Recently, several studies (Baker et al., 2014; Vidaurre et al., 2018a; Vidaurre et al., 2018b) have used a HMM to identify points in time at which distinct spatial patterns of oscillatory power occur. Results show that brain activity can be parcellated into ‘states’, each of which has a spatial signature that relates to canonical resting state networks. These networks, including the sensorimotor network, modulate on a very short (100 ms) time scale, much faster than AEC can reveal. Another benefit of HMMs is that they are data-driven but with an assumption – the only parameter that needs to be specified is the number of states. Instead of estimating connectivity for a limited window length as in AEC, the estimation is performed at state level – all the data corresponding to that state is pooled together to characterise the network (see Figure 5.1) and therefore much more robust.

Therefore there is no need to pre-specify the window width which is hugely advantageous.

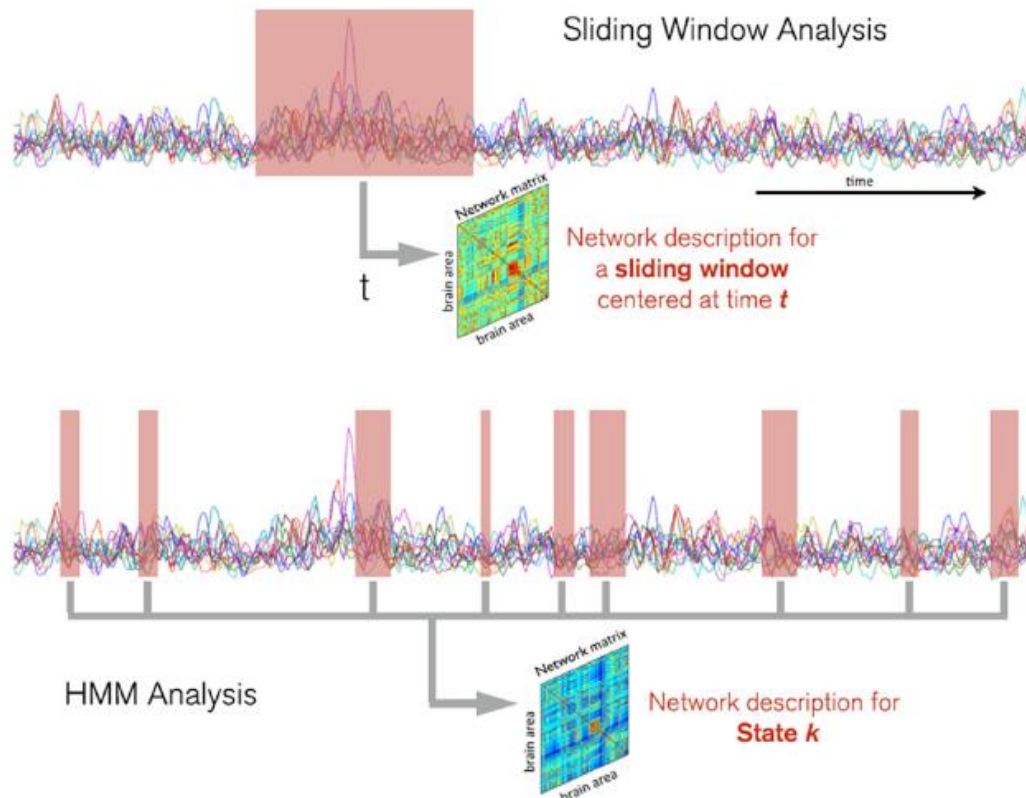


Figure 5.1. From (O'Neill et al., 2018). The top panel shows sliding window connectivity analysis: a window of fixed length t is taken, and connectivity measured in this window. In HMM analysis (bottom), networks are described by state occurrences across the entire data set. The states are inferred from the data itself, and are more robust than a sliding window as data is taken from the entire dataset rather than a window of limited length.

One of the first studies to apply an HMM to MEG data was Baker et al. (Baker et al., 2014). The authors used an HMM to investigate resting state MEG data and found the classical resting state networks, which have previously been seen with lower temporal resolution fMRI and MEG, but showed that the networks form and dissolve on rapid timescales, lasting only 100 to 200 ms in each instance, much more rapidly than had previously been shown. Vidaurre et al. (Vidaurre et al., 2016) presented an update to this HMM, which uses the phase information of the raw data. In this case the states are represented by multivariate autoregressive models (HMM-MAR) of the raw time series rather than power envelopes and can therefore use phase information. Vidaurre et al. (Vidaurre et al., 2018b) uses an HMM to identify brain networks described by power and phase connectivity that are spectrally resolved (as a function of frequency) in

resting state. By showing that these short-lived transient brain states have very specific frequency bands, they propose that this represents functional specialisation. Phase-locking at distinct frequencies across the cortex has been proposed as a means of transmitting information across the brain in an efficient way (Fries, 2005; Palva et al., 2005). HMMs have also been shown to be clinically useful in a study characterising the effects of benzodiazepines on multiple sclerosis (Van Schependom et al., 2019).

A hidden Markov model (HMM) is a statistical model which assumes a system can be described by a set of distinct states. In the HMM, the states are ‘hidden’ – they cannot be directly observed. Instead, they are inferred based on observations (the data). The transition from one state to the next depends only on the current state – this is a Markovian process (a memoryless random process, with Markov chain of order 1). The Markovian process is determined by the current state and the state transitions probabilities (Rabiner, 1989; Stamp, 2015).

To model a given observation sequence with a hidden Markov process, the only parameter to be specified is the number of states in the model. The model is then trained on the data to find the best model that fits the observations. Given the model and observations, the optimal state sequence can then be found.

The model (λ) is described by the parameters A , B , and π ,

$$\lambda = (A, B, \pi). \quad (5)$$

A is the matrix of state transitions – the probabilities of transitioning from one state to the next. A is a square matrix $N \times N$, where N is the number of states in the model. The A matrix is row stochastic, which means that each row must sum to one. The system has to be in one of the states at any given time point, and the states are mutually exclusive. The B matrix is based on real data and relates the hidden states to the observations. B is $N \times M$ where M is the number of different observations, which comes from the data. π is the initial state distribution.

Once the model has been determined, the most likely state sequence needs to be determined. For an HMM, the “best” sequence of states is not necessarily the most probable one, i.e. the one that maximises probability of the entire state path. Rather, the sequence of states is the one that maximises the expected number of correct states; an expectation maximisation algorithm.

A diagram of a HMM is shown in Figure 5.2. O represents the observation sequence and X represents the hidden state sequence. The goal of the HMM is to learn about the states X from the observables. The HMM results in a hidden state sequence $X_0, X_1, X_2, \dots, X_{T-1}$, where T is the length of the observation sequence. Note that each state in the sequence doesn't have to be different from the previous state. The dashed red line demonstrates what can be observed: above the red line is the Markov process which is hidden, below are the observables. Only the observation sequence, O , is able to be observed, which is related to the hidden states by the observation probability matrix, B . In the simplest case B is a Gaussian. The transitions between hidden states are described by probabilities in the matrix A .

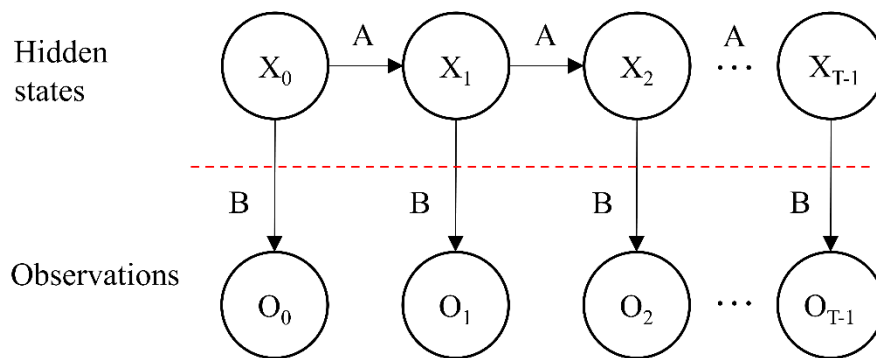


Figure 5.2. Diagram of a simple HMM. The observations, O (MEG data), can be described by a time series of hidden states, X . The hidden states are related to the observations by the observation probability matrix B . The transitions from state to state are governed by the matrix of state transitions, A .

In MEG data, it can be assumed that the MEG signals can be described by a set of networks that change over time, which are related to the observations of MEG data. These brain networks cannot be directly measured, but can be inferred from the measured MEG data. The HMM segments the MEG time series into a sequence of states, indicating at each time point which state is the most likely. Each state is characterised by a unique pattern of whole-brain spontaneous activity, which is modelled by a multivariate normal distribution (Baker et al., 2014). The HMM used in this thesis is similar to that used in Baker et al. (Baker et al., 2014).

5.4 Methods

5.4.1 Data Acquisition

The data used here are the data that were acquired and used in Chapter 4, see Chapter 4 for a full description of the paradigm. Briefly, fifteen subjects performed a right-handed grip contraction task. Firstly, individual maximum voluntary force (MVF) was determined. Then, in two separate runs, subjects were visually cued to exert 30% MVF for 2, 5 or 10 s (15 trials/condition, pseudo-random order), followed by 30 s rest. Data were acquired using a 275-channel CTF MEG system. Surface electromyography (EMG) was used to monitor forearm muscle activity.

5.4.2 Analysis

5.4.2.1 Amplitude Envelope Correlation

Following pre-processing (see Section 4.3.4 of previous chapter), each subject's brain anatomy was parcellated into 78 cortical regions using the AAL atlas (Tzourio-Mazoyer et al., 2002). The atlas was transformed to each subject's anatomical brain geometry using FLIRT (Jenkinson et al., 2012). The centre of mass of the region was found to provide a single representative location for each region. MEG data were source localised to this location using a linearly constrained minimum variance beamformer (Robinson & Vrba, 1998; Van Veen et al., 1997) with covariance measured over the whole experiment to derive virtual electrodes for the 78 cortical regions. The forward model used a dipole approximation (Sarvas, 1987) and a multiple spheres head model (Huang et al., 1999). Dipole orientation was determined by searching over 180° and finding the orientation with the greatest signal to noise ratio as described in Chapter 2.

For the functional connectivity analysis, data were filtered into the alpha (8 – 13 Hz) and beta (13 – 30 Hz) bands, where largest induced effects were seen in the average time courses in Chapter 4. To maximise the data from which to calculate the connectivity, data from the three stimulus durations were combined and effects during specific time periods of the task were explored. A four-second time window was chosen as this would be long enough for good signal to noise ratio, but short enough to capture the effects of the periods of interest irrespective of the contraction duration, as four seconds was the largest time window which could capture the ERD for the 2 s stimulus response. Three time windows were chosen to investigate the event-related

desynchronization (ERD), event-related synchronization, and baseline. For all stimulus durations, data were segmented into the three windows: ERD (defined -4 to 0 s relative to movement offset, i.e. during the task); ERS (1 to 5 s after movement offset, i.e. during the rebound); and baseline (20 to 24 s after movement offset) (see Figure 5.3). For each region, pairwise leakage correction was performed (Brookes et al., 2012; Hipp et al., 2012) and the amplitude envelope derived using a Hilbert transform. Connectivity was determined by measuring the Pearson correlation between amplitude envelopes of all 78 regions, to all regions. This was done on a trial by trial basis and the resulting 78 x 78 connectivity matrix was then averaged over all trials for each of the three time windows, for each subject. Connectivity matrices were averaged over regions to give a 78 x 1 matrix indicating the average connectivity strength from one region to all other regions, and averaged over subjects, which could be plotted to visualise the connections of each region to all other brain regions (see Figure 5.4 to Figure 5.7 in Results). To assess statistical differences in connectivity between time windows, connectivity across all regions was averaged to give one value of connectivity per subject and time window. A repeated measures ANOVA was used to assess statistical differences between connectivity in the different time windows. To investigate interhemispheric connectivity, the quarter-diagonal of the 78 x 78 connectivity matrix was plotted as this gives the connectivity between the same brain regions in the right and left hemispheres.

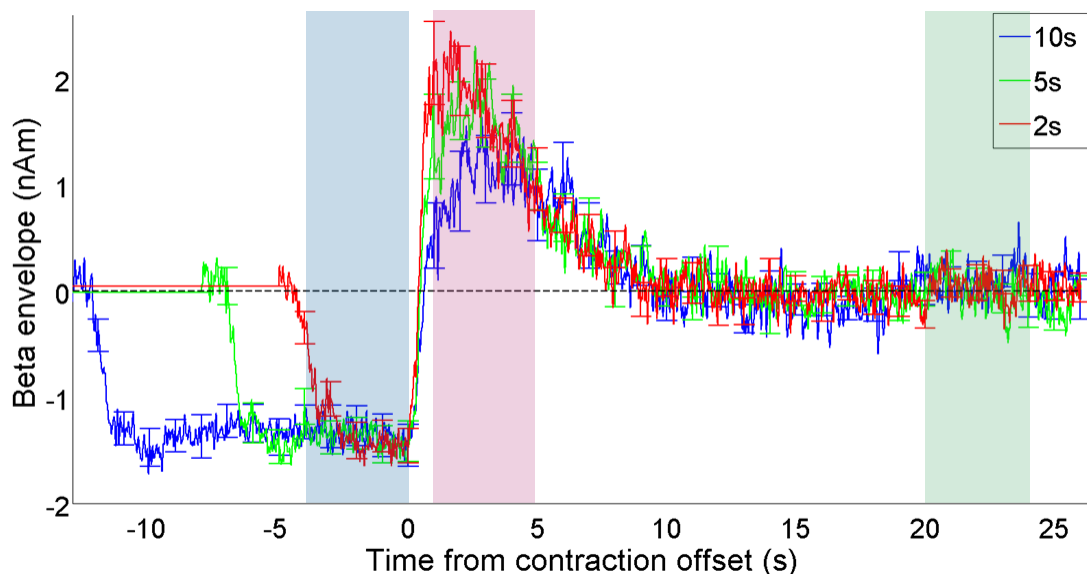


Figure 5.3. For AEC, data were segmented into 3 windows: ERD (-4 to 0 s relative to movement offset, blue block), ERS (1 to 5 s after movement offset, red block) and baseline (20 to 24 s after movement offset, green block). Displayed here overlaid on the beta envelope from Chapter 4 (Figure 4.3) to show the effects in each window for all contraction durations.

5.4.2.2 Hidden Markov Model

To gain insight into what is happening to the dynamics of the beta band amplitude envelope at the individual trial level, a hidden Markov model (HMM) (Baker et al., 2014; Rezek & Roberts, 2005; Woolrich et al., 2013) was used. Again, the brain was parcellated into 78 regions according to the AAL atlas (Tzourio-Mazoyer et al., 2002). Following this, an LCMV beamformer was used to derive a time course of estimated electrophysiological activity for each region (Brookes et al., 2016; Hillebrand et al., 2012). The beamformer was applied with a covariance window encompassing the 1-150 Hz frequency range and a time window capturing the entire experiment. Regularisation was applied to the covariance matrix using the Tikhonov method with a regularisation parameter equal to 5% of the maximum eigenvalue of the unregularised covariance matrix. Time courses were derived from a single virtual electrode at the centre of mass of each region and symmetrically orthogonalised (Colclough et al., 2015; Colclough et al., 2016) for leakage reduction. Prior to application of the HMM the source localised data were downsampled to 100 Hz and frequency filtered to 1 – 40 Hz (Baker et al., 2014). The data were limited to this frequency range as results from Chapter 4 showed effects in the alpha band as well as the beta band, and higher frequencies in the gamma band are difficult to detect with this approach (Quinn et al., 2019; Vidaurre et al., 2018b). The Hilbert transform was applied to generate the amplitude envelopes and data were concatenated across subjects and runs.

For the HMM itself, analysis is performed on the amplitude envelopes similar to that used in previous work (Baker et al., 2014; Quinn et al., 2018; Woolrich et al., 2013). This assumes that brain activity is well-described by a relatively small number of “states” and that, at any single point in time, only one of these states is active. Note that states are mutually exclusive. In addition, this also assumes that the underlying sequence of states is Markovian; i.e. the brain’s current state depends only on its previous state, rather than a complete history of past states. Each state was described by a multivariate normal distribution with a (78×1) mean vector and a (78×78) covariance matrix. Inference on the HMM is carried out using variational Bayes (VB) (Rezek & Roberts, 2005), to estimate the full posterior distribution on the model parameters (i.e. a probabilistic description of the likelihood of the unobserved state parameters, and state transition probabilities, conditional on the measured data was obtained). In addition, for every time-point, the state which the brain was most likely

to be in was determined. This was done using Viterbi decoding (Baker et al., 2014; Woolrich et al., 2013). The result is a binary time course for each state, showing whether, for any one point in time, that state was the most likely. A HMM with 4, 6, 8 and 10 states was run to identify the number of HMM states required to identify a bilateral motor state expected to be modulated by the post-stimulus response as identified in the results presented in Chapter 4. Each HMM was ran 10 times to test the variability of the states, and the inference with the lowest free energy was chosen (Quinn et al., 2018). Crucially, the HMM inference was carried out without knowledge of the task timings or structure. Based on this analysis, an 8-state HMM was chosen (see results), in agreement with that used previously (Baker et al., 2014) .

The resulting 8 binary state time courses were decomposed to obtain summary statistics. Specifically, for each state and subject: 1) Fractional occupancy: the fraction of the trial that the brain was in each state. 2) Number of occurrences: number of times a state is visited. 3) State lifetime: the mean time spent in each state on a single visit. 4) State interval: the mean time between state visits 5) State mean beta amplitude: the mean amplitude of the beta power in the left sensorimotor cortex during state visits (i.e. the time course derived from “conventional” analysis above multiplied with the binary state time course derived from the HMM to give beta power during state visits) were estimated. The mean values of these parameters were calculated by averaging over trials and then subjects. Each of these metrics was calculated individually for the three epochs, based on the results from the time-frequency analysis and the same periods used above in the AEC analysis: ERD (defined as a 4 s window -4 to 0 s relative to movement offset), ERS (defined as a 4 s window 1 to 5 s after movement offset), and baseline (20 – 24 s after movement offset) and averaged over all contraction durations. To test for significant differences in each of the metrics between the three time windows, a RM ANOVA was performed across the subjects and time windows. To interrogate the ERS period further, the same five metrics were calculated for the three separate contraction durations in the 4 s window after movement offset. RM ANOVA was then used to test for significant differences of the metrics between contraction durations during the ERS period.

5.5 Results

5.5.1 Amplitude Envelope Correlation

Figure 5.4 shows the networks present during each time window in the beta band. The panels show the correlation between each region and every other region over the whole brain. Significant differences between the three time windows ($p < 0.05$, RM ANOVA) were found in the mean beta band connectivity over the whole head, with the ERS period exhibiting the greatest connectivity. Mean connectivity (\pm SE) across subjects for beta band responses was 0.040 ± 0.005 , 0.054 ± 0.005 and 0.051 ± 0.005 during the ERD, ERS and baseline, respectively. During the ERS, connectivity to all other brain regions was greatest in the contralateral sensorimotor region for beta responses. The mean value (\pm SE) in the left (contralateral) precentral gyrus was 0.040 ± 0.005 , 0.063 ± 0.007 and 0.052 ± 0.007 during the ERD, ERS and baseline, respectively, a significant difference ($p < 0.05$, repeated measures ANOVA) in connectivity between time windows for this region. During baseline, bilateral connectivity patterns were observed with the strongest in motor-parietal areas.

Considering only regional inter-hemispheric connectivity (Figure 5.5) (the correlation between one region and the corresponding region in the other hemisphere), there was a significant difference in interhemispheric connectivity between the three time windows ($p < 0.05$, RM ANOVA) over the whole brain. The strongest connectivity during the ERS was observed in the sensorimotor strip for beta responses. Whilst during the ERD, higher order parietal areas exhibited the highest connectivity and during baseline, connectivity was strongest over the occipital and sensorimotor cortex. Mean interhemispheric connectivity was 0.043 ± 0.005 , 0.065 ± 0.005 and 0.059 ± 0.006 for the ERD, ERS and baseline, respectively. In particular, for the precentral gyrus, connectivity from the left precentral gyrus to the right precentral gyrus was 0.038 ± 0.007 , 0.09 ± 0.01 , 0.072 ± 0.009 for the ERD, ERS and baseline, respectively, again a significant difference between the three time windows ($p < 0.05$, RM ANOVA) in interhemispheric connectivity between time windows for this region. This shows that during the ERS window, homologous regions across the two hemispheres are more connected through beta band activity than during the other two time windows.

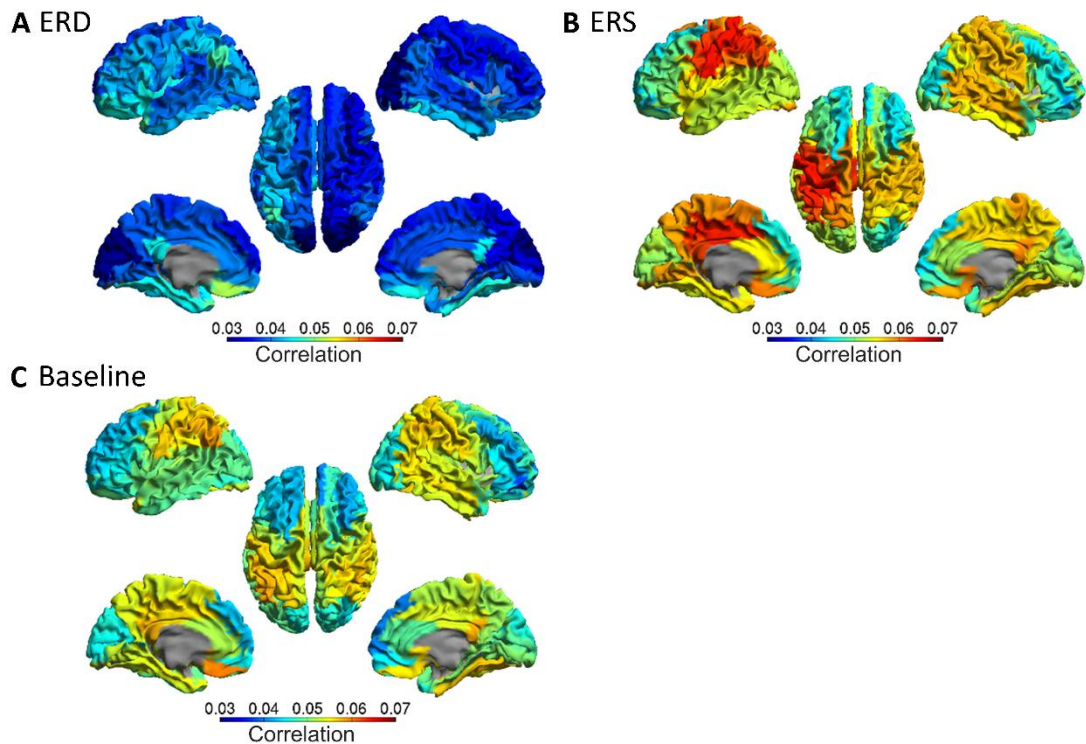


Figure 5.4. Beta connectivity: average correlation in the beta band between each node and every other node across all brain regions averaged across all subjects. Correlation values calculated for all stimulus durations combined in three separate time windows relative to movement offset: (A) ERD (-4 to 0 s), (B) ERS (1 to 5 s) and (C) baseline (20 to 24 s).

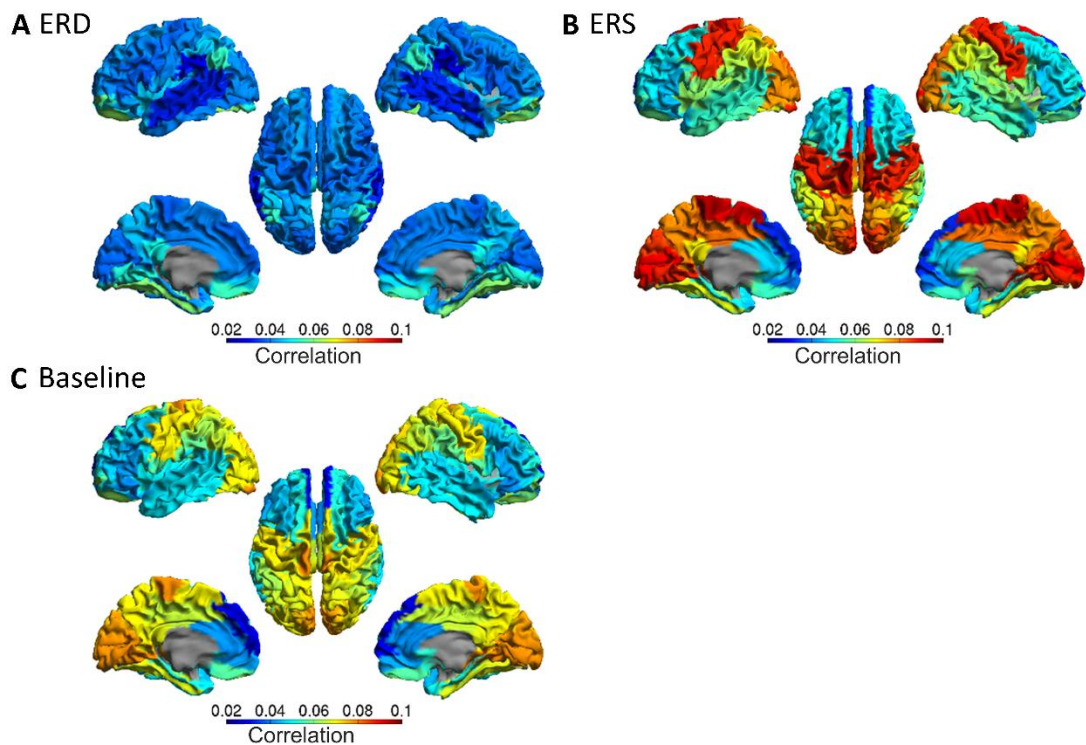


Figure 5.5. Beta inter-hemispheric connectivity: correlation in the beta band between node and corresponding node in other hemisphere averaged across all subjects. Correlations were calculated during three time windows relative to movement offset: (A) ERD (-4 to 0 s), (B) ERS (1 to 5 s) and (C) baseline (20 to 24 s), for all stimulus durations combined.

Similarly, Figure 5.6 and Figure 5.7 shows the alpha band results. Significant differences between the three time windows ($p < 0.05$, repeated measures ANOVA) were found in alpha band connectivity over all regions (Figure 5.6), with the greatest connectivity again seen during the ERS period. Mean connectivity (\pm SE) across subjects for alpha band responses was 0.04 ± 0.01 , 0.07 ± 0.01 , and 0.06 ± 0.01 during the ERD, ERS and baseline, respectively. During the ERS, connectivity to all other brain regions was greatest in the left parietal region, with strong correlations also in occipital regions. During baseline, bilateral connectivity patterns were observed with the strongest in the occipital-parietal area. In the occipital lobe (averaged over both hemispheres), connectivity in the three windows was 0.04 ± 0.01 , 0.07 ± 0.01 and 0.06 ± 0.01 for the ERD, ERS and baseline, respectively, a significant difference between the three time windows ($p < 0.05$, repeated measures ANOVA).

Considering only regional inter-hemispheric connectivity (Figure 5.7), the strongest connectivity during the ERS was observed in the occipital lobe for alpha responses (Figure 5.7B). Whilst during the ERD, higher order visual and parietal areas exhibited the highest connectivity (Figure 5.7A) and during baseline, connectivity was strongest over the occipital and parietal cortex (Figure 5.7C). Mean interhemispheric connectivity over all regions was 0.04 ± 0.01 , 0.08 ± 0.01 and 0.06 ± 0.01 for the ERD, ERS and baseline, respectively, a significant difference between the three time windows ($p < 0.05$, repeated measures ANOVA). The interhemispheric connectivity between left and right occipital lobe was 0.06 ± 0.01 , 0.11 ± 0.02 and 0.09 ± 0.02 for the ERD, ERS and baseline, respectively, again showing a significant difference ($p < 0.05$, repeated measures ANOVA) between the three time windows.

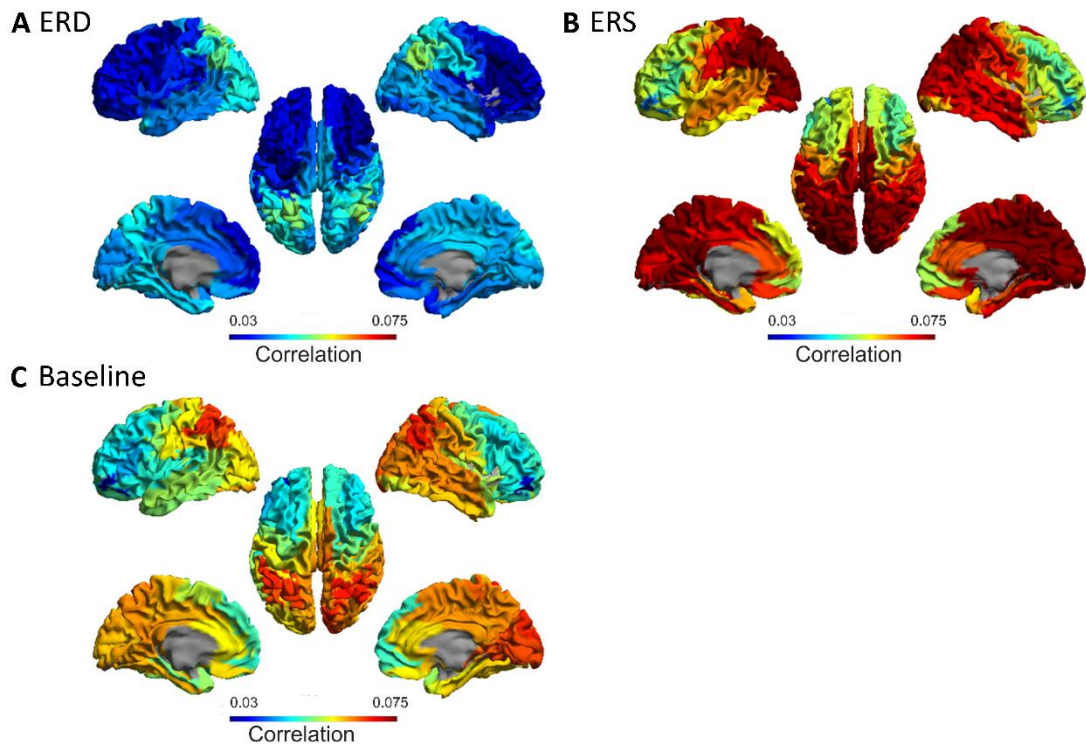


Figure 5.6. Alpha connectivity: correlation in the alpha band between each node and every other node averaged across all brain regions and all subjects. Correlations assessed in three time windows: (A) ERD (-4 to 0 s), (B) ERS (1 to 5 s) and (C) baseline (20 to 24 s) relative to movement offset.

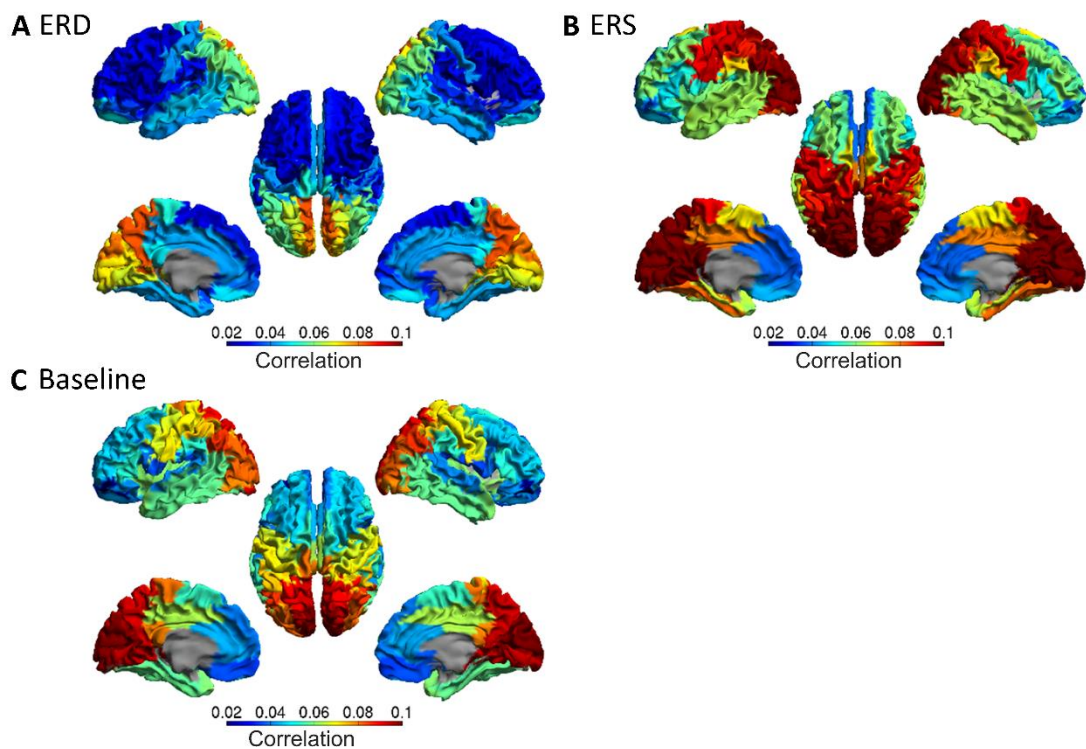


Figure 5.7. Alpha inter-hemispheric connectivity: correlation in the alpha band between node in one hemisphere and the corresponding node in the other hemisphere, averaged across subjects. Correlations measured in three time windows: (A) ERD (-4 to 0 s), (B) ERS (1 to 5 s) and (C) baseline (20 to 24 s) relative to movement offset.

5.5.2 Hidden Markov Model

The state maps for the HMM run with 4, 6, 8 and 10 states are shown in Figure 5.8. When fewer than 8 inferred states for the HMM are used, it was clear that multiple networks are grouped together due to insufficient states. When 10 states are inferred, the motor network of interest (state 7, $K = 8$, 3rd column) is split across three states (states 7, 8 and 9, $K = 10$, right column) which suggests that too many states have been assigned. Therefore 8 inferred states for the HMM were used for further analysis in agreement with previous work (Baker et al., 2014). Of these 8 inferred states, a single state (state 7) was selected for further analysis due to its spatial topography which covered bilateral sensorimotor cortices.

Detailed results are shown in Figure 5.9 for this chosen state, whilst the summary results of all eight states are shown in Figure 5.10. Figure 5.9A shows the state map where red shows brain areas with an increase in power and blue shows brain areas with a decrease in power when the brain entered brain that state, compared to overall average power. The spatial topography shows increased power in the sensorimotor network (extending to posterior parietal regions). Figure 5.9B shows the binary time courses of state occurrences shown for a subset of trials and subjects, with trials on the y-axis and time on the x-axis. Figure 5.9C shows a probabilistic interpretation of these data. Note that the sensorimotor state is most likely to be visited immediately after movement offset and least likely to be visited during movement. This means that the probabilistic time courses mirror the classical MRBD and PMBR (Figures 4.3 and 4.4). Variation with movement duration also mirrors the PMBR results, with a higher probability of the state occurrence for short duration contractions (2 s) compared to longer contraction (10 s). Given that the HMM was applied (in accordance with (Baker et al., 2014)) in the 1 to 40 Hz frequency window, the fact that a single state has been derived whose probabilistic dynamics mirrors those of the PMBR, even accounting for parametric variation with contraction duration, is compelling.

Figure 5.9D summarises the state statistics for the sensorimotor network; findings are averaged over conditions and subjects, but calculated separately for three time-windows: ERD, ERS and baseline, akin to AEC analyses time windows above. A significant ($p < 0.05$, RM ANOVA) difference in number of occurrences of state visits (Figure 5.9Di), state lifetime (Figure 5.9Dii) and fractional occupancy (Figure 5.9Div) between all three time-windows was found. This change in fractional occupancy was driven by both a drop in the number of occurrences during the movement period and a change in the length of the state visit. Significant differences between all three time windows were found for the state lifetime, meaning that during the beta rebound, the sensorimotor state was not only more likely to be found, but also its temporal stability was greater (i.e. state visits were longer). No significant differences across the three time windows were found for the mean interval length, i.e. the amount of time between visits to this state (Figure 5.9Diii). Interestingly, a significant difference in the beta amplitude in the left sensorimotor cortex when this state was visited was observed between the time windows (Figure 5.9Dv), with beta amplitude during state visitations being the greatest during the ERS time period. This suggests that the modulation of beta power in the conventional analyses seen in Figure 4.3C and 4.4C is not purely due to the number and duration of visitations to a given state.

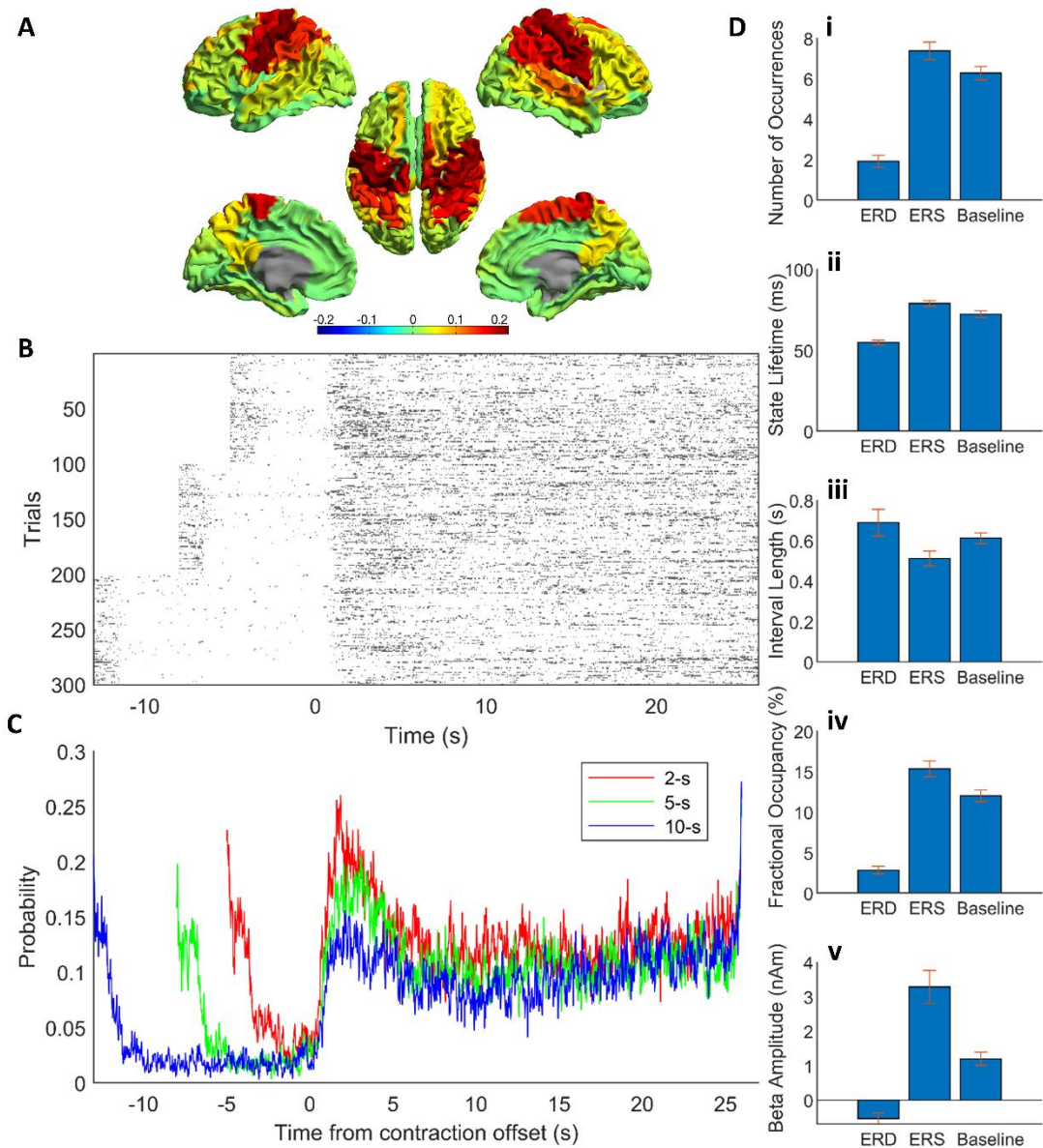


Figure 5.9. Results of sensorimotor state from the HMM. (A) State map of state 7 (see Figure 5.10) showing a sensorimotor state. (B) Plots of the binary time course for a subset of the first 100 trials for the three conditions (2, 5 and 10 s task duration) against time, where dark grey is 1 (in state 7) and white is 0 (not in state 7). (C) Probabilistic time course derived from (B) showing probability of being in state 7 at any given time, for the three conditions. Responses are aligned to contraction offset (time = 0 s). Red line shows 2 s task duration, green line is 5 s task duration and blue line is 10 s task duration. (D) Summary metrics for state 7, averaged over all conditions for each subject and then averaged over subjects, separated into three epochs relative to movement offset: ERD (-4 to 0 s), ERS (1 to 5 s) and baseline (20 to 24 s). Error bars show standard error over subjects. Additional analyses are shown in Figure 5.11.

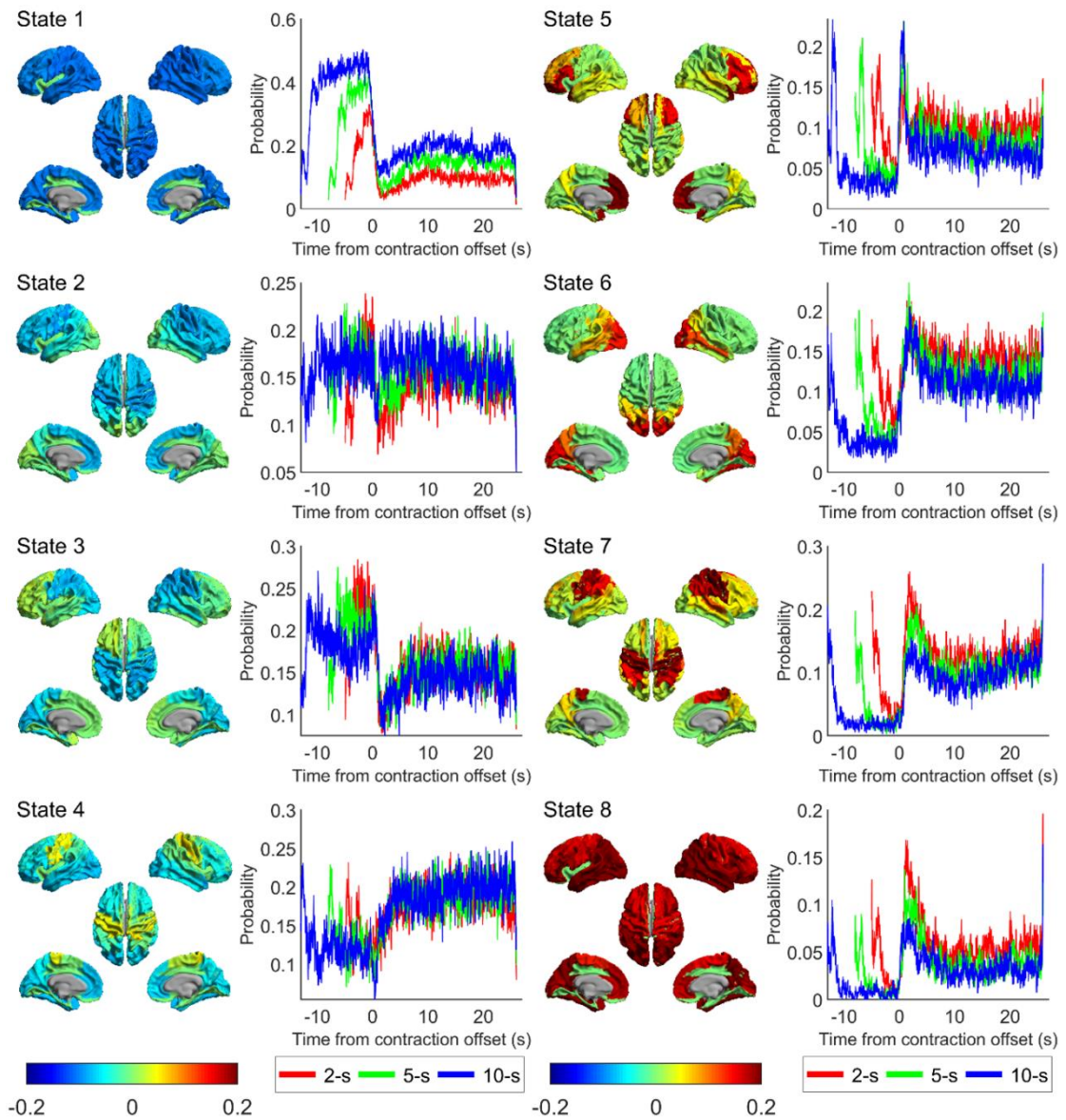


Figure 5.10. State maps from a HMM inferred with 8 states where red shows brain regions with increased power relative to average and blue decreased power, and associated state probability time courses for the three conditions, where red is 2 s, green is 5 s and blue is 10 s task duration.

Interrogating the ERS time window further for different contraction durations, a significant ($p < 0.05$, RM ANOVA) difference in number of occurrences (Fig. 5.11i) and fractional occupancy (Fig. 5.11iv) is seen between the three contraction durations. No difference in state lifetime (Fig. 5.11ii), mean interval length (Fig. 5.11iii), or beta amplitude during state visits (Fig. 5.11v) was seen for the contraction durations. This suggests that the modulation in beta power during the ERS is driven entirely by the number of the visitations to this state, in contrast to the modulation of signals throughout the task time-course. Overall, these results imply that, underlying the beta rebound are rapidly evolving state dynamics which change systematically, not only with movement, but also with stimulus parameters. This will be addressed further in the discussion below.

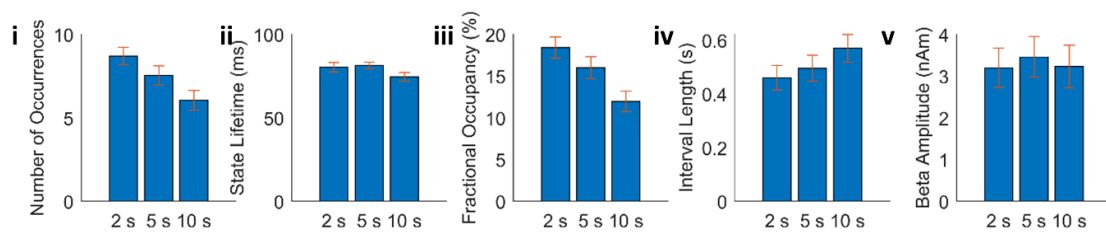


Figure 5.11. Summary metrics for state 7 (see Figure 5.9) during the ERS period (1 to 5 s post movement offset) for the three contraction durations (2, 5, and 10 s). Data are averaged over trials within each condition and then over subjects. Error bars show the standard error over subjects.

5.6 Discussion

The aim of this chapter was to investigate the functional role of the PMBR by exploring the functional brain networks involved in different stages of a task, using two analysis methods. Both the AEC and HMM analyses performed in this chapter showed clear changes in connectivity and brain networks recruited during the different task stages. As hypothesised, the highest connectivity (AEC analysis) was found during the PMBR period in the motor region in the beta band (Figure 5.4). Between hemispheres, the sensorimotor strip showed strong connectivity in the beta band (Figure 5.5) as well as strong connectivity between visual and parietal areas in the alpha band (Figure 5.7). The HMM analysis complemented this finding, identifying a state with a spatial topography that covered bilateral sensorimotor cortices, which was most likely to be visited during the PMBR period (Figure 5.9). The probability of visits to this state was also modulated by contraction duration, mirroring the observations in Chapter 4 with more classic analyses. This supports the idea that brain activity consists of bursts of activity. Furthermore, the beta amplitude during state visits was modulated between task stages but not between contraction durations during the PMBR period, suggesting more than one beta phenomenon is occurring, as explored more below. Overall, these findings support the hypothesis that the PMBR is facilitating a re-integration of brain networks post-stimulation and shed new information as to how the PMBR is formed.

AEC showed clear changes in connectivity during the different task stages. Inter-hemispheric connectivity in primary sensory regions in the beta band breaks down during the ERD and is re-established during the PMBR, producing the strongest connectivity, before returning to baseline (Figure 5.4 and Figure 5.5). The sensorimotor network observed during the rebound period was similar to networks previously observed in other explorations of task-based connectivity, as well as the finding that the PMBR coincides with an increase in connectivity (Quinn et al., 2018; Tewarie et al., 2018; Tewarie et al., 2019; Vidaurre et al., 2016). Together, with these previous studies, the data presented in this chapter supports the idea that the PMBR is required to reactivate networks that were suppressed during the task.

In the alpha band, again the highest connectivity was observed during the ERS period, supporting this hypothesis (Figure 5.6). The main difference observed in the alpha band results compared to the beta band was that connectivity was strongest over parietal and

visual cortex, whilst in the beta band connectivity is stronger over sensorimotor areas. The alpha results are more symmetric than beta (compare Figure 5.4B with Figure 5.6B), which could be explained by the fact the motor task was unilateral, whereas the visual component of the task was not lateralised, resulting in a bilateral visual response. The recruitment of the parietal areas in the alpha AEC analysis (Figure 5.6), suggests that higher order cognitive areas were required in the processing of this task as attention to the stimulus and visual feedback from the grip force were processed by the subject. The apparent recruitment of visual and parietal areas, may be due to two separate but inter-related networks being recruited as recent evidence suggested there may be more than one mechanism which drives alpha power modulations (Sokoliuk et al., 2019).

Further, the HMM analyses provide additional information with regards to the brain regions involved in the PMBR. A bilateral sensorimotor network was identified which is most likely to be visited during the PMBR period (Figure 5.9C), driven by the increased number of times the state is entered and the increased length of time spent in the state (Figure 5.9D). Moreover, the time course of this state has the same characteristics as the beta envelope seen in Chapter 4 (Figure 4.3), with the modulation of contraction duration exhibited by the PMBR also demonstrated by the probabilistic state dynamics, as increasing task duration decreases the probability of being in the state after movement offset (Figure 5.9C). This implies that rapidly evolving network dynamics underlie the observation of systematic variation of the PMBR with stimulus duration. Though the PMBR and MRBD are sustained over several seconds in the time frequency spectrogram analysis from Chapter 4, and the AEC results show networks on a 4 s time scale, the HMM analysis shows that the underlying these affects or individual beta events lasting on average 100 ms in duration.

The findings from both the HMM analysis and AEC support the premise that the PMBR is related to long range integrative processes over distributed networks (Mullinger et al., 2017; Mullinger et al., 2013a; Tewarie et al., 2018), perhaps re-integrating networks which divide during tasks to facilitate unilateral processing (Mullinger et al., 2017; Mullinger et al., 2013a). In particular, whilst it was not possible to interrogate networks on a very short time scale (sub-second) with AEC, the results of the HMM also complements the theoretical framework of network dynamics (Shenoy et al., 2013), whereby a rapid switching between networks which are recruited during movement preparation and movement onset, are proposed. Rapid changes in the number of visits

to the sensorimotor state were observed on movement onset and offset (Figure 5.9), whilst the change into resting state from the network primarily recruited in the PMBR period is more gradual. In future work, further insights into the network properties of the PMBR could be obtained using versions of the HMM able to find states that correspond to brain networks with distinct power spectra and phase-locking (Vidaurre et al., 2018b), to build a greater understanding of the role of the PMBR.

The HMM analyses also demonstrate that the length of each visit to the “rebound” state is greatest in the PMBR period (79 ± 7 ms) and least during the MRBD (55 ± 6 ms), whilst still an order of magnitude shorter than the duration of the PMBR seen through traditional analysis (Figure 4.3). The duration of the visits into this state are on the time scale of beta bursts (Sherman et al., 2016), perhaps suggesting that this state is denoting beta bursting activity. Bursting activity has been conceptualized as generating the modulations seen in traditional averaged oscillations by an increase in likelihood of transient bursts of beta activity at certain phases of a task with no systematic change in the amplitude of the beta bursts across time (Jones, 2016). The modulation of the PMBR presented in this chapter is consistent with this concept, with the frequency of visits to the “rebound” state reducing, whilst the amplitude of the beta band signal remains constant during the PMBR, with increasing contraction duration (Figure 5.11). This suggests that the modulation of the PMBR amplitude seen in Figure 4.3 is driven entirely by the number of state visits. In contrast, the amplitude modulation across the task periods i.e. MRBD, PMBR and rest appears to be explained by a combination of the bursting hypothesis and the traditional concept of the amplitude, duration and frequency of the beta “bursts” changing across the task. The difference in the apparent underlying sources of the beta envelope modulation (Figure 4.3) seen between task periods (MRBD, PMBR and baseline) and between contraction durations during the PMBR period suggests the different driving mechanisms generate the different types of modulation. It is plausible that the modulation in bursting activity between task periods is due to a difference in the number of neurons (i.e. size of the network) recruited during these different periods driving different amplitude beta bursts. This would agree with the idea that the MRBD and PMBR are generated through different beta networks, as discussed in the previous chapter.

The HMM used here was not optimised for detecting bursts, however recent work has explored the relationship between beta bursts and connectivity in more detail, by

employing the HMM as a burst detection method (Quinn et al., 2019; Seedat et al., 2020). Seedat et al. applies the time-delay embedded HMM (Vidaurre et al., 2018b) in this way to a right handed finger abduction task. Despite the differences in HMM used, the results agree with the findings presented here (Figure 5.9D); the study finds that the PMBR shows an increase in frequency of bursts in the left sensorimotor cortex, and the bursts last longer during the PMBR. However, Seedat et al. shows no change in the amplitude of the bursts across time windows, unlike the results shown in Figure 5.9Dv. This could be due to the relatively passive nature of the task in the work by Seedat et al., compared with an active task with visual feedback used here. Quinn et al. (Quinn et al., 2019) also uses a HMM to detect bursts. Again this study confirms the results here - that the beta rebound is due to increased occurrences of state events, and increased state lifetime. It also shows the drop in occupancy of the rebound state during the movement which is what was found here (Figure 5.9C). These results highlight the bursting nature of electrophysiological signals. Whether this will help understand the underlying neurophysiology of the PMBR remains to be seen, but bursts have been shown to provide extra information than the averaged beta envelope which has functional relevance (Little et al., 2018; Shin et al., 2017). Future work could look at using the burst detecting HMM on this data to further understand the PMBR.

Limitations and future work

The work in this chapter was based on amplitude coupling of signals. Measured amplitude coupling has been shown to be due to a combination of real amplitude coupling, and spurious amplitude coupling caused by phase coupling (Palva et al., 2018). Recent work showed that phase and amplitude coupling are similar but not identical (Siems & Siegel, 2020) which the authors claim, in part, is due to different neural mechanisms. If this is the case, it would be worthwhile to use phase coupling as well to study the PMBR, for example with phase difference derivative (Breakspear et al., 2004).

The AEC work is also limited as correlations were only explored within one frequency band. In reality, the frequency bands do not exist separately and it was shown in the previous Chapter that this task produces responses in the alpha and gamma bands. (Chapter 4). Therefore it would be interesting to explore connections between frequency bands, with a multilayer network to investigate any effects of cross-

frequency coupling (Boccaletti et al., 2014; Brookes et al., 2016; Kivelä et al., 2014; Tewarie et al., 2016b).

Although the HMM analysis offers greater time resolution over AEC, the HMM is still limited in that the number of states need to be chosen. However, this was accounted for by running multiple HMMs with different numbers of states (Figure 5.8), to find the best number of states to match the data. Another issue is that HMMs assume that the brain is in a state at all times, and that it can only be in one state at a time, which may not be true of brain activity. Further work using HMMs will be useful to gain greater insight into electrophysiological signals and also understand the limitations of these models.

5.7 Conclusion

Results from AEC and HMM analysis show that the PMBR is likely driven by underlying network dynamics, with a unified sensorimotor network demonstrating increased temporal stability (AEC analyses) and increased probability of occurrence (HMM analyses) during the rebound period. Furthermore, the results of this chapter suggest that the modulation of the PMBR by task duration may occur through a different process to the gross modulation of beta signals during different task stages. If proven, in future work this would suggest evidence for multiple beta rhythm generating mechanisms and suggesting both the classic oscillatory theory and the new bursting theory may both contribute to beta rhythm generation.

5.8 References

- Baker, A. P., Brookes, M. J., Rezek, I. A., Smith, S. M., Behrens, T., Smith, P. J. P., & Woolrich, M. (2014). Fast transient networks in spontaneous human brain activity. *Elife*, 3.
- Bastos, A. M., & Schoffelen, J.-M. (2016). A Tutorial Review of Functional Connectivity Analysis Methods and Their Interpretational Pitfalls. *Frontiers in Systems Neuroscience*, 9.
- Biswal, B., Zerrin Yetkin, F., Haughton, V. M., & Hyde, J. S. (1995). Functional connectivity in the motor cortex of resting human brain using echo-planar mri. *Magnetic Resonance in Medicine*, 34(4), 537-541.
- Boccaletti, S., Bianconi, G., Criado, R., Del Genio, C. I., Gómez-Gardenes, J., Romance, M., Sendina-Nadal, I., Wang, Z., & Zanin, M. (2014). The structure and dynamics of multilayer networks. *Physics Reports*, 544(1), 1-122.
- Breakspear, M., Williams, L. M., & Stam, C. J. (2004). A novel method for the topographic analysis of neural activity reveals formation and dissolution of 'dynamic cell assemblies'. *Journal of computational neuroscience*, 16(1), 49-68.
- Brookes, M. J., Hale, J. R., Zumer, J. M., Stevenson, C. M., Francis, S. T., Barnes, G. R., Owen, J. P., Morris, P. G., & Nagarajan, S. S. (2011a). Measuring functional connectivity using MEG: Methodology and comparison with fcMRI. *Neuroimage*, 56(3), 1082-1104.
- Brookes, M. J., Tewarie, P. K., Hunt, B. A. E., Robson, S. E., Gascoyne, L. E., Liddle, E. B., Liddle, P. F., & Morris, P. G. (2016). A multi-layer network approach to MEG connectivity analysis. *Neuroimage*, 132, 425-438.
- Brookes, M. J., Woolrich, M., Luckhoo, H., Price, D., Hale, J. R., Stephenson, M. C., Barnes, G. R., Smith, S. M., & Morris, P. G. (2011b). Investigating the electrophysiological basis of resting state networks using magnetoencephalography. *Proceedings of the National Academy of Sciences*, 108(40), 16783.
- Brookes, M. J., Woolrich, M. W., & Barnes, G. R. (2012). Measuring functional connectivity in MEG: A multivariate approach insensitive to linear source leakage. *Neuroimage*, 63(2), 910-920.
- Brovelli, A., Badier, J.-M., Bonini, F., Bartolomei, F., Coulon, O., & Auzias, G. (2017). Dynamic Reconfiguration of Visuomotor-Related Functional Connectivity Networks. *The Journal of Neuroscience*, 37(4), 839.
- Chang, C., & Glover, G. H. (2010). Time-frequency dynamics of resting-state brain connectivity measured with fMRI. *Neuroimage*, 50(1), 81-98.
- Colclough, G. L., Brookes, M. J., Smith, S. M., & Woolrich, M. W. (2015). A symmetric multivariate leakage correction for MEG connectomes. *Neuroimage*, 117, 439-448.
- Colclough, G. L., Woolrich, M. W., Tewarie, P. K., Brookes, M. J., Quinn, A. J., & Smith, S. M. (2016). How reliable are MEG resting-state connectivity metrics? *Neuroimage*, 138, 284-293.
- de Pasquale, F., Della Penna, S., Snyder, A. Z., Lewis, C., Mantini, D., Marzetti, L., Belardinelli, P., Ciancetta, L., Pizzella, V., Romani, G. L., & Corbetta, M. (2010). Temporal dynamics of spontaneous MEG activity in brain networks. *Proceedings of the National Academy of Sciences*, 107(13), 6040.

- de Pasquale, F., Della Penna, S., Sporns, O., Romani, G. L., & Corbetta, M. (2016). A Dynamic Core Network and Global Efficiency in the Resting Human Brain. *Cerebral Cortex*, *26*(10), 4015-4033.
- Florin, E., & Baillet, S. (2015). The brain's resting-state activity is shaped by synchronized cross-frequency coupling of neural oscillations. *Neuroimage*, *111*, 26-35.
- Fries, P. (2005). A mechanism for cognitive dynamics: neuronal communication through neuronal coherence. *Trends in Cognitive Sciences*, *9*(10), 474-480.
- Hillebrand, A., Barnes, G. R., Bosboom, J. L., Berendse, H. W., & Stam, C. J. (2012). Frequency-dependent functional connectivity within resting-state networks: An atlas-based MEG beamformer solution. *Neuroimage*, *59*(4), 3909-3921.
- Hipp, J. F., Hawellek, D. J., Corbetta, M., Siegel, M., & Engel, A. K. (2012). Large-scale cortical correlation structure of spontaneous oscillatory activity. *Nature Neuroscience*, *15*, 884.
- Hipp, Joerg F., & Siegel, M. (2015). BOLD fMRI Correlation Reflects Frequency-Specific Neuronal Correlation. *Current Biology*, *25*(10), 1368-1374.
- Huang, M., Mosher, J. C., & Leahy, R. (1999). A sensor-weighted overlapping-sphere head model and exhaustive head model comparison for MEG. *Physics in Medicine & Biology*, *44*(2), 423.
- Jenkinson, M., Beckmann, C. F., Behrens, T. E. J., Woolrich, M. W., & Smith, S. M. (2012). FSL. *Neuroimage*, *62*(2), 782-790.
- Jones, S. R. (2016). When brain rhythms aren't 'rhythmic': implication for their mechanisms and meaning. *Current Opinion in Neurobiology*, *40*, 72-80.
- Kivelä, M., Arenas, A., Barthelemy, M., Gleeson, J. P., Moreno, Y., & Porter, M. A. (2014). Multilayer networks. *Journal of complex networks*, *2*(3), 203-271.
- Lachaux, J. P., Rodriguez, E., Martinerie, J., & Varela, F. J. (1999). Measuring phase synchrony in brain signals. *Human Brain Mapping*, *8*(4), 194-208.
- Little, S., Bonaiuto, J., Barnes, G., & Bestmann, S. (2018). Motor cortical beta transients delay movement initiation and track errors. *bioRxiv*, 384370.
- Liu, Z., Fukunaga, M., de Zwart, J. A., & Duyn, J. H. (2010). Large-scale spontaneous fluctuations and correlations in brain electrical activity observed with magnetoencephalography. *Neuroimage*, *51*(1), 102-111.
- Mullinger, K. J., Cherukara, M. T., Buxton, R. B., Francis, S. T., & Mayhew, S. D. (2017). Post-stimulus fMRI and EEG responses: Evidence for a neuronal origin hypothesised to be inhibitory. *Neuroimage*, *157*, 388-399.
- Mullinger, K. J., Mayhew, S. D., Bagshaw, A. P., Bowtell, R., & Francis, S. T. (2013a). Poststimulus undershoots in cerebral blood flow and BOLD fMRI responses are modulated by poststimulus neuronal activity. *Proceedings of the National Academy of Sciences*, *110*(33), 13636-13641.
- Mullinger, K. J., Mayhew, S. D., Bagshaw, A. P., Bowtell, R., & Francis, S. T. (2013b). Poststimulus undershoots in cerebral blood flow and BOLD fMRI responses are modulated by poststimulus neuronal activity. *Proceedings of the National Academy of Sciences*, *110*(30), 13636-13641.
- Nolte, G., Bai, O., Wheaton, L., Mari, Z., Vorbach, S., & Hallett, M. (2004). Identifying true brain interaction from EEG data using the imaginary part of coherency. *Clinical Neurophysiology*, *115*(10), 2292-2307.
- Nunez, P. L., Srinivasan, R., Westdorp, A. F., Wijesinghe, R. S., Tucker, D. M., Silberstein, R. B., & Cadusch, P. J. (1997). EEG coherency: I: statistics, reference electrode, volume conduction, Laplacians, cortical imaging, and

- interpretation at multiple scales. *Electroencephalography and Clinical Neurophysiology*, *103*(5), 499-515.
- O'Neill, G. C., Barratt, E. L., Hunt, B. A. E., Tewarie, P. K., & Brookes, M. J. (2015). Measuring electrophysiological connectivity by power envelope correlation: a technical review on MEG methods. *Physics in Medicine and Biology*, *60*, R271 - R295.
- O'Neill, G. C., Tewarie, P., Vidaurre, D., Liuzzi, L., Woolrich, M. W., & Brookes, M. J. (2018). Dynamics of large-scale electrophysiological networks: A technical review. *Neuroimage*, *180*, 559-576.
- O'Neill, G. C., Barratt, E. L., Hunt, B. A. E., Tewarie, P. K., & Brookes, M. J. (2015). Measuring electrophysiological connectivity by power envelope correlation: a technical review on MEG methods. *Physics in Medicine and Biology*, *60*(21), R271-R295.
- O'Neill, G. C., Tewarie, P. K., Colclough, G. L., Gascoyne, L. E., Hunt, B. A. E., Morris, P. G., Woolrich, M. W., & Brookes, M. J. (2017). Measurement of dynamic task related functional networks using MEG. *Neuroimage*, *146*, 667-678.
- Palva, J. M., Palva, S., & Kaila, K. (2005). Phase Synchrony among Neuronal Oscillations in the Human Cortex. *The Journal of Neuroscience*, *25*(15), 3962.
- Palva, J. M., Wang, S. H., Palva, S., Zhigalov, A., Monto, S., Brookes, M. J., Schoffelen, J.-M., & Jerbi, K. (2018). Ghost interactions in MEG/EEG source space: A note of caution on inter-areal coupling measures. *Neuroimage*, *173*, 632-643.
- Preti, M. G., Bolton, T. A. W., & Van De Ville, D. (2017). The dynamic functional connectome: State-of-the-art and perspectives. *Neuroimage*, *160*, 41-54.
- Quinn, A. J., van Ede, F., Brookes, M. J., Heideman, S. G., Nowak, M., Seedat, Z. A., Vidaurre, D., Zich, C., Nobre, A. C., & Woolrich, M. W. (2019). Unpacking Transient Event Dynamics in Electrophysiological Power Spectra. *Brain Topography*, *32*(6), 1020-1034.
- Quinn, A. J., Vidaurre, D., Abeysuriya, R., Becker, R., Nobre, A. C., & Woolrich, M. W. (2018). Task-Evoked Dynamic Network Analysis Through Hidden Markov Modeling. *Frontiers in Neuroscience*, *12*(603).
- Rabiner, L. R. (1989). A tutorial on hidden Markov models and selected applications in speech recognition. *Proceedings of the IEEE*, *77*(2), 257-286.
- Rezek, I., & Roberts, S. (2005). Ensemble hidden markov models with extended observation densities for biosignal analysis. In D. R. Husmeier D, Roberts S (Ed.), *Probabilistic Modeling in Bioinformatics and Medical Informatics*. (pp. 419-450): London: Springer London.
- Robinson, S. E., & Vrba, J. (1998). Functional neuroimaging by synthetic aperture magnetometry. *Recent Advances in Biomagnetism*, 302-305.
- Sakoğlu, Ü., Pearlson, G. D., Kiehl, K. A., Wang, Y. M., Michael, A. M., & Calhoun, V. D. (2010). A method for evaluating dynamic functional network connectivity and task-modulation: application to schizophrenia. *Magnetic Resonance Materials in Physics, Biology and Medicine*, *23*(5-6), 351-366.
- Sarvas, J. (1987). Basic mathematical and electromagnetic concepts of the biomagnetic inverse problem. *Physics in Medicine & Biology*, *32*(1), 11.
- Seedat, Z. A., Quinn, A. J., Vidaurre, D., Liuzzi, L., Gascoyne, L. E., Hunt, B. A. E., O'Neill, G. C., Pakenham, D. O., Mullinger, K. J., Morris, P. G., Woolrich, M. W., & Brookes, M. J. (2020). The role of transient spectral 'bursts' in

- functional connectivity: A magnetoencephalography study. *Neuroimage*, 209, 116537.
- Shenoy, K. V., Sahani, M., & Churchland, M. M. (2013). Cortical Control of Arm Movements: A Dynamical Systems Perspective. *Annual Review of Neuroscience*, 36(1), 337-359.
- Sherman, M. A., Lee, S., Law, R., Haegens, S., Thorn, C. A., Hämäläinen, M. S., Moore, C. I., & Jones, S. R. (2016). Neural mechanisms of transient neocortical beta rhythms: Converging evidence from humans, computational modeling, monkeys, and mice. *Proceedings of the National Academy of Sciences*, 113(33), E4885.
- Shin, H., Law, R., Tsutsui, S., Moore, C. I., & Jones, S. R. (2017). The rate of transient beta frequency events predicts behavior across tasks and species. *Elife*, 6, e29086.
- Siems, M., & Siegel, M. (2020). Dissociated neuronal phase- and amplitude-coupling patterns in the human brain. *Neuroimage*, 209, 116538.
- Sokoliuk, R., Mayhew, S. D., Aquino, K. M., Wilson, R., Brookes, M. J., Francis, S. T., Hanslmayr, S., & Mullinger, K. J. (2019). Two Spatially Distinct Posterior Alpha Sources Fulfill Different Functional Roles in Attention. *The Journal of Neuroscience*, 39(36), 7183.
- Stam, C. J., de Haan, W., Daffertshofer, A., Jones, B. F., Manshanden, I., van Cappellen van Walsum, A. M., Montez, T., Verbunt, J. P. A., de Munck, J. C., van Dijk, B. W., Berendse, H. W., & Scheltens, P. (2008). Graph theoretical analysis of magnetoencephalographic functional connectivity in Alzheimer's disease. *Brain*, 132(1), 213-224.
- Stam, C. J., Nolte, G., & Daffertshofer, A. (2007). Phase lag index: assessment of functional connectivity from multi channel EEG and MEG with diminished bias from common sources. *Human Brain Mapping*, 28(11), 1178-1193.
- Stamp, M. (2015). A Revealing Introduction to Hidden Markov Models. *Topics in Machine Learning, Department of Computer Science, San Jose State University*.
- Tewarie, P., Bright, M. G., Hillebrand, A., Robson, S. E., Gascoyne, L. E., Morris, P. G., Meier, J., Van Mieghem, P., & Brookes, M. J. (2016a). Predicting haemodynamic networks using electrophysiology: The role of non-linear and cross-frequency interactions. *Neuroimage*, 130, 273-292.
- Tewarie, P., Hillebrand, A., van Dijk, B. W., Stam, C. J., O'Neill, G. C., Van Mieghem, P., Meier, J. M., Woolrich, M. W., Morris, P. G., & Brookes, M. J. (2016b). Integrating cross-frequency and within band functional networks in resting-state MEG: a multi-layer network approach. *Neuroimage*, 142, 324-336.
- Tewarie, P., Hunt, B. A. E., O'Neill, G. C., Byrne, A., Aquino, K., Bauer, M., Mullinger, K. J., Coombes, S., & Brookes, M. J. (2018). Relationships Between Neuronal Oscillatory Amplitude and Dynamic Functional Connectivity. *Cerebral Cortex*, bhy136-bhy136.
- Tewarie, P., Liuzzi, L., O'Neill, G. C., Quinn, A. J., Griffa, A., Woolrich, M. W., Stam, C. J., Hillebrand, A., & Brookes, M. J. (2019). Tracking dynamic brain networks using high temporal resolution MEG measures of functional connectivity. *Neuroimage*, 200, 38-50.
- Tzourio-Mazoyer, N., Landeau, B., Papathanassiou, D., Crivello, F., Etard, O., Delcroix, N., Mazoyer, B., & Joliot, M. (2002). Automated Anatomical

- Labeling of Activations in SPM Using a Macroscopic Anatomical Parcellation of the MNI MRI Single-Subject Brain. *Neuroimage*, 15(1), 273-289.
- van Ede, F., Quinn, A. J., Woolrich, M. W., & Nobre, A. C. (2018). Neural Oscillations: Sustained Rhythms or Transient Burst-Events? *Trends in Neurosciences*, 41(7), 415-417.
- Van Schependom, J., Vidaurre, D., Costers, L., Sjøgård, M., D'Hooghe, M. B., D'Haeseleer, M., Wens, V., De Tiège, X., Goldman, S., Woolrich, M., & Nagels, G. (2019). Altered transient brain dynamics in multiple sclerosis: Treatment or pathology? *Human Brain Mapping*, 40(16), 4789-4800.
- Van Veen, B. D., Van Drongelen, W., Yuchtman, M., & Suzuki, A. (1997). Localization of Brain Electrical Activity via Linearly Constrained Minimum Variance Spatial Filtering. *IEEE TRANSACTIONS ON BIOMEDICAL ENGINEERING*, 44(9), 867-880.
- Vidaurre, D., Abey Suriya, R., Becker, R., Quinn, A. J., Alfaro-Almagro, F., Smith, S. M., & Woolrich, M. W. (2018a). Discovering dynamic brain networks from big data in rest and task. *Neuroimage*, 180, 646-656.
- Vidaurre, D., Hunt, L. T., Quinn, A. J., Hunt, B. A. E., Brookes, M. J., Nobre, A. C., & Woolrich, M. W. (2018b). Spontaneous cortical activity transiently organises into frequency specific phase-coupling networks. *Nature Communications*, 9(1), 2987.
- Vidaurre, D., Quinn, A. J., Baker, A. P., Dupret, D., Tejero-Cantero, A., & Woolrich, M. W. (2016). Spectrally resolved fast transient brain states in electrophysiological data. *Neuroimage*, 126, 81-95.
- Woolrich, M. W., Baker, A., Luckhoo, H., Mohseni, H., Barnes, G., Brookes, M. J., & Rezek, L. (2013). Dynamic state allocation for MEG source reconstruction. *NeuroImage*, 77, 77-92.

CHAPTER 6

6 Investigating fMRI Post-stimulus Responses

6.1 Abstract

The neuronal origins of post-stimulus fMRI BOLD responses remain to be studied in detail, as their origin was thought to be vascular rather than linked to brain function. Yet, recent evidence suggests that the post-stimulus response provides additional neuronal information distinct to that occurring during stimulation, highlighting the importance of characterising the vascular and neuronal components of post-stimulus BOLD responses. In this chapter, a sequence was developed to provide combined Vascular Space Occupancy (VASO), Arterial Spin Labelling (ASL) and Blood Oxygenation Level Dependent (BOLD) contrasts to measure blood volume, blood flow, and oxygenation changes to a grip-force paradigm at 7 T. The grip-force paradigm, used previously with MEG recordings (Chapters 4 & 5), was performed in 10 healthy volunteers to measure motor cortex responses to 2 and 10 s duration grip contractions. Results showed no significant difference between the amplitude of the BOLD primary response for the 2 and 10 s grip contractions. The BOLD post-stimulus undershoot had a smaller amplitude for the 2 s than 10 s duration. VASO and arterial cerebral blood volume (aCBV) primary responses showed a modulation between the 2 and 10 s stimulus for the primary response, due to an artefact of the analysis pipeline and low temporal resolution. The VASO response showed a significant decrease in total CBV in the post-stimulus period, but no significant difference was found between contraction durations. The aCBV signal had no significant post-stimulus response. The decrease in total CBV, but not aCBV, suggests a reduction in venous CBV (vCBV) drives the VASO undershoot, the opposite of the balloon model. A decrease in vCBV would require an increase in $CMRO_2$ or reduction in CBF post-stimulus to produce a post-stimulus undershoot, neither of which were observed, suggesting further testing is needed to reveal the origins of the post-stimulus undershoot. Comparison to MEG responses showed a disparity between modulation of post-stimulus responses with stimulus duration, which may imply the post-stimulus response is a combination of competing vascular and neuronal effects.

6.2 Introduction

Over 25 years since fMRI was first introduced (Bandettini et al., 1992; Kwong et al., 1992; Ogawa et al., 1992), there is still no consensus on the origins of the BOLD post-stimulus undershoot (PSU). The BOLD response (outlined in Chapter 3) arises due to the combined change in cerebral blood flow (CBF), cerebral blood volume (CBV) and cerebral metabolic rate of oxygen consumption (CMRO₂), and the BOLD PSU was originally thought of as a purely vascular effect (Buxton et al., 1998). In recent years, it has been postulated that the BOLD PSU also relates to neuronal activity (Uludağ et al., 2004), yet to date it remains unclear whether the BOLD PSU is a neuronal, vascular or metabolic phenomenon, or a combination of these effects. If the post-stimulus BOLD response does reflect neuronal activity, it may provide additional information to the primary BOLD response and could provide a metric of brain function in health and disease. This highlights the importance of characterising PSU responses to further understand their origin.

It is widely recognised that electrophysiology recordings exhibit post-stimulus responses, such as the event related synchronization (ERS) of oscillatory activity upon stimulus cessation - in particular the post-movement beta rebound (PMBR). In Chapters 4 and 5 it was shown that stimulus duration modulates the amplitude of the magnetoencephalography (MEG) post-stimulus response but not the primary response - revealing distinct functional information to that of the primary response. fMRI is the most widely used methodology to study neuronal activity, but taking a multimodal approach will help to advance understanding of the signals measured. Using both MEG and fMRI findings to investigate post-stimulus responses will potentially provide a better understanding of the driving mechanisms behind all post-stimulus responses, enabling the electrophysiological ERS to be related to the BOLD PSU. In addition to providing haemodynamic information, fMRI also benefits from increased spatial resolution and access to imaging of deep brain structures which cannot be resolved with MEG and could be crucial in understanding the functional role of post-stimulus responses.

6.2.1 Mechanisms of the BOLD PSU

Three main mechanisms have been proposed to explain the origin of the BOLD PSU. The first describes the PSU as a vascular effect, with the balloon model (Buxton et al.,

1998) and Windkessel model (Mandeville et al., 1999) originating from biomechanical properties of veins, where the PSU is a result of elevated CBV after the end of the stimulus, while CBF and CMRO₂ return to baseline. The second states the PSU is a metabolic effect, due to elevated CMRO₂ caused by restoration of ionic gradients (Lu et al., 2004b). The third assumes the PSU is a neuronal effect, caused by a decrease in CBF below baseline (and reduction in CMRO₂) due to a decrease in neuronal activity (Uludağ et al., 2004). More recently, studies have suggested the PSU is a combination of these effects (Hua et al., 2011; van Zijl et al., 2012; Yacoub et al., 2005).

The first of these theories, the balloon model (Buxton et al., 1998), was one of the earliest models to explain the haemodynamic response function. It models the vascular bed as a balloon. Flow into the balloon increases, increasing the pressure in the balloon, until flow into the balloon matches the flow out and a steady state is reached. The balloon model is based on several assumptions: no capillary recruitment, all blood volume changes occur in veins and that the flow increase due to dilation of arterioles is negligible. The flow out of the balloon is assumed to be a function of its volume. The rate of change of volume (V) is therefore simply given by flow in (F_{in}) minus flow out (F_{out}):

$$\frac{dV}{dt} = F_{in}(t) - F_{out}(t) \quad (1)$$

Considering the concentration of deoxyhaemoglobin (Q), assuming all deoxyhaemoglobin is in the venous compartment, the concentration of deoxyhaemoglobin into the balloon will be the product of flow in, oxygen extraction (E) and arterial oxygen concentration (C_a). The concentration of deoxyhaemoglobin out of the balloon will be a function of flow out, concentration of deoxyhaemoglobin in the venous compartment, which will be the total deoxyhaemoglobin divided by the volume of the compartment. Therefore,

$$\frac{dQ}{dt} = F_{in}(t)EC_a - F_{out}(V)\frac{Q(t)}{V(t)}. \quad (2)$$

This equation can be normalised to describe values relative to their baseline level, by dividing by the variable at rest (subscript 0), e.g. $q(t) = Q(t)/Q_0$ where $\tau_0 = V_0/F_0$ is the mean transit time through venous compartment at rest.

$$\frac{dq}{dt} = \frac{1}{\tau_0} \left[f_{in}(t) \frac{E(t)}{E_0} - f_{out}(v) \frac{q(t)}{v(t)} \right] \quad (3)$$

Assuming oxygen delivery is limited, CMRO₂ increases as much as possible within the constraints of limited oxygen delivery. This is the oxygen limitation model which states that the large flow increase is due to the tight coupling of flow and oxygen metabolism, in the presence of limited oxygen. Net oxygen extraction is given by a nonlinear expression (Buxton & Frank, 1997) which is a function of flow in (f),

$$E(f_{in}) = 1 - (1 - E_0)^{1/f} \quad (4)$$

where E_0 is the resting net extraction of oxygen, which can be inserted in equation for rate of change of deoxyhaemoglobin (Equation 2). Different forms of flow out can then be modelled, representing different pressure/volume curves of the balloon. Grubb et al. (Grubb et al., 1974) found the steady state blood volume could be described as a power law relationship,

$$v = f^\alpha \quad (5)$$

where α is the Grubb constant, which was found to be 0.38.

In the balloon model, the BOLD primary response reflects increases in cerebral blood flow (CBF), blood volume (CBV) and metabolic rate of oxygen consumption (CMRO₂), while the post-stimulus undershoot is due to the slow recovery of CBV which remains elevated after CMRO₂ and CBF have returned to baseline. This is because the vessels rapidly dilate during activation to account for increased flow, but the vessels cannot constrict as quickly as the flow returns to baseline and therefore volume and flow become uncoupled. As a result, during the post-stimulus response it is possible Equation 5 does not hold.

One study supporting the balloon model is Feng et al. (Feng et al., 2001) which showed excellent correlation between the experimental BOLD time course and predicted time course from the balloon model. However, there was no post-stimulus undershoot observed. Many other studies all show experimental evidence for the balloon model (Friston et al., 2000; Mildner et al., 2001; Obata et al., 2004; Toronov et al., 2003).

Following this, studies went on to show that a slow recovery of CBV was not the whole explanation for the PSU. In 2004, Lu et al. (Lu et al., 2004b) collected three consecutive measures of VASO, BOLD and ASL at 1.5 T in response to a flashing checkerboard. The results showed that the BOLD PSU lasted much longer than CBV took to return to

baseline, suggesting elevated CBV could not be the sole explanation for the BOLD PSU. From these data the authors estimated that $CMRO_2$ remained elevated after the stimulus while CBF and CBV returned to baseline, and therefore postulated that the PSU is caused, in part, by increased oxygen metabolism. They attributed this to restoration of ionic gradients and speculated that flow and metabolism are not necessarily directly linked; instead CBF is controlled by neurotransmitter signalling rather than oxygen metabolism (Attwell & Iadecola, 2002). Many other studies (Dechent et al., 2010; Donahue et al., 2009; Frahm et al., 2008; Hua et al., 2011; Poser et al., 2011; Schroeter et al., 2006) have since also found evidence for CBV and CBF returning to baseline before the BOLD PSU, supporting the hypothesis of prolonged oxygen consumption.

Thirdly, other studies have found evidence for a decrease in CBF with a decrease in $CMRO_2$, suggesting that the BOLD PSU is caused by a decrease in neuronal activity (Uludağ et al., 2004). Early work supporting this was presented by Hoge et al. (Hoge et al., 1999) who showed that a radial checkerboard stimulus produced a reduction in post-stimulus CBF in visual cortex. They also showed that the PSU depended on the type of visual pattern presented, suggesting the PSU depends on neuronal activity. They suggested the reason this had not been observed previously was due to low SNR of CBF data in earlier studies, but also hypothesised that the reduced CBF was amplified by the slowly returning CBV. This was taken further by Sadaghiani and colleagues (Sadaghiani et al., 2009) who measured CBF during a static and flashing checkerboard. The authors found no difference in the primary BOLD response for the two types of stimulation, but found differences in the BOLD PSU, independent of luminance contrast of the stimuli, implying a neuronal activation or deactivation to modulate the BOLD PSU.

A different approach was taken by Logothetis (Logothetis et al., 2001) using local field potentials (LFPs) to compare with BOLD signal in primates. This study suggested that the primary BOLD response directly correlates to an increase in neural activity, and the BOLD PSU is due to inhibition of neuronal activity after stimulation, reflected by a decrease in LFPs relative to baseline. In a study using EEG-fMRI, Mullinger et al. (Mullinger et al., 2013b) found the amplitude and sign of the BOLD PSU correlates with EEG mu power resulting from median nerve stimulation, providing evidence for an association between the BOLD PSU and the electrophysiological PSU in humans.

Further work by Mullinger (Mullinger et al., 2017) showed that the amplitude of BOLD and CBF post-stimulus responses depended on the post-stimulus EEG visual alpha power, which could not have been predicted from the primary response. They also estimated CMRO₂ changes and found an altered coupling of CMRO₂ to CBF during the PSU. Taken together, this implied that the primary and post-stimulus responses are distinct and should be modelled separately. However, to my knowledge, the work supporting a reduction in CBF and CMRO₂ has not measured CBV and therefore the CBV post-stimulus response in these more recent studies is unknown.

There is still much controversy surrounding the origin of the post-stimulus undershoot (van Zijl et al., 2012), but it is clear the original balloon model should be further modified (Buxton, 2012) and perhaps the PSU is a combination of neuronal, metabolic and vascular factors. Chen and Pike (Chen & Pike, 2009b) found evidence for the slow return to baseline of CBV as described by the balloon model, but also found evidence of a CBF undershoot, and argue that the combination of these two factors accounts for the BOLD PSU. It is possible that some of this controversy is driven by low SNR of CBF and CBV measures collected in past studies at low field strengths (generally 1.5 T and 3 T).

In order to better understand the origins of the BOLD PSU, it is necessary to determine the changes in CBF, CBV and CMRO₂ on which the BOLD signal depends. Total CBV can be measured using vascular space occupancy (VASO), while arterial spin labelling (ASL) can be used to measure CBF and arterial CBV (aCBV), and calibrated fMRI can be used to estimate CMRO₂. By moving to higher field strength such as 7 T, SNR will be increased, improving the data sensitivity as described in Section 6.3.

6.2.2 Stimulus Duration in fMRI

If the primary response drives the post-stimulus BOLD response, as predicted by the balloon model or a metabolism response due to a rebalancing of ionic gradients, then a larger primary response would be expected to result in a larger post-stimulus response. One simple way to interrogate this relationship between the primary and post-stimulus response is to investigate the effects of stimulus duration. Stimulus duration has been found to modulate the primary response in a number of studies as outlined below.

Early work investigating the effect of task duration used finger tapping of different durations in fMRI studies at 1.5 T (Glover, 1999; Miller et al., 2001). These studies

found a non-linear relationship between stimulus duration and the primary BOLD response, with short duration stimuli producing lower amplitude responses, and the amplitude plateauing for stimulus durations around 6 to 8 s. The amplitude of responses to longer duration stimuli were not able to be predicted from the amplitude to shorter stimuli in a linear way. These findings were corroborated by Stevenson et al. in a study at 3 T who also showed that the primary BOLD did not increase linearly with finger tapping duration (Stevenson et al., 2011). However, these studies did not investigate the BOLD PSU and used quite short baseline periods for considering hemodynamics (19 s (Miller et al., 2001), 14 – 29 s (Glover, 1999), 24 – 29 s (Stevenson et al., 2011)). Further, these experiments used finger tapping which is hard to control for speed and movement. This is important as a higher force gives higher amplitude BOLD signal (Peck et al., 2001) and rate of movement also affects the amplitude of the BOLD response (Jäncke et al., 1998) which is hard to standardise for finger tapping.

Using 3 T MRI, Birn et al. (Birn et al., 2001) showed that the primary BOLD response to stimuli does not scale linearly with stimulus duration, and that shorter duration stimuli give a higher amplitude primary BOLD response than predicted by a linear model. The same effect has also been observed for different durations of epileptic activity (Bagshaw et al., 2005). Furthermore, Birn et al. (Birn et al., 2001) noted that using short inter-stimulus intervals (ISI) is a concern as there is a need to leave time for the BOLD PSU to recover, but they found results for a 16 s ISI and 30 s ISI were well correlated.

Few studies have investigated the effect on non-BOLD fMRI responses of modulated task duration. One study (Gu et al., 2005) used simultaneous VASO, ASL and BOLD to measure responses in visual cortex to different duration stimuli at 3 T, and found that increasing stimulus duration increased the amplitude and width of the response for VASO, ASL and BOLD. They did not, however, investigate the PSU. What is more, most VASO-fMRI studies use long task durations (~30 s) due to the low temporal resolution and SNR of the technique, where the effects of nonlinearity are not observed. For example, Beckett et al. (Beckett et al., 2019; Huber et al., 2018) used a 30 s tap and Lu and van Zijl (Lu & van Zijl, 2005) used 30 s visual stimulation. Therefore the interaction of CBV, CBF and CMRO₂ in generating the primary response to short stimuli is poorly documented.

Despite these studies investigating the effects of stimulus duration on the primary BOLD response, research into the effects on the PSU remains limited. The existing studies are largely unable to investigate the post-stimulus undershoot as most do not leave a sufficient inter-stimulus interval for the PSU to fully return to baseline. A critical question, therefore, is how task duration affects BOLD, CBV, aCBV and CBF during both the primary response and PSU. The balloon model would predict that if the stimulus duration is longer, and the primary response amplitude is larger and the post-stimulus undershoot would be larger.

6.2.3 Aim

A thorough approach to task design, controlling force, speed, and using long ISI, is required to investigate the PSU. Here, the task which was previously developed to modulate post-stimulus neuronal responses with MEG (Chapters 4 and 5) is adapted for fMRI. It was evident from MEG experiment that the largest differences in PSU were observed between the 2 s stimulus and 10 s stimulus, so these two grip durations were used. By using this task, investigation of the neuronal component of the measured fMRI responses is possible. Acquiring VASO and ASL concurrently with BOLD weighted images allows interrogation of the combination of total CBV, aCBV and CBF, and CMRO₂ which underlie the BOLD responses throughout the experimental paradigm. Using 7 T provides greater BOLD, total CBV and CBF/aCBV contrast to noise ratio (CNR), allowing higher spatial resolution than achieved in previous studies (Gu et al., 2005). First, a VASO-ASL sequence was implemented and optimised to measure VASO, aCBV, CBF and BOLD concurrently to allow assessment of the contribution of the vascular origin to the post-stimulus response.

6.3 Optimisation of the VASO-ASL-BOLD Sequence

BOLD fMRI is an indirect measure of neuronal activity and depends on a combination of CBF, CBV and $CMRO_2$. In order to better understand the origins of the PSU, it is necessary to separate the effects of CBF, CBV and $CMRO_2$ on the BOLD signal. Total CBV (the sum of arterial CBV (aCBV) and venous CBV (vCBV)) can be measured using VASO, CBF is measured using ASL and can also be used to estimate aCBV, while calibrated fMRI can be used to estimate $CMRO_2$.

6.3.1 Vascular Space Occupancy (VASO)

Vascular space occupancy (VASO) fMRI (Lu et al., 2003) is based on changes in total CBV. VASO works by nulling the signal from blood whilst retaining the signal from tissue using an inversion recovery pulse sequence. This sequence is dependent on the difference in T_1 between blood and tissue, with blood T_1 being longer than that of tissue (tissue T_1 is of the order of 1100 ms at 3 T and 1800 ms at 7 T (Huber et al., 2018; Wright et al., 2008), and T_1 of blood is 1624 ms at 3 T (Lu et al., 2004a) and 2100 ms at 7 T (Zhang et al., 2013)), and T_1 increasing at higher magnetic field strength (Hoogenraad et al., 2001). This difference in T_1 between blood and tissue causes the null point - the time at which the magnetizations cross zero following an inversion pulse - of blood and tissue to differ, as shown in Figure 6.1. VASO is proportional to $1 - CBV$ and is usually measured as a percentage signal change, so a decrease in VASO intensity corresponds to an increase in total CBV which is generally coupled to an increase in neuronal activation (Lu & van Zijl, 2012). The percentage signal changes of VASO are on the order of 1% at 7T.

There is only a short window in which to acquire images after the blood nulling in a VASO sequence as the sensitivity rapidly decreases with time (Fig. 6.1B), hence only a small number of slices can be acquired. Further, as magnitude data is collected, the slice acquisition should not cross the null point, but be collected after the null point, so that the sign of the signal intensity due to a blood volume change does not vary across slices. Simultaneous multi slice EPI (SMS-EPI) or multiband EPI (MB-EPI) can overcome issues with spatial coverage by exciting multiple slices at the same time (Huber et al., 2018) (see Chapter 3 Section 3.4.6).

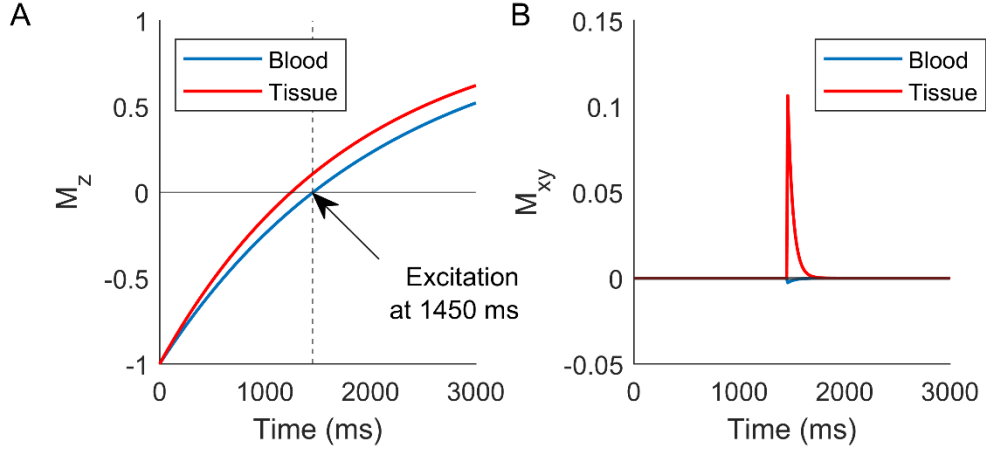


Figure 6.1. (A) Recovery of longitudinal magnetization of blood and tissue at 7 T after an inversion pulse. Data simulated assuming blood T_1 of 2100 ms (Zhang et al., 2013) and tissue T_1 of 1800 ms (Wright et al., 2008). (B) Measured transverse magnetisation for a 90° excitation pulse applied at a delay TI of 1450 ms. Note the blood signal is nulled but the tissue signal has crossed the null point.

To null the signal from blood, an inversion recovery sequence with inversion time (TI) at the blood null point is used, whilst retaining the tissue signal. Since blood in the voxel is continuously replaced, a non-slice-selective inversion pulse must be used. The relationship between TI and T_1 is

$$1 - 2e^{-\frac{TI}{T_1}} + e^{-\frac{TR}{T_1}} = 0. \quad (6)$$

For a long TR, this can be simplified to

$$TI = T_1 \ln(2). \quad (7)$$

Therefore, to calculate the required inversion time for a VASO scheme, it is required to accurately know the T_1 of blood. T_1 is dependent on temperature and field strength, with the T_1 of blood at 7 T of approximately 2100 ms (Zhang et al., 2013) resulting in a required inversion time to null the blood signal TI of 1450 ms (Equation 7). For blood nulling to be effective to estimate the total blood volume, both arterial and venous blood need to be nulled, which is possible as arterial and venous blood have similar T_1 values (Lu et al., 2003).

6.3.2 Arterial Spin Labelling (ASL)

While VASO measures total CBV, ASL is a technique primarily used for imaging CBF (Detre et al., 1992) and can also be used to measure aCBV. ASL is a non-invasive imaging technique to measure tissue perfusion by labelling the arterial blood delivered to the tissue. This results in a response which is better localised to capillary beds than

BOLD, as BOLD reflects venous outflow (Buxton, 2009). However, the SNR and temporal resolution of ASL are much poorer than that of BOLD (Liu & Brown, 2007). ASL and BOLD techniques can be used together to measure BOLD signal and CBF simultaneously (Wong et al., 1997) which can be helpful for understanding the origins of the BOLD signal (Mullinger et al., 2017; Mullinger et al., 2013b).

To collect an ASL image, magnetization of water in arterial blood is first inverted with a 180° adiabatic RF pulse outside the region being imaged. This labelled blood then flows into tissue and is imaged after a time, the inversion time TI, when the labelled blood has flowed into the image plane and exchanged with the tissue (label image). A control image with no labelling of arterial blood, where the inflowing spins are fully relaxed is then collected, which is subtracted from the label image. This results in a perfusion-weighted image proportional to the amount of arterial blood delivered in the time TI (Buxton, 2009).

ASL experiments are generally conducted using pulsed ASL (PASL) or pseudo-continuous ASL (PCASL). FAIR (flow-sensitive alternating inversion recovery) (Kim, 1995) is a type of PASL, in which the label image is acquired with a non-selective inversion pulse, and the control image is acquired with a slice-selective pulse. The concept is that the inflowing arterial blood is inverted with the non-selective pulse, whilst inflowing blood is fully relaxed following the slice-selective pulse. Inflowing blood will then perfuse into the tissue and exchange. An example of this is shown in Figure 6.2. Traditionally, ASL is used to measure CBF, but at short inversion times ASL is sensitive to the arterial cerebral blood volume (aCBV) as the blood flows through the arterioles (Brookes et al., 2007; Francis et al., 2008).

6.3.3 Combining BOLD, VASO and ASL

The simultaneous acquisition of VASO, ASL and BOLD to measure total CBV, CBF and blood oxygenation in the same sequence has many benefits. It allows the collection of data to the exact same stimulus, removing habituation and learning effects if the same experiment is repeated multiple times, and removes motion differences between separately acquired scans. Combining parameters provides complementary information to better understand the relationship between neuronal activity, haemodynamic and the MR signal, and is highly desirable for understanding post-stimulus responses. Both VASO and the FAIR ASL protocol are based on an inversion recovery scheme. For

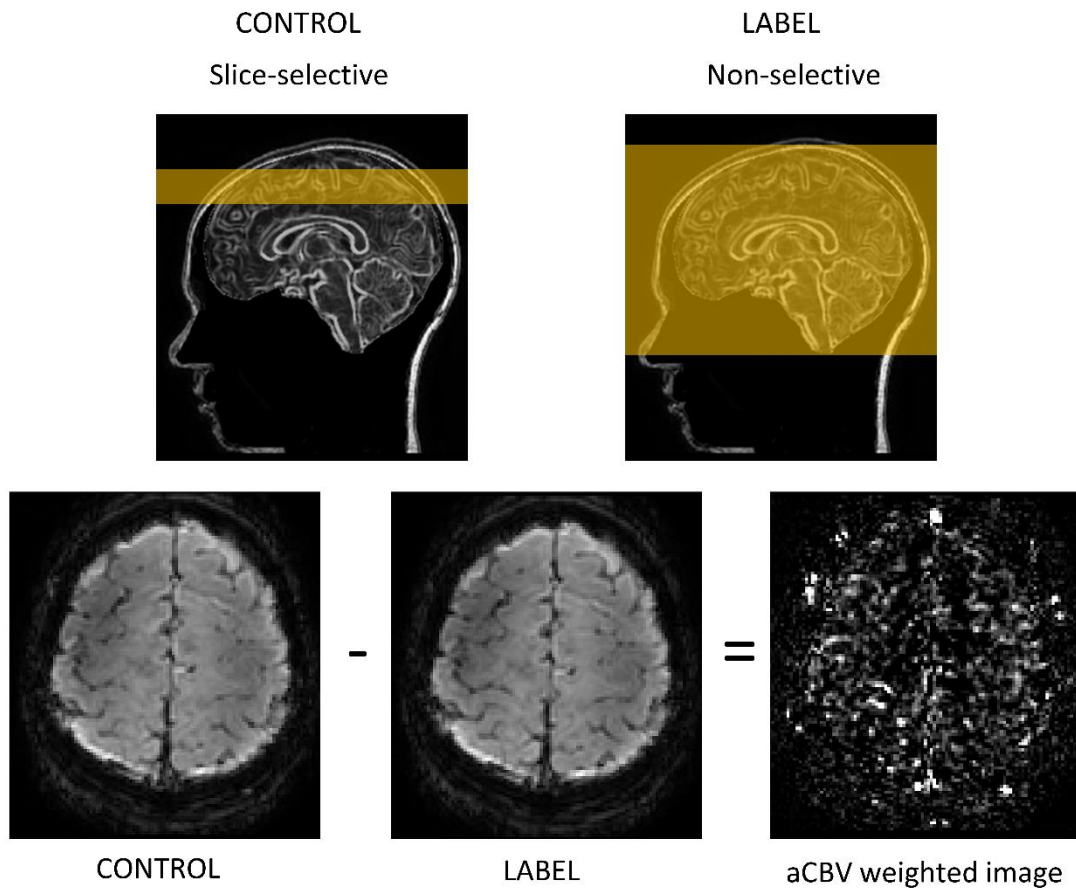


Figure 6.2. Schematic of the FAIR ASL scheme, showing the slice selective control and non-selective label image. An aCBV weighted image is created by subtracting the label image from the control image using an early TI.

concurrent acquisition, an inversion recovery scheme with double excitation can be used. This can be used to collect a VASO image at the blood-nulling point after the non-selective inversion, and an ASL image at a later time when the labelled spins have perfused the image plane.

An early example of simultaneous VASO, ASL and BOLD was developed by Yang et al. (Yang et al., 2004). In Yang et al., an inversion recovery sequence is used where the VASO image is collected at first inversion time delay, and ASL and BOLD images are collected at the second inversion time delay with a double acquisition: the first with a short TE to provide high SNR for ASL and the second with a longer TE to provide T₂*-weighting for BOLD contrast. The inversion alternates between non-selective (label) and slab-selective (control) to allow ASL images to be derived.

Using an inversion recovery sequence with a double excitation requires a modification to the inversion delay TI to use for VASO (Equation 7), with the solution to the Bloch equation for a double excitation yielding

$$M_z = M_0 \left(1 - e^{-\frac{t}{T_1}} \right) + M_z(0) e^{-\frac{t}{T_1}}. \quad (8)$$

To null M_z at TI_1 requires

$$0 = M_0 \left(1 - 2e^{-\frac{TI_1}{T_1}} + e^{-\frac{TR+TI_1-TI_2}{T_1}} \right). \quad (9)$$

Solving this gives

$$TI_1 = T_1 \ln \left(2 - e^{-\frac{TR-TI_2}{T_1}} \right). \quad (10)$$

Several studies have successfully combined VASO, ASL and BOLD to measure total CBV, CBF, and enable CMRO₂ calculation at 1.5 T and 3 T (Hua et al., 2011; Lin et al., 2009; Lu et al., 2004b). Moving to 7 T is advantageous for BOLD fMRI as it provides increased BOLD CNR. However, the implementation of VASO at 7 T is more challenging as the application of homogeneous inversion requires improved adiabatic inversion pulses. Further, the VASO signal can be more contaminated with BOLD effects at higher field strength due to the shortening of T₂*. It is possible, however, to remove any BOLD contamination, by collecting data without blood-nulling acquired (i.e. solely BOLD-weighted) along with VASO (BOLD-contaminated) data (Huber et al., 2014). If the BOLD-contaminated VASO data is divided by the BOLD data, uncontaminated VASO data is obtained.

As described above, with VASO there is only a short time in which to acquire the imaging slices after blood nulling. As a consequence of each slice taking a finite time to acquire, each of the slices will have a slightly different inversion time TI. This variation in TI will result in a variation in signal intensity across slices. To keep differences in signal intensity to a minimum, only a small number of 2D slices can be collected consecutively, limiting the spatial coverage of VASO. To demonstrate the variation in signal intensity across slices, the VASO signal was simulated in Figure 6.3 for a five slice 2D EPI readout. The signal from each slice is simulated, showing that after the VASO-delay, each slice is collected at a slightly different TI resulting in different magnetisation in each slice. One solution to this is to use a 3D EPI readout

rather than 2D EPI readout, as with 3D EPI the whole volume can be collected with the same TI (see Chapter 3), enabling greater spatial coverage and matched VASO contrast across all slices. 3D EPI has been found to provide higher BOLD contrast compared to 2D EPI at 7 T for GE-BOLD responses (Poser et al., 2010; van der Zwaag et al., 2012) and has been used as the readout scheme in VASO at 7 T (Huber et al., 2018). Huber and colleagues (Huber et al., 2018) directly compared 2D and 3D EPI VASO at 7 T. 3D EPI was found to give higher temporal stability than 2D, but to be more dominated by physiological noise. However, a disadvantage of 3D EPI with VASO is T_1 blurring as the signal is not in steady state. To overcome this, a variable flip angle can be used across the 3D EPI readout (Gai et al., 2011) so that a constant signal is measured across the 3D acquisition.

A further compromise with combining VASO, ASL and BOLD is the choice of echo time. For the greatest BOLD signal, the ideal is for $TE = T_2^*$ of grey matter, whereas for ASL and VASO a short TE is preferred for high SNR. One solution is to use a double echo with different echo times for each acquisition so that the TE is optimised. Previous studies have used multiple echo times, including Yang et al. (Yang et al., 2004), (Lu & van Zijl, 2005) and the DABS sequence (double-acquisition background suppression) (Mullinger et al., 2017; Mullinger et al., 2013b; Wesolowski et al., 2009) uses a double echo. The other option is to use a single echo time between the ideal echo times with reduced sensitivity to both ASL and BOLD. The choice here is often dependent on the spatial resolution required, at higher spatial resolution the two echo times can be too long to provide sufficient SNR.

A further adaptation is to implement the VASO scheme with a measure of arterial CBV using ASL and BOLD. aCBV has the advantage of having a significantly greater SNR than CBF and is localised to the arterioles in proximity to the active brain regions. In the following sub-sections, optimisation of the implementation of a VASO-ASL-BOLD sequence at 7 T is described.

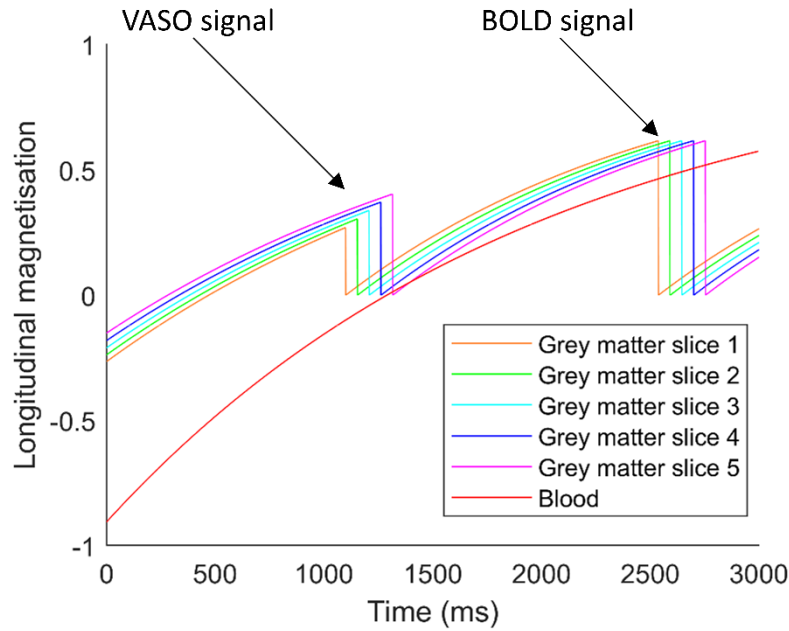


Figure 6.3. Simulated signal from the grey matter of each slice (orange, green, blue, purple and pink lines) for a 2D EPI readout where pulses are applied to measure the magnetisation in the transverse plane at VASO collection time and BOLD collection time. Since each slice is collected at a slightly different TI time after the VASO-delay (1050 ms) it can be seen that each slice has a different magnetisation, whereas at the BOLD-weighted acquisition (2500 ms) the slices recover to the same magnetisation. Shows relaxation of blood (red line) without any pulses applied for comparison.

6.3.4 Methods

Pilot experiments were first performed to develop and optimise a sequence for combined measures. The plan was to compare 2D EPI with 3D EPI, including 3D EPI with a constant flip angle and variable flip angle, with various multiband and SENSE factors, in order to find the optimum sequence. This was defined as the sequence which provided greatest tSNR, but also took into account greater spatial coverage, as well as the sequence which better equalised signal intensity between slices and between the different measures. In this work a FAIR ASL scheme is combined with a VASO scheme and a double excitation, as shown in Figure 6.4. VASO data is formed from the non-selective data at TI_1 corrected for BOLD contamination by dividing by the BOLD-weighted data collected at TI_2 (BOLD2), aCBV data can be created from the difference of the slice-selective and non-selective data at TI_1 , CBF data is acquired from the difference of the slice-selective and non-selective data at TI_2 , and BOLD data can be collected from the second excitation following both the selective and non-selective inversion using either a 2D EPI or 3D EPI readout. For a 2D readout, the TI will vary across slices whereas a 3D readout will collect the whole volume with the same TI.

However 3D readout will have blurring due to T_2^* decay and T_1 blurring if the flip angles are not corrected using a variable flip angle across the echo train.

6.3.5 Optimisation of the VASO Scheme Using Non-task Data

The first aim was to optimise the VASO scheme to provide the optimal sequence with good spatial coverage. For this, a 2D EPI readout without and with multiband

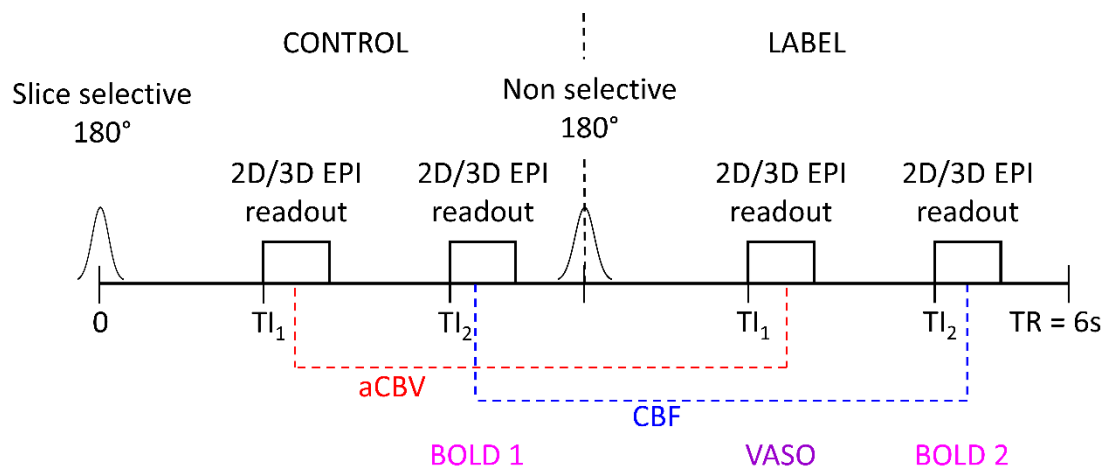


Figure 6.4. VASO-ASL-BOLD pulse sequence diagram, typical parameters use $TI_1 = 1050$ ms, $TI_2 = 2300$ ms, $TR = 6000$ ms with either a 2D or 3D EPI readout. In the first phase, the blood nulled data is acquired at TI_1 . In the second phase, BOLD weighted data is acquired at TI_2 . BOLD2 data are used to correct VASO data for T_2^* dependence. An aCBV image is created from control minus label of the first phase, and a CBF image from the control minus label of the second phase. The sequence simultaneously measures total CBV (VASO), aCBV and CBF (ASL), and BOLD.

acquisition, and 3D EPI readout were compared. The 2D EPI readout had 6 slices, yielding 12 slices for a multiband factor of 2, and the 3D EPI acquisition had 12 slices. All data were collected with 2 mm isotropic resolution at the minimum echo time TE of 20 ms. Data were all acquired in the same scan session on the same subject. Following this, the 3D EPI readout was compared for various SENSE factors to find the optimum acceleration which gives the best SNR for accelerated acquisition without artefacts. Further, to mitigate the effects of T_1 blurring across the slices when using 3D EPI with a constant flip angle, an acquisition with a variable flip angle to correct for T_1 blurring was also performed. The 3D EPI constant flip angle was set to 18°, whilst the variable flip angle was optimised to ensure a steady state signal was obtained over the 3D EPI readout with a train of flip angles of FA=18°, 19°, 20°, 22°, 24°, 26°, 28°, 33°, 35°, 39°, 41°, 52° and 90° over the 13 TFE factors.

6.3.5.1 Results

As shown in Figure 6.5, the 2D EPI readout (panels A and B) results in variation in signal intensity across the slices for VASO, as expected from the simulations (Figure 6.3) as the images are collected at different TI values. In contrast, for the 3D EPI readout (Figure 6.5C) a uniform signal intensity across the slices is seen. Figure 6.6 shows the corresponding tSNR for these scans. The tSNR was used to assess data quality and the multiband data were found to be highly unstable with poor tSNR. It later became clear the low tSNR of the multiband sequence (Figure 6.6B) was due to intrinsic issues with the scanner, rather than the pulse sequence itself, and the scanner was out of use for approximately 4 months throughout this sequence development period whilst the scanner was repaired. When comparing between the different contrasts (Figure 6.6), as expected the BOLD signal had the highest SNR for the 2D-EPI readout, whereas for the 3D-EPI readout the VASO and BOLD SNR became comparable. In addition, as was expected the aCBV images had a higher SNR than the CBF images.

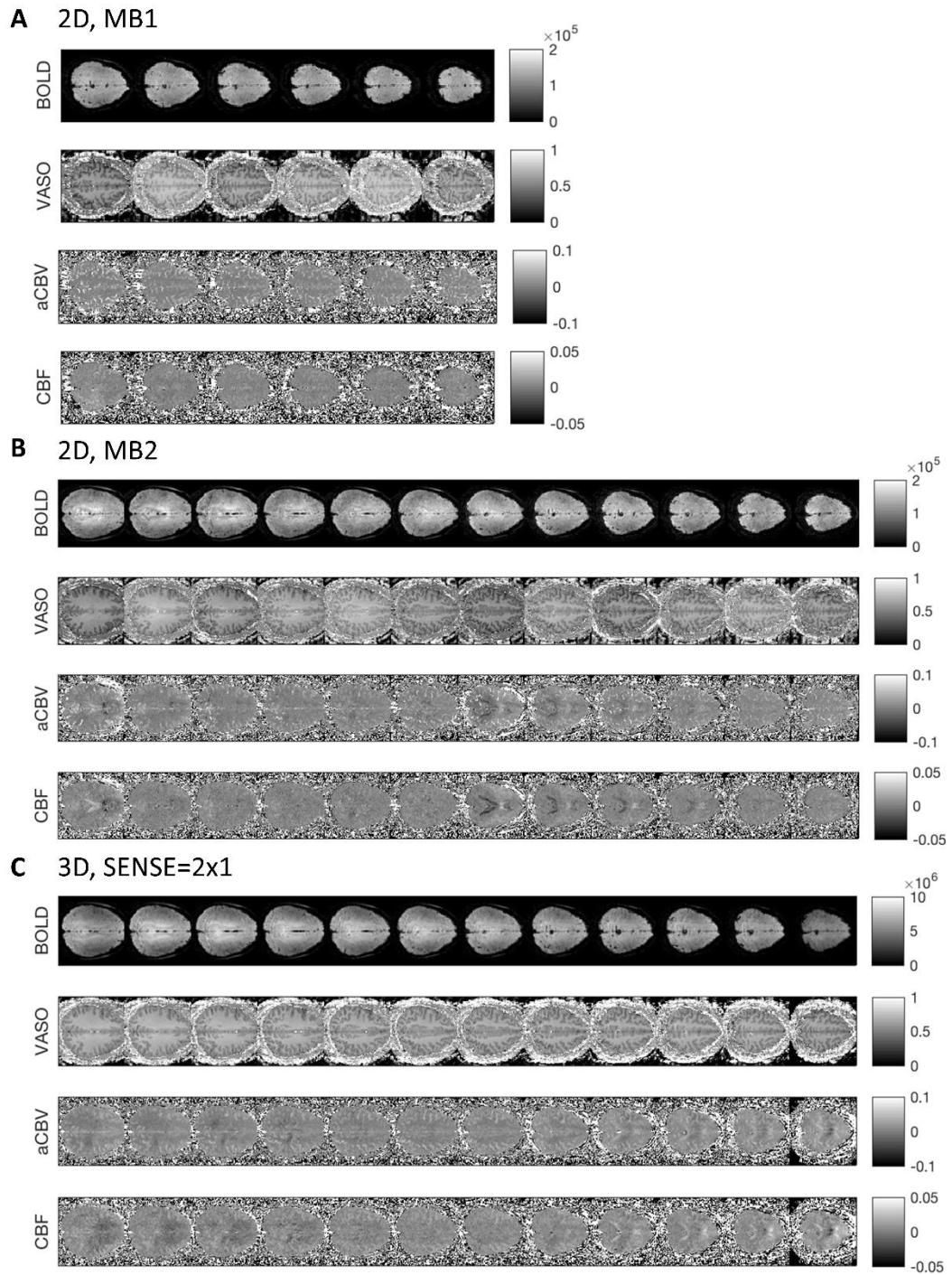


Figure 6.5. Comparison of 2D EPI readout collected without (A) and with multiband (MB) factor 2 (B), and with 3D EPI readout (constant flip angle (C)). Data collected using SENSE factor 2 throughout.

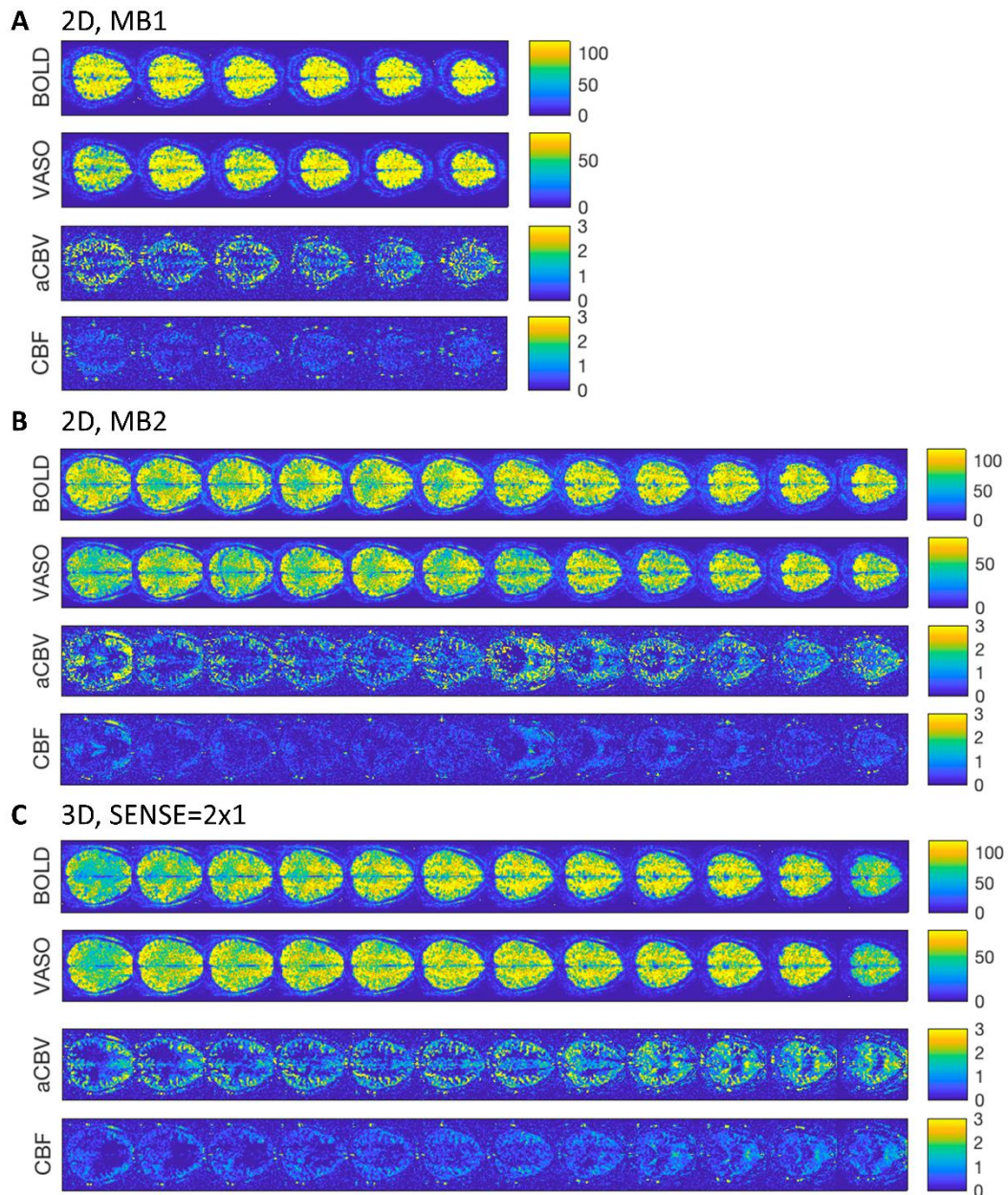


Figure 6.6. Comparison of $tSNR$ for (A) 2D EPI MB1, (B) 2D EPI MB2 and (C) 3D EPI constant flip angle, where mean images are shown in Figure 6.5.

As 3D EPI provides better coverage than 2D EPI, as well as being more robust than 2D EPI with multiband, it was decided to optimise the 3D EPI scheme further to reduce the acquisition time for collection of the imaging volume to reduce T_2^* and T_1 blurring effects. For this, the in-plane x through-slice SENSE factor was compared for SENSE 2x1, SENSE 2x1.5, and SENSE 2x2. It can be seen from Figure 6.7 that as the SENSE factor is increased, an artefact appears in the CBF and aCBV data.

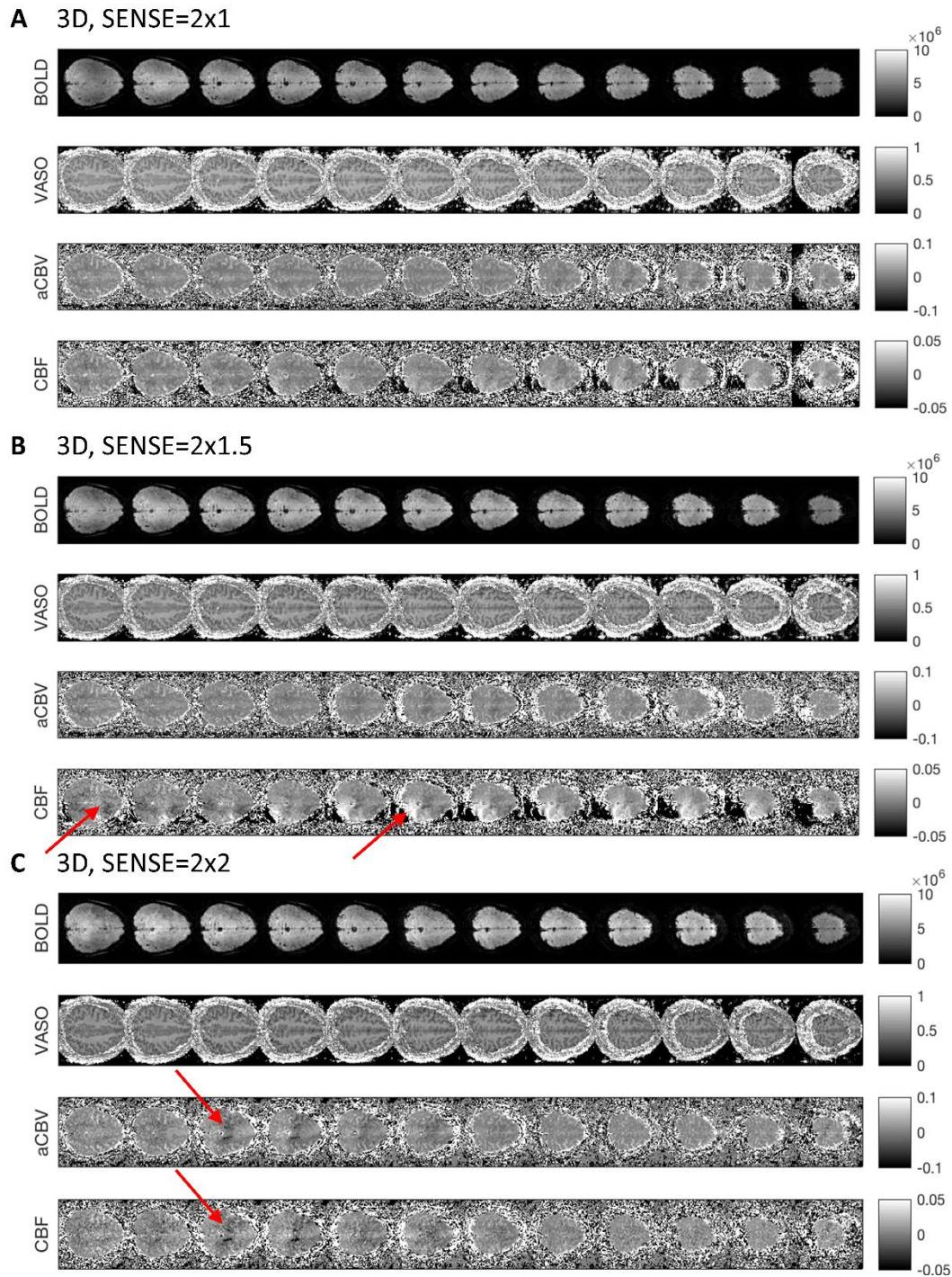


Figure 6.7. Comparing different SENSE factors for 3D EPI readout, with (A) SENSE 2x1, (B) SENSE 2x1.5, (C) SENSE 2x2. Arrows highlight artefacts observed in aCBV and CBF data with increasing SENSE acceleration.

Figure 6.8 shows the effect of using a constant flip angle in the 3D EPI readout versus a variable flip angle, all acquired with SENSE factor of 2.5 in-plane and no through plane acceleration. This provided a compromise of the results seen in Figure 6.7 to minimise the artefact whilst also minimising the readout time. The 3D EPI variable flip angle gives a more homogenous signal across slices, and between the BOLD and VASO

schemes whereas for the constant flip angle regime, the signal intensities are very different for VASO and BOLD (Figure 6.8). Similar signal intensities between VASO and BOLD are important as better realignment of images can be achieved. The tSNR of the VASO and BOLD data compared for constant and variable flip angles was calculated (Figure 6.9). Mean tSNR was 21 and 39 for VASO and BOLD data respectively for constant flip angle, and 33 and 32 for VASO and BOLD data respectively for the variable flip angle. The variable flip angle has improved SNR for VASO compared to constant flip angle, whilst BOLD tSNR is reduced slightly compared to constant flip angle but overall the variable flip angle provides better compromise on SNR, since BOLD data inherently has a higher SNR than VASO data.

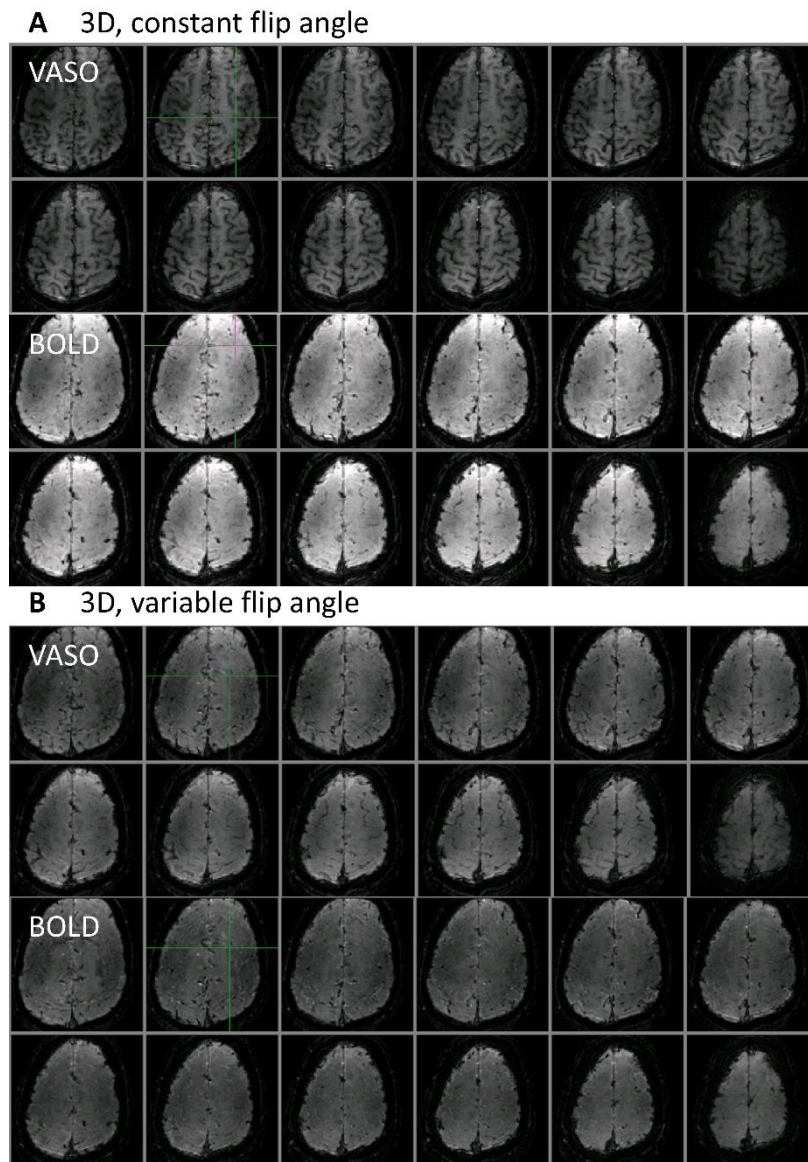
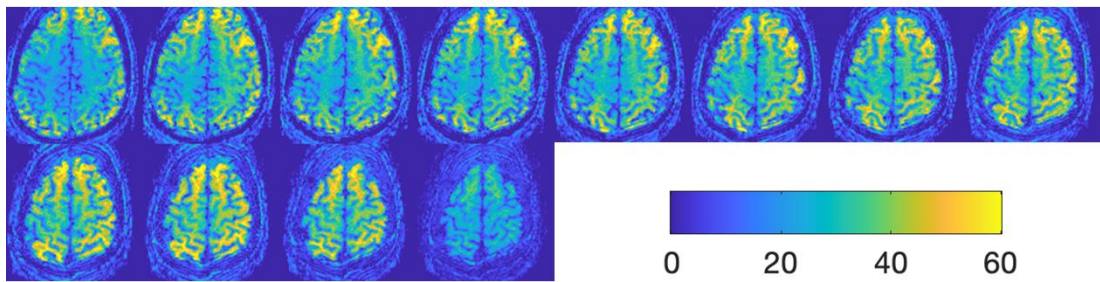


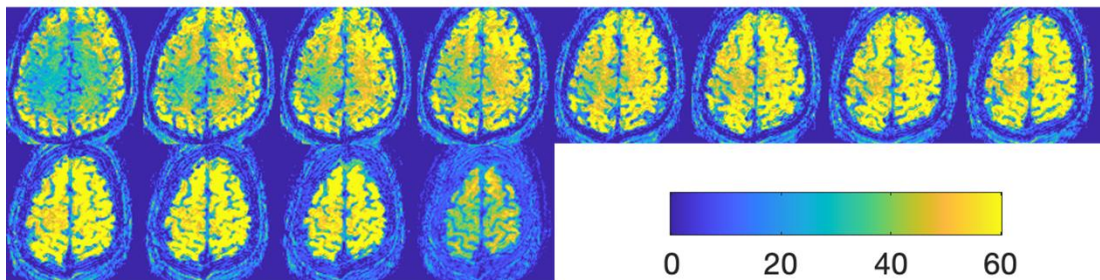
Figure 6.8. Comparison of absolute signal for (A) 3D EPI constant flip angle with (B) 3D EPI variable flip angle for VASO and BOLD, both with SENSE factor: 2.5×1 .

A 3D, constant flip angle
VASO



BOLD

B 3D, variable flip angle
VASO



BOLD

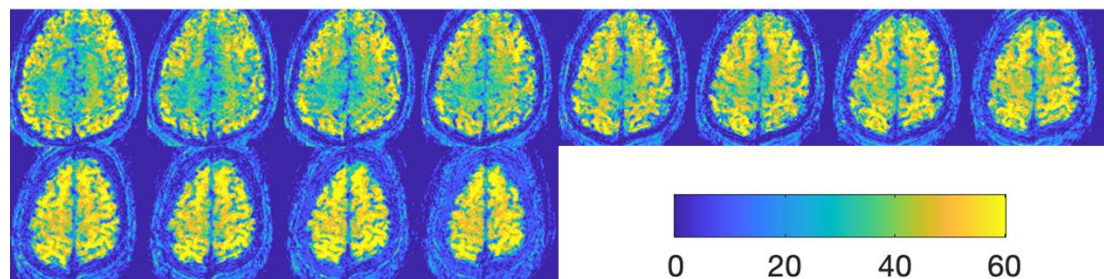


Figure 6.9. $tSNR$ of VASO and BOLD for (A) 3D EPI constant flip angle and (B) 3D EPI variable flip angle, where mean images are shown in Figure 6.8.

6.3.6 Task Data

Having optimised the 2D and 3D readout VASO acquisitions, the question was whether the sequence had enough sensitivity to detect functional activity. A robust, long duration functional task was first used to compare the 2D EPI and 3D EPI readout schemes, with 3D EPI readout data collected to compare both a constant flip angle and variable flip angle of excitation pulses. For each acquisition scheme, data were collected at 1.5 mm isotropic resolution and used a $TE = 18$ ms, $TI_1 = 1050$ ms and TI_2

= 2300 ms, SENSE factor = 2.5×1 with 112 volumes. Table 6.1 provides the parameters for each of the readout schemes. For each readout scheme, the timings were optimised to maximise the blood-nulling of the VASO scheme across slices, and to obtain sufficient signal-to-noise of the BOLD data using a complete simulation of the scheme using modified Bloch equations (data not shown in this thesis).

A block-design experiment was performed using right-handed finger tapping paradigm with 48 s initial rest period, followed by 8 repeats of 30 s task and 48 s rest. The paradigm included a visual cue to instruct the participant when to tap their fingers using Presentation (Neurobehavioral systems Inc, Berkeley, CA, USA). Data were collected for all readouts on the same subject in the same scan session. Data were analysed in mrTools (Gardner, 2018) using a GLM of the timings of the cued movements.

	2D EPI	3D EPI constant	3D EPI variable
Slices	5	12	12
TE (ms)	18	18	18
Resolution (mm)	1.5x1.5x1.5	1.5x1.5x1.5	1.5x1.5x1.5
Volumes	112	112	112

Table 6.1 Parameters for each of the readout schemes.

6.3.6.1 Results

Results of data collected using each of the 2D EPI, 3D EPI constant and 3D EPI variable readout schemes are shown in Figure 6.10 (2D), Figure 6.11 (3D EPI constant flip angle) and Figure 6.12 (3D EPI variable flip angle). Time courses of the whole run and activation maps are shown. The 3D EPI variable flip angle gives the most similar response across the image contrasts; BOLD, VASO and aCBV each produce a clear response to the stimulus period. Although the BOLD response when using the 3D constant flip angle is stronger than this response with the variable flip angle, the VASO data is much worse with no clear response to the stimulation periods when a constant flip angle is used with the 3D readout. The tSNRs of each contrast were also compared, for BOLD tSNR = 43, 36, 32 (for 2D, 3D, 3D variable); for VASO tSNR = 27, 16, 27; aCBV tSNR = 2.3, 1.4, 1.6; CBF tSNR 1.5, 0.9, 1.3 for 2D, 3D and 3D variable respectively. Although the 2D scan has higher tSNR for BOLD, the 2D scan is limited as it only has 5 slices compared to 12 slices for the 3D scan, therefore due to considerably better coverage the final sequence used was a 3D single echo with flip angle modulation. After initial visualisation of the CBF data, along with tSNR analysis,

the CBF data were found to be of poor quality. Therefore, the CBF data were not analysed any further. It is hypothesised this may have been due to the instability of the MRI scanner at the time of acquisition rather than the pulse sequence.

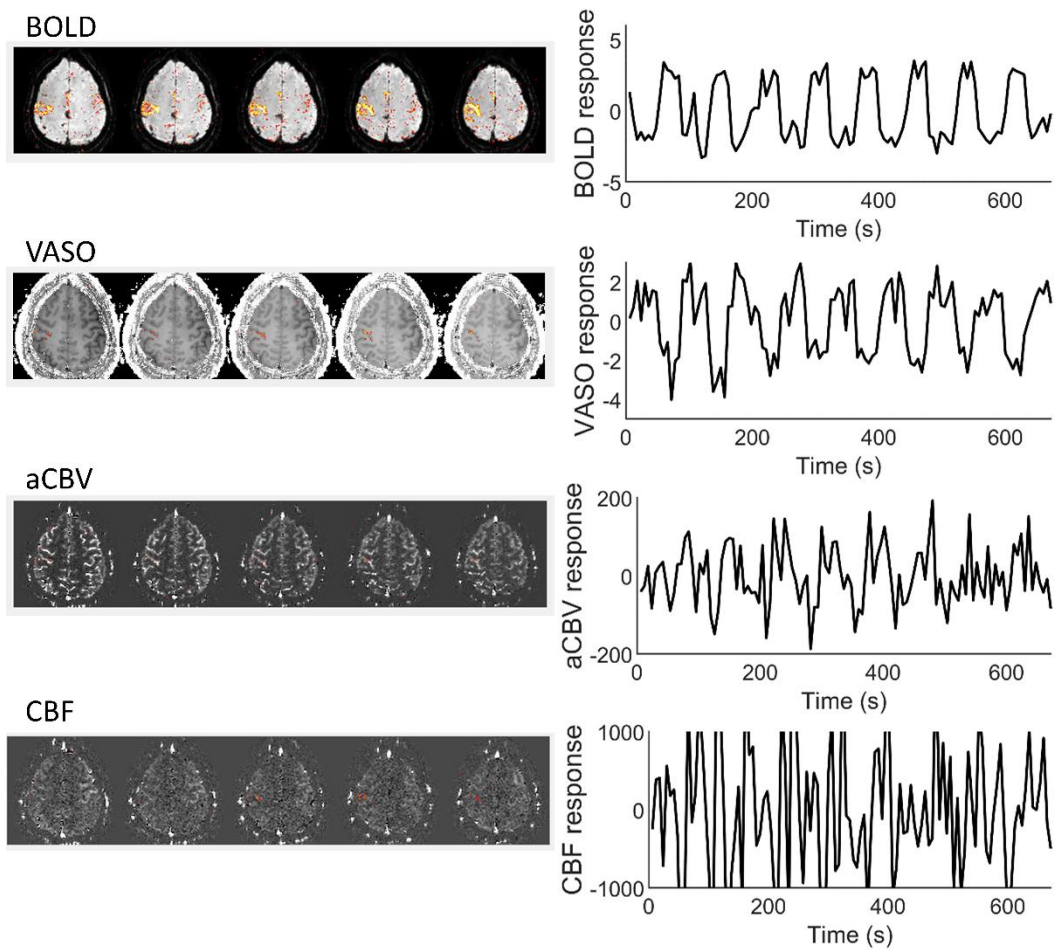


Figure 6.10. fMRI for 2D EPI. Showing task activation for (top to bottom) BOLD, VASO, aCBV and CBF. Right-hand column shows time courses of activation from region of interest in contralateral sensorimotor area (% change from baseline). Threshold at $p < 0.05$ FDR corrected.

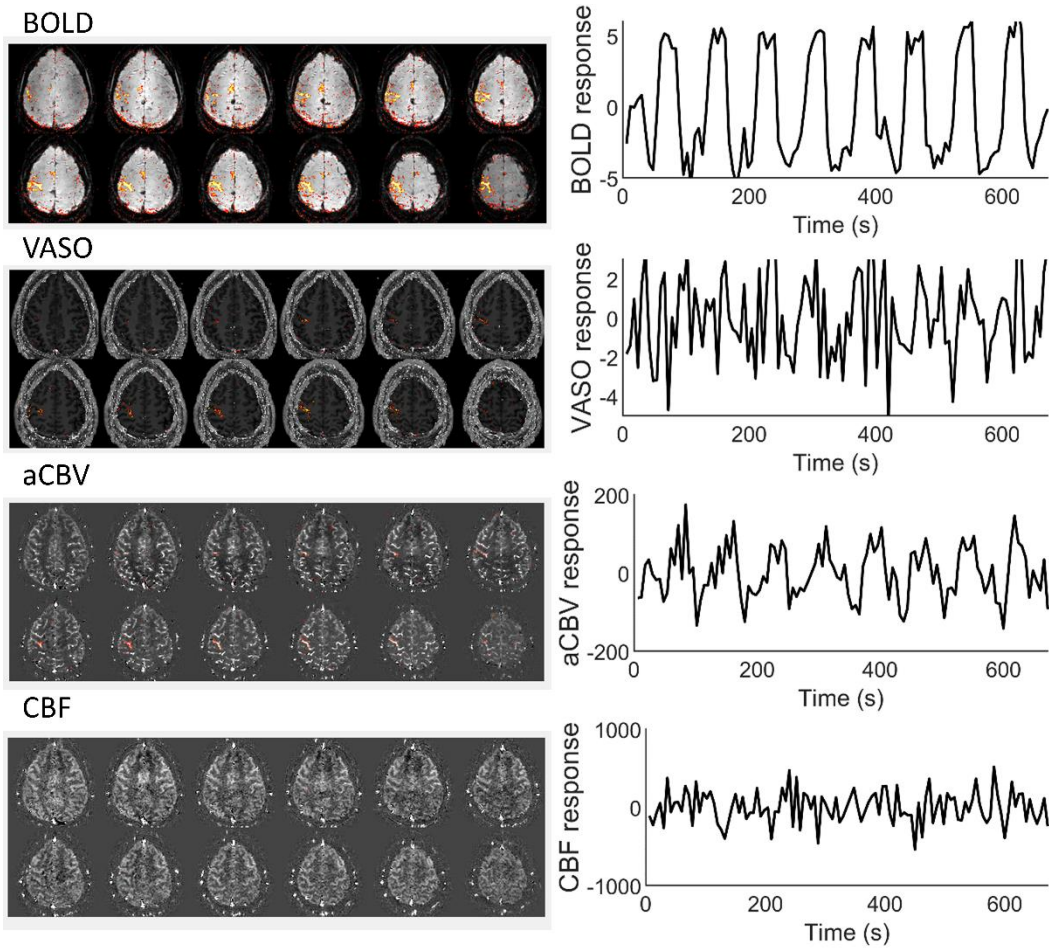


Figure 6.11. fMRI for 3D EPI with constant flip angle. Showing task activation for (top to bottom) BOLD, VASO, aCBV and CBF. Right-hand column shows time courses of activation from region of interest in contralateral sensorimotor area (% change from baseline). Threshold at $p < 0.05$ FDR corrected.

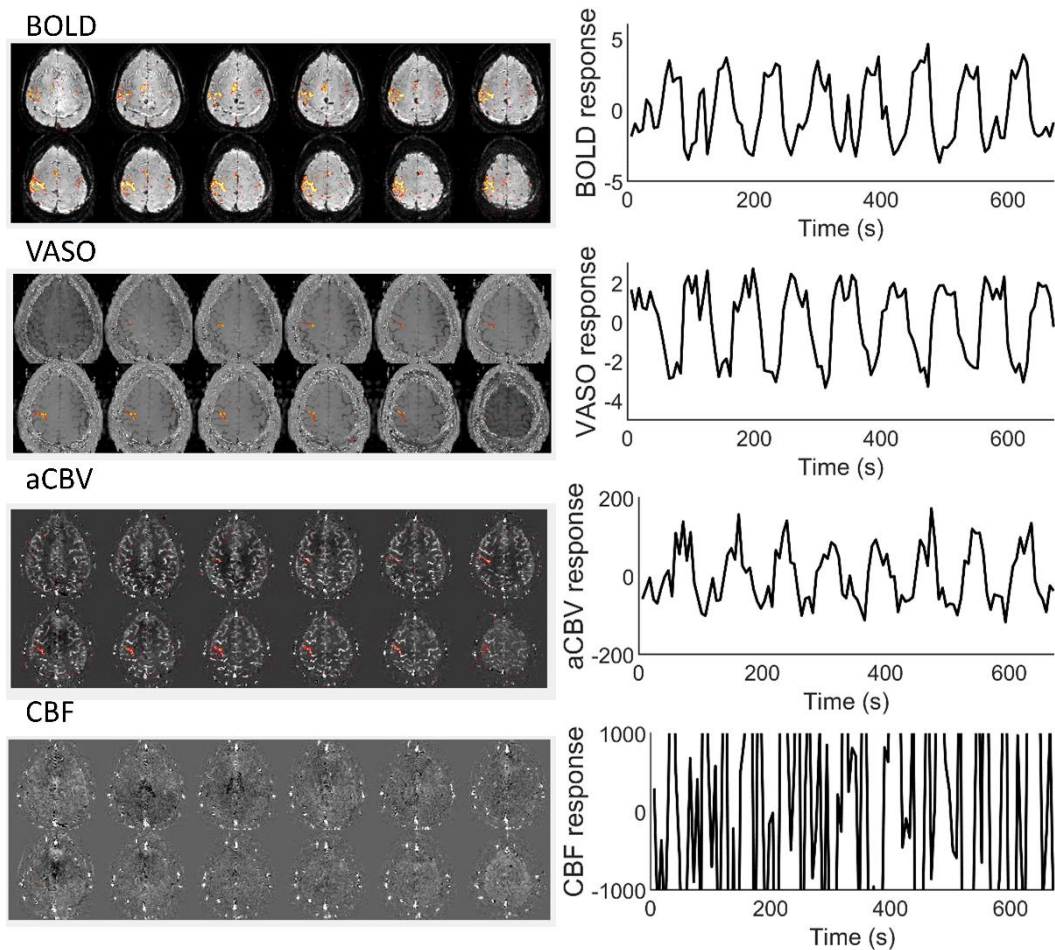


Figure 6.12. *fMRI for 3D EPI with variable flip angle. Showing task activation for (top to bottom) BOLD, VASO, aCBV and CBF. Right-hand column shows time courses of activation from region of interest in contralateral sensorimotor area (% change from baseline). Threshold at $p < 0.05$ FDR corrected.*

6.3.6.2 Conclusion

Based on this preliminary optimisation work, it was concluded that the optimal sequence was the 3D EPI variable flip angle sequence, which provides similar contrasts for VASO and BOLD compared to a constant flip angle, and equal signal intensities across slices compared to a 2D readout. The VASO-ASL-BOLD sequence was able to reliably detect functional activation for BOLD, aCBV and VASO, but little effects were seen for CBF data, due to reduced SNR of CBF measures and scanner instability issues at the time of data collection. The 3D variable flip angle sequence (Figure 6.4) can therefore be used in studying post-stimulus responses, to measure BOLD, total CBV and aCBV during a grip-force paradigm which will be described in the rest of this chapter.

6.4 Assessing the BOLD PSU Using Combined VASO-ASL-BOLD

10 healthy right-handed volunteers (mean age 28 ± 4 years, 3 male) took part in this study, with pilot data collected on one additional subject (male, age 26). All participants gave written, informed consent and the study was approved by the University of Nottingham Medical School ethics committee.

6.4.1 Paradigm

Subjects lay supine in the scanner bore, wearing prism glasses to view a screen onto which the visual presentation was projected. The paradigm was adapted from that used in Chapter 4 for the MEG experiment (see Figure 4.1), and consisted of a series of grip-contractions using an MR-compatible grip-force bar in their right hand (Current Designs, Philadelphia, USA) in order to reach the target profile. The target profile appeared on screen 2 s before the subject was required to grip, onto which the real-time force output from the grip-force bar was plotted. The height of the boxcar was set at 30% of the subject's maximum voluntary force (MVF). MVF was determined prior to the start of the scan session, when the subject was in the bore with their hand in position for the experiment. After each stimulus was a 60 s rest period where a fixation cross was presented to allow the haemodynamic response to fully return to baseline. Subjects were instructed to relax their right hand during the rest period between stimuli. Six trials of each stimulus (2 and 10 s) were presented in one run in a pseudo random order (12 trials in each run). Three runs were performed, with different ordering of trials for each run. The ordering of trials was designed so that the trial onsets were jittered in a controlled way relative to the MRI acquisition, creating a sampling rate which was one third of the nominal 6 s TR of the MRI sequence.

6.4.2 Data Acquisition

fMRI data were acquired on a 7 T Philips Achieva MR scanner (Philips Healthcare, The Netherlands) with 32-channel Nova head coil (Nova Medical, Wilmington, MA, USA). A localiser was performed first to identify locations of activation in the motor cortex to facilitate slice selection for the main experiment. The localiser consisted of a GE 2D EPI sequence, TR = 2 s, TE = 25 ms, 20 slices, 1.75 mm isotropic resolution, 72 volumes. The same visual presentation and grip-force task employed for the main

experiment was used for the localiser, but with fixed stimulus duration of 8 s on and 16 s off, repeated 6 times. IViewBOLD (Philips) was used to analyse these functional data on the scanner, to visualise areas of activation from the grip task. Activation maps were then overlaid on an anatomical image and slices for the main experiment were chosen based on these activation maps. Subsequently, three fifteen-minute runs of the task were acquired using the optimised VASO-ASL-BOLD sequence with a 3D EPI variable flip angle readout (see Section 6.3 for more details), with scan parameters: TR = 6 s; TE = 18 ms; TI₁ = 1050 ms; TI₂ = 2300 ms; 3D EPI FA = 18°, 19°, 20°, 22°, 24°, 26°, 28°, 33°, 35°, 39°, 41°, 52° and 90°; voxel size 1.5 mm isotropic and 12 slices; 104 x 102 matrix, FOV 154 x 18 x 154 mm, SENSE 2.5 x 1; 147 volumes per run. The jitter in paradigm presentation resulted in an effective TR of TR/3 (2 s) for aCBV, CBF and VASO, and 1 s for BOLD since BOLD data is collected following both the selective and non-selective inversions.

The task runs were separated by the acquisition of anatomical images to allow the subjects to rest between experimental runs. These comprised 1) FLASH (TE = 11.4 ms, resolution 0.5 x 0.5 x 1.5 mm, 360 x 360 matrix, 74 slices), 2) high-resolution phase-sensitive inversion recovery (PSIR) (0.7 mm isotropic resolution, 320 x 320 matrix, 224 slices) 3) B₀ map (TE = 5.92 ms, 4 mm isotropic resolution, 64 x 64 matrix, 40 slices) and 4) B₁ map (4.5 mm isotropic resolution, 44 slices, 64 x 64 matrix).

Surface electromyography (EMG) was recorded from the subject's right forearm to measure exact movement times and monitor movement. Surface Ag/AgCl electrode pairs (EasyCap GmbH, Germany) were positioned in a bipolar configuration over the forearm extensor bundle (channel 1) and forearm flexor bundle (channel 2) muscle groups. As in Chapter 4, EMG data were acquired using an ExG amplifier (Brain Products GmbH, Germany) and BrainVision recorder (v 1.1), with a sampling rate of 5000 Hz and frequency range of 0.016–250 Hz (with 30 dB roll-off at high frequencies). The EMG clock was synchronised to the MR scanner clock and markers were inserted at the start of each TR period to ensure temporally synchronised data, to allow for gradient artefact correction. In addition, grip-force bar data were recorded throughout the task via MATLAB. The 100% MVF contractions performed in the MEG experiment to monitor fatigue were not performed in this experiment, as the results from Chapter 4.4.1 did not show effects of fatigue. It was decided these were not needed as the fMRI

experiment had longer rest periods between trials and less trials overall, so was even less likely to cause fatigue.

6.4.3 Analysis

6.4.3.1 EMG

EMG data were corrected to remove the gradient artefact and filtered. Gradient artefact correction was performed in BrainVision Analyzer 2.2 using the TR value of 6 s and a sliding average calculation with 51 repeats. Data were filtered to 1 – 150 Hz and rectified. Data were then analysed to extract onset and offset times of movement from the EMG trace using an in-house MATLAB program, modified from that used in Chapter 4. The standard deviation of baseline EMG activity was determined in a time window 45 to 55 s after the visual cue for contraction offset from all contractions, independently for each EMG channel and subject. This baseline period was used to determine a noise threshold which was defined as three times the standard deviation of the baseline (Cheyne et al., 2008; Muthukumaraswamy, 2010). Subsequently, the onset of contraction was defined as the first time point, in a 0.5 s window either side of the visual cue, when the signal was greater than the noise threshold. Unlike in Chapter 4, (4.3.4.1), for each subject, the best channel was chosen (channel with cleanest EMG trace) from which to define the movement times as the channels were noisier than the MEG-EMG data (see Results). In addition, extra movements during the rest period were unable to be detected in these EMG data due to higher noise in the fMRI-EMG data. Grip-force and motion parameter data were visually inspected for any large movements and none were found, therefore all subjects and trials were included for further analysis.

To investigate the performance of the task, the mean EMG amplitude was determined during the grip period. The Hilbert envelope of the signal was taken, and the mean amplitude during the grip (excluding the first and last 0.5 s of each trial) was found. This was compared across runs and durations to assess whether there was any difference in EMG signal during the different runs of the experiment or the two experimental conditions.

Similarly, the mean force from the grip-force data were measured. Data were converted to a percentage of the subject's MVF and the mean grip-force during each contraction was determined, with the first and last 0.5 s excluded so that only steady force output was captured.

6.4.3.2 MRI pre-processing

BOLD data from the label and control acquisitions were interleaved, to provide a TR of 3 s. Data were motion corrected to the first volume within each run using SPM12 (<http://www.fil.ion.ucl.ac.uk/spm/software/spm12/>) and coregistered between runs by registering all data to the first volume of the second run in FSL using FLIRT. ASL-weighted data collected at TI_1 and TI_2 were linearly interpolated to an effective TR of 3 s. Tag-control pairs from the first phase were subtracted to produce aCBV-weighted images (see Figure 6.4). VASO data were corrected for BOLD weighting by dividing the VASO-weighted images acquired after the non-selective pulse at the earlier TI_1 , by the BOLD-weighted image at TI_2 (see Figure 6.4). PSIR data were corrected for field bias to produce high resolution T_1 -weighted PSIR image (Mougin et al., 2016; Van de Moortele et al., 2009) and brain extracted using FSL (Jenkinson et al., 2012). fMRI data were co-registered to the individual subject's PSIR using FLIRT (FSL). A vein mask was created (Figure 6.13) from the T_2^* -weighted FLASH image by high-pass filtering the unwrapped phase images and using a threshold to identify veins (Besle et al., 2014). If signal remains from large veins, it can limit the spatial resolution achievable of activation maps. Barth and Norris showed that removal of veins can improve spatial specificity of activation maps (Barth & Norris, 2007), however reduces the activated volume by 25%. Excluding the draining vein effects ensured that signals measured were dominated by microvasculature more closely related to neurons rather than by large draining veins. The brain extracted PSIR image was segmented into grey matter, white matter and cerebrospinal fluid (CSF) masks using segment in SPM12 (Figure 6.14). The resultant maps were then transformed to the functional space in which the BOLD, VASO and aCBV data resided using FLIRT (FSL).

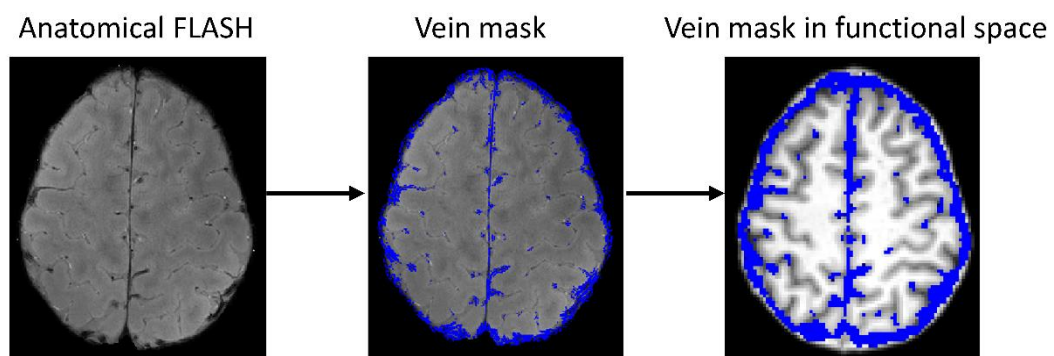


Figure 6.13. Example of a vein mask (blue) created from FLASH image of individual subject and transformed to functional space, overlaid on the PSIR image.

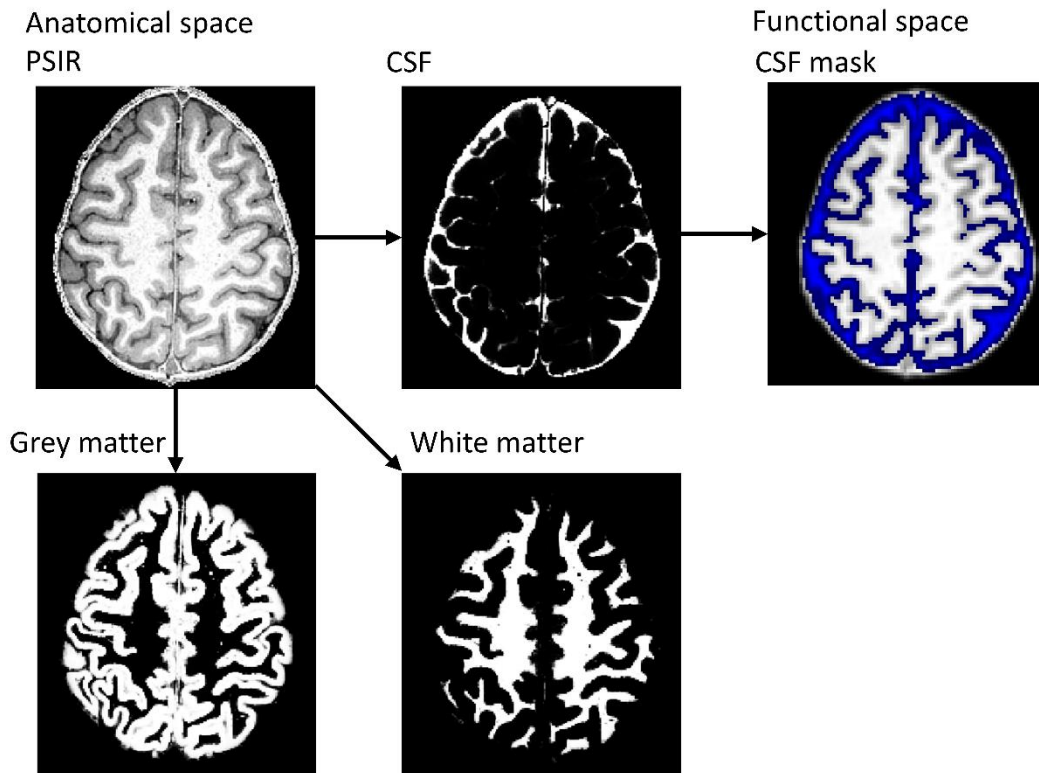


Figure 6.14. PSIR is segmented into grey matter, white matter and CSF probability maps for each subject. Maps were transformed to functional space and thresholded to create an individual subject mask of CSF (shown in blue, overlaid on the PSIR image).

6.4.3.3 Basic General Linear Model

The main focus of this work was to compare BOLD responses to a task where the electrophysiological response was already known (Chapter 4) and elucidate the origins of the haemodynamic response. For this, a general linear model (GLM) was used for each subject to locate regions of activation to the task. Analysis was carried out in SPM12. Data were modelled with a boxcar regressor of constant amplitude, using the onset and offset times of the grip-contraction determined from the EMG data. This boxcar was convolved with a conventional canonical double-gamma 6 s peak haemodynamic response function (HRF) available in SPM12. A regressor was made for each run with both 2 and 10 s stimuli modelled in the same regressor, as no spatial difference was expected in the region of the brain activated by these two conditions. Motion parameters were also included in the design matrix for each run as nuisance regressors. GLMs were performed separately for the BOLD, aCBV and VASO data. For the BOLD data, positive task contrasts to the stimulus regressor were assessed, with a threshold at $p < 0.05$, FWE corrected with a 5 voxel extent, to identify regions of correlation with the task. Negative contrasts were assessed for VASO data whilst

positive contrasts were assessed for aCBV data. For both these data, a lower threshold of $p < 0.001$ uncorrected, 5 voxel extent was used for VASO and aCBV due to the intrinsically lower SNR of these sequences. Following this, the activation maps from each image contrast were binarised and summed to find voxels where activation occurred in conjunction in BOLD, aCBV and VASO responses, thus producing maps of activation of the spatial conjunction all three contrasts.

6.4.3.4 Regions of Interest (ROIs) and Time Courses

From the MEG study, (Chapter 4) it was observed that the PMBR was localised more to the precentral gyrus which is known to be the primary motor area, therefore, regions of interest (ROIs) were taken from within the precentral gyrus. A mask of the precentral gyrus created from the Harvard-Oxford cortical atlas was transformed into each subject's functional space using FLIRT (FSL). ROIs were taken as a $3 \times 3 \times 3$ voxel cubic region (total = 27 voxels) surrounding a number of peak responses within the contralateral precentral gyrus for each subject. Firstly, an ROI was formed from the peak BOLD T-stat within the conjunction mask of the BOLD, aCBV and VASO activation (termed 'Large ROI'). This ROI was then refined to remove potentially confounding signals. Due to the fact that BOLD responses can be dominated by large draining veins, the vein masks created from the FLASH images were used to exclude veins from the conjunction activation mask. The VASO signal will also be modulated by partial voluming of CSF or white matter (Lu et al., 2003). If a voxel is only 50 % grey matter, uncertainty is introduced in the proportionality between VASO signal change and CBV (Lu et al., 2013). Therefore, the CSF mask created from the PSIR was used to exclude any voxels containing a large fraction of CSF from the conjunction activation mask, resulting in a cleaned conjunction activation mask which excluded both draining veins and voxels with large CSF contributions. With these confounding factors removed, a second ROI was created centred on the peak of the BOLD T-stat within the cleaned conjunction activation mask (termed 'Small ROI'). Only voxels which were not CSF or veins could be included in this ROI, as such ROIs often contained fewer than the nominal 27 voxels defined as an ROI (5 ± 4 voxels, range 1 – 11). To interrogate signal quality for each contrast, further ROIs were created centred on the peak i) BOLD ii) VASO and iii) aCBV t-stat within the contralateral precentral gyrus (Appendix A).

Time courses of BOLD, VASO and aCBV response were extracted from the large and small ROI. The time courses were interpolated to 1 s temporal resolution and segmented based on timings of movement from the EMG. Each run was converted to a percentage signal change relative to baseline, where baseline was defined as the last 10 s of each trial, before the next visual cue was presented. Responses were averaged over trials, separately for 2 and 10 s stimuli, and then subjects to produce a subject average.

To test for significant differences between stimulus conditions, the peak of the primary response (a minimum for VASO) was found in the 1 to 20 s period after stimulus onset, averaged over 1 TR period around the peak, this was determined separately for the 2 and 10 s datasets, and a paired Student's t-test was used to compare the peak amplitude of the haemodynamic responses between the two conditions. If the data were not normally distributed, as was the case for the aCBV data, a Wilcoxon signed rank test was used. The minimum of the post-stimulus response (PSR) (maximum signal for VASO) was found in the 15 to 35 s period after stimulus onset and averaged over 1 TR period around the minimum, again this was determined for 2 and 10 s and paired t-tests (Wilcoxon signed rank test for aCBV data) were performed to assess differences between the amplitudes of the responses for the two conditions for BOLD, VASO and aCBV responses. The minimum of the PSR was also tested if it was a significant effect for each stimulus duration and response (one sample t-test).

6.4.3.5 Using MEG Regressors in the GLM

The analysis in Section 6.4.3.3 uses a GLM comprising of a boxcar convolved with a standard canonical HRF. When a canonical HRF is convolved with a boxcar stimulus duration of 10 s, the undershoot is larger than the undershoot for a 2 s stimulus duration (Figure 6.15, bottom row). This is what the GLM will be modelling, so the GLM results will clearly show the highest t-stat results in regions which show this form of modulation of the PSR. However, if the PSR is neuronally driven, then the MEG results from Chapter 4 predict a larger undershoot for the 2 s than 10 s stimulus. To explore this possibility, a second GLM was created using the known MEG responses as inputs to the GLM. This GLM was designed to determine if the activation identified from the MEG input model was spatially different or stronger than that identified by the conventional boxcar model from Section 6.4.3.3.

Different components of the MEG response were convolved with a HRF and used to model the fMRI responses. The MEG beta band time course was divided into the movement related beta decrease (MRBD) component measured during the stimulus and the post-movement beta rebound (PMBR) component measured post-stimulus. To reduce noise in the model the trapezoid and Weibull fits to the average MEG MRBD and PMBR responses were used and each convolved with a 10 s single-gamma HRF (Mullinger et al., 2013a). Since BOLD and beta are expected to be negatively correlated (Yuan et al., 2010), the MEG beta band time course was multiplied by -1 to give positive correlations. These were input as the first two regressors in the GLM. As well as exploring effects in the beta frequency band, gamma band responses and BOLD have been shown to be positively correlated (Goense & Logothetis, 2008; Logothetis et al., 2001; Zumer et al., 2010), with gamma band activity thought to most closely relate to the primary BOLD response (Goense & Logothetis, 2008). Therefore, the gamma response was also modelled in the GLM. Again to reduce noise, a Weibull distribution was fit to the subject average gamma response (Chapter 4.4.4) and this was input as a third regressor, convolved with a 6 s single-gamma HRF (Mullinger et al., 2013a).

Using this GLM of MEG responses, analysis was performed on the BOLD, VASO and aCBV images to identify regions of the brain which significantly correlated with each regressor. Positive contrasts with each regressor were assessed with a threshold at $p < 0.001$ uncorrected. Separately for each regressor, the peak active voxel in the BOLD image was found in the contralateral precentral gyrus and a 3 x 3 x 3 ROI was centred on this voxel. From this ROI, the mean time course was found and averaged over subjects to identify the temporal profiles of responses generated from each regressor, and to determine if there were regions where the PSR behaved in a manner predicted by the classic boxcar (i.e. larger PSR for the 10 s stimulus) or other regions which behaved as predicted by the MEG data (i.e. larger PSR for the 2 s stimulus).

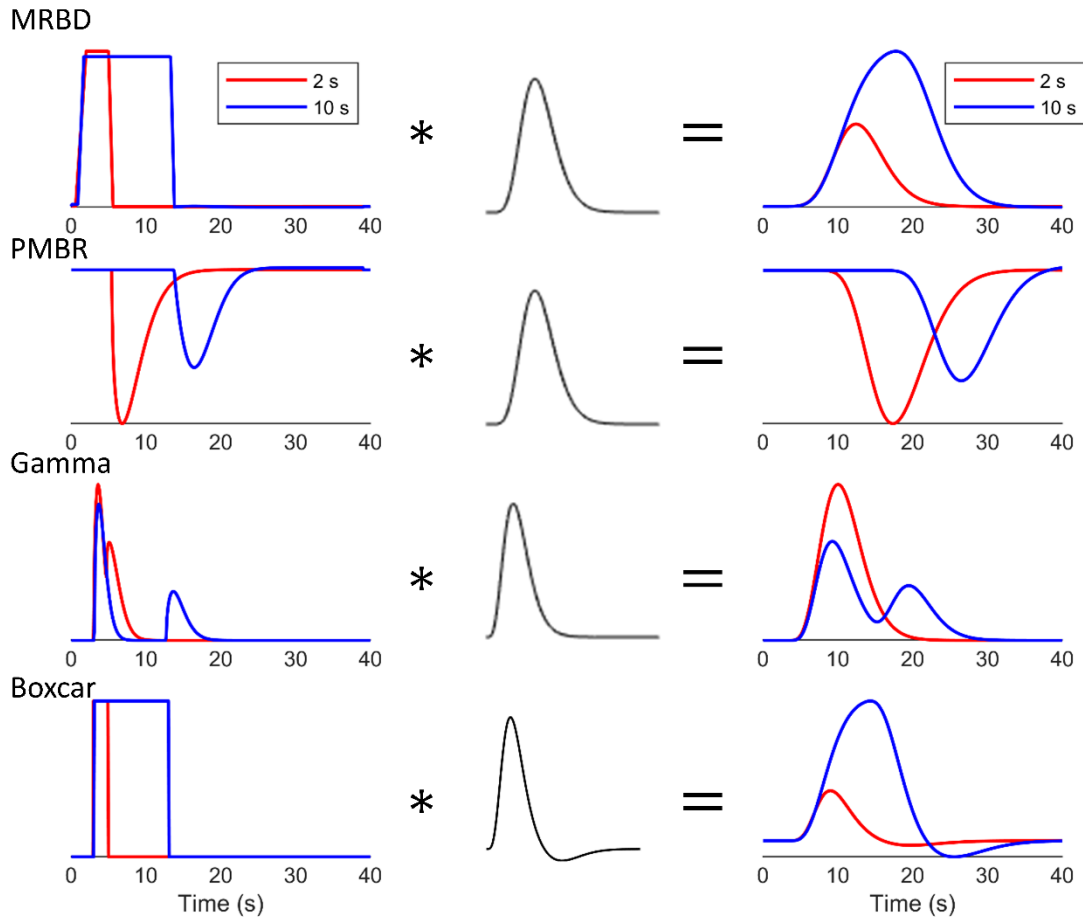


Figure 6.15. MEG regressors (MRBD, PMBR and Gamma) shown compared with the stimulus boxcar regressor used in Section 6.4.3.3. The average MRBD and PMBR responses for the 2 s (red) and 10 s (blue) stimuli from Chapter 4 were convolved with a 10 s single gamma HRF to create MRBD and PMBR regressors, the gamma responses were convolved with a 6 s single gamma HRF and a boxcar of the stimulus duration was convolved with a 6 s double gamma HRF to produce the boxcar regressor.

6.4.3.6 Simulation

Based on these MEG models in Section 6.4.3.5 a simulated time course was created. This was used to investigate the effects of sampling rate on the time courses to understand the time courses observed for each of the fMRI contrasts (BOLD, VASO and aCBV) (see Results 6.5.2). Appendix B provides details of these simulations.

6.4.3.7 CMRO₂ estimation

On the basis of the results of the different GLM analyses (see Results) CMRO₂ calculations were performed on the time courses from the conventional boxcar GLM which gave the most robust responses across contrasts. The CMRO₂ change during the primary and post-stimulus response was estimated using the Davis model (Davis et al., 1998), described in terms of CBV rather than CBF (Guidi et al., 2016). Combining the

Davis model (Davis et al., 1998), which gives BOLD signal change as a function of CBV, CBF and CMRO₂, with Grubb's law (Chen & Pike, 2009a; Grubb et al., 1974), and the relationship between the VASO signal and CBV (Lu et al., 2013), the change in BOLD signal (δS) can be written as a function of CBV and CMRO₂ (Guidi et al., 2016),

$$\delta S = M(1 - v_t^{(\alpha_v - \beta)/\alpha_t} r^\beta) \quad (11)$$

where M is the maximum BOLD signal change (a calibration constant), v_t is relative CBV in the total blood compartment, α_t is Grubb's coefficient in the total blood compartment and α_v in the venous compartment. r is relative CMRO₂ and β is a constant dependent on transverse relaxation rate and deoxyhaemoglobin concentration, which is approximately 1 at 7 T (Martindale et al., 2008). Equation 11 can be rearranged to calculate CMRO₂,

$$\left(\frac{CMRO_2}{CMRO_{2,0}}\right)^\beta = \left(1 - \frac{\left(\frac{\Delta BOLD}{BOLD_0}\right)}{M}\right) \left(\frac{CBV_t}{CBV_{t,0}}\right)^{\beta - \alpha_v/\alpha_t} \quad (12)$$

where subscript '0' represents the quantity at rest (baseline). This was used to calculate CMRO₂ using $\alpha_v = 0.2$ (Chen & Pike, 2009a), $\alpha_t = 0.38$ (Grubb et al., 1974) and $\beta = 1$ (Martindale et al., 2008). M depends on baseline quantities, TE and field strength and was estimated from literature hypercapnic challenges. A study with the same field strength and TE found $M = 11$ (Guidi et al., 2016), therefore this value was used for the main analysis. Further values of M were found in the literature and normalised to the field strength and TE used in this experiment, and a wider range of values of M ($M = 18$ and $M = 25$) were explored in Appendix C. The change in CMRO₂ was calculated during the primary response and the PSR using the BOLD and VASO time courses from the peak BOLD response ROI within the contralateral precentral gyrus (Small ROI). The maximum BOLD signal change in the 1 to 20 s period from stimulus onset for each subject was computed and averaged over a period of ± 1 s. The VASO signal change was measured at the time point that the BOLD peak occurred and averaged over a period of ± 3 s. The change in CMRO₂ was then calculated for each subject using Equation 5. From the results of Appendix B, the primary VASO response for the 2 s stimulus was found to be consistently smaller than the 10 s response which was not seen in the BOLD responses. From Appendix B it was shown that the 2 s stimulus VASO peak amplitude was consistently under-represented (80% of true VASO

amplitude) due to the sampling rate of the VASO sequence. Therefore measured amplitudes of the 2 s VASO primary response were scaled by a factor of 1.25 to compensate for the artefact of the analysis method. This scaled VASO measure was used for the CMRO₂ calculation. Percentage change CMRO₂ during the primary response and PSR was compared for the 2 and 10 s grip contraction using a paired Student's t-tests. A one sample t-test was used to test whether the percentage change CMRO₂ differed significantly from baseline.

6.5 Results

One subject was removed from further analysis due to considerably lower tSNR (17 ± 1) than all other subjects (28 ± 4). Therefore, results are presented for nine subjects.

6.5.1 EMG

After gradient artefact correction, the EMG data collected inside the MRI scanner were considerably noisier than in the MEG environment as shown in Figure 6.16A. To investigate if the residual noise was at a specific frequency, EMG data were Fourier transformed. Figure 6.17 clearly shows there are gradient artefact residuals which remain in the data, as well as higher broadband noise due to the MRI static field. The fMRI-EMG results also show large spikes at movement onset and offset (Figure 6.16A) which was not seen in the MEG-EMG. This is probably due to movement of the wires in the magnetic field. Although the large spikes on movement onset and offset are not true muscle activity, they are clearly time-locked to movement onset and offset and as a result were used in this analysis. Despite these differences in EMG, little difference was observed between grip-force data in the fMRI and MEG experiments (Figure 6.16B), showing the two experiments were performed similarly.

As is apparent from Figure 6.16A, EMG channel 2 (measuring forearm flexor bundle activity) was cleaner than channel 1 (measuring forearm extensor bundle activity). The traces were visually inspected for each subject, and it was clear that one channel always contained less noise - channel 2 for 8 subjects, and channel 1 for 1 subject. The channel with the least noise was used to determine the movement onsets and offsets together with amplitude, and the other channel discarded.

The mean EMG amplitude for runs 1, 2 and 3 were $277 \pm 181 \mu\text{V}$, $249 \pm 122 \mu\text{V}$ and $267 \pm 138 \mu\text{V}$ respectively. These values were not statistically different across runs ($p > 0.05$, RM-ANOVA). The mean grip-force output (across subjects and durations \pm standard deviation) was $29 \pm 1\%$ MVF during run 1, $30 \pm 1\%$ MVF during run 2 and $30 \pm 1\%$ MVF during run 3, with a significant difference between runs ($p = 0.02$, RM-ANOVA), driven by the difference between run 1 and run 2. However, given the highly similar values of force output and no significant difference in EMG amplitudes, the runs were considered to be the same. The grip-force data show excellent performance of the task, with subjects reaching the desired 30% MVF.

Figure 6.18 compares EMG and grip-force data for the two task durations. The mean EMG amplitude for the 2 s grip was $275 \pm 163 \mu\text{V}$ and $253 \pm 131 \mu\text{V}$ for the 10 s grip. There was no significant difference across durations ($p > 0.05$, Wilcoxon signed rank test). Accordingly for the grip-force data, mean %MVF for the 2 s grip was 30 ± 1 %MVF, and 29 ± 1 %MVF for the 10 s grip, with no significant difference ($p > 0.05$, paired t-test). These data show that there was no difference in performance between the two task durations.

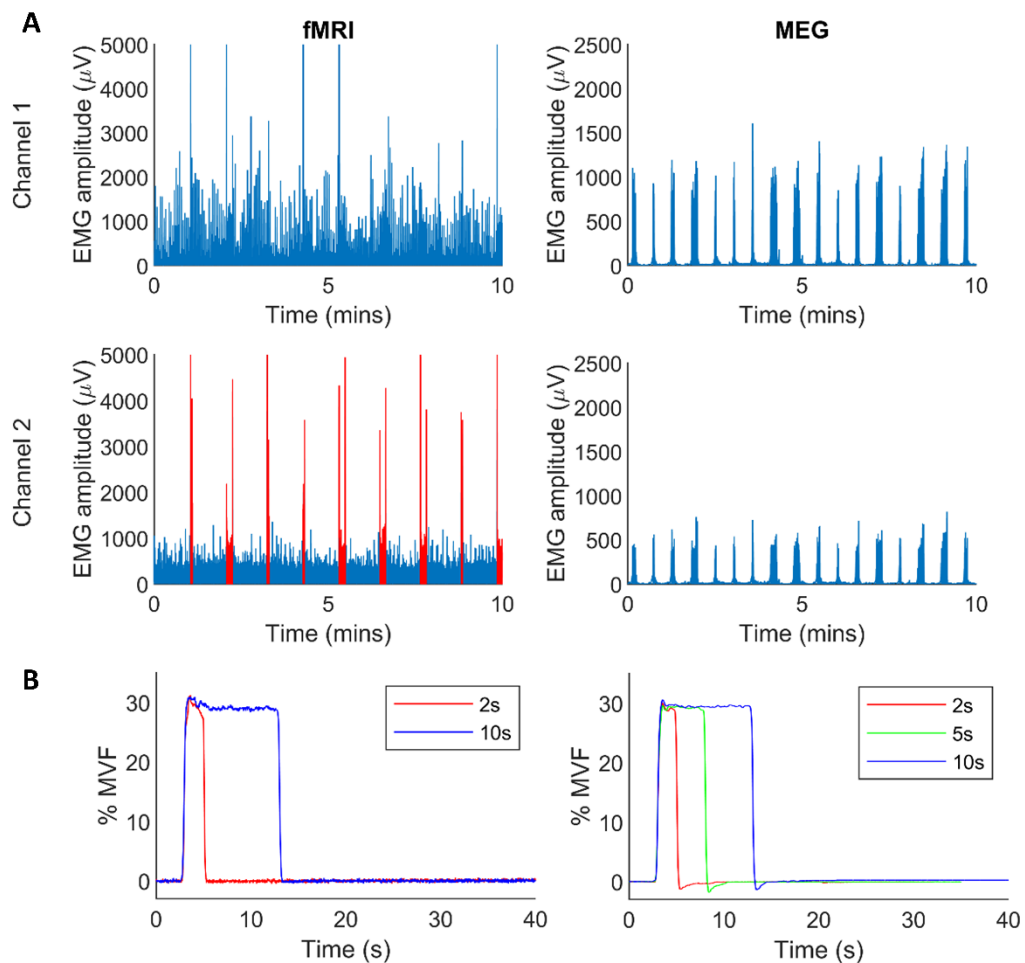


Figure 6.16. Comparison of fMRI and MEG EMG and grip-force measures for the same subject who completed both fMRI and MEG experiments. (A) EMG time courses for run 1 of the fMRI (left) and MEG (right) experiments in channel 1 (top) and channel 2 (bottom), note the difference in timings in the two experiments: baseline between contractions was 60 s for the fMRI and 30 s for the MEG experiment. As channel 2 in this case contained much less noise than channel 1, channel 2 was used for determining movements which are displayed in red. (B) Time courses of fMRI-grip-force (left) and MEG-grip-force (right) averaged over the different contraction durations (red – 2 s; green – 5 s; blue – 10 s).

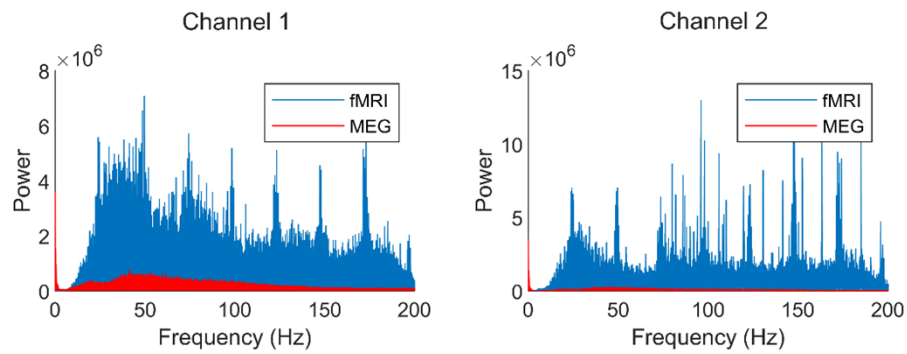


Figure 6.17. Fourier transforms of fMRI-EMG (blue) and MEG-EMG (red) experiments, for channel 1 (left) and channel 2 (right) for the same subject in Figure 6.16.

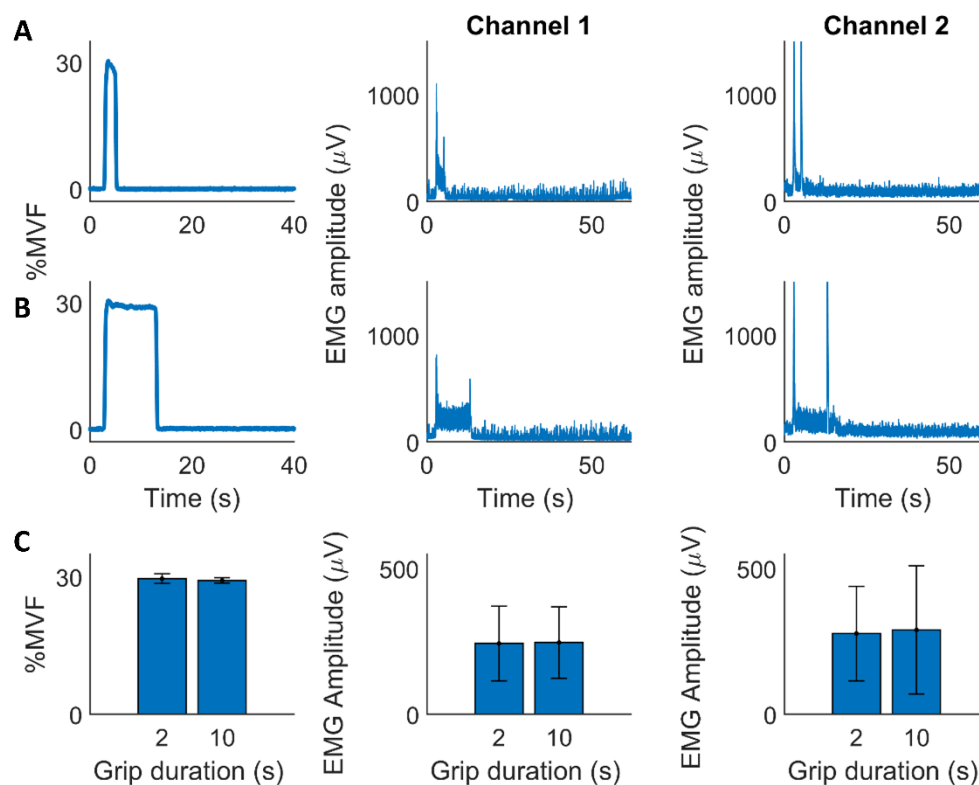


Figure 6.18 Comparing average grip and EMG for 2 and 10 s grip contraction. Rows A and B are for 1 subject: Row A shows average grip and EMG response to 2 s contraction, and row B shows average grip and EMG responses to 10 s contraction. Row C is the subject average, showing the average grip and EMG for 2 s and 10 s contraction, with error bars showing the standard deviation over subjects.

6.5.2 fMRI Responses

The motor task produced BOLD, aCBV and VASO responses in the contralateral motor area for all subjects, as shown in Figure 6.19. As expected, the BOLD response was stronger than VASO and aCBV due to the higher CNR of the sequence and the increased sampling rate (two BOLD images acquired for each VASO and aCBV

image). Figure 6.20 shows activation maps derived using a boxcar GLM across all 12 slices for Subject 2, illustrating that the task activation in the sensorimotor cortex was not limited to one slice. The average time course from the peaks of activation within the precentral gyrus was computed over all subjects for each contrast (Figure 6.28). Appendix A provides these data for all participants showing that all data acquired were of good quality with clear responses.

In all subjects, common active voxels were detected in BOLD, aCBV and VASO images with this ‘conjunction activation’ map shown for one slice in each subject in Figure 6.19 (right column), and in Figure 6.20 (bottom row) for all slices in a single subject. The peak t-stat of the BOLD was then found within this common activation and an ROI was created centred on this BOLD peak (Section 6.4.3.4). Time courses of BOLD, VASO and aCBV signals obtained from this Large ROI were averaged over trials for each condition and are shown in Figure 6.21 with an example of the Large ROI for one subject.

Vein and CSF masks were created for each subject as shown in Figure 6.13 and Figure 6.14. The peak BOLD t-stat was found within the conjunction activation, excluding CSF and veins from which a Small ROI was created which excluded veins and CSF. This resulted in an average (\pm standard deviation) of 5 ± 4 voxels (range 1 – 11 voxels) in the Small ROI over all subjects. An example of the Small ROI is shown in Figure 6.22A and corresponding subject average time courses are shown in Figure 6.22B. It was decided to use the Small ROI in further analysis, since this ROI better represents tissue responses which are more likely driven by a neuronal origin. Appendix A shows the time courses for each individual subject for the small ROI (Figure 6.29).

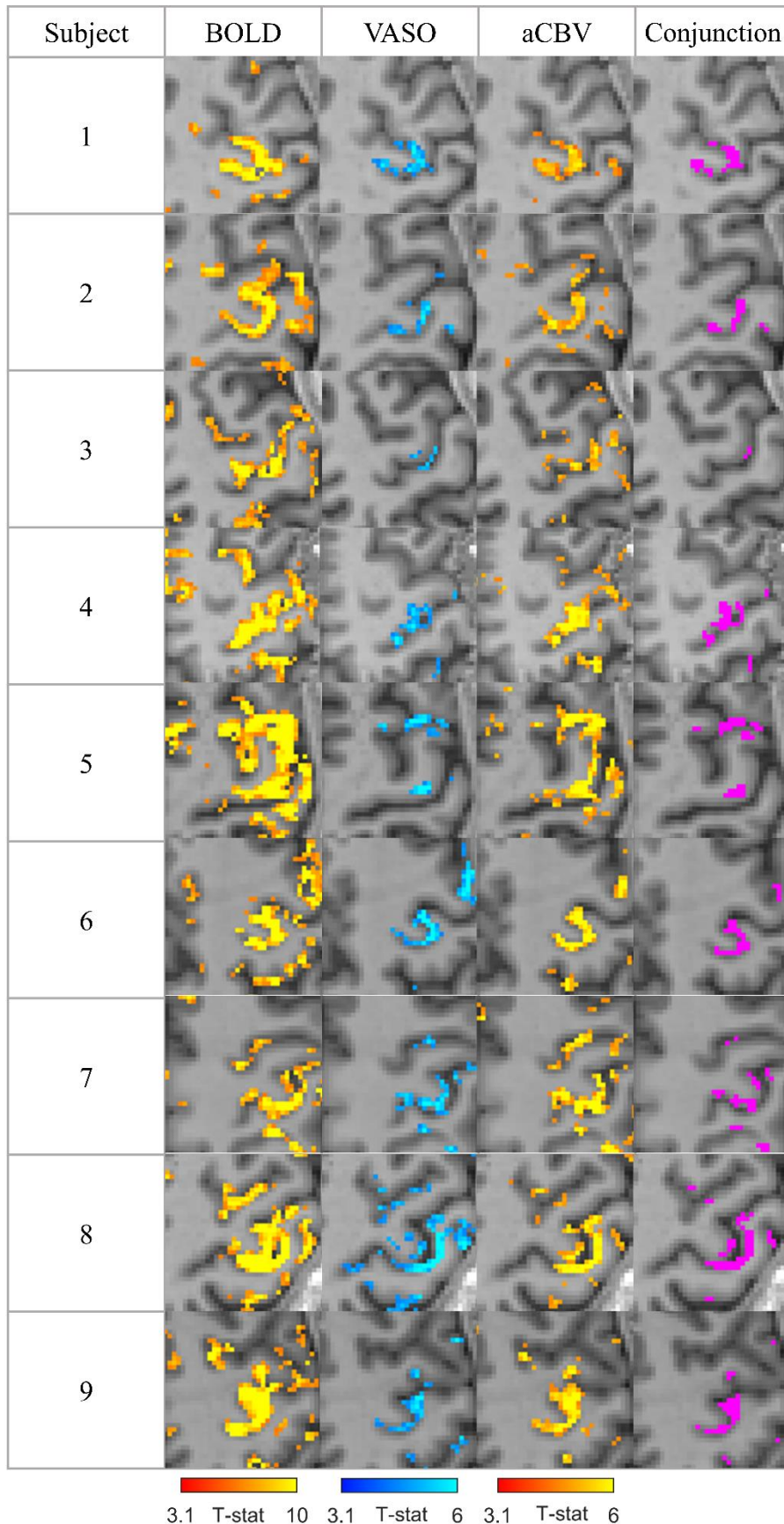


Figure 6.19. Individual subject activation maps for BOLD, VASO and aCBV responses and the conjunction of all three response maps. BOLD threshold at $p = 0.05$ FWE corrected, 5 voxel extent; VASO and aCBV threshold at $p = 0.001$ uncorrected, 5 voxel extent.

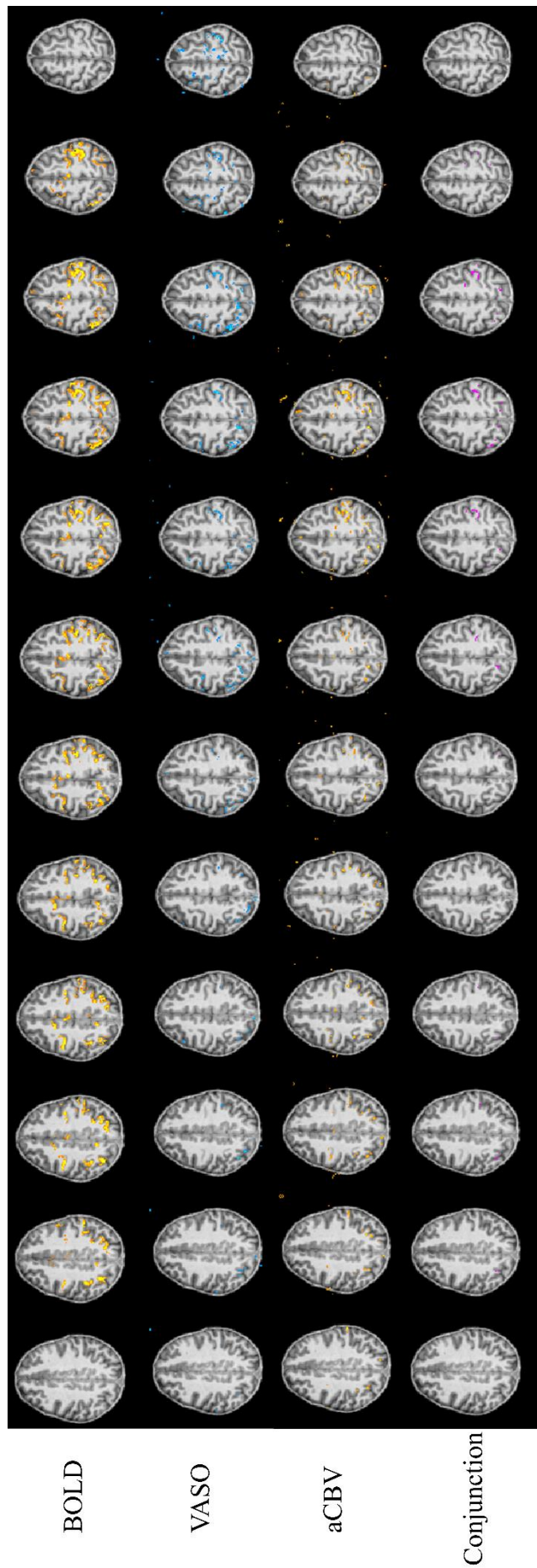


Figure 6.20. Activation maps over all slices for one subject (Subject 2) in radiological view. Showing, from top row to bottom row, BOLD (top), VASO, aCBV responses, and the conjunction of active voxels from BOLD, VASO and aCBV responses (bottom), respectively.

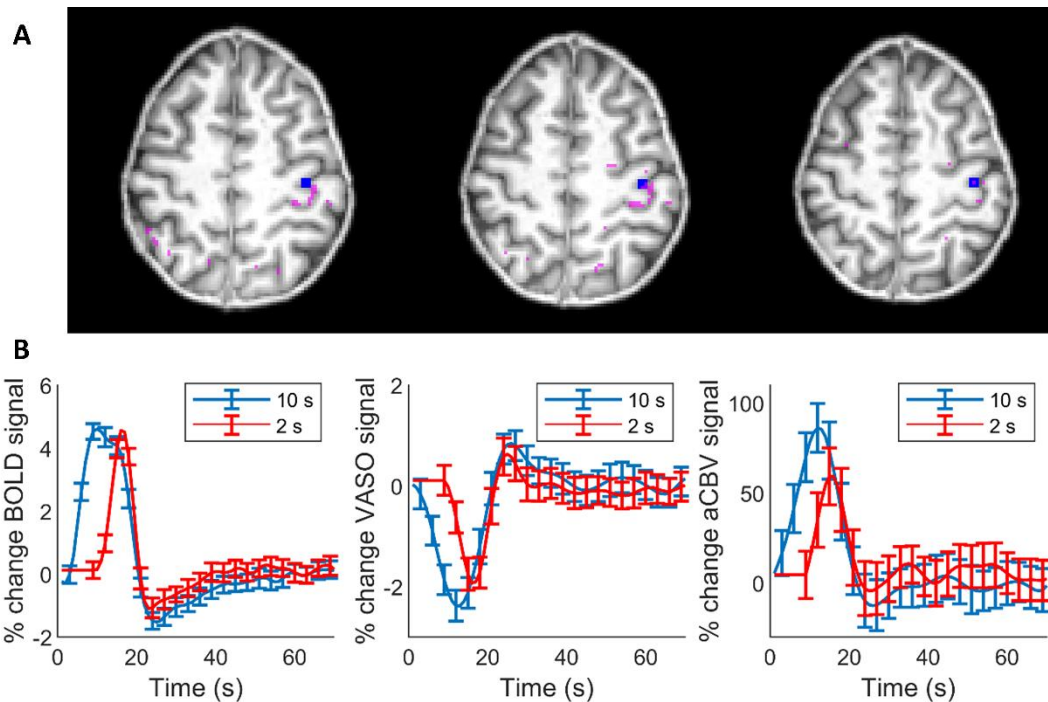


Figure 6.21. (A) Example of Large ROI (blue cube) used for one subject (Subject 2) determined from the peak BOLD response within the conjunction activation (overlaid in pink), constrained to precentral gyrus (radiological view). (B) Time courses from subject specific Large ROIs, for BOLD, VASO and aCBV signals averaged over subjects for 2 s and 10 s contraction durations. Error bars show the standard error over subjects. Note, initial 8 s of the 2s contraction time courses are padded to align response with stimulus offset of 10 s contraction time.

Results from the Small ROI BOLD time course showed a clear positive BOLD primary response, with a percentage signal change of 4.7 ± 0.5 % for both the 2 and 10 s task durations (Figure 6.23Ai). The primary BOLD response took, on average from contraction onset, 6.8 ± 0.4 s to peak for the 2 s contraction and 9 ± 3 s to peak for the 10 s contraction. There was no significant difference (paired t-test, $p = 0.78$) in the amplitude of the peak of the primary response for the 2 and 10 s contraction duration of the BOLD over all subjects, in contrast to the prediction from the boxcar GLM (Figure 6.15, bottom row). As can be seen in Figure 6.22B, the BOLD post-stimulus undershoot lasted around 20 s from when the BOLD signal passed zero following the primary response before returning to baseline, reaching -1.1 ± 0.3 % for the 2 s contraction and -1.7 ± 0.3 % for the 10 s contraction (Figure 6.23Bi). The post-stimulus undershoot was significantly different between the two task durations (paired t-test, $p = 0.01$) with the 10 s duration producing a larger (more negative) undershoot, in agreement with the model from the boxcar GLM (Figure 6.15, bottom row).

The VASO response showed, as expected, a primary negative percentage signal change (implying a positive CBV change) of -2.5 ± 0.3 % for the 2 s contraction duration and

$-3.0 \pm 0.3 \%$ for the 10 s contraction duration (Figure 6.23Aii), followed by a small positive post-stimulus response (Figure 6.22 and Figure 6.23Bii). There was no significant difference ($p = 0.13$) between the VASO primary amplitude response 2 and 10 s contraction duration. The PSR amplitude was significantly different from zero over all contraction durations ($p = 0.002$), but there was no significant difference in post-stimulus response amplitude between the 2 and 10 s contraction durations ($p = 0.09$). The aCBV response showed a large positive primary response, with a $114 \pm 23 \%$ signal change for the 2 s contraction duration and $160 \pm 45 \%$ signal change for the 10 s contraction duration, which were significantly different ($p = 0.008$), Figure 6.23Aiii. The post-stimulus response amplitudes were not significantly different from zero (Figure 6.23Biii).

These time courses for the BOLD responses reveal clear discrepancies in the primary response to those predicted by the boxcar model. Therefore, the modulation of the post-stimulus response seen here may be driven by boxcar model. The next section provides results modelled based on the known electrophysiology MEG response, to assess whether other brain regions are revealed which exhibit PSR modulation which matches the neuronal modulation measured in Chapter 4.

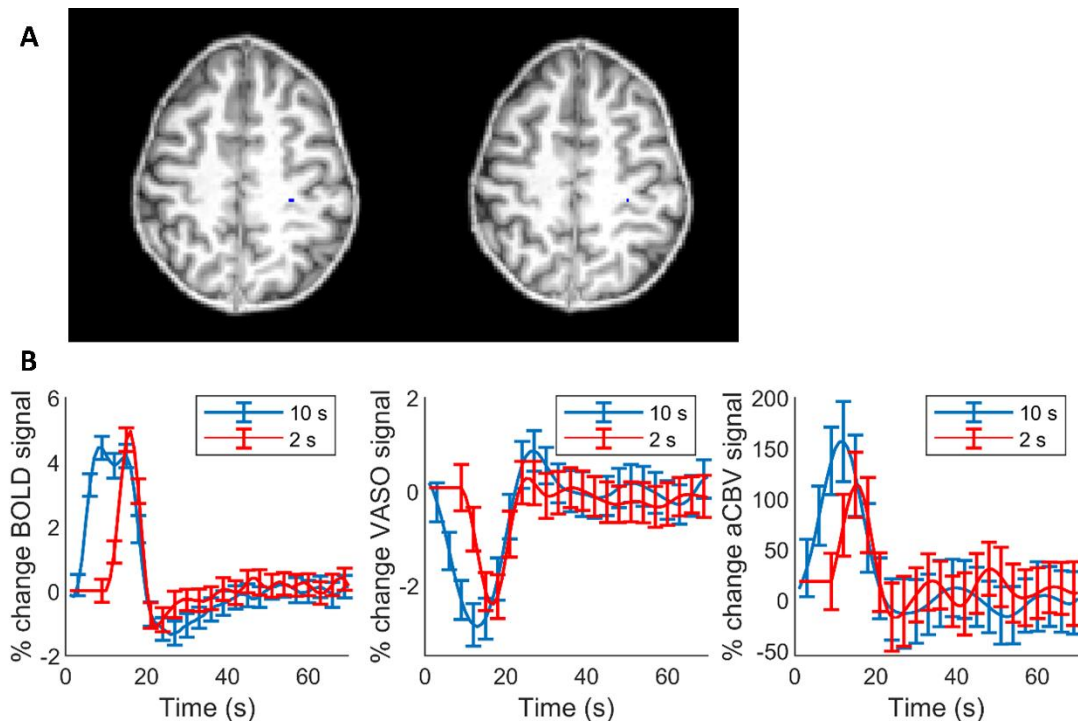


Figure 6.22. (A) Example Small ROI (blue) from one subject (Subject 2), created from location of peak BOLD t -stat in conjunction activation with CSF and veins excluded and constrained to the left precentral gyrus (radiological view) (B) Subject average time course for BOLD, VASO and aCBV signals from the Small ROI.

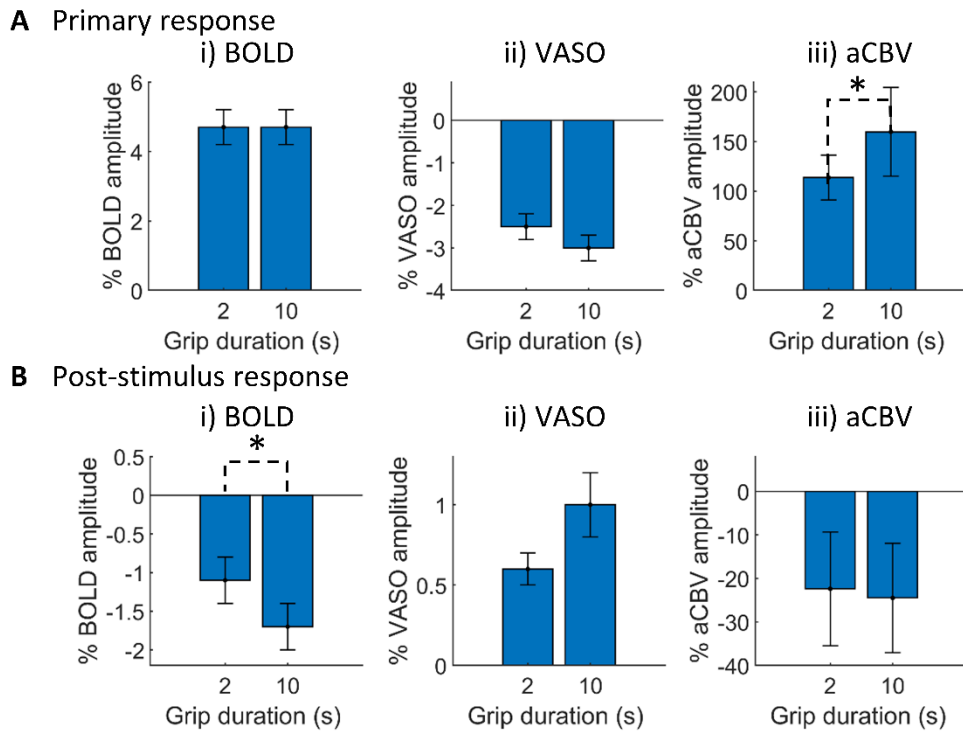


Figure 6.23. Summary of results from time courses of (left to right) BOLD, VASO and aCBV responses from the Small ROI. Top panel (A) shows results of the amplitude of the primary response, bottom panel (B) shows results the post-stimulus response compared for the 2 and 10 s grip duration. * indicates a significant difference ($p < 0.05$, paired t-test) between task duration. Note that the aCBV post-stimulus responses were not a significant effect.

6.5.3 Using MEG Regressors in the GLM

The orthogonality between the three regressors (cosine of angle) in the design matrix was: PMBR and MRBD = -0.19, PMBR and gamma = -0.04, MRBD and gamma = 0.59, highlighting that the MRBD and gamma regressor are not orthogonal, which means that the regressors are correlated and the results may be unreliable. Hence, another GLM was performed with only the two MRBD and PMBR regressors. Positive contrasts of the PMBR regressor gave the same peak t-stat voxel location for both the 2-regressor (MRBD and PMBR) and 3-regressor GLM (MRBD, PMBR, and gamma). Resultant t-stat maps from each of the MEG regressors for the BOLD data are shown in Figure 6.24 using the 3-regressor model, as well as the combined positive contrast to all 3 regressors. The PMBR regressor produced a small localised area of activation in the left motor cortex in all subjects. The MRBD regressor showed less activation than the PMBR regressor. For some subjects the gamma regressor showed less active regions and smaller t-stat values than the PMBR regressor, for others gamma produced a stronger response. There was no clear change in spatial location of the peak t-stats between the three regressors. Surprisingly, the VASO (Figure 6.25) and aCBV (Figure

6.26) contrasts show very little activation to any of these MEG regressors, or the combination of all three.

As there was little activation for VASO and aCBV, only the BOLD data were analysed further. Time courses were taken from an ROI at the location of the peak BOLD t-stat of the positive contrasts of the PMBR regressor, and the positive contrast of all three regressors for each subject, with veins and CSF excluded. Table 6.2 shows the peak voxel location of the PMBR regressor compared to all regressors. Figure 6.27 shows time courses from this ROI averaged over all subjects. No significant differences were observed in the maximum percentage change in BOLD signal during the primary response, and the minimum percentage change in BOLD signal during the post-stimulus undershoot, between any of the regressors.

In addition, the primary response amplitude for the 2 s and 10 s contraction duration did not significantly differ for any of the time courses shown in Figure 6.27. However, the PSR still showed a significantly larger ($p = 0.008$) amplitude for the 10 s contraction duration than the 2s even when the PMBR regressor was used for the ROI definition. With this ROI, the PSR amplitude was $-1.2 \pm 0.5\%$ for the 2 s contraction duration, whereas the 10 s contraction duration had an amplitude of $-1.7 \pm 0.6\%$.

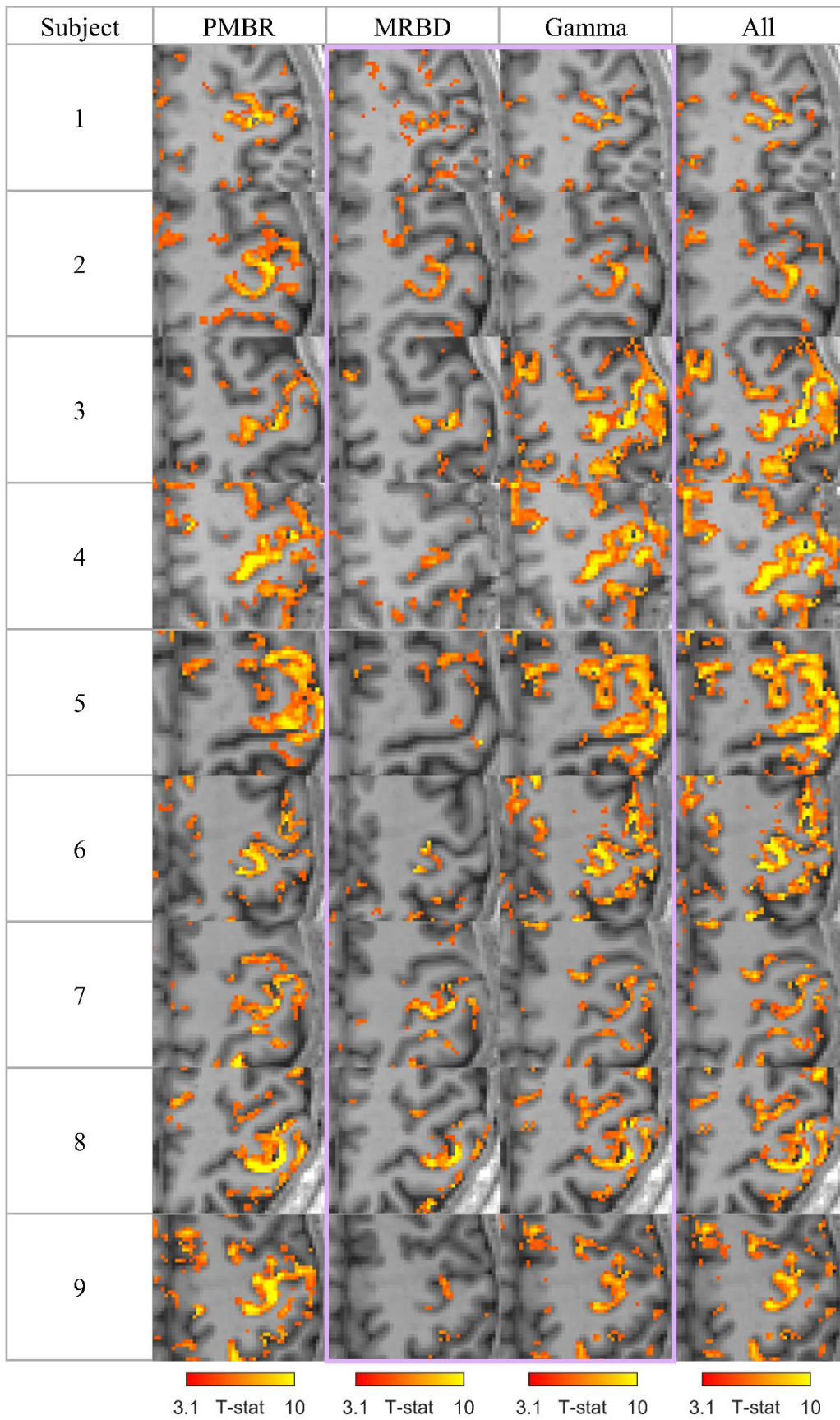


Figure 6.24. BOLD activation (t -statistic) maps with threshold at $p = 0.001$ uncorrected 5 voxel extent for MRBD regressor, PMBR regressor, Gamma regressor and all contrasts. Box highlights regressors that were not orthogonal in the 3-regressor GLM.

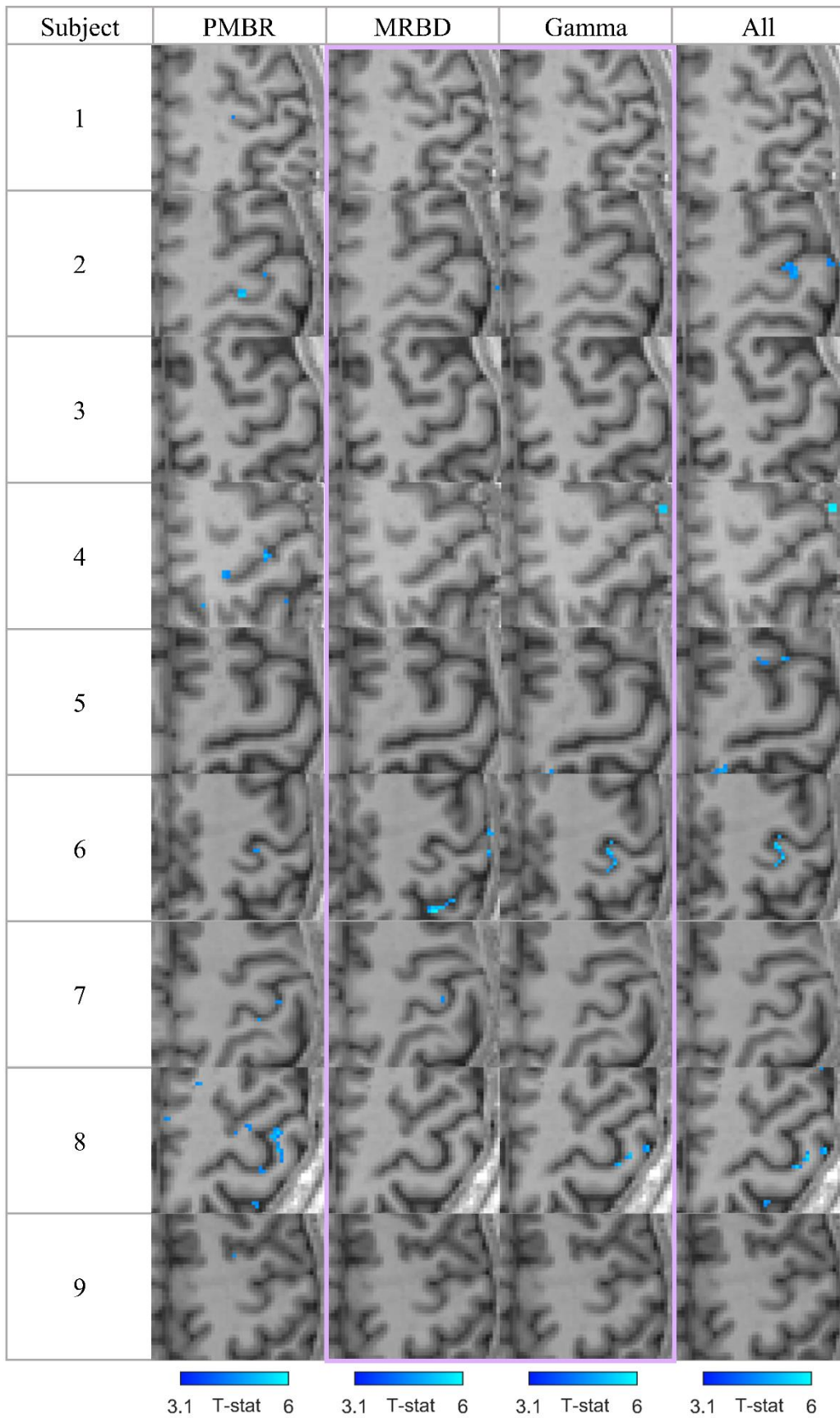


Figure 6.25. Activation maps (t -statistic) for VASO data of MRBD regressor, PMBR regressor, Gamma regressor and all contrasts, threshold at $p = 0.001$ uncorrected 5 voxel extent. Box highlights regressors that were not orthogonal in the 3-regressor GLM.

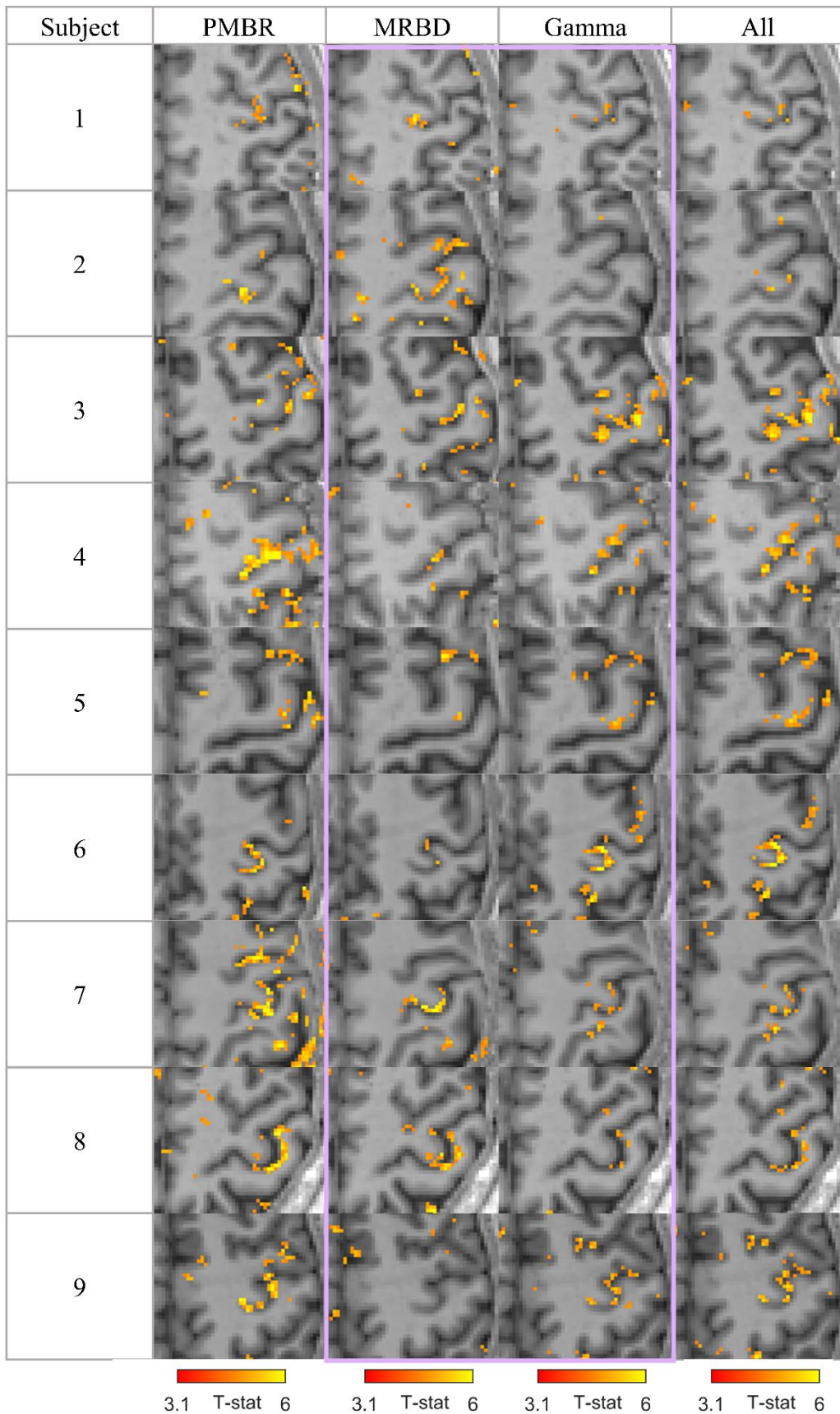


Figure 6.26. Activation maps (*t*-statistic) for aCBV data of MRBD regressor, PMBR regressor, Gamma regressor and all contrasts, threshold at $p = 0.001$ uncorrected 5 voxel extent. Box highlights regressors that were not orthogonal in the 3-regressor GLM.

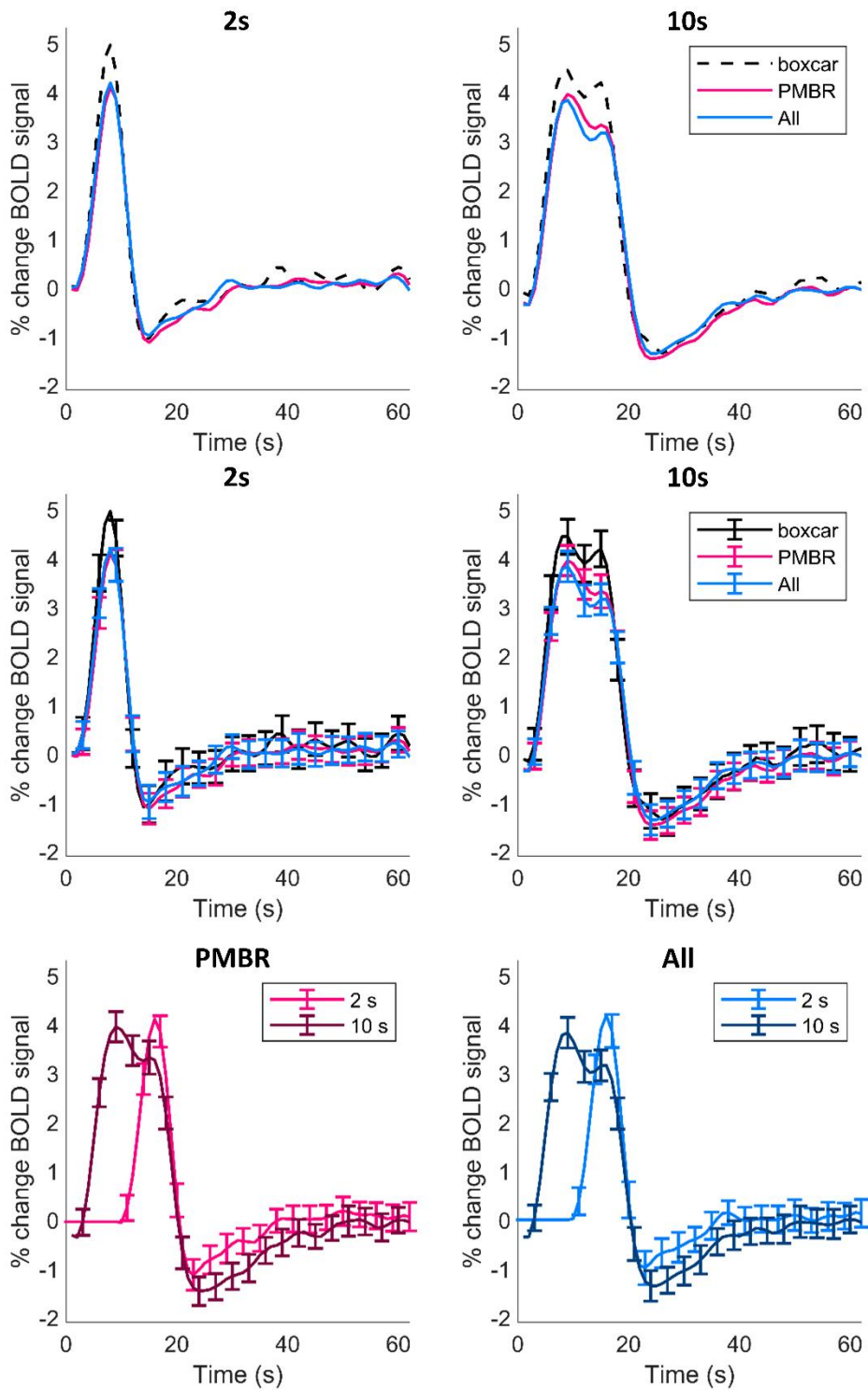


Figure 6.27. Subject average time courses of BOLD data from peak t -stat location of PMBR regressor (pink), and all regressors (blue) compared to boxcar regressor (black, from Figure 6.22) for 2 s contraction duration and 10 s contraction duration. Shown without (top row) and with (middle row) error bars for ease of comparison. Bottom row: 2 and 10 s contraction response for PMBR regressor and all regressor shown individually. Error bars show standard error across subjects.

Subject	PMBR			All		
	X	Y	Z	X	Y	Z
1	83	58	9	77	57	5
2	76	48	8	80	53	10
3	79	50	10	79	50	10
4	78	46	4	78	46	4
5	74	47	5	75	47	4
6	89	54	2	88	53	2
7	83	43	7	74	52	4
8	88	35	3	88	35	3
9	85	54	5	85	54	5

Table 6.2. Peak voxel locations in MNI space of the PMBR regressor and all regressors compared for each subject. These locations were used to produce the time courses in Figure 6.27.

6.5.4 CMRO₂

CMRO₂ was estimated during the primary and post-stimulus response period for each subject. Based on the results of simulations in Appendix B, CMRO₂ was calculated using the upscaled VASO data for the 2 s stimulus for the primary response. Since the PSR is assumed to have a long duration, the VASO response amplitude was not upscaled in the post-stimulus phase for these calculations.

Table 6.3 shows the results of the CMRO₂ calculation for a value of $M = 11$ (Guidi et al., 2016), results for other values of M values (18 and 25) are given in Appendix C. The BOLD and VASO data used in the calculation are also provided. As expected, the results for the 2 and 10 s primary response show a significant increase in CMRO₂ above zero during the primary phase, but no significant difference ($p = 0.19$, paired samples t-test) between the 2 and 10 s grip duration. However, the change in CMRO₂ from baseline during the PSR were not found to differ significantly from baseline.

	% CMRO ₂ for each subject									Average ± SE
	1	2	3	4	5	6	7	8	9	
2 s primary response	57	32	37	17	46	36	57	5	-10	31 ± 7*
10 s primary response	45	35	24	4	35	20	79	10	-31	25 ± 10*
2 s post-stimulus response	3	-1	-7	-8	41	29	64	-20	-17	9 ± 9
10 s post-stimulus response	-4	-22	-36	-36	18	18	41	-56	17	-7 ± 10
BOLD amplitude (% change)										
2 s primary response	4.4	3.8	4.0	6.8	3.2	4.3	3.1	4.9	8.0	4.7 ± 0.5
10 s primary response	4.6	3.7	3.5	7.3	3.0	4.7	3.6	4.7	6.9	4.7 ± 0.5
2 s post-stimulus response	-0.9	-1.4	-0.4	-2.4	-0.7	-1.1	-0.6	-0.7	-2.4	-1.2 ± 0.2
10 s post-stimulus response	-1.6	-1.1	-1.5	-3.1	-0.9	-2.0	-0.7	-1.5	-2.7	-1.7 ± 0.3
VASO amplitude (% change)										
2 s primary response	-3.2	-2.2	-2.4	-3.8	-2.3	-2.6	-2.5	-2.0	-4.2	-2.8 ± 0.2
10 s primary response	-3.0	-2.2	-1.8	-3.9	-1.9	-2.3	-3.3	-2.0	-1.8	-2.5 ± 0.2
2 s post-stimulus response	0.1	0.3	0.3	0.7	-0.8	-0.4	-1.3	0.7	0.9	0.1 ± 0.2
10 s post-stimulus response	0.4	0.8	1.3	1.5	-0.2	0.0	-0.8	2.0	0.2	0.6 ± 0.3

Table 6.3. Results of CMRO₂ calculation. The CMRO₂ percentage during primary response showed a significant change from baseline levels (*, $p < 0.05$, paired Student's t -test), the results of the PSR did not differ significantly from baseline levels. The VASO data used in the 2 s primary response calculation were multiplied by 1.25 to account for errors due to low sampling rate. BOLD and VASO data used in the calculation are provided.

6.6 Discussion

Using 7 T fMRI, with a VASO-ASL-BOLD sequence, fMRI responses to a controlled grip-force task were investigated for two stimulus durations. No difference in the peak amplitude of the primary BOLD response was observed between the 2 s and 10 s task durations, but there was a difference in amplitude of the post-stimulus undershoot, with reduced amplitude for the 2 s contraction compared to the 10 s contraction. This is in contrast to the results found in Chapter 4, of the MEG response to the same stimulus, where a larger post-stimulus response was seen in the beta band for the shorter 2 s stimulus.

Non-BOLD fMRI responses were also investigated. Both VASO (total CBV) and aCBV (arterial CBV, primary driver of CBF responses) showed an apparent difference in amplitude of the 2 and 10 s contraction primary response. However, this can be explained as an artefact of the low time resolution of the sequences, short stimulus duration and analysis pipeline. Unexpectedly, the VASO time courses for both stimulus durations showed a small, significant, positive post-stimulus response suggesting total CBV reduces below baseline during the PSR for shorter duration stimuli investigated here than previously investigated stimulus durations (Beckett et al., 2019; Huber et al., 2018; Lu & van Zijl, 2005). Interestingly, no significant post-stimulus effect for aCBV was observed. Calculations of $CMRO_2$ were performed which showed a significant increase in $CMRO_2$ during the primary response, with no difference between the 2 and 10 s task duration but no measurable change in $CMRO_2$ during the PSR relative to baseline.

Finally, the effects of using MEG responses to model fMRI data were explored. Little difference was seen in activation profiles or response time courses from ROIs between the different models for BOLD. The different MEG regressors used produced limited activation for VASO and aCBV data, yet, the BOLD data were modelled well by the MEG regressors.

Effect of Stimulus Duration on Primary Response

In this chapter it was shown that the duration of the contraction did not change the amplitude of the fMRI primary response. This is contrary to previous literature which suggests that shorter duration stimuli should give smaller amplitude primary BOLD responses than long duration stimuli (Glover, 1999; Miller et al., 2001; Soltysik et al.,

2004). This discrepancy in the findings here compared with previous work could be due to differences in the types of movement used. Most previous studies using a finger tap, which could give different responses to a grip contraction. A finger tap is also harder to control for force and rate of movement, which could affect the BOLD response if force and speed of the movement for different stimulus durations are not controlled, then it is possible that the amplitude of the haemodynamic response would modulate based on change of force, rather than change of stimulus duration. The performance data recorded during this task (Figure 6.18 and Figure 6.19) suggest that the task was performed well, and that the 2 and 10 s grip contraction were performed equivalently. Finger tapping and flashing checkerboards which are often used as stimuli are also quite passive, whereas the task employed in this study involves visual feedback and requires the subject to pay attention. Another possibility for the difference observed is that previous studies have generally been performed at lower field strengths. 7 T, as was used in this chapter, has higher spatial resolution and also higher extravascular contribution to the signal from the capillary bed, which is much more closely related to neuronal activity (Duong et al., 2003; Yacoub et al., 2001), therefore 7 T is perhaps more sensitive to the true neuronal BOLD response. Finally, many of the previous studies did not leave a long enough inter-stimulus intervals for the haemodynamic response to return to baseline which could obscure differences in the BOLD response if baseline is not characterised correctly. If the inter-stimulus interval is not long enough, the period used as baseline may still be during the PSU, and therefore when the primary response is compared to the PSU the primary response will appear larger. This could cause a longer duration stimulus to appear larger in amplitude if the PSU is also longer and/or has a larger amplitude than short stimulus durations. This is a similar argument to that made about the observations of the MRBD in the literature compared with the findings in Chapter 4.

Comparing the haemodynamic responses to the electrophysiological responses measured by the MEG (Chapter 4), it should be noted that the movement related beta decrease (MRBD) in MEG signal also reached the same amplitude for the different task durations during the stimulus. This could imply the fMRI responses observed in this chapter are directly linked to neuronal activity, perhaps generated by a combination of the beta and gamma band responses during stimulation. In addition, the MEG and BOLD responses appeared in similar locations between the two modalities.

The primary BOLD response showed clear transients during the 10 s stimulus, with a biphasic peak to the response. These transients have previously been reported in BOLD responses (Duff et al., 2007; Fox et al., 2005; Harms & Melcher, 2003). The work in this thesis allows direct comparison of the BOLD responses to MEG responses in Chapter 4. By comparing these responses, it can be seen that the BOLD transients are similar to the gamma band activity which was observed in the MEG response at contraction onset and offset, but not during the sustained contraction period (Figure 4.8). This complements previous work suggesting the primary positive BOLD response is most strongly coupled to the gamma band response (Goense & Logothetis, 2008; Koch et al., 2009; Logothetis et al., 2001). An alternative explanation for the observed transients could be that there is an increase in grip force at the start and end of the contraction causing the observed response profile. Whilst there was often an overshoot in %MVF at the start of the contraction, it can be seen in Figure 6.16 and Figure 6.18 that the %MVF is largely flat throughout the contraction, and no overshoot was observed in grip-force data or EMG amplitude at the end of the contraction, so this is unlikely to be the explanation for the BOLD transients observed.

In this study, responses to a very short stimulus were investigated, compared to the stimuli which are often used in fMRI, especially in the field of VASO-fMRI. Short stimuli are more realistic to real-life situations and cognitive processing, therefore establishing a method to collect data and understand the BOLD response to basic short stimuli will help interpret more complex cognitive processes. However, investigating short stimulus responses with non-BOLD fMRI measures such as VASO is challenging due to the sampling rate of the sequences. The results presented here showed the primary VASO and aCBV response to the 2 s may be smaller than to the 10 s contraction duration (Figure 6.21 and Figure 6.22), which would be supported by previous literature that shorter stimuli give smaller primary responses. However, further analysis showed this to be an artefact of the analysis pipeline and the VASO and aCBV primary responses to these short stimuli track that of the BOLD response (Figure 6.32). This artefact occurred despite best efforts to maximise temporal resolution through jittering the stimuli relative to data acquisition in the study design.

Effect of Stimulus Duration on the Post-stimulus Response

In contrast to the primary response, the BOLD PSU was found to be significantly smaller for the 2 s contraction than the 10 s contraction. This was accompanied by an apparent reduction in total CBV (increase in VASO signal) for both stimulus durations, with no significant difference between the two task durations (Figure 6.23). In both the total and arterial CBV measures there was no clear evidence of CBV remaining elevated post-stimulation, contrary to that proposed by the balloon model (Buxton et al., 1998). Furthermore, the $CMRO_2$ calculations (Table 6.3) showed no evidence of $CMRO_2$ remaining elevated during the during the post-stimulus phase, inconsistent with the elevated $CMRO_2$ theory (Lu et al., 2004b). However it is important to note that the $CMRO_2$ results in this chapter were quite unreliable and further work is needed before conclusions about $CMRO_2$ can be drawn. What does stand out is that the VASO and aCBV response showed different responses. aCBV is thought to be the primary driver of CBF responses, therefore the lack of an aCBV undershoot could also imply no undershoot in CBF, which is inconsistent with the decrease in CBF theory (Chen & Pike, 2009b; Sadaghiani et al., 2009). Rather, a PSU in total CBV but not aCBV suggests the PSU is driven by reduction in vCBV. This would suggest that there is a constriction of veins following the primary response. This is supported by recent work which showed a reduction in deoxygenated CBV during the post-stimulus period (Liu et al., 2019). However, if there is a reduction only in vCBV then a BOLD overshoot would be expected (i.e. the opposite of the balloon model) which is clearly not observed. The possible ways to produce a decrease in BOLD signal, given a reduction in vCBV, would require an increase in $CMRO_2$ or a reduction in CBF. No post-stimulus change was observed in $CMRO_2$ in this study, yet this is likely due to the uncertainties in the method, as calibration constants were estimated. CBF could not be measured due to insufficient SNR and instability of the scanner. In addition, the SNR of the VASO sequence is inherently relatively low which is likely to result in inaccuracies in estimating $CMRO_2$ from the VASO signal on an individual subject basis. Therefore it is not possible in this study to fully elucidate the origin of the PSR.

However, the fact that primary response amplitude remained the same, yet the PSU was modulated by stimulus duration, suggests that the post-stimulus response is in some way independent of the primary response, supporting what was found in Chapter 4 for the MRBD and PMBR. Likewise, the PMBR has been shown to be reduced in people

with schizophrenia, which has also been observed in the post-stimulus undershoot (Hanlon et al., 2016). The PSU is also reduced in people with autism, which suggests the PSU is related to neural inhibition (Murray et al., 2020). Indeed, for such a short stimulus, the post-stimulus undershoot observed in these data was larger than expected if the response was purely haemodynamic (Figure 6.15, bottom row).

A direct comparison of the haemodynamic results to the electrophysiological MEG results in Chapter 4 does not show a clear coupling as was hypothesized from previous work (Mullinger et al., 2017; Mullinger et al., 2013b). The PMBR measured in Chapter 4 was largest for the 2 s contraction duration whereas the PSU is larger for the 10 s contraction duration. This finding may have been driven by the fact that a larger undershoot for the 10 s stimulus than the 2 s stimulus was built into the basic boxcar model (Figure 6.15). To account for this, regressors from the MEG data were used to further interrogate these responses, where the PMBR was used to locate any BOLD regions where modulation matched that seen in the MEG data. Still, this did not reveal an area of the brain where the 2 s stimulus produced a larger post-stimulus undershoot than the 10 s stimulus (Figure 6.27). The PMBR regressor did show a larger post-stimulus undershoot to both contraction durations, however not statistically different to the standard boxcar model. It was not possible to fully interrogate the three MEG regressors in the model independently since the MRBD and gamma response were not orthogonal. However, the PMBR regressor was orthogonal to the other regressors in the model, and when compared to a model with only 2 regressors (PMBR and MRBD response only), the peak location of the activation to the PMBR regressor did not change. Whilst the regions investigated did not reveal a larger PSU for the 2 s stimulus than 10 s stimulus, it is conceivable that this was not found due to the model used. One interesting area to explore would be to assess model independence. In future investigations, it would be interesting to generate a time course over all voxels and identify any voxels which have a larger PSU for 2 s compared to 10 s.

A possible explanation for the difference between this study and previous work (Mullinger et al., 2017; Mullinger et al., 2013b) is the type of stimulus used. The previous works used entirely passive stimuli and were looking primarily at natural trial by trial variations compared with stimulus driven variations investigated here. Here, the trial averaged PMBR was used as input as the regressor, rather than trial-by-trial variations. Yet, in Chapter 5 it was shown that the PMBR is not a continuous increase

in oscillatory amplitude, but rather an increase in occurrence of transitory bursts of activity. To better model the beta response, the individual trial responses would need to be input as regressors, however this would only be possible with simultaneous EEG-fMRI, which would present a number of additional challenges at 7 T with the VASO-ASL-BOLD sequence employed in this study.

It is important to note that the MEG regressors did not produce significant activation for either the VASO or aCBV data. This is interesting as the data were modelled well by the boxcar regressor, which was similar to the MRBD regressor. This could be purely an SNR issue, or, alternatively, these results may suggest the PSU is not wholly driven by neuronal activity. Instead, the PSU could be a combination of both neuronal and vascular effects. In a study investigating functional connectivity, Bright et al. suggest that brain networks are formed from a coupling of two separate systems, one which is neuronal and the other vascular (Bright et al., 2020). The work of Bright et al. may provide evidence that the BOLD response is due to coupling of distinct neuronal and vascular systems. A recent study (Liu et al., 2019) suggested that slow changes in CBV only occur for long duration stimuli ($\sim >40$ s). This could suggest that there is an interplay between neuronal and haemodynamic effects, and haemodynamic effects take over at longer stimulus times. Understanding how these systems compete to form the post-stimulus responses in different stimulation scenarios will be key to unlocking the potential of the post-stimulus response for the study of neuronal function. The limitations of this study mean that this aim of understanding the competition between vascular and neuronal systems could not be fully elucidated from the results presented here. However, further work using similar MRI sequences and learning from the limitations of this study should be able to shed further light on the origins of the BOLD post-stimulus response.

Limitations

One of the biggest issues in the data presented here is the low sampling rate due to the long TR required for VASO and aCBV measures. In order to mitigate this low temporal resolution, a jitter was designed in the paradigm to give higher temporal resolution. However, since a motor task was employed, reaction times caused further issues as the movements did not occur exactly when cued. To overcome the variation in sampling times relative to contraction onset times, interpolation was used in the analysis pipeline

in order to segment the data into trials. The result of this interpolation was that for the long TR contrasts (aCBV and VASO), the primary response to the short duration stimulus was underestimated, resulting in a consistent drop in amplitude of 80% for the 2 s stimulus (Appendix B) with a TR of 6 s. As the results from Appendix B show, using a TR of 3 s gives 99% of the expected amplitude of a simulated time course, therefore this should be a sufficient sampling rate for a short stimulus. In future, it would of interest to assess only the VASO-BOLD sequence with 3 s TR rather than 6 s used in this chapter if the label and control used for ASL were removed from the sequence. Another option is to remove the jitter in stimuli which would help reduce the problem of uneven sampling, but would require carefully designing the experiment to plan where the images are acquired in relation to the stimulus onset. Alternatively, a passive somatosensory stimulus could be used in which the applied stimulus is always time-locked allowing jittering to be used, however, then electrophysiological responses to as somatosensory stimulus would also need to be characterised.

Another possible limiting factor is the spatial resolution and accuracy of masks used. Probability maps of precentral gyrus, CSF and veins were created at high resolution (0.7 mm isotropic and 0.5 x 0.5 x 1.5 mm for veins) in their native space. These were transformed into functional space with reduced their resolution (1.75 x 1.75 x 1.75 mm). Although attempts were made to remove signal from veins and CSF using strict thresholds, maps of veins and CSF may not have worked as well as intended, meaning the signal is still contaminated by veins or partial voluming effects. On the other hand, the masks used were very conservative so contamination is unlikely to be a significant effect. The strictness of the masks resulted in the small ROIs containing few voxels (5 ± 4) which will mean data may contain more noise than if a larger area was averaged over, but the signal is more specific to the tissue of interest.

VASO signals will be affected by the proportion of grey matter in a voxel as the proportionality between VASO signal and CBV breaks down when the voxel is less than 50% grey matter (Scouten & Constable, 2008). Although CSF was masked out, the fraction of CSF in the voxel may change throughout the experiment as vascular dilation and contraction takes place (Jin & Kim, 2010). This effect is of particular concern for VASO as the signal from blood is nulled but CSF signal still remains. Due to the T_1 of white matter and CSF, at the inversion time (TI) of blood nulling, there will be negative contributions from CSF and positive signal contributions from WM

(Donahue et al., 2006). However, Donahue et al. suggest that functional changes in CSF are generally less than 1% (Donahue et al., 2006). Coupled with the fact the VASO response did not change substantially with the inclusion of the CSF mask, this suggests that these results support that small proportions of CSF in the voxels selected for the ROIs used in this work were not a large confound.

The CMRO₂ calculation relies on a number of assumptions. One key assumption is the coupling of CBV and CBF via a power law relationship (Equation 5) (Grubb et al., 1974). Ideally, it would have been better to use CBF measures in conjunction with the CBV measures for this calculation as this would negate the assumed coupling necessary in the work presented here. With the low temporal resolution of the VASO time course used to estimate CMRO₂ in this work, the CMRO₂ calculation was unreliable for the 2 s contraction duration. The CMRO₂ results also show large variation across subjects, which could be improved by increasing the number of subjects and number of trials per subject. However, increasing the number of trials per subject presents new challenges due to the long off periods needed in this study. The scan session was over an hour in duration, and as such any increase in time in the scanner would increase the likelihood of movement, as well as participants becoming fatigued which may affect motor responses. One possible solution is that the experiment could be performed in two separate runs with a break in between. However this approach then introduces coregistration issues between the two runs, particularly problematic with the limited coverage used here, and the potential for habituation effects. It was not possible to scan more subjects at the time as there were issues with the 7 T scanner, which resulted in 4 months of downtime.

Another possibility would be to use aCBV, rather than VASO, to calculate CMRO₂, which would require additional modelling work and is a possibility for future studies. The increased SNR in aCBV measures compared with VASO measures may overcome the challenges in calculating CMRO₂ presented in the current study. However, assumed coupling between the aCBV and venous CBV which would be necessary might add further confounds to the interpretation of estimated CMRO₂ results and shows that such an expansion of modelling in this direction is non-trivial.

As discussed, there would have been considerable benefit to this work of measuring CBF as well as CBV, which the sequence should allow. Unfortunately the CBF data

collected in this experiment were poor due to the technical issues with the scanner at time of data collection reducing the tSNR, as discussed in the preliminary experiments (Section 6.3). It would be very interesting to investigate what happens to CBF during this experiment in a future study, which should be possible with the sequence developed and a stable scanner.

As well as CBF, future research should be undertaken to investigate the changes in arterial CBV compared to venous CBV. This would help confirm whether the VASO post-stimulus response observed was due to changes in vCBV. vCBV can be measured using hyperoxia to increase venous blood oxygenation, to measure absolute vCBV during rest (Bulte et al., 2007), or to measure the fractional change in vCBV during a task (Blockley et al., 2012). Such measures would be useful to combine with the measures already employed in this chapter to further understand the origins of the PSU.

Conclusion

The results in this chapter showed that the amplitude of the primary BOLD response did not vary with task duration for a grip contraction, but the BOLD post-stimulus undershoot had smaller amplitude for the shorter task duration. Non-BOLD fMRI showed a decrease in total CBV during the post-stimulus period, which coupled aCBV returning to baseline suggests the change is due to a decrease in vCBV post-stimulus. These results add weight to the idea that the balloon model is not the full description of the BOLD response. Combined with work of the previous chapters, this chapter allows direct comparison between fMRI and MEG. The post-stimulus undershoot was not found to modulate in the same way as the MEG response, which may suggest the post-stimulus undershoot is not entirely driven by neuronal activity but a combination of competing vascular and neuronal effects.

6.7 References

- Attwell, D., & Iadecola, C. (2002). The neural basis of functional brain imaging signals. *Trends in Neurosciences*, 25(12), 621-625.
- Bagshaw, A. P., Hawco, C., Bénar, C.-G., Kobayashi, E., Aghakhani, Y., Dubeau, F., Pike, G. B., & Gotman, J. (2005). Analysis of the EEG–fMRI response to prolonged bursts of interictal epileptiform activity. *Neuroimage*, 24(4), 1099-1112.
- Bandettini, P. A., Wong, E. C., Hinks, R. S., Tikofsky, R. S., & Hyde, J. S. (1992). Time course EPI of human brain function during task activation. *Magnetic Resonance in Medicine*, 25(2), 390-397.
- Barth, M., & Norris, D. G. (2007). Very high-resolution three-dimensional functional MRI of the human visual cortex with elimination of large venous vessels. *NMR in Biomedicine*, 20(5), 477-484.
- Beckett, A. J. S., Dadakova, T., Townsend, J., Huber, L., Park, S., & Feinberg, D. A. (2019). Comparison of BOLD and CBV using 3D EPI and 3D GRASE for cortical layer fMRI at 7T. *bioRxiv*, 778142.
- Besle, J., Sánchez-Panchuelo, R.-M., Bowtell, R., Francis, S., & Schluppeck, D. (2014). Event-related fMRI at 7T reveals overlapping cortical representations for adjacent fingertips in S1 of individual subjects. *Human Brain Mapping*, 35(5), 2027-2043.
- Birn, R. M., Saad, Z. S., & Bandettini, P. A. (2001). Spatial Heterogeneity of the Nonlinear Dynamics in the FMRI BOLD Response. *Neuroimage*, 14(4), 817-826.
- Blockley, N. P., Driver, I. D., Fisher, J. A., Francis, S. T., & Gowland, P. A. (2012). Measuring venous blood volume changes during activation using hyperoxia. *Neuroimage*, 59(4), 3266-3274.
- Bright, M. G., Whittaker, J. R., Driver, I. D., & Murphy, K. (2020). Vascular physiology drives functional brain networks. *Neuroimage*, 116907.
- Brookes, M. J., Morris, P. G., Gowland, P. A., & Francis, S. T. (2007). Noninvasive measurement of arterial cerebral blood volume using look-locker EPI and arterial spin labeling. *Magnetic Resonance in Medicine*, 58(1), 41-54.
- Bulte, D., Chiarelli, P., Wise, R., & Jezard, P. (2007). Measurement of cerebral blood volume in humans using hyperoxic MRI contrast. *Journal of Magnetic Resonance Imaging: An Official Journal of the International Society for Magnetic Resonance in Medicine*, 26(4), 894-899.
- Buxton, R. B. (2009). Introduction to Functional Magnetic Resonance Imaging: Principles and Techniques. *Cambridge University Press, Second Edition*.
- Buxton, R. B. (2012). Dynamic models of BOLD contrast. *Neuroimage*, 62(2), 953-961.
- Buxton, R. B., & Frank, L. R. (1997). A Model for the Coupling between Cerebral Blood Flow and Oxygen Metabolism during Neural Stimulation. *Journal of Cerebral Blood Flow & Metabolism*, 17(1), 64-72.
- Buxton, R. B., Wong, E. C., & Frank, L. R. (1998). Dynamics of blood flow and oxygenation changes during brain activation: The balloon model. *Magnetic Resonance in Medicine*, 39(6), 855-864.
- Chen, J. J., & Pike, G. B. (2009a). BOLD-specific cerebral blood volume and blood flow changes during neuronal activation in humans. *NMR in Biomedicine*, 22(10), 1054-1062.

- Chen, J. J., & Pike, G. B. (2009b). Origins of the BOLD post-stimulus undershoot. *Neuroimage*, *46*(3), 559-568.
- Davis, T. L., Kwong, K. K., Weisskoff, R. M., & Rosen, B. R. (1998). Calibrated functional MRI: Mapping the dynamics of oxidative metabolism. *Proceedings of the National Academy of Sciences*, *95*(4), 1834.
- Dechent, P., Schütze, G., Helms, G., Merboldt, K. D., & Frahm, J. (2010). Basal Cerebral Blood Volume during the Poststimulation Undershoot in BOLD MRI of the Human Brain. *Journal of Cerebral Blood Flow & Metabolism*, *31*(1), 82-89.
- Detre, J. A., Leigh, J. S., Williams, D. S., & Koretsky, A. P. (1992). Perfusion imaging. *Magnetic Resonance in Medicine*, *23*(1), 37-45.
- Donahue, M. J., Blicher, J. U., Østergaard, L., Feinberg, D. A., MacIntosh, B. J., Miller, K. L., Günther, M., & Jezzard, P. (2009). Cerebral blood flow, blood volume, and oxygen metabolism dynamics in human visual and motor cortex as measured by whole-brain multi-modal magnetic resonance imaging. *Journal of Cerebral Blood Flow & Metabolism*, *29*(11), 1856-1866.
- Donahue, M. J., Lu, H., Jones, C. K., Edden, R. A. E., Pekar, J. J., & van Zijl, P. C. M. (2006). Theoretical and experimental investigation of the VASO contrast mechanism. *Magnetic Resonance in Medicine*, *56*(6), 1261-1273.
- Duff, E., Xiong, J., Wang, B., Cunnington, R., Fox, P., & Egan, G. (2007). Complex spatio-temporal dynamics of fMRI BOLD: A study of motor learning. *Neuroimage*, *34*(1), 156-168.
- Duong, T. Q., Yacoub, E., Adriany, G., Hu, X., Ugurbil, K., & Kim, S.-G. (2003). Microvascular BOLD contribution at 4 and 7 T in the human brain: Gradient-echo and spin-echo fMRI with suppression of blood effects. *Magnetic Resonance in Medicine*, *49*(6), 1019-1027.
- Feng, C. M., Liu, H. L., Fox, P. T., & Gao, J. H. (2001). Comparison of the experimental BOLD signal change in event-related fMRI with the balloon model. *NMR in Biomedicine: An International Journal Devoted to the Development and Application of Magnetic Resonance In Vivo*, *14*(7-8), 397-401.
- Fox, M. D., Snyder, A. Z., Barch, D. M., Gusnard, D. A., & Raichle, M. E. (2005). Transient BOLD responses at block transitions. *Neuroimage*, *28*(4), 956-966.
- Frahm, J., Baudewig, J., Kallenberg, K., Kastrup, A., Merboldt, K. D., & Dechent, P. (2008). The post-stimulation undershoot in BOLD fMRI of human brain is not caused by elevated cerebral blood volume. *Neuroimage*, *40*(2), 473-481.
- Francis, S. T., Bowtell, R., & Gowland, P. A. (2008). Modeling and optimization of look-locker spin labeling for measuring perfusion and transit time changes in activation studies taking into account arterial blood volume. *Magnetic Resonance in Medicine*, *59*(2), 316-325.
- Friston, K. J., Mechelli, A., Turner, R., & Price, C. J. (2000). Nonlinear responses in fMRI: the Balloon model, Volterra kernels, and other hemodynamics. *Neuroimage*, *12*(4), 466-477.
- Gai, N. D., Talagala, S. L., & Butman, J. A. (2011). Whole-brain cerebral blood flow mapping using 3D echo planar imaging and pulsed arterial tagging. *Journal of Magnetic Resonance Imaging*, *33*(2), 287-295.
- Gardner, J. L., Merriam, E. P., Schluppeck, D., Besle, J., & Heeger, D. J. (2018). mrTools: analysis and visualization package for functional magnetic resonance imaging data. *Zenodo*, June, 28.

- Glover, G. H. (1999). Deconvolution of impulse response in event-related BOLD fMRI. *Neuroimage*, 9(4), 416-429.
- Goense, J. B. M., & Logothetis, N. K. (2008). Neurophysiology of the BOLD fMRI Signal in Awake Monkeys. *Current Biology*, 18(9), 631-640.
- Grubb, R. L., Raichle, M. E., Eichling, J. O., & Ter-Pogossian, M. M. (1974). The Effects of Changes in PaCO₂ Cerebral Blood Volume, Blood Flow, and Vascular Mean Transit Time. *Stroke*, 5(5), 630-639.
- Gu, H., Stein, E. A., & Yang, Y. (2005). Nonlinear responses of cerebral blood volume, blood flow and blood oxygenation signals during visual stimulation. *Magnetic Resonance Imaging*, 23(9), 921-928.
- Guidi, M., Huber, L., Lampe, L., Gauthier, C. J., & Möller, H. E. (2016). Lamina-dependent calibrated BOLD response in human primary motor cortex. *Neuroimage*, 141, 250-261.
- Hanlon, F. M., Shaff, N. A., Dodd, A. B., Ling, J. M., Bustillo, J. R., Abbott, C. C., Stromberg, S. F., Abrams, S., Lin, D. S., & Mayer, A. R. (2016). Hemodynamic response function abnormalities in schizophrenia during a multisensory detection task. *Human Brain Mapping*, 37(2), 745-755.
- Harms, M. P., & Melcher, J. R. (2003). Detection and quantification of a wide range of fMRI temporal responses using a physiologically-motivated basis set. *Human Brain Mapping*, 20(3), 168-183.
- Hoge, R. D., Atkinson, J., Gill, B., Crelier, G. R., Marrett, S., & Pike, G. B. (1999). Stimulus-dependent BOLD and perfusion dynamics in human V1. *Neuroimage*, 9(6), 573-585.
- Hoogenraad, F. G. C., Pouwels, P. J. W., Hofman, M. B. M., Reichenbach, J. R., Sprenger, M., & Haacke, E. M. (2001). Quantitative differentiation between BOLD models in fMRI. *Magnetic Resonance in Medicine*, 45(2), 233-246.
- Hua, J., Stevens, R. D., Huang, A. J., Pekar, J. J., & van Zijl, P. C. M. (2011). Physiological origin for the BOLD poststimulus undershoot in human brain: Vascular compliance versus oxygen metabolism. *Journal of Cerebral Blood Flow & Metabolism*, 31(7), 1599-1611.
- Huber, L., Ivanov, D., Handwerker, D. A., Marrett, S., Guidi, M., Uludağ, K., Bandettini, P. A., & Poser, B. A. (2018). Techniques for blood volume fMRI with VASO: From low-resolution mapping towards sub-millimeter layer-dependent applications. *Neuroimage*, 164, 131-143.
- Huber, L., Ivanov, D., Krieger, S. N., Streicher, M. N., Mildner, T., Poser, B. A., Möller, H. E., & Turner, R. (2014). Slab-selective, BOLD-corrected VASO at 7 Tesla provides measures of cerebral blood volume reactivity with high signal-to-noise ratio. *Magnetic Resonance in Medicine*, 72(1), 137-148.
- Jäncke, L., Specht, K., Mirzazade, S., Loose, R., Himmelbach, M., Lutz, K., & Joni Shah, N. (1998). A parametric analysis of the 'rate effect' in the sensorimotor cortex: a functional magnetic resonance imaging analysis in human subjects. *Neuroscience Letters*, 252(1), 37-40.
- Jenkinson, M., Beckmann, C. F., Behrens, T. E. J., Woolrich, M. W., & Smith, S. M. (2012). FSL. *Neuroimage*, 62(2), 782-790.
- Jin, T., & Kim, S.-G. (2010). Change of the cerebrospinal fluid volume during brain activation investigated by T1ρ-weighted fMRI. *Neuroimage*, 51(4), 1378-1383.
- Kim, S.-G. (1995). Quantification of relative cerebral blood flow change by flow-sensitive alternating inversion recovery (FAIR) technique: Application to functional mapping. *Magnetic Resonance in Medicine*, 34(3), 293-301.

- Koch, S. P., Werner, P., Steinbrink, J., Fries, P., & Obrig, H. (2009). Stimulus-Induced and State-Dependent Sustained Gamma Activity Is Tightly Coupled to the Hemodynamic Response in Humans. *The Journal of Neuroscience*, 29(44), 13962.
- Krieger, S. N., Ivanov, D., Huber, L., Roggenhofer, E., Sehm, B., Turner, R., Egan, G. F., & Gauthier, C. J. (2014). Using carbogen for calibrated fMRI at 7Tesla: Comparison of direct and modelled estimation of the M parameter. *Neuroimage*, 84, 605-614.
- Kwong, K. K., Belliveau, J. W., Chesler, D. A., Goldberg, I. E., Weisskoff, R. M., Poncelet, B. P., Kennedy, D. N., Hoppel, B. E., Cohen, M. S., & Turner, R. (1992). Dynamic magnetic resonance imaging of human brain activity during primary sensory stimulation. *Proceedings of the National Academy of Sciences*, 89(12), 5675.
- Lin, A.-L., Fox, P. T., Yang, Y., Lu, H., Tan, L.-H., & Gao, J.-H. (2009). Time-dependent correlation of cerebral blood flow with oxygen metabolism in activated human visual cortex as measured by fMRI. *Neuroimage*, 44(1), 16-22.
- Liu, E. Y., Haist, F., Dubowitz, D. J., & Buxton, R. B. (2019). Cerebral blood volume changes during the BOLD post-stimulus undershoot measured with a combined normoxia/hyperoxia method. *Neuroimage*, 185, 154-163.
- Liu, T. T., & Brown, G. G. (2007). Measurement of cerebral perfusion with arterial spin labeling: Part 1. Methods. *Journal of the International Neuropsychological Society: JINS*, 13(3), 517.
- Logothetis, N. K., Pauls, J., Augath, M., Trinath, T., & Oeltermann, A. (2001). Neurophysiological investigation of the basis of the fMRI signal. *nature*, 412(6843), 150-157.
- Lu, H., Clingman, C., Golay, X., & van Zijl, P. C. M. (2004a). Determining the longitudinal relaxation time (T1) of blood at 3.0 Tesla. *Magnetic Resonance in Medicine*, 52(3), 679-682.
- Lu, H., Golay, X., Pekar James, J., & van Zijl Peter, C. M. (2003). Functional magnetic resonance imaging based on changes in vascular space occupancy. *Magnetic Resonance in Medicine*, 50(2), 263-274.
- Lu, H., Golay, X., Pekar, J. J., & van Zijl, P. C. M. (2004b). Sustained Poststimulus Elevation in Cerebral Oxygen Utilization after Vascular Recovery. *Journal of Cerebral Blood Flow & Metabolism*, 24(7), 764-770.
- Lu, H., Hua, J., & van Zijl, P. C. M. (2013). Noninvasive functional imaging of cerebral blood volume with vascular-space-occupancy (VASO) MRI. *NMR in Biomedicine*, 26(8), 932-948.
- Lu, H., & van Zijl, P. C. M. (2005). Experimental measurement of extravascular parenchymal BOLD effects and tissue oxygen extraction fractions using multi-echo VASO fMRI at 1.5 and 3.0 T. *Magnetic Resonance in Medicine*, 53(4), 808-816.
- Lu, H., & van Zijl, P. C. M. (2012). A review of the development of Vascular-Space-Occupancy (VASO) fMRI. *Neuroimage*, 62(2), 736-742.
- Mandeville, J. B., Marota, J. J. A., Ayata, C., Zaharchuk, G., Moskowitz, M. A., Rosen, B. R., & Weisskoff, R. M. (1999). Evidence of a Cerebrovascular Postarteriole Windkessel with Delayed Compliance. *Journal of Cerebral Blood Flow & Metabolism*, 19(6), 679-689.

- Martindale, J., Kennerley, A. J., Johnston, D., Zheng, Y., & Mayhew, J. E. (2008). Theory and generalization of monte carlo models of the BOLD signal source. *Magnetic Resonance in Medicine*, *59*(3), 607-618.
- Mildner, T., Norris, D. G., Schwarzbauer, C., & Wiggins, C. J. (2001). A qualitative test of the balloon model for BOLD-based MR signal changes at 3T. *Magnetic Resonance in Medicine*, *46*(5), 891-899.
- Miller, K. L., Luh, W. M., Liu, T. T., Martinez, A., Obata, T., Wong, E. C., Frank, L. R., & Buxton, R. B. (2001). Nonlinear temporal dynamics of the cerebral blood flow response. *Hum Brain Mapp*, *13*(1), 1-12.
- Mougin, O., Abdel-Fahim, R., Dineen, R., Pitiot, A., Evangelou, N., & Gowland, P. (2016). Imaging gray matter with concomitant null point imaging from the phase sensitive inversion recovery sequence. *Magnetic Resonance in Medicine*, *76*(5), 1512-1516.
- Mullinger, K. J., Cherukara, M. T., Buxton, R. B., Francis, S. T., & Mayhew, S. D. (2017). Post-stimulus fMRI and EEG responses: Evidence for a neuronal origin hypothesised to be inhibitory. *Neuroimage*, *157*, 388-399.
- Mullinger, K. J., Mayhew, S., Bagshaw, A., Bowtell, R., & Francis, S. (2013a). *Intrinsic connectivity network activity revealed by the independent modelling of the primary and post-stimulus components of the BOLD response*. Paper presented at the ISMRM, Salt Lake City, Utah, USA.
- Mullinger, K. J., Mayhew, S. D., Bagshaw, A. P., Bowtell, R., & Francis, S. T. (2013b). Poststimulus undershoots in cerebral blood flow and BOLD fMRI responses are modulated by poststimulus neuronal activity. *Proceedings of the National Academy of Sciences*, *110*(33), 13636.
- Murray, S. O., Kolodny, T., Schallmo, M.-P., Gerdtts, J., & Bernier, R. A. (2020). Late fMRI response components are altered in autism spectrum disorder. *Frontiers in Human Neuroscience*, *14*, 241.
- Obata, T., Liu, T. T., Miller, K. L., Luh, W.-M., Wong, E. C., Frank, L. R., & Buxton, R. B. (2004). Discrepancies between BOLD and flow dynamics in primary and supplementary motor areas: application of the balloon model to the interpretation of BOLD transients. *Neuroimage*, *21*(1), 144-153.
- Ogawa, S., Tank, D. W., Menon, R., Ellermann, J. M., Kim, S. G., Merkle, H., & Ugurbil, K. (1992). Intrinsic signal changes accompanying sensory stimulation: functional brain mapping with magnetic resonance imaging. *Proceedings of the National Academy of Sciences*, *89*(13), 5951.
- Peck, K. K., Sunderland, A., Peters, A. M., Butterworth, S., Clark, P., & Gowland, P. A. (2001). Cerebral activation during a simple force production task: changes in the time course of the haemodynamic response. *NeuroReport*, *12*(13).
- Poser, B. A., Koopmans, P. J., Witzel, T., Wald, L. L., & Barth, M. (2010). Three dimensional echo-planar imaging at 7 Tesla. *Neuroimage*, *51*(1), 261-266.
- Poser, B. A., van Mierlo, E., & Norris, D. G. (2011). Exploring the post-stimulus undershoot with spin-echo fMRI: Implications for models of neurovascular response. *Human Brain Mapping*, *32*(1), 141-153.
- Sadaghiani, S., Ugurbil, K., & Uludağ, K. (2009). Neural activity-induced modulation of BOLD poststimulus undershoot independent of the positive signal. *Magnetic Resonance Imaging*, *27*(8), 1030-1038.
- Schroeter, M. L., Kupka, T., Mildner, T., Uludağ, K., & von Cramon, D. Y. (2006). Investigating the post-stimulus undershoot of the BOLD signal—a simultaneous fMRI and fNIRS study. *Neuroimage*, *30*(2), 349-358.

- Scouten, A., & Constable, R. T. (2008). VASO-based calculations of CBV change: Accounting for the dynamic CSF volume. *Magnetic Resonance in Medicine*, 59(2), 308-315.
- Soltysik, D. A., Peck, K. K., White, K. D., Crosson, B., & Briggs, R. W. (2004). Comparison of hemodynamic response nonlinearity across primary cortical areas. *Neuroimage*, 22(3), 1117-1127.
- Stevenson, C. M., Brookes, M. J., & Morris, P. G. (2011). Beta-band correlates of the fMRI BOLD Response. *Human Brain Mapping*, 32(2), 182-197.
- Toronov, V., Walker, S., Gupta, R., Choi, J. H., Gratton, E., Hueber, D., & Webb, A. (2003). The roles of changes in deoxyhemoglobin concentration and regional cerebral blood volume in the fMRI BOLD signal. *Neuroimage*, 19(4), 1521-1531.
- Uludağ, K., Dubowitz, D. J., Yoder, E. J., Restom, K., Liu, T. T., & Buxton, R. B. (2004). Coupling of cerebral blood flow and oxygen consumption during physiological activation and deactivation measured with fMRI. *Neuroimage*, 23(1), 148-155.
- Van de Moortele, P.-F., Auerbach, E. J., Olman, C., Yacoub, E., Uğurbil, K., & Moeller, S. (2009). T1 weighted brain images at 7 Tesla unbiased for Proton Density, T2* contrast and RF coil receive B1 sensitivity with simultaneous vessel visualization. *Neuroimage*, 46(2), 432-446.
- van der Zwaag, W., Marques, J. P., Kober, T., Glover, G., Gruetter, R., & Krueger, G. (2012). Temporal SNR characteristics in segmented 3D-EPI at 7T. *Magnetic Resonance in Medicine*, 67(2), 344-352.
- van Zijl, P. C. M., Hua, J., & Lu, H. (2012). The BOLD post-stimulus undershoot, one of the most debated issues in fMRI. *Neuroimage*, 62(2), 1092-1102.
- Wesolowski, R., Gowland, P., & Francis, S. (2009). *Double acquisition background suppressed (DABS) FAIR at 3T and 7T: Advantages for simultaneous BOLD and CBF Acquisition*. Paper presented at the ISMRM.
- Wong, E. C., Buxton, R. B., & Frank, L. R. (1997). Implementation of quantitative perfusion imaging techniques for functional brain mapping using pulsed arterial spin labeling. *NMR in Biomedicine*, 10(4-5), 237-249.
- Wright, P., Mouglin, O., Totman, J., Peters, A., Brookes, M., Coxon, R., Morris, P., Clemence, M., Francis, S., & Bowtell, R. (2008). Water proton T1 measurements in brain tissue at 7, 3, and 1.5 T using IR-EPI, IR-TSE, and MPRAGE: results and optimization. *Magnetic Resonance Materials in Physics, Biology and Medicine*, 21(1-2), 121.
- Yacoub, E., Shmuel, A., Pfeuffer, J., Van De Moortele, P.-F., Adriany, G., Andersen, P., Vaughan, J. T., Merkle, H., Ugurbil, K., & Hu, X. (2001). Imaging brain function in humans at 7 Tesla. *Magnetic Resonance in Medicine*, 45(4), 588-594.
- Yacoub, E., Ugurbil, K., & Harel, N. (2005). The Spatial Dependence of the Poststimulus Undershoot as Revealed by High-Resolution BOLD- and CBV-Weighted fMRI. *Journal of Cerebral Blood Flow & Metabolism*, 26(5), 634-644.
- Yang, Y., Gu, H., & Stein, E. A. (2004). Simultaneous MRI acquisition of blood volume, blood flow, and blood oxygenation information during brain activation. *Magnetic Resonance in Medicine*, 52(6), 1407-1417.
- Yuan, H., Liu, T., Szarkowski, R., Rios, C., Ashe, J., & He, B. (2010). Negative covariation between task-related responses in alpha/beta-band activity and

- BOLD in human sensorimotor cortex: An EEG and fMRI study of motor imagery and movements. *Neuroimage*, 49(3), 2596-2606.
- Zhang, X., Petersen, E. T., Ghariq, E., De Vis, J. B., Webb, A. G., Teeuwisse, W. M., Hendrikse, J., & van Osch, M. J. P. (2013). In vivo blood T1 measurements at 1.5 T, 3 T, and 7 T. *Magnetic Resonance in Medicine*, 70(4), 1082-1086.
- Zumer, J. M., Brookes, M. J., Stevenson, C. M., Francis, S. T., & Morris, P. G. (2010). Relating BOLD fMRI and neural oscillations through convolution and optimal linear weighting. *Neuroimage*, 49(2), 1479-1489.

6.8 Appendices

A. Data Quality Assessment

To interrogate signal quality for each contrast, additional ROIs were created centred on the peak of the i) BOLD ii) VASO and iii) aCBV t-stat within the contralateral precentral gyrus for the corresponding image (i.e. peak aCBV t-stat for the aCBV images, peak VASO t-stat for the VASO images) with vein and CSF masking applied. Figure 6.28 shows the subject average time course from ROIs centred on the peak of the BOLD, VASO and aCBV response, in comparison to Figure 6.22 which shows all time courses taken from an ROI centred on the peak of the BOLD response.

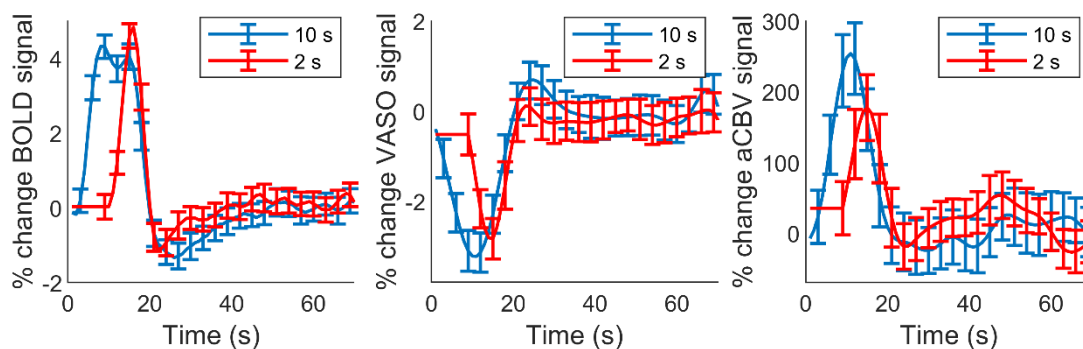


Figure 6.28 Subject average time courses of BOLD from ROI centred on the peak BOLD t-stat, VASO from ROI centred on peak of VASO T-stat and aCBV from ROI centred on peak of aCBV T-stat. Voxels containing veins or CSF were excluded (i.e. Small ROIs).

Further checks on data quality were made by assessing the individual participant responses to the task as shown in Figure 6.29 for subject time courses from the Small ROI, for BOLD, VASO and aCBV.

Since the VASO and aCBV data have low SNR, the effect of spatial smoothing was investigated to increase SNR for this data quality check. Data were spatially smoothed with a Gaussian smoothing kernel with full-width half maximum of 3 mm using SPM and another GLM with a boxcar regressor was performed on these smoothed data. Figure 6.30 shows the t-stat maps for the smoothed BOLD, VASO and aCBV data.

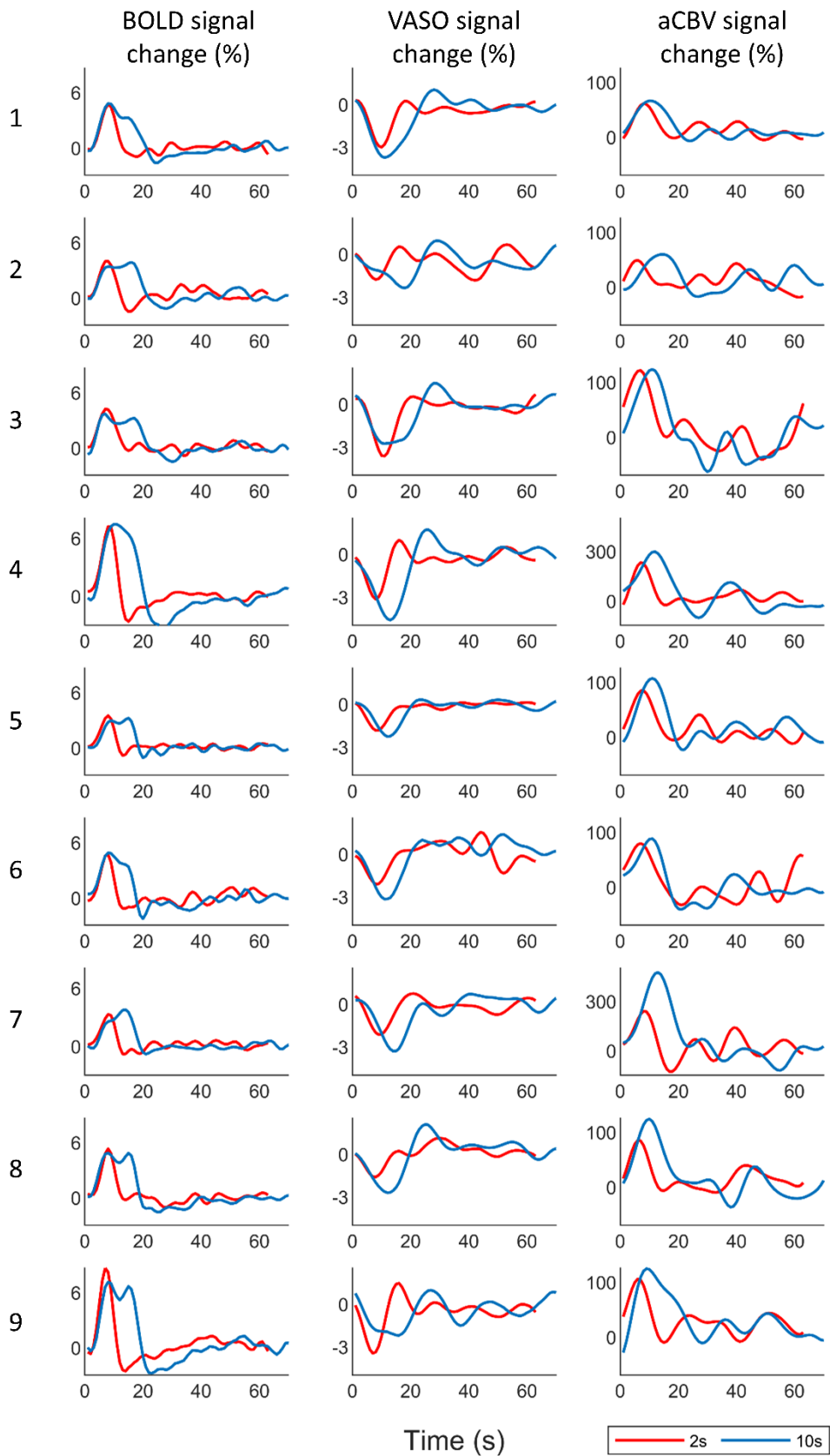


Figure 6.29. Individual subject (1–9) time courses of BOLD, VASO and aCBV % signal change from the Small ROI, corrected for veins and CSF.

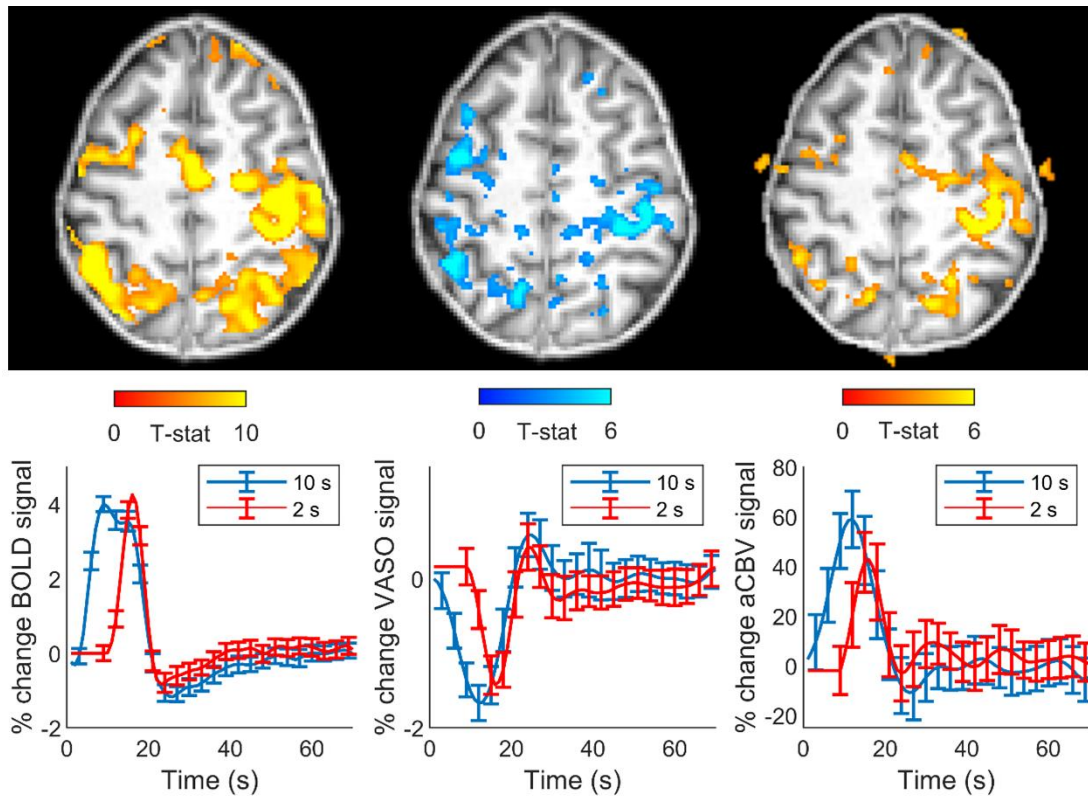


Figure 6.30 Example *t*-stat maps of smoothed (3 mm FWHM) BOLD, VASO and aCBV data for an individual subject (Subject 2). BOLD FWE $p = 0.001$ 5 voxel extent, VASO and aCBV $p = 0.001$ uncorrected 5 voxel extent. Time courses of BOLD, VASO and aCBV signal from peak BOLD *t*-stat in contralateral post-central gyrus from smoothed data, averaged over subjects. Error bars show standard error across subjects.

B. Simulating BOLD, VASO and aCBV Time Courses

As outlined in Methods Section 6.4.3.4, the fMRI time courses were interpolated to a sample rate of 1 s, in order to be segmented into trials. However, interpolation is only an estimate of the true data points and may miss maxima or minima. To explore this potential for error, the effect of interpolation was simulated on a model time course. Models were created using a boxcar and PMBR, MRBD, gamma MEG responses, as outlined in Section 6.4.3.5, using movement onset times derived from the EMG each subject. These were combined to produce a time course that resembled the fMRI response to a 2 and 10 s stimulus (Figure 6.31A) with 0.1 s time resolution.

When segmented into trials at this high temporal resolution, this time course gives the expected response shape (Figure 6.31B). To simulate the BOLD and VASO data, the time course was downsampled to $TR = 3$ and $TR = 6$ s, and then interpolated to 1 s and segmented into trials in the same way as with the real data analysis pipeline (Section 6.4.3.4). As can be seen in Figure 6.31C, for $TR = 3$ s (as for BOLD data), there is little difference between these interpolated and the non-interpolated data, apart from the artefactual appearance of a small initial dip. The amplitude of the response is 99% of the amplitude before being segmented into trials for both 2 and 10 s contraction durations. The time to peak of the responses is approximately 1 s later for both contraction durations when using the interpolation method compared to the simulated $TR = 0.1$ s. However, for simulated data with $TR = 6$ s (as for VASO data) (Figure 6.31D), the amplitude of the 2 s response drops to 80% of its true simulated value. This occurs because the 2 s contraction is short, so the time that the peak response is maintained is also short and the response will not always be sampled at the peak. Unless the 2 s contraction is directly sampled at the time of the peak, the peak will be missed and, when averaged, the 2 s peak will be diminished compared to the 10 s peak, which is maintained for a longer period so the peak amplitude is more likely to be sampled. The time to peak for the 2 s response is 1 s later and time to peak of 10 s response is 3.6 s later compared to the high time resolution trials. Different amplitudes of the initial response were tested to demonstrate that the 2 s response always gave a 20% drop in amplitude at the 6 s TR compared to the high temporal resolution simulation. Therefore, amplitudes of responses to the 2 s VASO and aCBV time courses were scaled by 1.25 to account for this (Figure 6.32). Scaled VASO data were also in the $CMRO_2$ calculation (Section 6.5.4).

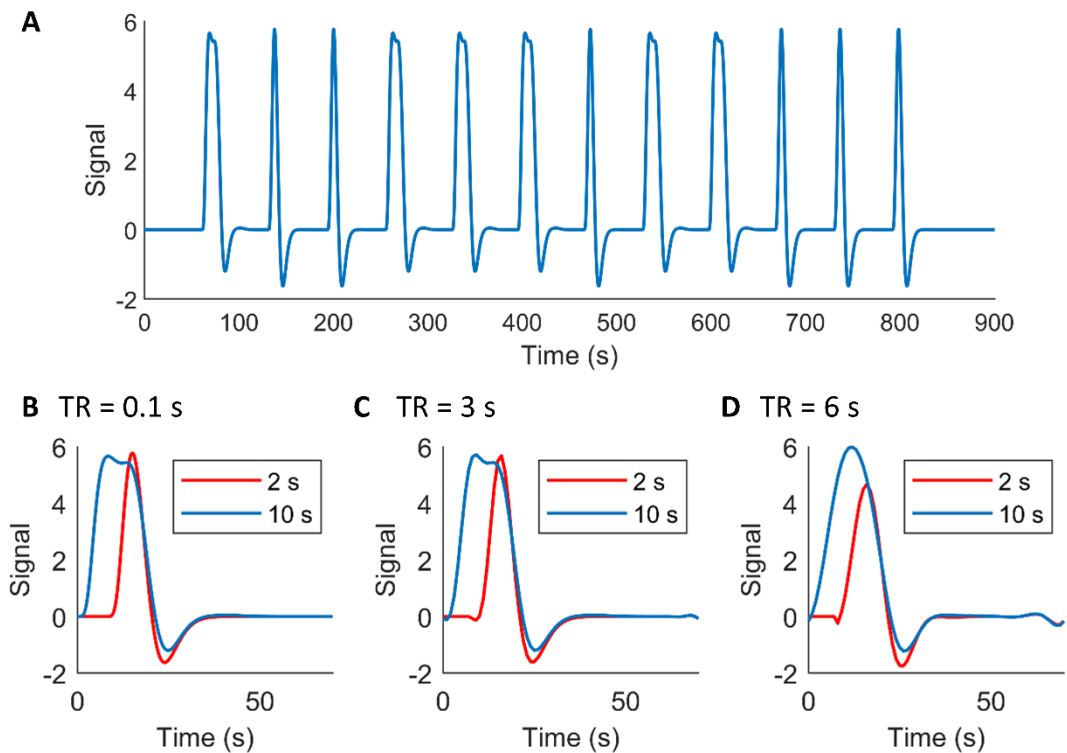


Figure 6.31 (A) Simulated model time course of the fMRI response to a 2 and 10 s stimulus with 0.1 s resolution. (B) Simulated time courses segmented into trials and averaged. (C) Simulated time course downsampled to TR = 3 s to match BOLD data, interpolated to 1 s, segmented into trials and averaged. (D) Simulated time course downsampled to TR = 6 s to match VASO data, then interpolated to 1 s, segmented into trials and averaged.

Figure 6.32 shows the subject average time courses from the Small ROI scaled (i.e. data multiplied by scaling factor of 1.25) for the 2 s contraction VASO and aCBV time courses. It can be seen that, with this scaling factor, the VASO and aCBV response to the 2 s grip contraction is similar to the response for the 10 s grip contraction. Statistical analysis showed there was no significant difference between the 2 and 10 s grip contraction for VASO ($p = 0.79$, paired samples t-test) or aCBV ($p = 0.86$, Wilcoxon signed rank test) after scaling. Therefore, it is inferred that the results from Section 6.5.2 which showed significant differences between 2 and 10 s response for VASO and aCBV primary response were an artefact of the combination of poor sampling and the use of interpolation for the 2 s stimulus.

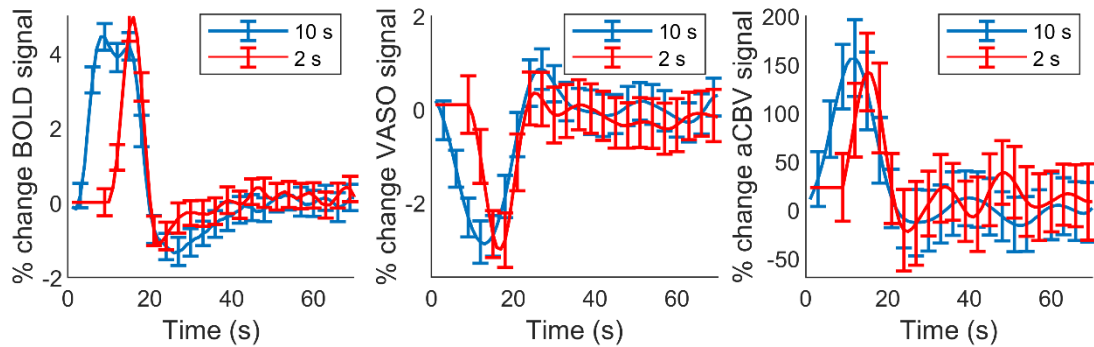


Figure 6.32 Time courses of BOLD, VASO and aCBV response from the Small ROI, where 2-s response for VASO and aCBV has been upscaled (multiplied by 1.25) to account for poor sampling. Compare with Figure 6.22 without upscaling.

One way to overcome this artefact of the analysis procedure would be not to interpolate but merge the data acquired at different points and average. The experiment was designed with this in mind and cues for the onset of the contractions relative to the sampling of the responses were jittered. However, in reality movement times in relation to the cued time were not constant. Therefore, there is variation in sample times resulting in an uneven number of samples at each time point and in some cases only one sample per time point, meaning the average response time course can be dominated by noise. To test if this would be possible, the BOLD data were padded with time points with no data to a time resolution of 1 s, then segmented into trials and averaged over all trials for all subjects. This had the effect of interleaving only measured data points from different trials with no interpolation. Similarly, the VASO data were upsampled to 2 s resolution. For aCBV, since the data were interpolated before performing the subtraction it was not possible to get back to the true data, so these data were upsampled to 1 s resolution. Figure 6.33 shows time courses from the small ROI using the upsampling method. Although the time courses are much noisier, it can be seen from comparing Figure 6.22 with Figure 6.33 that whilst the BOLD time courses follow a similar pattern regardless of analysis method, the VASO and aCBV data exhibit similar primary peak amplitudes for the 2 and 10 s durations when upsampling (Figure 6.33) is used rather than the interpolation method (Figure 6.22). This confirms that the results from the interpolated time courses were due to an artefact of the low temporal resolution, stimulus duration combined with the analysis method. While it would be preferable to use the real data and not interpolate, the time courses in Figure 6.33 have a clear oscillation in the data which limits their use. The noise does not have a clear source and requires further in depth investigation through simulation and experimental

work which is beyond the scope of this thesis. The noise could be due to interleaving the BOLD data from the two labels, but cannot be purely from this as it should average out across trials, and noise is still apparent in VASO and aCBV which were not interleaved. The data could be analysed separately for the two labels, however, this would leave the BOLD with a 6 s TR which would then have the sampling issues as apparent in the VASO and aCBV data. Another potential source for this noise is that the movement times vary on a shorter time scale than can be accounted for with the resolution of these data, so onset times could still be incorrectly assigned by ± 1 s or ± 2 s (for BOLD and VASO respectively) which could cause this. However, it is conceivable this is an SNR problem and with more data this might disappear.

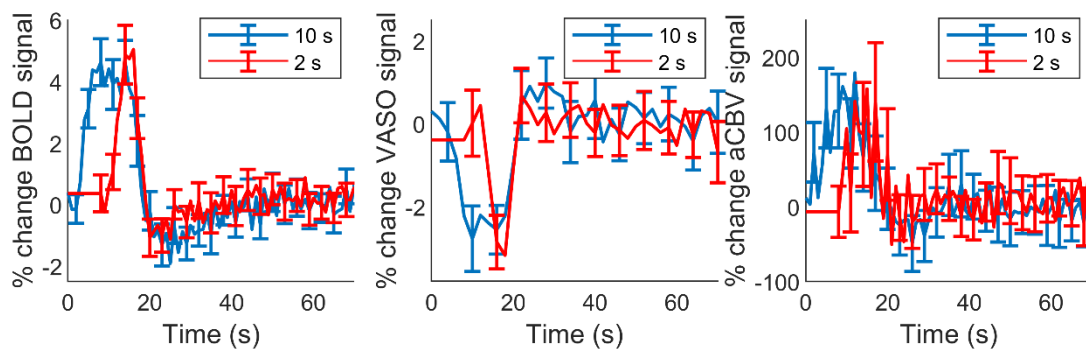


Figure 6.33 Subject average time courses without interpolation from the Small ROI. BOLD and aCBV data were upsampled to a resolution of 1 s and VASO were upsampled to a resolution of 2 s before averaging over trials and subjects. Error bars show standard error across subjects.

C. CMRO₂

CMRO₂ calculations were performed for varying values of M. Table 6.4 shows the results for M = 18, Table 6.5 shows the results for M = 25 (Krieger et al., 2014). Data show that regardless of M value used the primary response shows a significant difference in the CMRO₂ from baseline where as the PSR does not.

	% CMRO ₂ for each subject									Average ± SE
	1	2	3	4	5	6	7	8	9	
2s primary response	98	59	67	90	70	71	81	39	84	73 ± 6*
10s primary response	86	62	47	83	55	55	113	42	13	62 ± 9*
2s post-stimulus response	-1	-5	-9	-15	38	24	60	-22	-23	5 ± 9
10s post-stimulus response	-9	-25	-39	-41	14	11	38	-58	8	-11 ± 10

Table 6.4. CMRO₂ calculation using M = 18. The CMRO₂ percentage during primary response showed a significant change from baseline levels (*, p<0.05, one-sample t-test), the results of the PSR did not differ significantly from baseline levels.

	% CMRO ₂ for each subject									Average ± SE
	1	2	3	4	5	6	7	8	9	
2s primary response	116	71	80	122	80	86	91	53	125	92 ± 7*
10s primary response	104	73	57	118	63	71	128	56	32	78 ± 10*
2s post-stimulus response	-2	-7	-9	-18	37	22	59	-23	-26	4 ± 9
10s post-stimulus response	-11	-26	-40	-44	13	8	36	-59	4	-13 ± 10

Table 6.5. CMRO₂ using M = 25. The CMRO₂ percentage during primary response showed a significant change from baseline levels (*, p<0.05, one-sample t-test), the results of the PSR did not differ significantly from baseline levels.

CHAPTER 7

7 Using fMRI to Map Touch in Focal Hand Dystonia

7.1 Abstract

Focal hand dystonia (FHD) is a motor disorder causing involuntary movements of the hand, leading to the inability to perform specific tasks and aspects of everyday life. Yet, the pathophysiological basis of FHD is not fully known. Mapping finger representations in somatosensory cortex may help to better understand FHD. However, digit representations in the cortex are small and require high spatial resolution to successfully map each of the 5 digits of the hand, requiring the use of ultra-high-field MRI for sufficient spatial resolution. Here, a somatosensory and motor travelling wave paradigm were performed using 7 T fMRI to explore any changes in digit representations in 7 patients with FHD compared to age- and sex-matched healthy controls. The experiment was performed both ~4 weeks after patients had received treatment of botulinum toxin (Botox), and 3 months later once the treatment had worn off to assess the effects of treatment. Functional data were analysed in two ways: using a phase-encoding analysis as standard for travelling wave paradigms, and a general linear model (GLM). Maps of finger representation were successfully mapped in patients with FHD and healthy controls, with little difference observed between the maps in patients and healthy controls for either task. Comparison between the two analysis methods showed that a winner-takes-all GLM analysis is valid, and has the additional benefit that it can be used to measure the overlap of digit representations which is not possible to measure with phase-encoding methods. No significant difference in the degree of digit overlap was found between patients with FHD and healthy controls.

The work in this chapter was presented as a power pitch and poster at ISMRM 2019, Montreal, Canada, entitled 'Assessing somatotopic and mototopic organisation in Focal Hand Dystonia using high-resolution 7 T fMRI', and a poster at the Postgraduate Symposium of the British Chapter of ISMRM 2019, Birmingham, UK.

7.2 Introduction

Chapter 6 focussed on characterising fMRI responses in the motor cortex in healthy individuals. In this chapter, the utility of fMRI to investigate responses to motor and somatosensory tasks in a clinical population is explored. Ultra-high-field, high spatial resolution fMRI is applied to participants with focal hand dystonia (FHD). Dystonia is a neurological movement disorder that manifests as the uncontrollable spasms of muscles in the body, and is estimated to affect over 100,000 people in the UK (dystonia.org.uk, 2019). FHD specifically affects the hand area, causing involuntary cramping of the hand. For a long time, no physiological disturbances were recognised in people with dystonia and seemingly little differences were observed in the brain (Hallett, 1995). With the advent of modern neuroimaging techniques, dystonia has become better understood and is now classed as a neurological movement disorder. However, the pathophysiology is still not completely known (Breakefield et al., 2008) hence, the drive here to study changes in brain function associated with FHD. The work in this chapter formed part of a larger project ‘TOUCHMAP’ funded by the Medical Research Council (MR/M022722/1).

Dystonia is a neurological movement disorder now thought to be caused by incorrect signalling from the brain. Symptoms include abnormal and often painful movements in the hand, which can affect the ability to write (writer’s cramp) and the fine motor control required in everyday tasks and the ability to work. FHD is diagnosed by a neurologist. Treatment for dystonia includes physical rehabilitation such as movement therapy, and injections of botulinum toxin (Botox) into the affected muscles which acts to reduce the amount of muscle activity, allowing patients to regain some use of their hand. This is repeated every three months as the injection wears off. Despite dystonia being thought of as a largely motor disorder, the sensory system is thought to play an important role (Hallett, 1995): dystonia may develop after a sensory injury, sensory ticks can be present and anaesthetic can be used as treatment (Butterworth et al., 2003). The causes of FHD are not always clear, as FHD can be caused by an interaction between genetics, neurobiology and environmental factors, such as stress and trauma (Hinkley et al., 2009). It has been suggested that patients with FHD can exhibit abnormal somatosensory digit representations and a blurring of somatotopic arrangement (Butterworth et al., 2003). fMRI may help understand these disturbances and whether these changes modulate with Botox treatment.

To gain a better understanding of dystonia and its pathophysiology, there is a need to investigate the localised parts of the brain responsible for sensory representations of the hand, and therefore how, or if, they are altered in FHD. This can be achieved by mapping digit representations in the human brain, to assess whether there is a difference in the representations of the digits in somatosensory cortex in subjects with FHD compared to healthy controls. These representations of digits in somatosensory cortex are known as somatotopic maps, and such maps can reveal distorted sensory representations of the digits in neurological disorders. In this study both a somatosensory and motor task are used to investigate the responses in the primary somatosensory cortex. It has been previously been shown that motor tasks involving digit movements produce large responses in the somatosensory cortex. For example, Kolasinski et al. (Kolasinski et al., 2016) used a motor travelling wave paradigm (similar to that implemented in this chapter) and showed that finger movements evoke robust activation of somatosensory cortex, rather than motor cortex. Strong somatosensory responses have also been previously reported during active hand movements (Porro et al., 1996) and illusory hand movements (Naito et al., 2005). The somatosensory cortex acts broadly as both a processing region for afferent sensory inputs and a more central node in the redirection of incoming sensory information across the sensorimotor network. The somatosensory cortex has highly organized reciprocal connections with primary motor cortex and is thought to strongly influence the function of the motor cortex (Jacobs et al., 2014; Platz et al., 2012) with it being shown to affect motor learning (Vidoni et al., 2010). It is due to this structural and functional interplay between somatosensory and motor cortices that a natural digit movement task will elicit robust activation of somatosensory cortex. Further studies also suggest that motor representations may be encoded in a higher dimensionality space rather than as individual body parts (Diedrichsen et al., 2013; Overduin et al., 2012; Wiestler & Diedrichsen, 2013), limiting the mapping of digits in the motor cortex itself. This study also allows the relationship between somatosensory and motor cortex to be explored, by comparing the motor and somatosensory task data collected on the dominant hand in the same scan session.

Assessing the effectiveness of treatment for FHD is also important. Neither treatment with botulinum toxin nor rehabilitative training are completely successful at returning normal motor control (Hinkley et al., 2009). In particular, it has been hypothesised that

Botox may not only affect the muscles at the local injected site, but also cause remote effects at distant parts of the body as it acts through the central nervous system (Giladi, 1997). Studies using transcranial magnetic stimulation have suggested that Botox can affect the cortical representation of the hand, and that treatment with Botox can reverse reorganisation (Byrnes et al., 1998; Thickbroom et al., 2003). In a study of spatial discrimination thresholds, Walsh et al. (Walsh & Hutchinson, 2007) showed that thresholds improved 1 month after Botox injection, suggesting Botox has an indirect effect on the sensory cortex. Therefore, it is important to study patients with FHD both with and without Botox treatment. Most studies on people with FHD have been performed with patients not receiving treatments (≥ 3 months after Botox injection).

Previous studies have assessed somatosensory and motor topography in the brain both invasively and non-invasively. Cortical representation of the hand area was first accomplished in 1937 by Penfield and Boldrey (Penfield & Boldrey, 1937), using electrical stimulation during invasive operations. They explored motor and sensory representation in the cerebral cortex of electrical-induced finger movements and finger sensation, and found finger movements were localised to the precentral gyrus whilst finger sensation was largely localised to the postcentral gyrus. It is now commonly accepted that the precentral gyrus is the primary motor cortex and the postcentral gyrus is the primary somatosensory cortex. Woolsey et al. (Woolsey et al., 1979) recorded electrically-induced cortical evoked potentials during neurosurgery and showed that digit representations are ordered in the cortex, with the thumb (D1) being most inferior and lateral, moving through the digits to the little finger (D5) being more superior and medial. Figure 7.1 shows the hand representation on the cortical homunculus as defined from invasive imaging, where thumb = D1, index = D2, middle = D3, ring = D4 and little = D5. However, invasive electrophysiology is not ideal to investigate brain function on people who do not require neurosurgery as there is no benefit to the individual. Advances in fMRI allow brain function to be indirectly investigated non-invasively with high spatial resolution for much more accurate mapping of digit representations to natural tasks than achievable in the past.

Mapping of the motor and sensory cortex has been performed since fMRI was first developed in the early 1990s. Puce et al. (Puce et al., 1995) used fMRI at 1.5 T to measure responses when performing a motor task (squeezing a sponge) and sensory task (brushing of palms and air blown over palms). The authors observed considerable

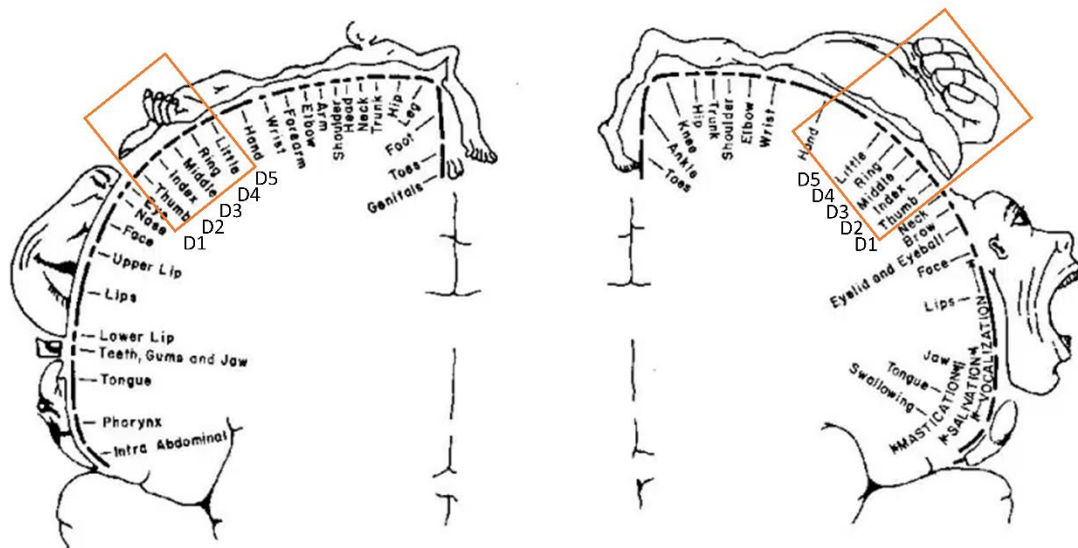


Figure 7.1 Cortical homunculus showing mapping of primary somatosensory cortex (left) and primary motor cortex (right) with representations of thumb to little finger moving more superior through the cortex. From Penfield & Rasmussen (Penfield & Rasmussen, 1950).

overlap of activated regions around the contralateral central sulcus for both tasks. Sakai et al. (Sakai et al., 1995) successfully mapped areas of somatosensory cortex corresponding to the toes, fingertips and the tongue using fMRI at 1.5 T. A manual scrubbing stimulation was applied to the fingertips of digits 1 to 3, however, they were not able to distinguish different fingertips. In 2000, as higher field strengths were available, Francis et al. (Francis et al., 2000) mapped cortical representations of digits 2 and 5 of the hand using 3 T fMRI. This was achieved using a piezoelectric stimulator, which was specifically developed to stimulate digits without interacting with the magnetic field. This allowed independent control of the amplitude and frequency of the somatosensory stimulation to produce an accurate and reproducible map of cortical representations.

To achieve a more detailed map which can distinguish all 5 digits of the hand, higher spatial resolution is needed. MRI at ultra-high-field (7 T and above) provides higher signal-to-noise ratio and increased BOLD contrast-to-noise ratio enabling the acquisition of smaller voxels thus the possibility of resolving detailed maps representing the individual fingertips. Further, the increase in BOLD signal with field strength (Yacoub et al., 2001) allows the detection of weaker responses such as those in somatosensory cortex, or for fewer trials to be acquired to identify functional responses reducing the time of data acquisition which is particularly beneficial in patient groups. However, at higher magnetic field, there is increased vulnerability to susceptibility induced geometric distortions and signal loss in EPI due to the shorter

T_2^* , but this can be overcome using parallel imaging (e.g. SENSE) to reduce the echo train length (see Chapter 3).

In 2010, Sanchez-Panchuelo et al. used 7 T fMRI to successfully map all five digits of the hand in the brain on an individual subject basis (Sanchez-Panchuelo et al., 2010) using a travelling wave somatosensory paradigm which had previously been used for visual retinotopic mapping (Engel et al., 1997). An explanation of the travelling wave paradigm is given in Appendix A. The travelling wave design has been shown to be more efficient than an equivalent event-related paradigm (Besle et al., 2013), whilst still providing accurate maps of fingertip representation. A travelling wave paradigm requires less data than event-related paradigms to produce a similar quality map, which again is advantageous for patients. However, since the travelling wave paradigm works by assigning a voxel to a digit based on the phase of the response, the standard phase analysis used in a travelling wave paradigm design cannot be used to estimate overlapping representations of digits. Therefore, an objective of this study was to investigate analysis of the digit mapping paradigm using the phase-encoding analysis compared with a GLM analysis (Chapter 3, Section 3.6.2.2).

Previous studies investigating digit representations in patients with FHD have been performed. Bara-Jimenez et al. (Bara-Jimenez et al., 1998) mapped cortical representations of the thumb (D1) and little finger (D5) of the dystonic hand in primary somatosensory cortex in six dystonia patients using somatosensory evoked potentials by stimulation from ring electrodes. They found the Euclidean distance between the peak voxels representing D1 and D5 was 12.7 ± 5.7 mm in healthy controls and decreased to 6.5 ± 3.0 mm in patients. They also found the topography of D1 and D5 to be inverted in 50% of patients which correlated with dystonia severity.

Magnetoencephalography (MEG) has also been used to image digit representations. In 2001, Meunier et al. (Meunier et al., 2001) used MEG to map D1, D2, D3 and D5 of both hands in 23 patients with FHD by measuring evoked responses from electrical stimulation of the digits. They found cortical representations of digits were more disordered in patients compared to healthy controls, which was more marked in the non-dominant hemisphere (contralateral response to non-dominant non-dystonic hand). Their results suggested overlap of representations in severely affected patients. McKenzie et al. (McKenzie et al., 2003) used MEG to measure the evoked response

from air puffs on digits 1-5 on both hands. Similarly to Meunier et al., the authors found digit representations were also more topographically disordered in FHD than in healthy controls, in this case on both affected and unaffected hemispheres.

Using 3 T fMRI with surface coils for improved spatial resolution, Butterworth et al. (Butterworth et al., 2003) explored the representations of digits 2 and 5 in the sensory cortex in 9 patients with FHD using vibrotactile stimulation. They found significantly decreased distances between representations of D2 and D5 to stimulation of the dominant (dystonic) hand, with absolute 3D separation between D2 and D5 was 4.14 ± 0.23 mm in patients, and 9.60 ± 1.24 mm in controls. As well, there was smaller extent of activity in patients with FHD compared to controls. This work therefore complemented the findings of Bara-Jimenez et al. (Bara-Jimenez et al., 1998).

With advancing methods, Nelson et al. (Nelson et al., 2009) mapped each digit (D1-5) of the dominant (dystonic) hand using high-resolution 3 T fMRI in 12 patients with FHD. Vibrotactile stimuli were used, with 8 seconds of vibration and 22 seconds rest performed on a single digit. Patients had reduced Euclidean distance between D1 and every other digit compared to controls. The distance between D1 and D5 was 12.8 ± 4.7 mm for patients and 17.9 ± 4.5 mm for controls. They found disordered representations in one third of patients including overlapping activation of digit representations, with different digits occupying similar locations.

Whilst previous studies investigated task-based differences, Dresel et al. (Dresel et al., 2014) used resting-state fMRI at 3 T to investigate functional connectivity in 15 patients with FHD. Patients showed lower correlation of the left primary motor cortex to right somatosensory cortex compared to controls, which correlated with disease severity. They propose that this reflects an underlying abnormality of network architecture.

In patients with FHD, sensory discrimination abilities have previously been found to be altered. Somatosensory temporal discrimination thresholds (TDT) and spatial discrimination thresholds (SDT), measure the ability to discriminate sensory stimulation in time and space respectively. Bara-Jimenez et al. found temporal discrimination thresholds to be raised in patients (96.7 ± 43.6 ms) compared to controls (64.4 ± 15.5 ms), which correlated with dystonia severity and age in patients (Bara-Jimenez et al., 2000). In agreement with this, Sanger et al. also found significantly raised temporal discrimination thresholds in patients (107 ± 41 ms) compared to

controls (46 ± 49 ms) (Sanger et al., 2001). Using a grating orientation task, Sanger et al. also measured spatial discrimination thresholds and found patients had raised (2.48 ± 0.72 mm) SDT compared to controls (1.49 ± 0.61 mm) (Sanger et al., 2001). Similarly, Molloy et al. found SDT of patients to be 2.61 ± 0.38 mm compared to 1.46 ± 0.26 in healthy controls (Molloy et al., 2003), and SDT was found to increase significantly with age. Zeuner et al. (Zeuner et al., 2002) also found raised SDT (2.38 ± 1.09) in patients compared to controls (1.95 ± 1.01) but this was not a significant difference, which was thought to be due to small sample size ($n = 10$).

7.2.1 Aims and Hypotheses

The above literature suggests there may be altered sensory representation of digits in patients with FHD, with studies showing disorganised cortical representation (McKenzie et al., 2003; Meunier et al., 2001) and reduced distance between digits (Bara-Jimenez et al., 1998; Butterworth et al., 2003; Nelson et al., 2009). Therefore, it is hypothesised that patients will have disorganised maps of digit representation and reduced map size compared to controls. The majority of previous fMRI studies of patients with FHD have used lower field strength MRI (<7 T). Here, this hypothesis will be tested by using advances in ultra-high field fMRI for better spatial resolution, and a travelling wave paradigm to efficiently assess the somatosensory topographic digit organisation in patients with FHD compared with healthy controls. The second aim of this study was to develop a method by which the overlap of digit representation in the cortex could be assessed to provide a metric of organisational blurring. Using this methodology, for the first time, the effects of Botox treatment on digit representations will be explored with fMRI. The aim was to compare maps with and without Botox treatment to test whether patients treated with Botox appear more similar to healthy controls, compared to patients scanned at 3 months when the treatment had worn off. It is hypothesised that patients without treatment will have more disorganisation and overlap than patients with treatment.

7.3 Methods

The study was approved by NHS ethics (17/EM/0368). 10 patients with FHD with unilateral impairments (mean age 54 ± 12 , 4 female) were recruited by Dr Miles Humberstone, a neurologist from Queen's Medical Centre, Nottingham, UK. Two patients' data could not be analysed due to excessive movement in the scanner and one patient was unable to complete the scan session due to claustrophobia, resulting in data from seven patients in total. Patients were scanned within 4 weeks of receiving Botox treatment. 6 of the 7 subjects returned for a follow-up scan session at least 3 months after their last Botox injection treatment (no Botox), on average 21 weeks after the first scan. One subject dropped out from the no Botox scan due to claustrophobia, but was able to complete the behavioural tasks for the no Botox session, hence there were 7 patients for no Botox behavioural data and 6 for fMRI. For six patients, their right hand was their affected hand, one patient had their left hand affected. 7 age- and sex-matched healthy controls were scanned for comparison to the patients.

All data we acquired by myself and Dr Michael Asghar, a postdoctoral research fellow on the TOUCHMAP project. The phase analysis was conducted and previously presented by Michael Asghar (Asghar, 2019) and was not the main aim of this thesis chapter, but are necessary to be presented here for comparison. All other analysis was conducted by myself.

7.3.1 Behavioural Measures

First, to characterise differences in sensory discrimination between patients with FHD and healthy controls, behavioural measures were taken. This involved a 1 hour behavioural session of various tasks testing the sensory sensitivity of the subject's hands. Measures included a somatosensory temporal discrimination task (TDT), amplitude threshold, and grating orientation spatial discrimination task (SDT). Tasks were performed on both visits prior to the fMRI scan session, in the order of TDT (piezos), TDT (brain gauge), amplitude threshold, and SDT.

The spatial discrimination threshold was assessed using a grating orientation task. This assesses the smallest distance participants are able to distinguish on their fingertips. Square-wave gratings cut into plastic domes (Figure 7.2) were presented to the subject's index finger of the affected hand (dominant for healthy controls) for approximately 1 second in either proximal or lateral orientation. Subjects had no line of sight to the

domes and were asked to describe which orientation they felt. 20 trials of each dome were presented, with the widths of the grating gradually decreasing in size and the subject's responses recorded. Eight domes were used in total with grating widths spanning 0.75 to 4.0 mm. Subjects unable to achieve correct responses for the largest grating (4 mm) were assigned a threshold of 4 mm.

Spatial Acuity

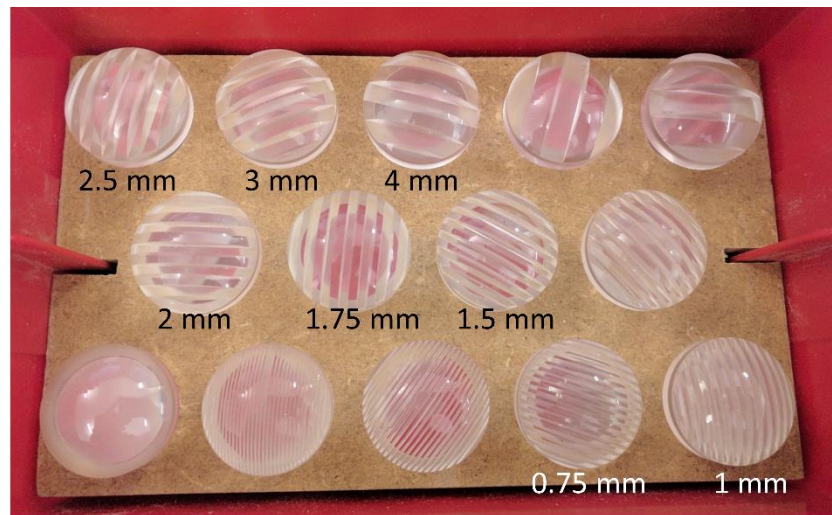


Figure 7.2. Plastic domes with square-wave gratings of varying widths used for the grating orientation task to assess SDT. Domes were placed with gratings horizontal or vertical on D2. Participants were asked which orientation the grating is presented in. Eight gratings of widths labelled were used, presented from 4 mm to 0.75 mm.

Amplitude threshold is the threshold at which subjects can no longer feel a stimulus. This was assessed using piezoelectric stimulators (Dancer Design, UK, Figure 7.3A) cased in a custom-built plexiglass “hand” (Figure 7.3B), the same stimulators as those used in the somatosensory fMRI paradigm. The plexiglass hand allowed individual adjustment of the stimulators such that the stimulators could lie directly below the subject's fingertips. The devices delivered suprathreshold vibrotactile stimuli to ~ 1 mm² of the fingertip. In each trial (Figure 7.3C), the stimulator would vibrate twice separated by a fixed short temporal gap, with one stimulation being delivered at a larger amplitude than the other. Subjects were asked to determine whether the first or second stimulation was of larger amplitude. This amplitude threshold task was performed on the index finger (D2) of both the affected and non-affected hands with stimulation delivered at two frequencies of 31 and 200 Hz. If the response was correct twice, the amplitude difference was decreased; conversely, if the response was incorrect, the amplitude difference was increased. This was performed for 8 reversals until an amplitude threshold was determined.

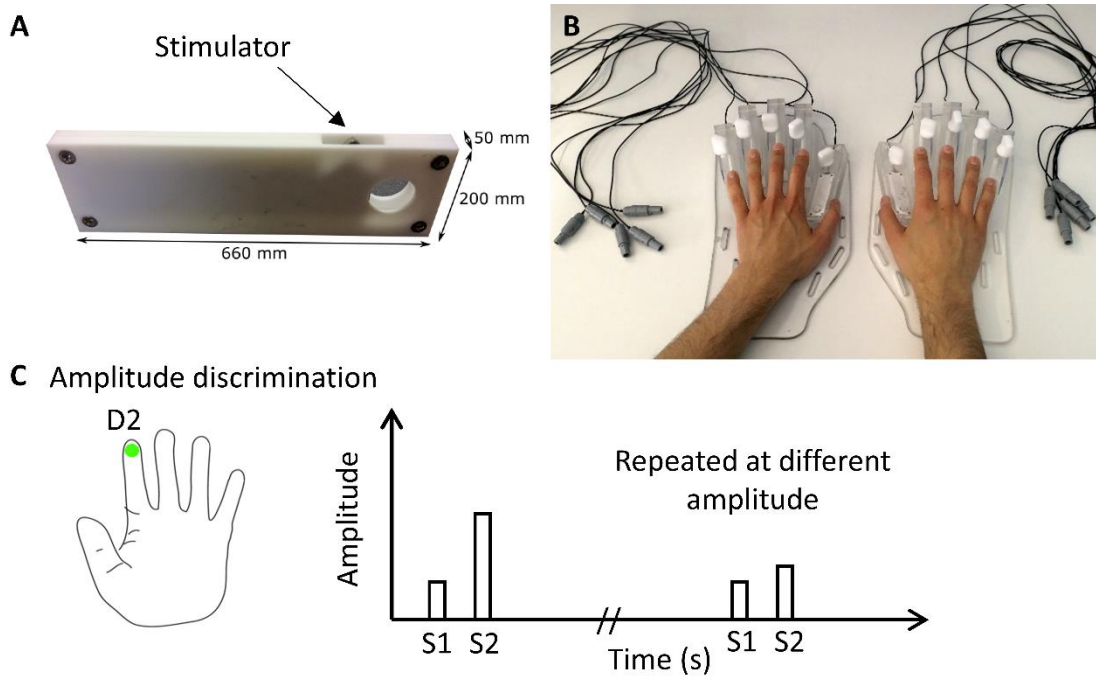


Figure 7.3. (A) Piezoelectric stimulator. (B) Piezoelectric stimulators mounted in plexiglass hands, one stimulator per digit. The position of the stimulators can be adjusted to match the subject's hands. (C) Schematic for amplitude discrimination task. Two stimuli (S1 and S2) of varying amplitude are presented to D2 separated by a fixed temporal gap and the subject is asked whether the first or second stimulus had the higher amplitude. The task is repeated and amplitude decreased until the subject's amplitude threshold is found.

The temporal discrimination task was also performed using the same piezoelectric stimulators as used for the amplitude threshold task (Figure 7.4). The aim was to establish the subject's temporal discrimination threshold (the shortest time the subject can distinguish between two stimuli 75% of the time). Two stimuli of the same amplitude were presented to D2 and D3 (index and middle finger) of the hand separated by a temporal gap (Figure 7.4C) Subjects were asked which stimulation came first temporally (D2 or D3). If the response was correct, the temporal gap was decreased; if incorrect, the temporal gap was increased, this was repeated in a staircase procedure until a temporal threshold was found. This was performed on both the affected and non-affected hand. A similar temporal discrimination task was then also carried out for both affected and non-affected hands using a Brain Gauge stimulator (Cortical Metrics, NC, United States) (Figure 7.4B). This device has larger sensory stimulators mounted within a mouse for comparison with the piezoelectric stimulators. The Edinburgh handedness questionnaire was also taken to complete the behavioural testing (see Appendix A). To determine the reliability of the behavioural measures, the behavioural tasks were repeated on a group of 10 healthy controls to assess test-retest reliability. Each subject performed the behavioural tests twice, with two weeks between each session. The

coefficient of variation (CV) was calculated over the two sessions. A low CV implies small variation between different sessions of the test.

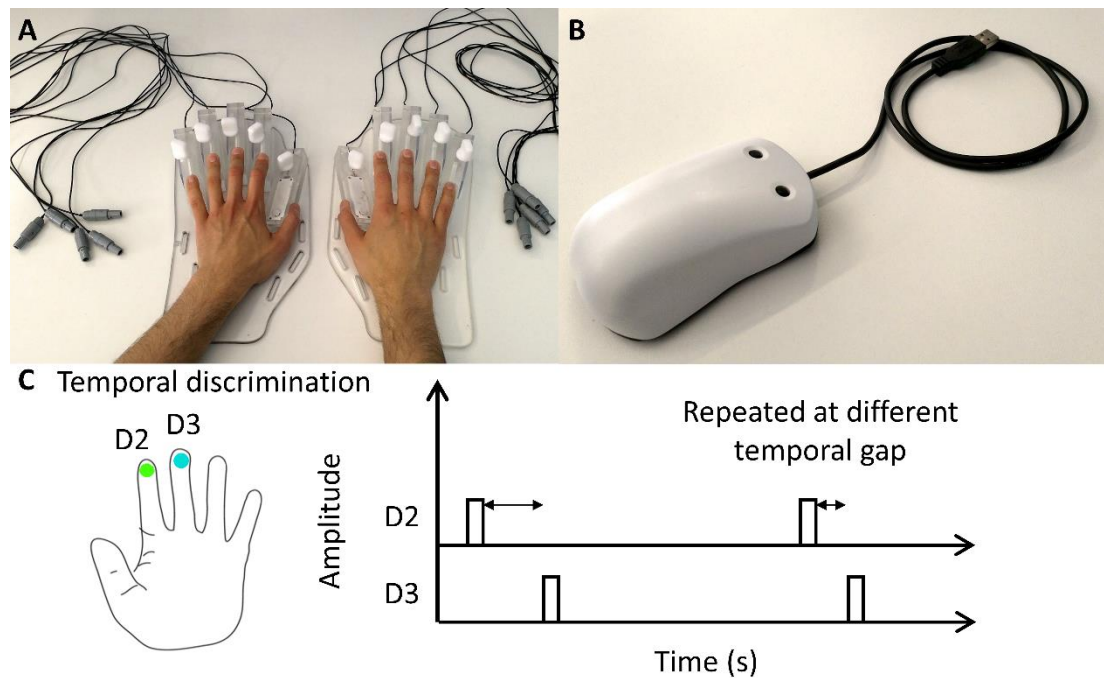


Figure 7.4. Schematic of temporal discrimination task performed with (A) piezoelectric stimulators and (B) Brain Gauge stimulator. D2 and D3 are stimulated with varying temporal gap. Participants are asked which digit was stimulated first.

7.3.2 fMRI

7.3.2.1 Paradigm and Data Acquisition

Data were acquired on a 7 T Philips Achieva MR scanner (Philips Healthcare, The Netherlands) using a single transmit Nova head coil with 32-receive channel (Nova Medical, Wilmington, MA, USA). Participants were placed in the scanner bore with prism glasses to view a screen onto which visual cues were projected. A peripheral pulse unit was placed on the participant's finger to record heart rate and a respiratory belt was used to record the respiratory trace throughout the scan. The participant's hands were positioned onto the MR compatible piezoelectric stimulators housed in the plexiglass hands (shown in Figure 7.3B) and adjusted so that the stimulators were directly under the finger tips. The session consisted of a 5-minute resting state scan (multiband = 4, TR = 1.5 s, 200 dynamics), somatosensory travelling wave scans in the forwards and reverse directions on both left and right hands (details below), an event-related somatosensory on-off paradigm, a high resolution T_2^* -weighted FLASH image (0.5×0.5×1.5 mm resolution, 74 slices, TE = 9.7 ms), a whole brain 1 mm isotropic

structural MPRAGE scan ($1 \times 1 \times 1$ mm resolution, 180 slices, TE = 3.44 ms) and a whole brain high resolution PSIR ($0.7 \times 0.7 \times 0.7$ mm resolution, 224 slices, TE = 2.64 ms). The scanner bed was then briefly removed from the scanner bore, and the subject was instructed to not move their head as the accelerometer glove was applied to the subject's dominant (affected) hand. The scanner bed was then returned to its original position in the bore and the motor travelling wave task was performed (see details below). Due to time constraints of the entire protocol it was not feasible to perform the motor task on both hands. Analysis of the resting state scan, event-related paradigm and structural data are beyond the scope of this thesis and were performed by Dr Michael Asghar.

The somatosensory travelling wave data were collected using a 2D gradient-echo EPI acquisition (2D GE-EPI, TE = 25 ms, SENSE 1.5, 1.5 mm isotropic voxels, multiband factor 3, TR = 2 s, 80 dynamics, flip angle = 80° , 48 slices, halfscan 0.7) and performed in forward (fingertip of D1 to D5) and reverse directions (fingertip of D5 to D1), on both hands (resulting in 4 scans in total). In one run, each digit was stimulated sequentially for 4 s using the piezoelectric stimulator placed under each fingertip. One cycle (sequential 4 s stimulation of each of the 5 digits) was 20 s in total, which was repeated for 8 cycles in both the forward and reverse direction, resulting in a total scan time of 2 minutes 40 s for each scan. See Figure 7.5 A&B for a diagram of the travelling wave somatosensory paradigm.

For the motor travelling wave paradigm, a custom-built MR compatible accelerometer system monitored the movement of each digit (Figure 7.5C). The motor travelling wave paradigm consisted of subjects tapping the fingers of their dominant (affected) hand in the air (to reduce any effects of somatosensory stimulation) in time to a 1 Hz visual cue of a flashing dot (Figure 7.5D) displayed on a screen and viewed using prism glasses, to elicit a solely motor proprioception response. Five dots on the screen represented each digit, each of which would flash sequentially for 4 s. Subjects were instructed to move each finger in time with the flashing dot, to ensure a similar speed of movement between all finger movements and participants. Each finger movement was recorded throughout the scan using the accelerometer glove and an associated MATLAB programme (The MathWorks, United States). GE-EPI acquisition parameters were identical to the somatosensory paradigm, with the motor task also performed in both the forward and reverse directions.

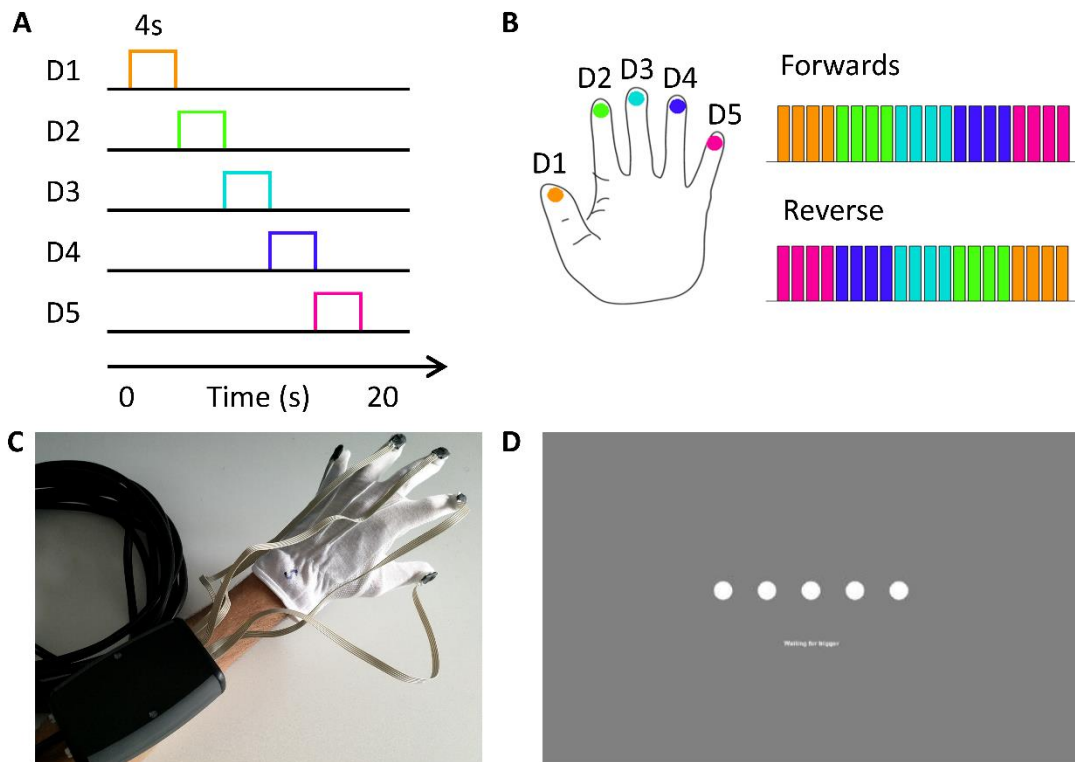


Figure 7.5. (A) Timings of the somatosensory and motor travelling wave paradigm. Each digit was stimulated/moved sequentially for 4 s, resulting in a 20 s cycle. Each cycle was repeated 8 times, for both the forward and reverse directions (shown here for the forward direction). Somatosensory stimulation was repeated in left and right hands, finger tapping (motor) was performed in affected/dominant hand only. (B) Demonstration of sequential digit ordering in the forward (D1-D5) and reverse (D5-D1) directions. (C) Accelerometer glove used to record finger movement during the motor paradigm. (D) Visual cue for finger movements in the motor paradigm. Each dot represents one of digits 1-5 and flashed for 4 s. Subjects were instructed to move their finger at the same rate as the flash to ensure consistent speed of movements across digits and individuals.

7.3.2.2 Pre-processing of fMRI Data

Physiological noise correction was conducted using the recorded cardiac and respiratory traces with RETROICOR (Glover et al., 2000), coded in MATLAB. The MPRAGE was processed through Freesurfer (Fischl, 2012) to generate white and grey matter boundaries and generate surfaces. Flattening was performed in mrTools (mrFlat) to produce individual flat maps for each subject. All fMRI analysis was then performed in mrTools (Gardner, 2018). Functional data were first motion corrected and aligned to the high resolution T_2^* -weighted anatomical FLASH scan using mrAlign (mrTools) and the time series were high-pass filtered with a 0.01 Hz cutoff.

7.3.2.3 Phase Analysis to Define Digit Maps

Digit maps were produced from the sensory and motor mapping task using phase analysis (Asghar, 2019; Besle et al., 2013). fMRI data collected in the reverse-direction

scan was reversed and shifted by one TR (2 s) to correct for the slice timing of the acquisition (see Appendix A). Averaging of forward and reverse scans was then performed to reduce the effect of the haemodynamic delay (Besle et al., 2013). A cosine function at the stimulation frequency was fitted to the forward and reverse scans and averaged across runs resulting in a phase map, where the phase of a voxel represents the stimulation of a given finger based on the phase bin. Coherence maps were also created which measures the correlation between the fitted cosine and the voxel time series. The phase maps were generated at a threshold of coherence = 0.3 and binned into five equal phase bins of widths $2\pi/5$ to produce ROIs of each digit representation. This process was performed for both the somatosensory data of both hands and the motor data of the dominant hand.

7.3.2.4 GLM Analysis to Define Digit Maps

The somatosensory and motor data were also analysed using a general linear model (GLM) in mrTools (Gardner, 2018). The purpose of this analysis was to determine whether digit maps could be robustly generated using a GLM, and secondly whether the overlap between digits could be measured. The latter is not possible with a phase analysis as this solely attributes a given phase to a single digit. Use of a GLM also allowed the exact times of movement from the accelerometer to be used for the motor task, rather than the visually cued movement times. To do this, separate GLMs were ran for each digit. A boxcar was created with the timings of stimulation for an individual digit which was convolved with a double-gamma haemodynamic response function. To compare the GLM analysis with the phase analysis, the positive beta weights from each digit were combined in a winner-takes-all approach (WTA), i.e. each voxel was assigned to a given digit based on its maximum beta value. The WTA analysis from the GLM was constrained to the digit ROIs as previously defined from the phase analysis. To quantitatively compare GLM analysis with the phase analysis, a Dice coefficient between the GLM winner-takes-all map and the phase map was computed. In order to do this, firstly the phase distribution from the phase analysis was converted into discrete maps of D1 to D5 by dividing the phase distribution (0 to 2π) into five (see Figure 7.6). Then the Dice coefficient was computed between this discrete phase map and the WTA map. For two images, A and B, which represent the binary digit maps, the Dice coefficient is given by

$$Dice(A, B) = \frac{2 |A \cap B|}{|A| + |B|} \quad (1)$$

where $A \cap B$ is the intersection of A and B. The Dice coefficient assesses the similarity between two images and will range from 0 (not similar) to 1 (complete similarity).

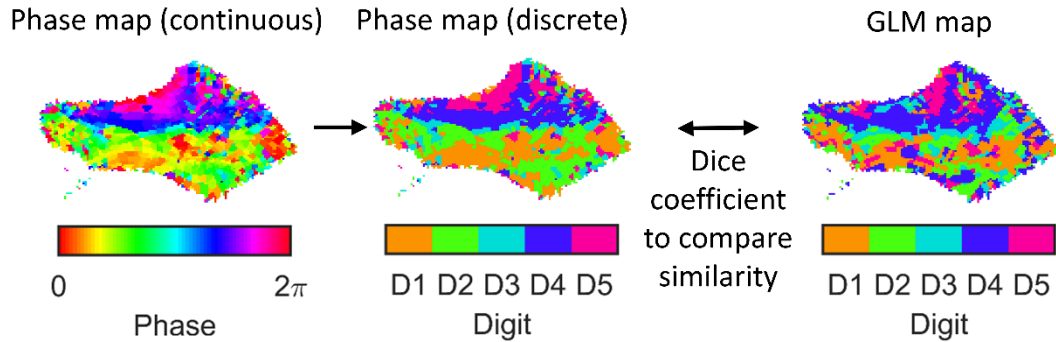


Figure 7.6. Schematic of how Dice coefficient is measured between phase and GLM maps. The phase distribution is converted into a discrete digit map, which can then be compared to the GLM map, see Equation 1.

For the motor paradigm, the accelerometer data were input into the GLM to provide more accurate timings based on actual movements of each digit for each participant. The accelerometer measures movement in each of the three orthogonal directions, these traces were root-mean-squared (RMS) to capture the timing of the movement. An example RMS time course of movements detected by the accelerometer is displayed in Figure 7.7. The accelerometer data was then analysed to determine the movement onset and offset times, using a similar analysis method to that performed on the EMG data in Chapter 4. The RMS accelerometer data were filtered and the Hilbert envelope taken. A noise threshold was determined as 3 times the standard deviation of the data, and movement periods were classified as the periods above this threshold. The exact times of movement onset and offset were then input as timings into the GLM for the motor paradigm. In 6 of 20 scan sessions (3 FHD patients no Botox, 3 healthy controls) the accelerometer data were unusable or not present due to issues with hardware and scanner triggers. In these cases the timings of the visual stimulus were used.

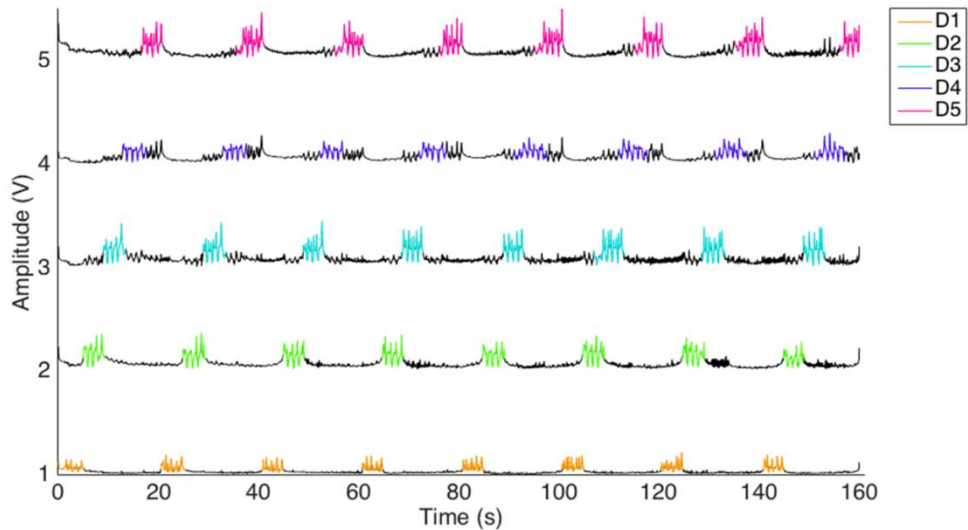


Figure 7.7. Example RMS accelerometer trace for one subject for the forward direction motor task with detected movements highlighted for each of the five digits. (digit 1 = orange, digit 2 = green, digit 3 = cyan, digit 4 = purple, digit 5 = pink).

7.3.2.5 GLM Analysis of Overlap of Digits

The advantage of using a GLM to study the mapping data is it provides a potential method by which to measure the overlap between the digits (Besle et al., 2014), a parameter which cannot be extracted from phase analysis of the data. To assess the degree of digit overlap, the beta weights from each of the separate digit GLMs were assessed for each digit ROI, defined from the phase analysis for each subject. To combine the data across the subjects within each group, the individual subjects were normalised to between 0 and 1 and averaged over the group. In order to quantify the spread in activity over digits, a Gaussian distribution was fitted to the digit beta weights, where digit ordering was shifted so the stimulated digit was in the centre. This enabled the width of the fitted Gaussian to be compared between subject groups.

7.4 Results

7.4.1 Behavioural Measures

Behavioural results are shown for the 7 patients with FHD (mean age 51 ± 10 years, 4 female) collected within 4 weeks of receiving Botox treatment (Botox) and the same patients at least 3 months after the last injection (mean age 52 ± 11 years) after treatment effects had worn off (no Botox), which was on average 21 ± 11 weeks after the first scan, and 7 age- and sex-matched healthy controls (mean age 50 ± 12 years, 4 female).

Mean values (\pm standard deviation) of SDT from the grating orientation task were 2.9 ± 0.9 mm and 2.8 ± 0.9 mm, for FHD patients with Botox and no-Botox respectively, and 1.8 ± 0.2 mm for healthy controls, as shown in Figure 7.8. The FHD patient group had a larger SDT and larger variance compared to the healthy controls, with a significant difference between the means of the three groups ($p = 0.046$, one way ANOVA). SDT was found to correlate with age (Figure 7.9) across the groups with a Pearson correlation coefficient of 0.443. This was largely driven by the patients, with the correlation between SDT and age of patients only 0.587, $p = 0.027$. Patient demographics including age, sex, handedness, Botox dose received and their SDT score are shown in Table 7.1. There was no significant correlation between Botox dose and SDT.

Amplitude discrimination thresholds at 31 Hz and 200 Hz on each hand averaged across groups are shown in Figure 7.10. Individual amplitude thresholds were compared between patients with Botox, patients no Botox and healthy controls for stimulation at 31 and 200 Hz on both hands. No significant differences were found between groups in any of the measures (one-way ANOVA). Temporal discrimination thresholds using both piezoelectirc stimulators and the Brain Gauge device, for each hand, are shown in Figure 7.11. Again, no significant differences were observed between groups for any of the measures showing this lack of difference was independent of stimulus type. There was a significant difference in the type of stimulus used, with the Brain Gauge which has a larger stimulation area giving a significantly lower TDT across the group ($P < 0.001$ paired samples t-test).

The within-subject coefficient of variation (CV) was measured for the behavioural tests performed on a group of 10 healthy controls, to assess the test-retest reliability. The

CV for: i) grating orientation task was 6.2%, ii) amplitude threshold at 31 Hz was 24.5% and at 200 Hz was 38.9%, iii) temporal discrimination task for piezoelectric stimulation was 43.1% and Brain Gauge stimulation was 30.9%. These results suggest that the between session variation was lowest in the measure of SDT with the grating orientation task.

Subject	Age	Sex	Handedness	Botox dose (U)	SDT (mm)
1	37	F	R	56	1.47
2	39	M	L	10	2.46
3	68	F	R	16	2.98
4	63	M	R	24	4
5	49	F	R	28	4
6	52	M	R	24	3.05
7	52	F	R	12	2.06

Table 7.1. Patient demographic information including age of the patients, handedness, Botox dose received approximately 4 weeks before the scan and spatial discrimination threshold.

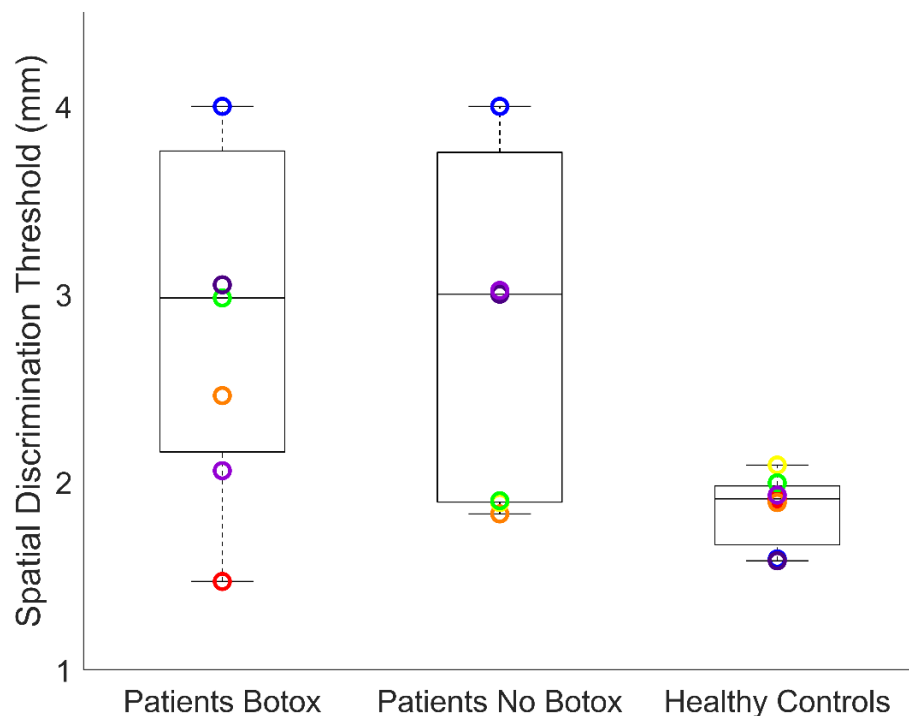


Figure 7.8. Box plots of SDT results for FHD patients with Botox and no-Botox and healthy controls. Each colour represents an individual subject and their age-matched control.

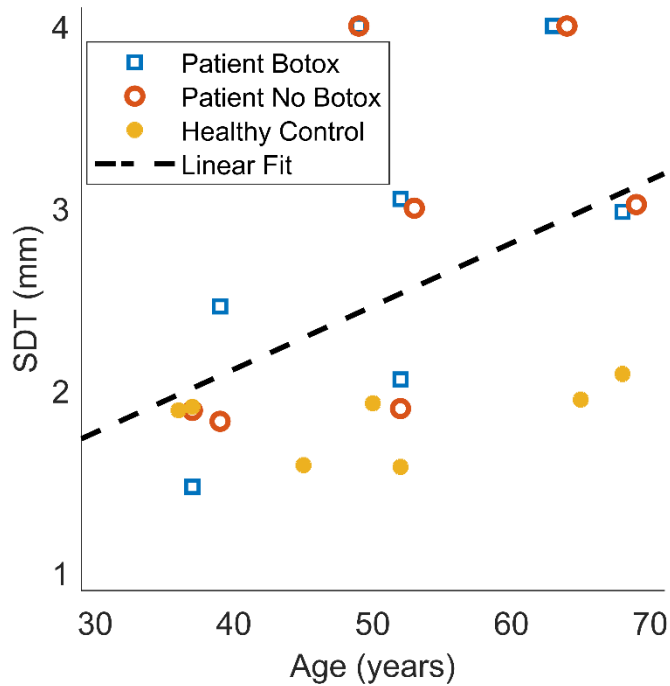


Figure 7.9. Correlation between SDT and age across all groups (Pearson correlation = 0.443, $p = 0.044$). Squares represent FHD patients with botox, circles FHD patients with no Botox, solid dots represent healthy controls. The dashed line shows the linear fit to the data ($R^2 = 0.196$).

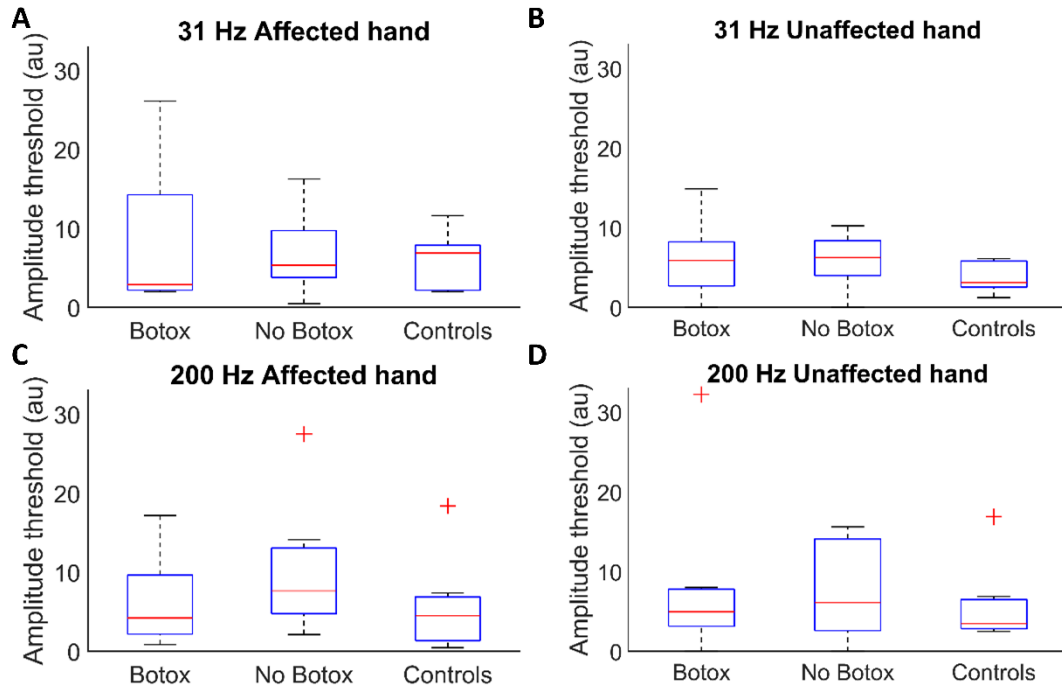


Figure 7.10. Box plots of amplitude thresholds for patients with Botox, patients no Botox and healthy controls for (A) 31 Hz affected/dominant hand, (B) 31 Hz unaffected/non-dominant hand, (C) 200 Hz affected/dominant hand and (D) 200 Hz unaffected/non-dominant hand. No statistical difference was seen between the means of the three groups for any measure (one-way ANOVA). Red crosses indicate outliers.

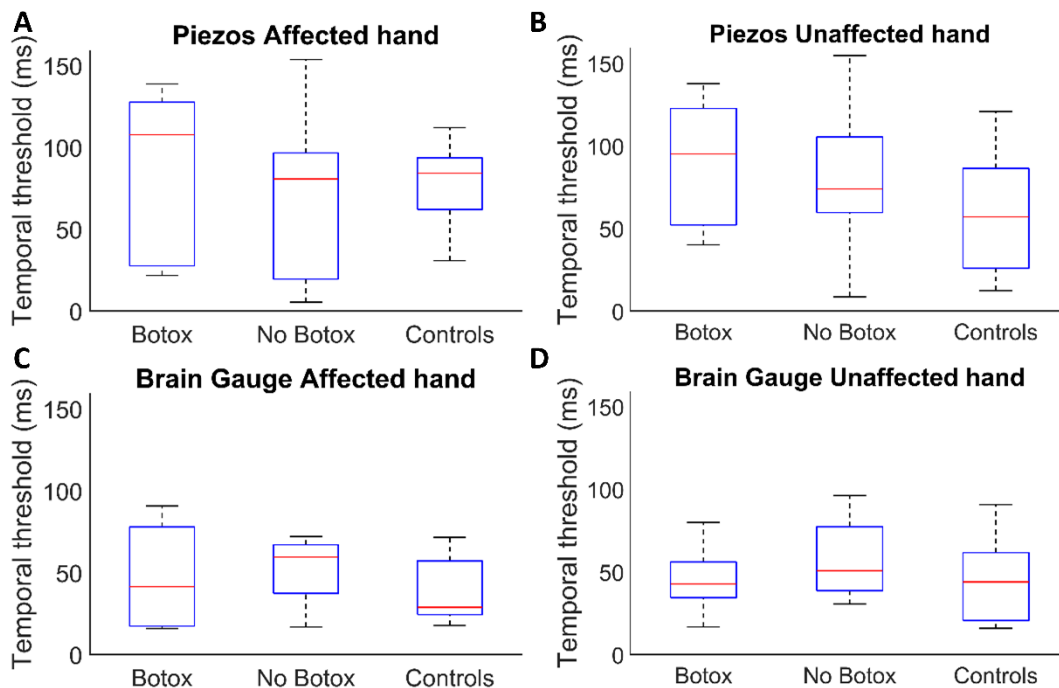


Figure 7.11. Box plots of temporal discrimination thresholds for patients with Botox, patients no Botox and healthy controls for (A) piezoelectric stimulators, affected/dominant hand, (B) piezoelectric stimulators, unaffected/non-dominant hand, (C) Brain Gauge affected/dominant hand, (D) Brain Gauge unaffected/non-dominant hand. No statistical difference was seen between the means of the three groups for any measure (one-way ANOVA).

7.4.2 fMRI

fMRI mapping results are shown for FHD patients with Botox ($n = 7$) and six of these patients (mean age 54 ± 10) who returned at least 3 months after last Botox injection (no Botox), together with the age- and sex-matched healthy controls. One patient did not return for the no Botox scan session due to claustrophobia.

7.4.2.1 Phase Analysis

Phase analysis of the somatosensory and motor travelling wave datasets produced maps of fingertip digit representation in the somatosensory cortex of the contralateral hemisphere. Individual digits were able to be distinguished, with the expected lateral to medial progression of digits observed (D1 is expected to be lateral and inferior to D5) (Figure 7.12B). Also, as expected the motor task resulted in a large digit specific response in the somatosensory cortex but limited activation in motor cortex. An example of the map from the somatosensory task for one FHD patient (Subject 6, Botox) is shown in Figure 7.12I. The associated coherence (Figure 7.12A) and phase (Figure 7.12B) maps are displayed on the flattened cortical patch. Figure 7.12C shows

the same digit representations on whole head geometry. The bottom panels of Figure 7.12 show the progression of the individual digits D1-D5 from lateral (D1) to medial (D5). Figure 7.12II shows the results from the motor task for the same subject for comparison. The motor and somatosensory tasks can be seen to evoke similar cortical representations in the somatosensory cortex, with the motor task producing stronger responses denoted by greater coherence (panel A). The phase maps for all subjects are shown in Figure 7.13 for the somatosensory task on the dominant/affected hand, Figure 7.14 for the somatosensory task on the non-dominant/unaffected hand and Figure 7.15 for motor task on the dominant/affected hand. The first column shows FHD patients with Botox treatment, the second column FHD patients without Botox, and the third column is the age- and sex-matched healthy control.

In Figure 7.13, 16 out of 20 maps show the expected digit topography, with no visual difference in the number of disordered representations between patients and healthy controls. Maps where the expected order of digits is not followed are marked with an asterisk. For the non-dominant hand, Figure 7.14, a similar number of maps are successfully produced, with 16 out of 20 maps showing expected digit topography. Again maps where digit representations appear disordered are marked with an asterisk. For the motor task (Figure 7.15), clear maps are produced in all subjects.

Across all paradigms, for most patients, there is little difference between the maps of finger representation with Botox and no Botox. For two patients (subject 1 and 3), the maps between Botox and no Botox are very different.

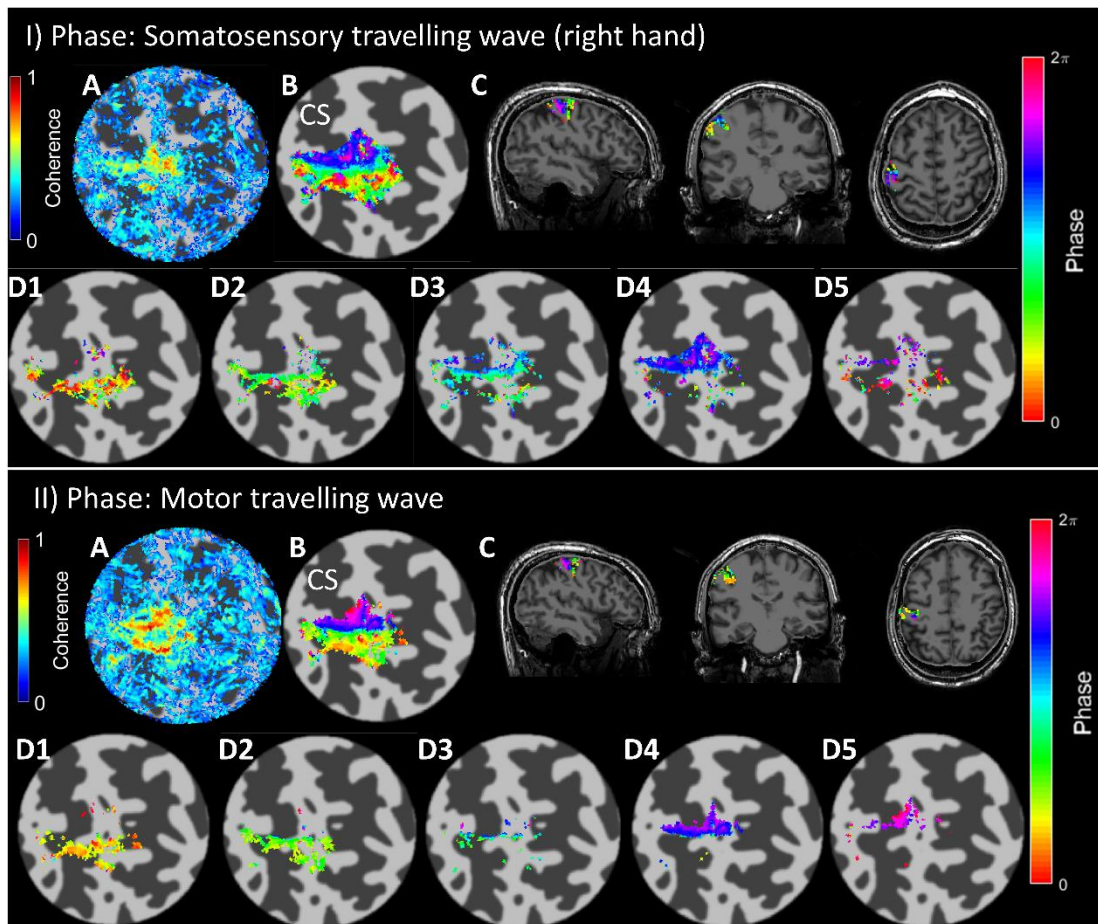


Figure 7.12. (I) Phase analysis of somatosensory travelling wave for one patient on individual flattened cortical patch in the contralateral hemisphere (left hemisphere) to the dominant (right) hand where dark grey represents negative curvature (sulci) and light grey represents positive curvature (gyri). Central sulcus (CS) is marked. (II) Phase analysis of motor travelling wave for same subject. (A) Coherence map. (B) Phase map. (C) Phase map from B shown on whole head. D1-5: ROIs of individual digits.

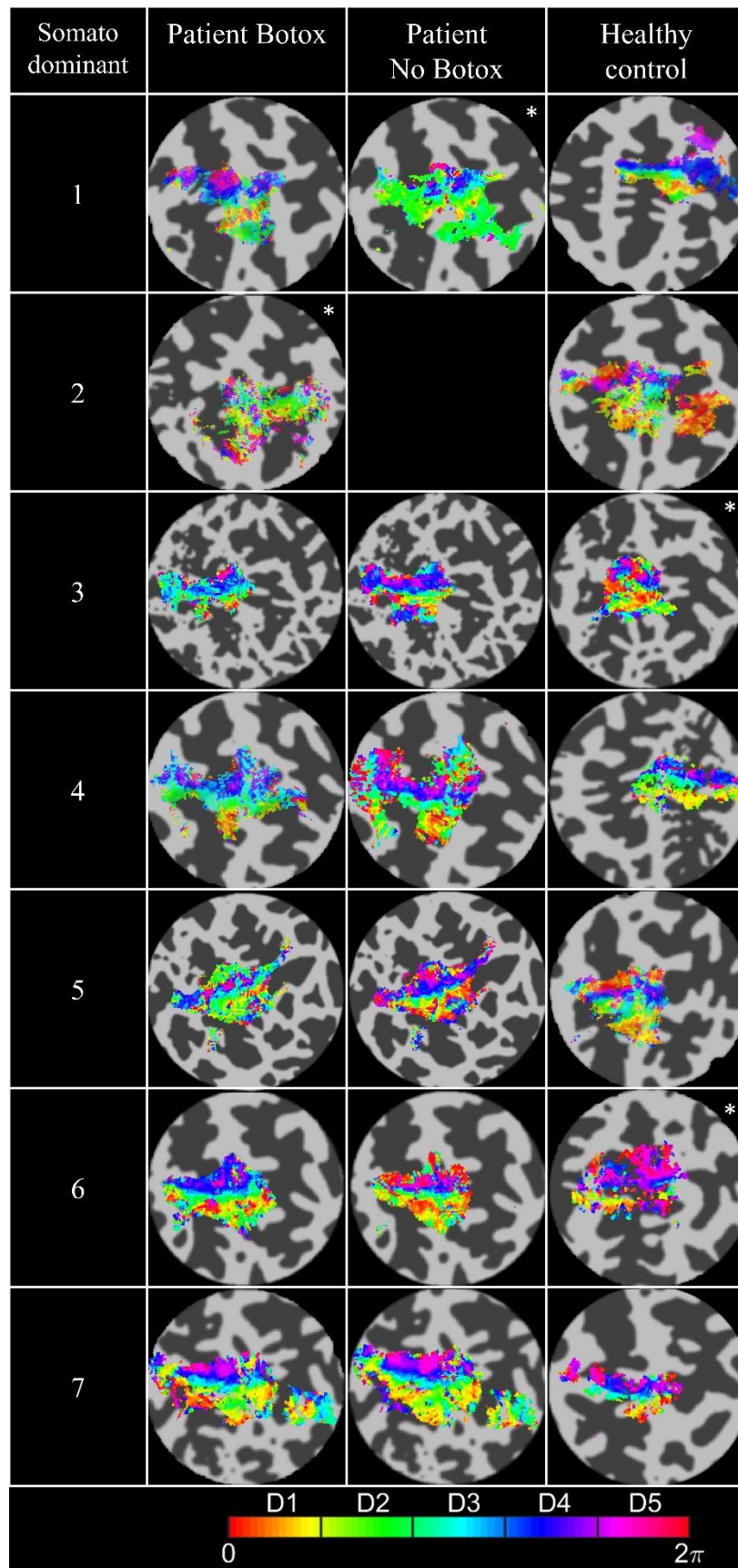


Figure 7.13. Somatosensory travelling wave phase maps (dominant/affected hand) from phase analysis for all subjects, in contralateral hemisphere. Data not collected for subject 2 as subject did not return for no Botox scan. Disordered digit maps are marked with an asterisk.

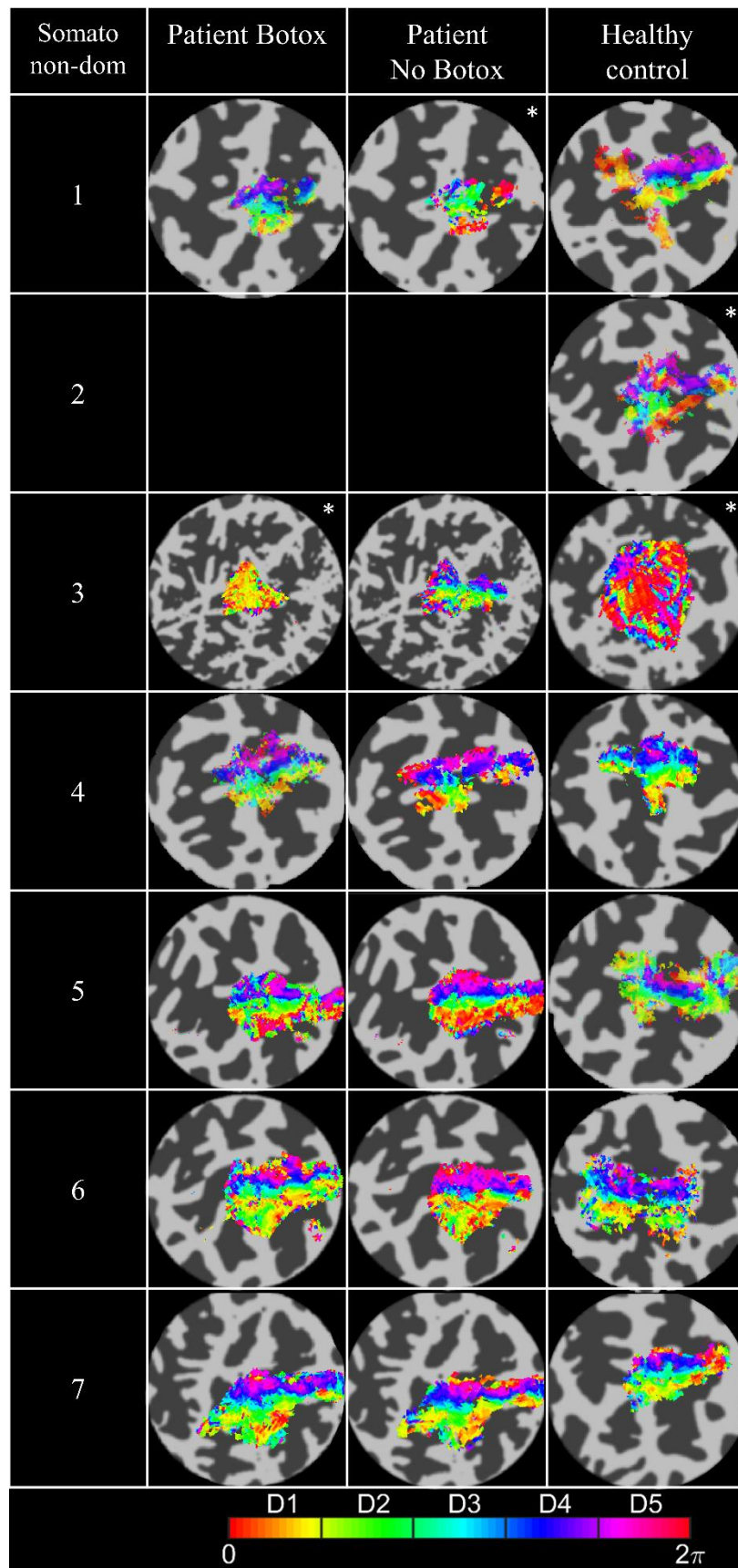


Figure 7.14. Somatosensory travelling wave phase maps (non-dominant/non-affected hand) for all subjects, in contralateral hemisphere. Data not collected for Subject 2 as subject had no non-dominant hand. Disordered digit maps are marked with an asterisk.

7.4.2.2 GLM Results

GLM analysis of the motor and somatosensory travelling wave paradigms produced activation of individual digits in the contralateral hemisphere. These are shown for each hand for the somatosensory paradigm (Figure 7.16A&B) and for the dominant hand for the motor paradigm (Figure 7.16C) for an example FHD patient (Subject 6). The expected progression of digits can be seen and individual digits were able to be distinguished. Comparing Figure 7.16A&B (somatosensory task) with Figure 7.16C (motor task), it can be seen that the motor task produced stronger activation than the somatosensory task, which was also observed for the phase analysis. Individual digit beta weights from the GLMs were combined and the maximum beta weight per voxel was found to produce a map of all 5 digits. The resulting maps of digit representations are shown for all subjects in Figure 7.17 (somatosensory affected hand), Figure 7.18 (somatosensory non-affected hand) and Figure 7.19 (motor affected hand).

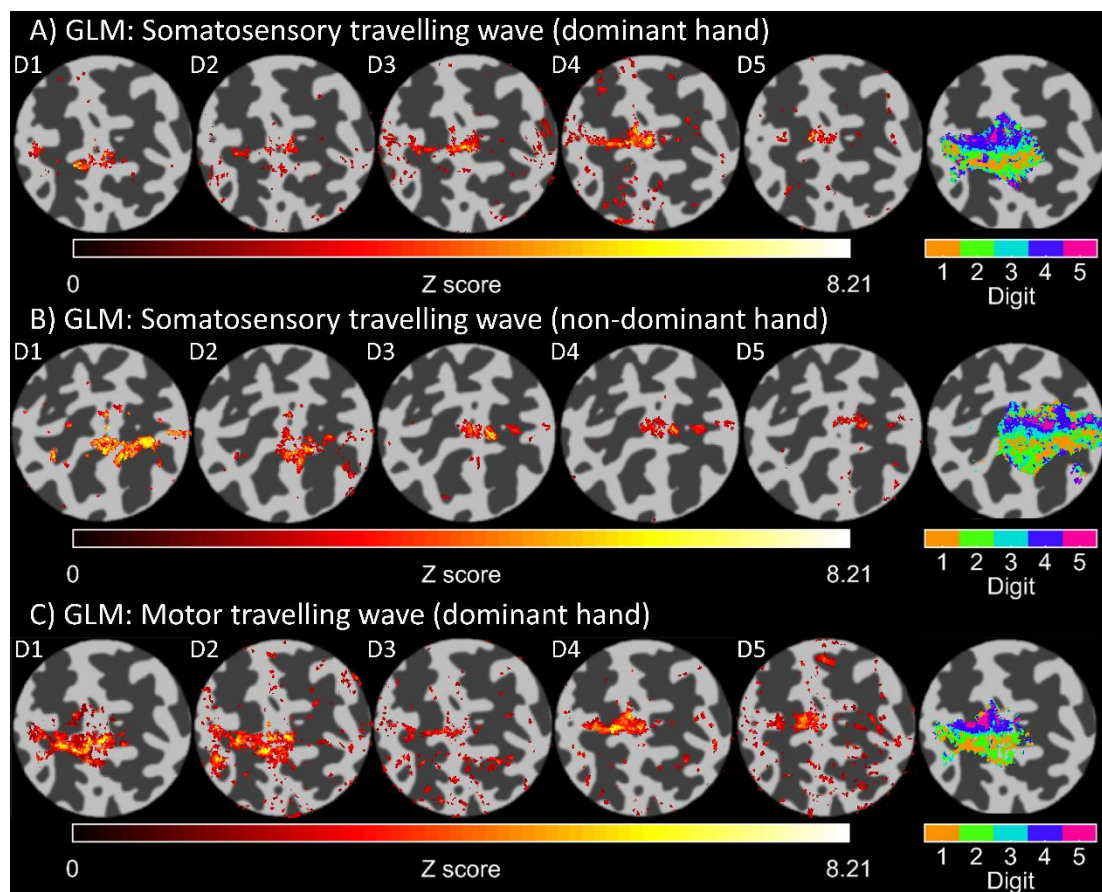


Figure 7.16. GLM analysis of (A) somatosensory travelling wave in right (dominant and affected) hand, (B) left (non-dominant and non-affected) hand and (C) motor travelling wave in right (dominant and affected) hand. Showing activation (FDR corrected Z-score) in the contralateral hemisphere to stimulation, for the same patient as Figure 7.12. Right image shows the individual digits combined using winner-takes-all analysis.

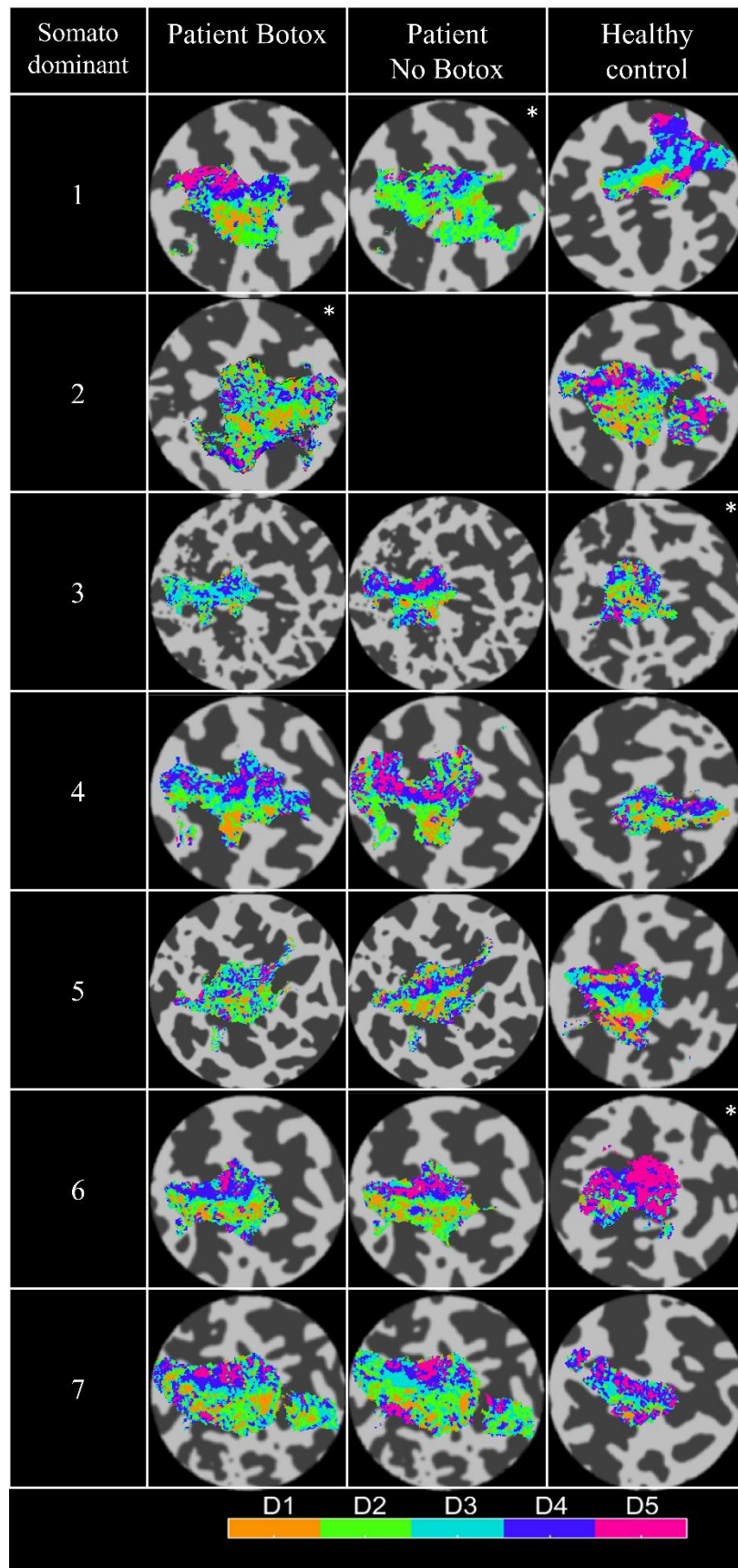


Figure 7.17. GLM winner takes all analysis of somatosensory travelling wave from affected/dominant hand in contralateral hemisphere. Data missing for subject 2 as subject did not return for no Botox scan. Disordered digit maps are marked with an asterisk.

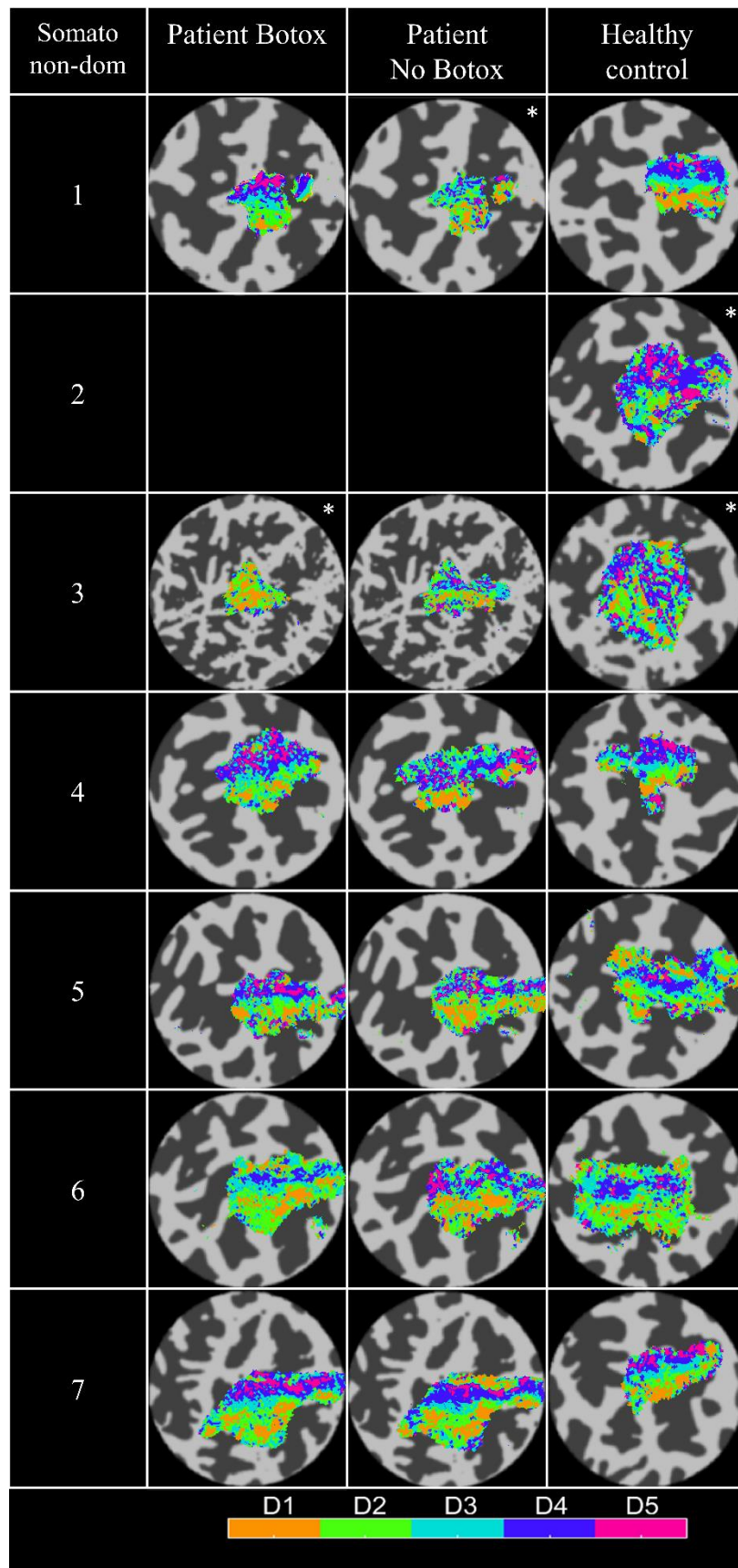


Figure 7.18. GLM winner-takes-all analysis of somatosensory travelling wave from non-dominant/non-affected hand, in contralateral hemisphere. Data missing for subject 2 as subject had no non-dominant hand. Disordered digit maps are marked with an asterisk.

7.4.2.3 Comparison of GLM and Phase Analysis Digit Maps

Maps of digit representations from the GLM winner-takes-all analysis and phase analysis of the same scans were compared. Figure 7.20 shows a GLM winner-takes-all and phase analysis map for an example subject (Subject 6, whose data is also shown in Figure 7.12 and Figure 7.16) for the motor and somatosensory tasks. Qualitatively, the two analysis methods can be seen to show good agreement for this subject. To quantitatively compare the two methods across all subjects, the Dice coefficient between the GLM winner-takes-all and phase maps was computed for each digit. The average Dice coefficient matrices across subjects are shown in Figure 7.21. The Dice coefficient for each digit (diagonal elements of the Dice matrix) averaged across subjects for each of the tasks is shown in Figure 7.22. Individual results are shown in Appendix C. The overall mean Dice coefficient across all subjects and digits was 0.64 ± 0.17 for the motor task (dominant/affected hand), compared to 0.50 ± 0.15 (dominant/affected hand) and 0.49 ± 0.19 (non-dominant/unaffected hand) for the somatosensory task. Since the Dice coefficient shows good agreement between the two analysis methods for the motor scans, this validates the use of the GLM analysis for a travelling wave paradigm, where commonly the phase analysis is used. However, the Dice coefficients for the somatosensory task, on both the dominant and non-dominant hand is lower, indicating less similarity. As a result, the motor maps are used to assess overlap of digit measures, but the somatosensory maps are not analysed further in this Chapter.

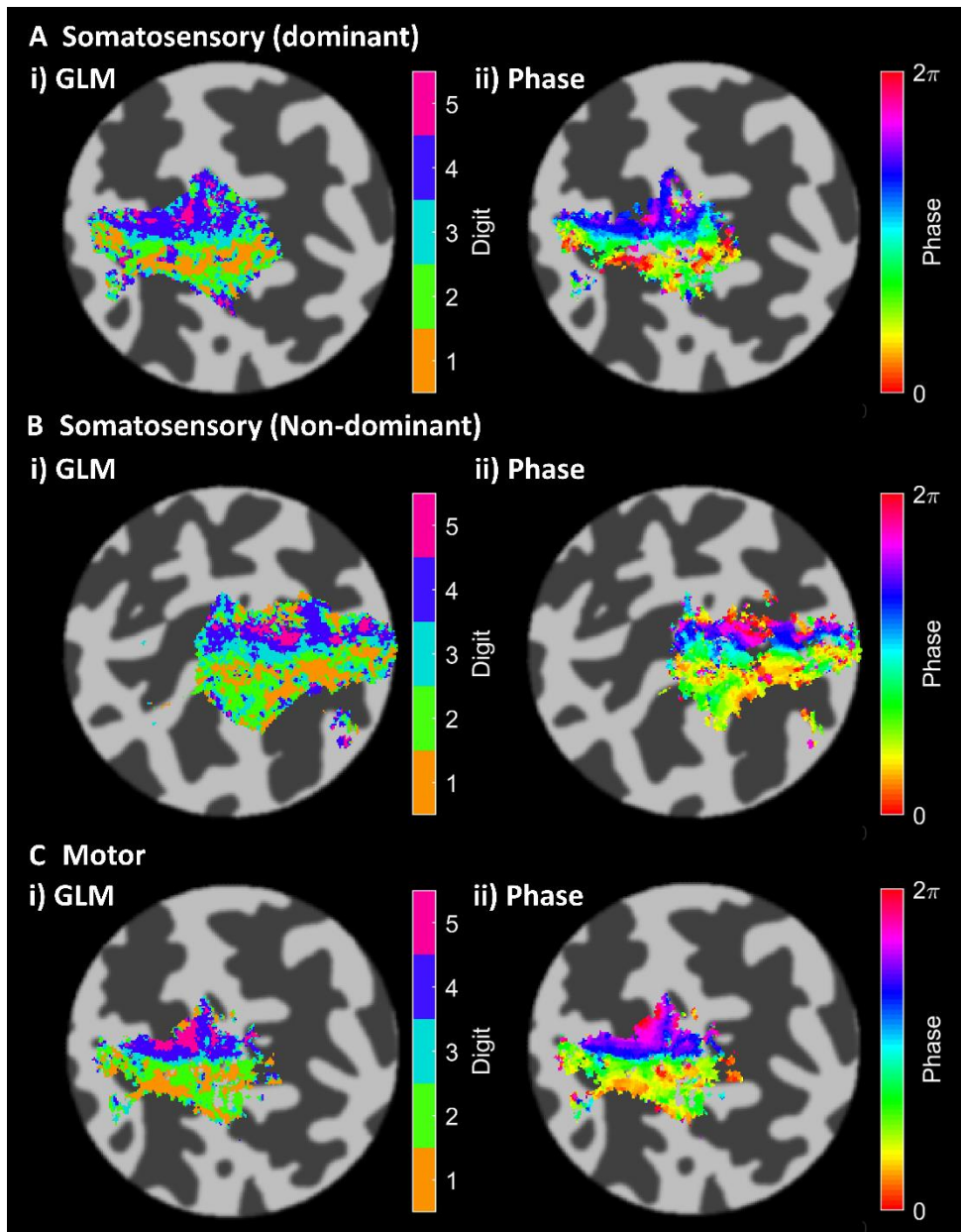


Figure 7.20. GLM winner-takes-all analysis (left) compared with phase analysis (right) for (A) somatosensory dominant hand, (B) somatosensory non-dominant hand and (C) motor (dominant hand) for Subject 6 (same subject as previous figures).

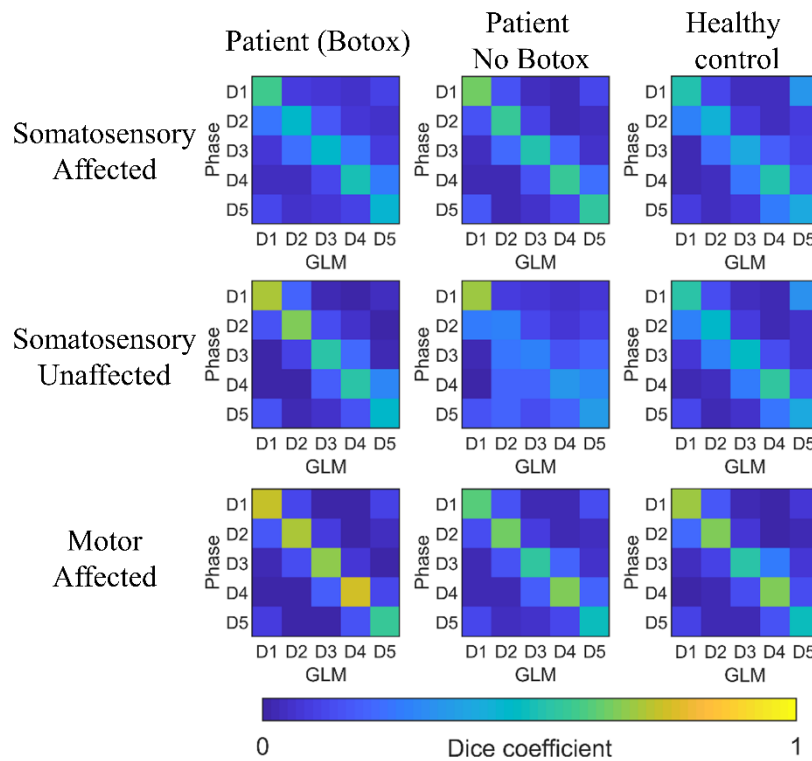


Figure 7.21. Dice coefficient matrices between digits of the winner-takes-all GLM analysis and phase analysis averaged over subjects for somatosensory travelling wave on affected hand (top row), somatosensory unaffected hand (middle row) and motor task on affected hand (bottom row) averaged across subjects for patients with Botox (first column) patients with no Botox (middle column) and healthy controls (last column).

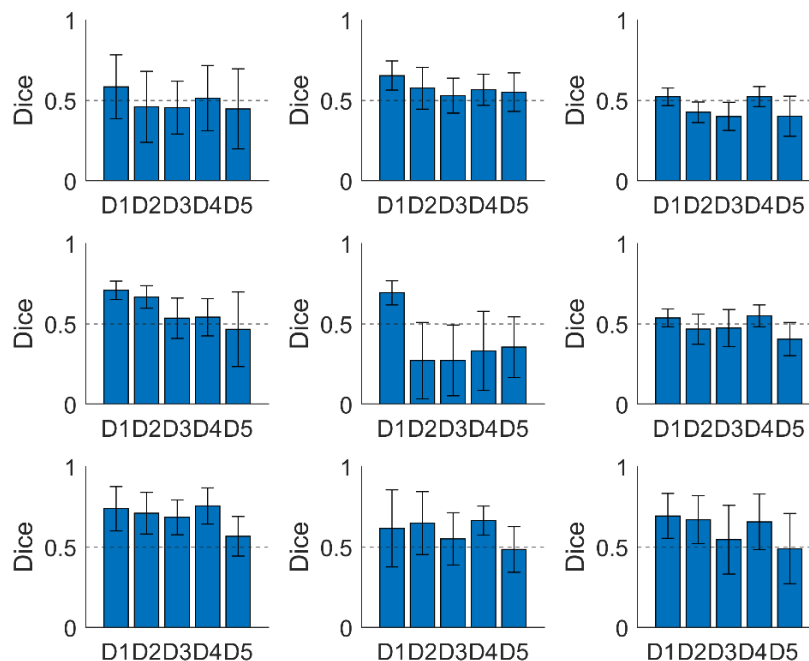


Figure 7.22. Dice coefficient between digit maps from the winner-takes-all GLM analysis and phase analysis (diagonal of Figure 7.21) averaged over subjects for somatosensory travelling wave on affected hand (top row), somatosensory unaffected hand (middle row) and motor task on affected hand (bottom row) averaged across subjects for patients with Botox (first column) patients with no Botox (middle column) and healthy controls (last column).

7.4.2.4 Digit Overlap Measures

Since Section 7.4.2.3 showed that the GLM method produces more robust digit maps for the motor task than the somatosensory task, the GLM results for the motor task were investigated further to assess overlap of digit representation. The resulting normalised beta values are shown in Figure 7.23. As expected, the plots show strongest beta weights in the digit that was stimulated, but also shows considerable overlap with neighbouring digits, with high beta weights in these digits too. The average Gaussian fit is shown in Figure 7.24.

The mean width (averaged over all digits \pm standard deviation) was 1.34 ± 0.04 , 1.5 ± 0.2 and 1.35 ± 0.03 for FHD patients with Botox, FHD patients no Botox and healthy controls respectively (Figure 7.25). The FHD patients with Botox treatment and healthy controls were very similar, whilst the width for the patients with no Botox was the largest (Figure 7.25), however, there was no significant difference between the three groups (Kruskal-Wallis test, $p = 0.6$).

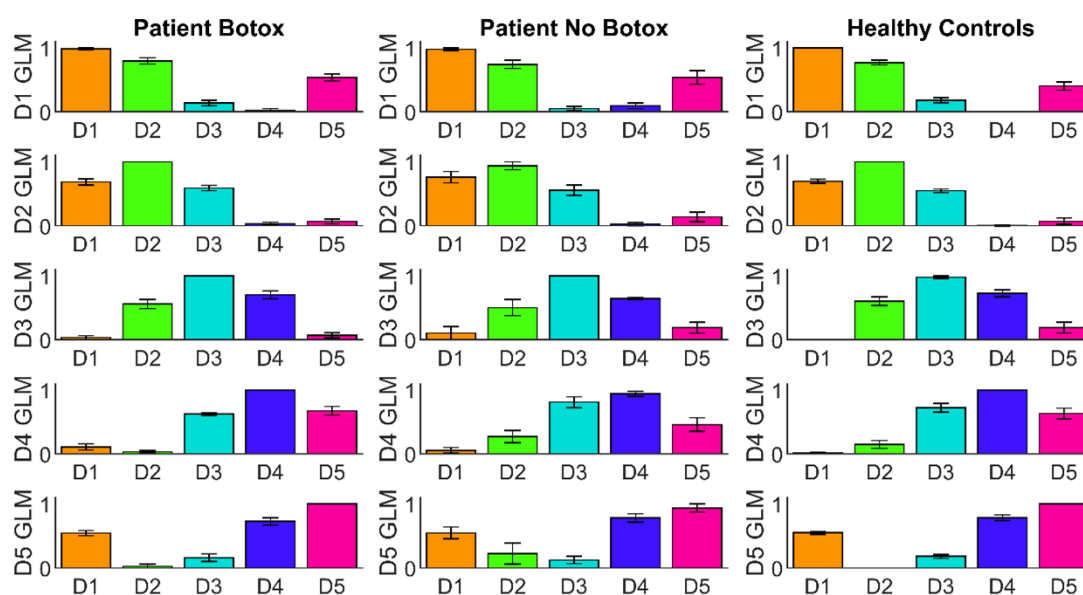


Figure 7.23. Digit overlap in patients with Botox, patients no Botox and healthy controls from motor experiment, showing the average normalised beta weight from the individual digit GLM (y-axis) in each digit ROI (x-axis).

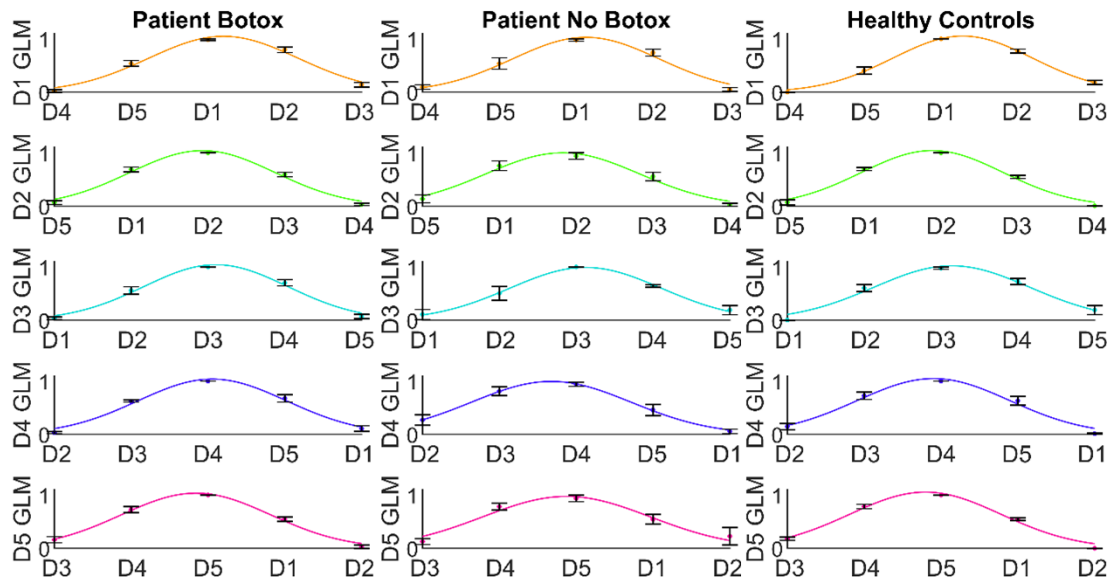


Figure 7.24. Average Gaussian fitted to digits for healthy controls, patients with Botox and patients no Botox in the motor experiment.

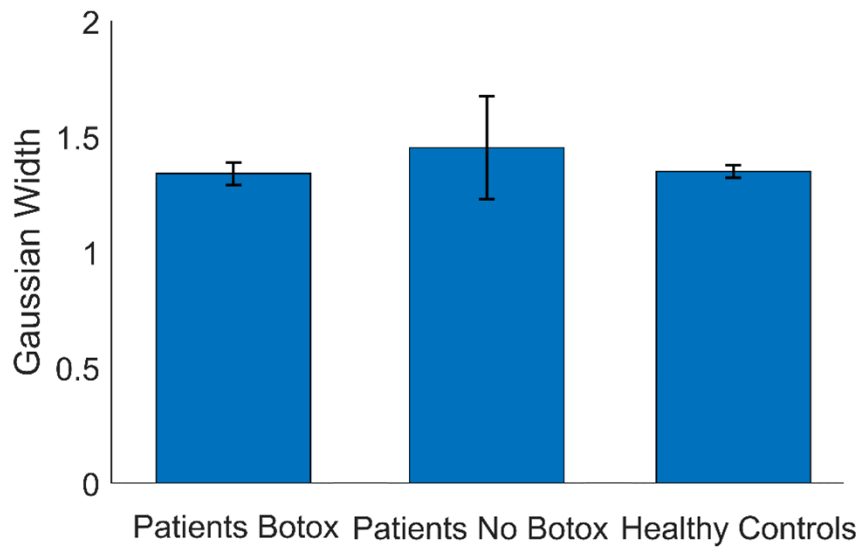


Figure 7.25 Average width of Gaussian fitted to beta weights (representing overlap) for patients with Botox, patients no Botox and healthy controls.

7.5 Discussion

The results in this chapter show that there was only a significant difference in spatial discrimination threshold (SDT) between patients with FHD and matched healthy controls (Figure 7.8) but no difference in amplitude or temporal threshold between groups (Figure 7.10 and Figure 7.11). Using UHF MRI, digit representations for a motor and somatosensory travelling wave paradigm were mapped onto the cortex for both healthy controls and patients with FHD (Figure 7.13, Figure 7.14 and Figure 7.15). It was also shown that in addition to the established phase analysis methods used to assess digit representation with travelling wave paradigms, GLM analyses of these data could produce similar maps of the digit representation if the BOLD response was sufficiently robust, as found for the motor paradigm (Figure 7.19). Using a GLM allowed assessment of overlap in the cortical representation of the digits. This assessment indicated that there may be greater overlap of digit representations in the somatosensory cortex of the patients with no Botox treatment compared to when they had Botox treatment to help their symptoms or their matched healthy controls.

7.5.1 Behavioural Measures

SDT of the dominant hand was found to be raised in patients with FHD (2.9 ± 0.9 mm/ 2.8 ± 0.9 mm for Botox/ no-Botox) compared to healthy controls (1.8 ± 0.2 mm), in agreement with previous literature which have shown spatial acuities in healthy controls to be on the order of 1 to 2 mm (Grant et al., 2006; Molloy et al., 2003; Sanger et al., 2001; Zeuner et al., 2002), consistent with the finding here. Previous literature has shown SDT of patients with FHD to be raised by the order of 1 mm compared with healthy controls, in agreement with this study (Figure 7.8). This shows that FHD affects sensory discrimination levels. Furthermore, it was shown that SDT correlated with age, as has previously been shown (Molloy et al., 2003). Whilst the correlation was over all three groups, the correlation was driven by the patients, suggesting that SDT might not correlate with age in the general population but does with FHD. It would be interesting to explore whether SDT correlated with years since onset of illness, however these data were not available.

However, no clear difference was observed between SDT of patients with and without Botox treatment, suggesting no change due to the effects of Botox in this measure. Previous literature has shown that SDT scores improved 1 month after Botox injection

(Walsh & Hutchinson, 2007), suggesting that here it would be hypothesised that SDT with Botox treatment would be lower than SDT with no treatment and more similar to controls. The lack of difference between Botox and no Botox here could be due to small sample size, as Walsh et al. compared 20 patients. A limiting factor in the grating orientation task was that it was only performed on the index finger of the affected hand, which is not necessarily where the dystonia is localised in all the patients (for example, some subjects may experience most severe symptoms in their thumb).

No significant difference was observed between groups in the amplitude or temporal threshold assessments, contrary to other studies (Bara-Jimenez et al., 2000; Sanger et al., 2001). This may be due to these tests having higher coefficients of variation between sessions than the SDT test. The coefficients of variation were in line with previous literature (Mikkelsen et al., 2020), suggesting that the tests were performed in line with previous studies, however with a lower sample size. Therefore, it is most likely that the lack of significant effect is because of the small sample size in this study ($n = 7$), and any differences between patient and controls are within the coefficient of variation and therefore not detectable. Previous studies where significant behavioural effects were seen had cohorts of 9 to 15 patients (Bara-Jimenez et al., 2000; Mikkelsen et al., 2020; Sanger et al., 2001).

A significant difference was seen between the two types of temporal discrimination test (piezoelectric stimulators and Brain Gauge device). This is likely to be due to the fact that the Brain Gauge device has a larger area of contact with the finger. The Brain Gauge device also had a lower coefficient of variation suggesting it is a more reproducible measure of TDT. Despite this, no differences were seen in temporal discrimination thresholds between patients and controls for the Brain Gauge device.

7.5.2 fMRI

This study is consistent with previous studies (Besle et al., 2013; Sanchez-Panchuelo et al., 2010), which showed that the travelling wave paradigm is a robust and reproducible method to assess functional organisation in somatosensory cortex. The maps of digit representations showed the expected ordering of digits (Penfield & Rasmussen, 1950), with D1 more lateral, anterior and inferior to the location of D5. This corroborates a great deal of previous work which showed that the digits are represented cortically in an organised manner.

Despite the hypothesis and previous work (Bara-Jimenez et al., 1998; McKenzie et al., 2003; Meunier et al., 2001) suggesting that patients with FHD would show disordered representations, no clear differences were observed in the amount of disorder between the digit representations of the patients with FHD and age-matched healthy controls in this small group. Previous work has commonly reported differences in cortical distance between digit representations (Bara-Jimenez et al., 1998; Butterworth et al., 2003; Nelson et al., 2009) however in this chapter cortical distances were not compared. Analysis has previously been performed on these data (Asghar, 2019) which showed no difference in digit distance between patients and controls, and was not the main aim of this thesis. In fact, previous measures of distance (Butterworth et al., 2003) are limited as they involve measuring peak t-stat locations on folded brains, which does not take into consideration individual anatomical differences. Instead, a better approach would be to compare individual digit representations to a probabilistic atlas (O'Neill et al., 2020).

There are several possible explanations for the lack of difference between controls and patients seen in this chapter. The first is that the previous studies were at lower spatial resolution, since surface electrophysiology used in Bara-Jimenez et al. (Bara-Jimenez et al., 1998) has inherently lower spatial resolution than fMRI, and 3T fMRI used in Butterworth et al. and Nelson et al. was at lower spatial resolution (3 mm and 2.08 mm voxels respectively) (Butterworth et al., 2003; Nelson et al., 2009) than this study where voxel size was 1.5 mm. In addition, there is less spatial specificity at 3 T due to the signal being more intravenously weighted than at 7 T, again reducing the spatial accuracy of the previous work compared with this study. Despite this lower spatial accuracy in previous studies at lower field strength, a recent study (Mancini et al., 2019) using fMRI at 3 T investigated somatotopic representation in patients with chronic pain conditions, which were hypothesised to cause reorganisation of somatotopic representation of the affected limb. However, the authors found digit representation between affected and unaffected hands of patients and between patients and healthy controls to be comparable, contradicting the hypothesis. This recent work supports the results presented here, leading to the hypothesis that focal hand dystonia does not relate to gross map reorganisation.

Another possible explanation for this discrepancy is the effectiveness of the Botox treatment. The fact that patient and healthy control maps are comparable could be a

sign that the Botox treatment is working, as all patients regularly receive Botox injections, which could imply that Botox treatment is affecting cortical digit representations. Yet, if this were the case, it might be expected that there would be large differences in maps between Botox and no Botox scans, which was not found. No behavioural differences were seen between the Botox and no Botox scans also. It could be possible that the Botox had not completely worn off in the no Botox scan, despite acquiring the data on patients at least 3 months after their last injection. Botox injections are administered every 3 months so this was the longest gap that could be left. However, sometimes patients reported that the beneficial effects can last longer which perhaps is what is seen in these data. Still, this would not explain why SDT was raised in patients compared to controls but digit maps were similar.

It has been noted in a previous study (Kolasinski et al., 2016) that there are large amounts of inter-subject variability in digit representation maps. Therefore, it may be that the difference between subjects is much larger than any difference due to FHD, as much larger differences in anatomical and functional architecture obscure any subtle changes due to FHD. If this is the case, it is possible that such changes may be revealed with a larger group size, and across a much wider range of disease severity.

Comparing somatosensory and motor responses, the spatial location of the activation from the two tasks was similar. Despite aiming to evoke only a motor response by using finger tapping in the air for the motor task, a large response is seen in somatosensory cortex for the motor task. This is in agreement with what has previously been observed when a similar motor task was performed (Kolasinski et al., 2016). The similarity between responses of the two tasks suggests that finger-moving motor tasks do produce a largely somatosensory response. This suggest strong interplay between motor and somatosensory cortex. Interestingly, the response to the motor task was more robust (better correlation in the phase analysis and higher Z score in the GLM analysis) than the somatosensory task (Figure 7.12 and Figure 7.16). This could be because the motor task was more active than the somatosensory task thus requiring greater cortical recruitment. In future, it may be feasible to only use the motor task to assess cortical digit representations, rather than the somatosensory task.

Whilst the maps were largely the same between the phase and GLM analysis methods (see Figure 7.20), using the GLM method allowed measurement of overlap between

digit representations during the motor task. Overlap measures showed that cortical activation for a given fingertip overlaps with cortical activation for other fingertips (Figure 7.23 and Figure 7.24). This effect was most strongly seen in the adjacent digits (e.g. D2 and D4 are most likely to overlap with D3), in agreement with previous literature (Besle et al., 2014). An increase in digit overlap was found for patients with no Botox compared to patients with Botox treatment and healthy controls, however, this was not statistically significant. Again, this could be due to small cohort size, or, it could imply that patients do not have more organisational blurring than healthy controls. Further investigation using the methods developed here is therefore warranted. In addition, the methods used here could also be applied to other pathologies which are believed to affect the sensorimotor cortex and particularly the hands, although in principle there is no reason such methods could not be expanded to investigate the cortical representation of other body parts.

Limitations and Future Work

One limitation of this study was the low number of patients, which may have resulted in limited statistical power to determine differences between groups. However, all the patients available that were being treated by the neurologist were invited to take part in the study. Out of this limited number of patients, in some cases patients were claustrophobic and so could not go in the 7 T scanner, due to its long and narrow bore. This is a problem if 7 T MRI is to be used clinically and needs to be made more patient friendly. Another issue is that two of the patients recruited and scanned were removed from the analysis due to large motion artefacts during the scans. In future, to improve motion artefacts, real-time motion tracking could be used which corrects fMRI data in real-time rather than retrospectively (Speck et al., 2006). However there are challenges with implementing this at 7 T and work is ongoing (Bortolotti et al., 2020). The scan session could also be shortened, to reduce scan time and chance of movement, however scans were already optimised to minimise acquisition time by using the travelling wave paradigm and SENSE and multiband to accelerate the acquisition. As mentioned previously, it could be suggested to only use the motor paradigm in future as this was more robust than the somatosensory paradigm, which would save time.

In some patients and healthy controls, ordered digit maps were not produced. One possible explanation for this could be motion during the scans. Whilst data were motion

corrected and motion was ensured to be less than 1.5 mm (1 voxel), it could be that movement occurred between scans, which is an issue as the forward and reverse scans are combined in the travelling wave analysis which will affect the phase.

It is important to note that throughout this chapter analysis was performed on the maps generated in the contralateral hemisphere to the stimulated hand. Future work will also investigate whether any responses were observed on the ipsilateral hemisphere, particularly for the digit overlap. Such investigation would allow exploration of interhemispheric sensorimotor communication, and whether it breaks down in the patients. The scan session also involved a resting state scan and event-related paradigm, the analysis of which is beyond the scope of this thesis. Future work will investigate whether there are any differences in the functional connectivity of resting state networks between patients and healthy controls, as well as analyse the event-related on-off paradigm. All of these analyses will clearly complement the work presented here to get a fuller picture of the source of the problem in FHD.

7.6 Conclusion

This chapter has shown that high-resolution 7 T fMRI can be used in a clinical population to produce maps of somatosensory representations of fingertips in individual patients. However, no difference between patient and healthy control maps was evident in this small cohort, suggesting that FHD does not cause cortical reorganisation. It was shown that it is possible to measure overlap of individual digits in a travelling wave paradigm by using GLM analysis. This analysis revealed a slight difference between the digit overlap when patients with FHD had been treated with Botox compared with when they had no Botox. This effect was not significant but this may be due to the small cohort and warrants further investigation in a larger sample size.

7.7 References

- Asghar, M. (2019). *Sensory mapping using High-Resolution 7 T fMRI*. (PhD), University of Nottingham. Retrieved from <http://eprints.nottingham.ac.uk/56234/>
- Bara-Jimenez, W., Catalan, M. J., Hallett, M., & Gerloff, C. (1998). Abnormal somatosensory homunculus in dystonia of the hand. *Annals of Neurology*, *44*(5), 828-831.
- Bara-Jimenez, W., Shelton, P., Sanger, T. D., & Hallett, M. (2000). Sensory discrimination capabilities in patients with focal hand dystonia. *Annals of Neurology*, *47*(3), 377-380.
- Besle, J., Sánchez-Panchuelo, R.-M., Bowtell, R., Francis, S., & Schluppeck, D. (2013). Single-subject fMRI mapping at 7 T of the representation of fingertips in S1: a comparison of event-related and phase-encoding designs. *Journal of Neurophysiology*, *109*(9), 2293-2305.
- Besle, J., Sánchez-Panchuelo, R.-M., Bowtell, R., Francis, S., & Schluppeck, D. (2014). Event-related fMRI at 7T reveals overlapping cortical representations for adjacent fingertips in S1 of individual subjects. *Human Brain Mapping*, *35*(5), 2027-2043.
- Bortolotti, L., Mougin, O., & Bowtell, R. (2020). Measurement of head motion using a field camera in a 7T scanner. *Oral presentation presented at ISMRM virtual conference 2020*, 0464.
- Breakefield, X. O., Blood, A. J., Li, Y., Hallett, M., Hanson, P. I., & Standaert, D. G. (2008). The pathophysiological basis of dystonias. *Nature Reviews Neuroscience*, *9*(3), 222-234.
- Butterworth, S., Francis, S., Kelly, E., McGlone, F., Bowtell, R., & Sawle, G. V. (2003). Abnormal cortical sensory activation in dystonia: An fMRI study. *Movement Disorders*, *18*(6), 673-682.
- Byrnes, M. L., Thickbroom, G. W., Wilson, S. A., Sacco, P., Shipman, J. M., Stell, R., & Mastaglia, F. L. (1998). The corticomotor representation of upper limb muscles in writer's cramp and changes following botulinum toxin injection. *Brain*, *121*(5), 977-988.
- Diedrichsen, J., Wiestler, T., & Ejaz, N. (2013). A multivariate method to determine the dimensionality of neural representation from population activity. *Neuroimage*, *76*, 225-235.
- Dresel, C., Li, Y., Wilzeck, V., Castrop, F., Zimmer, C., & Haslinger, B. (2014). Multiple changes of functional connectivity between sensorimotor areas in focal hand dystonia. *Journal of Neurology, Neurosurgery & Psychiatry*, *85*(11), 1245.
- dystonia.org.uk. (2019). <https://www.dystonia.org.uk/what-is-dystonia>.
- Engel, S. A., Glover, G. H., & Wandell, B. A. (1997). Retinotopic organization in human visual cortex and the spatial precision of functional MRI. *Cerebral Cortex*, *7*(2), 181-192.
- Fischl, B. (2012). FreeSurfer. *Neuroimage*, *62*(2), 774-781.
- Francis, S. T., Kelly, E. F., Bowtell, R., Dunseath, W. J. R., Folger, S. E., & McGlone, F. (2000). fMRI of the Responses to Vibratory Stimulation of Digit Tips. *Neuroimage*, *11*(3), 188-202.
- Gardner, J. L., Merriam, E. P., Schluppeck, D., Besle, J., & Heeger, D. J. (2018). mrTools: analysis and visualization package for functional magnetic resonance imaging data. *Zenodo*, June, 28.

- Giladi, N. (1997). The mechanism of action of Botulinum toxin type A in focal dystonia is most probably through its dual effect on efferent (motor) and afferent pathways at the injected site. *Journal of the Neurological Sciences*, *152*(2), 132-135.
- Glover, G. H., Li, T. Q., & Ress, D. (2000). Image-based method for retrospective correction of physiological motion effects in fMRI: RETROICOR. *Magnetic Resonance in Medicine: An Official Journal of the International Society for Magnetic Resonance in Medicine*, *44*(1), 162-167.
- Grant, A. C., Fernandez, R., Shilian, P., Yanni, E., & Hill, M. A. (2006). Tactile spatial acuity differs between fingers: A study comparing two testing paradigms. *Perception & Psychophysics*, *68*(8), 1359-1362.
- Hallett, M. (1995). Is dystonia a sensory disorder? *Annals of Neurology*, *38*(2), 139-140.
- Hinkley, L. B. N., Webster, R. L., Byl, N. N., & Nagarajan, S. S. (2009). Neuroimaging Characteristics of Patients with Focal Hand Dystonia. *Journal of Hand Therapy*, *22*(2), 125-135.
- Jacobs, M. F., Tsang, P., Lee, K. G. H., Asmussen, M. J., Zapallow, C. M., & Nelson, A. J. (2014). 30 Hz Theta-burst Stimulation Over Primary Somatosensory Cortex Modulates Corticospinal Output to the Hand. *Brain Stimulation*, *7*(2), 269-274.
- Kolasinski, J., Makin, T. R., Jbabdi, S., Clare, S., Stagg, C. J., & Johansen-Berg, H. (2016). Investigating the Stability of Fine-Grain Digit Somatotopy in Individual Human Participants. *The Journal of Neuroscience*, *36*(4), 1113.
- Mancini, F., Wang, A. P., Schira, M. M., Isherwood, Z. J., McAuley, J. H., Iannetti, G. D., Sereno, M. I., Moseley, G. L., & Rae, C. D. (2019). Fine-grained mapping of cortical somatotopies in chronic complex regional pain syndrome. *Journal of Neuroscience*, *39*(46), 9185-9196.
- McKenzie, A., Nagarajan, S., Roberts, T., Merzenich, M., & Byl, N. (2003). Somatosensory representation of the digits and clinical performance in patients with focal hand dystonia. *American Journal of Physical Medicine & Rehabilitation*, *82*(10), 737-749.
- Meunier, S., Garnero, L., Ducorps, A., Mazières, L., Lehericy, S., Tézenas Du Montcel, S., Renault, B., & Vidailhet, M. (2001). Human brain mapping in dystonia reveals both endophenotypic traits and adaptive reorganization. *Annals of Neurology*, *50*(4), 521-527.
- Mikkelsen, M., He, J., Tommerdahl, M., Edden, R. A., Mostofsky, S. H., & Puts, N. A. (2020). Reproducibility of flutter-range vibrotactile detection and discrimination thresholds. *Scientific Reports*, *10*(1), 1-14.
- Molloy, F. M., Carr, T. D., Zeuner, K. E., Dambrosia, J. M., & Hallett, M. (2003). Abnormalities of spatial discrimination in focal and generalized dystonia. *Brain*, *126*(10), 2175-2182.
- Naito, E., Roland, P. E., Grefkes, C., Choi, H., Eickhoff, S., Geyer, S., Zilles, K., & Ehrsson, H. H. (2005). Dominance of the right hemisphere and role of area 2 in human kinesthesia. *Journal of Neurophysiology*, *93*(2), 1020-1034.
- Nelson, A. J., Blake, D. T., & Chen, R. (2009). Digit-specific aberrations in the primary somatosensory cortex in Writer's cramp. *Annals of Neurology*, *66*(2), 146-154.
- O'Neill, G. C., Sengupta, A., Asghar, M., Barratt, E. L., Besle, J., Schluppeck, D., Francis, S. T., & Sanchez Panchuelo, R. M. (2020). A probabilistic atlas of finger dominance in the primary somatosensory cortex. *Neuroimage*, *217*, 116880.

- Overduin, S. A., d'Avella, A., Carmena, J. M., & Bizzi, E. (2012). Microstimulation activates a handful of muscle synergies. *Neuron*, *76*(6), 1071-1077.
- Penfield, W., & Boldrey, E. (1937). Somatic motor and sensory representation in the cerebral cortex of man as studied by electrical stimulation. *Brain*, *60*(4), 389-443.
- Penfield, W., & Rasmussen, T. (1950). *The cerebral cortex of man; a clinical study of localization of function*.
- Platz, T., Roschka, S., Christel, M. I., Duecker, F., Rothwell, J. C., & Sack, A. T. (2012). Early stages of motor skill learning and the specific relevance of the cortical motor system – a combined behavioural training and theta burst TMS study. *Restorative Neurology and Neuroscience*, *30*, 199-211.
- Porro, C. A., Francescato, M. P., Cettolo, V., Diamond, M. E., Baraldi, P., Zuiani, C., Bazzocchi, M., & Di Prampero, P. E. (1996). Primary motor and sensory cortex activation during motor performance and motor imagery: a functional magnetic resonance imaging study. *Journal of Neuroscience*, *16*(23), 7688-7698.
- Puce, A., Constable, R. T., Luby, M. L., McCarthy, G., Nobre, A. C., Spencer, D. D., Gore, J. C., & Allison, T. (1995). Functional magnetic resonance imaging of sensory and motor cortex: comparison with electrophysiological localization. *83*(2), 262.
- Sakai, K., Watanabe, E., Onodera, Y., Itagaki, H., Yamamoto, E., Koizumi, H., & Miyashita, Y. (1995). Functional Mapping of the Human Somatosensory Cortex with Echo-Planar MRI. *Magnetic Resonance in Medicine*, *33*(5), 736-743.
- Sánchez-Panchuelo, R.-M., Besle, J., Mougín, O., Gowland, P., Bowtell, R., Schluppeck, D., & Francis, S. (2014). Regional structural differences across functionally parcellated Brodmann areas of human primary somatosensory cortex. *Neuroimage*, *93*, 221-230.
- Sanchez-Panchuelo, R. M., Francis, S., Bowtell, R., & Schluppeck, D. (2010). Mapping Human Somatosensory Cortex in Individual Subjects With 7T Functional MRI. *Journal of Neurophysiology*, *103*(5), 2544-2556.
- Sanger, T. D., Tarsy, D., & Pascual-Leone, A. (2001). Abnormalities of spatial and temporal sensory discrimination in writer's cramp. *Movement Disorders*, *16*(1), 94-99.
- Speck, O., Hennig, J., & Zaitsev, M. (2006). Prospective real-time slice-by-slice motion correction for fMRI in freely moving subjects. *Magnetic Resonance Materials in Physics, Biology and Medicine*, *19*(2), 55.
- Thickbroom, G. W., Byrnes, M. L., Stell, R., & Mastaglia, F. L. (2003). Reversible reorganisation of the motor cortical representation of the hand in cervical dystonia. *Movement Disorders*, *18*(4), 395-402.
- Vidoni, E. D., Acerra, N. E., Dao, E., Meehan, S. K., & Boyd, L. A. (2010). Role of the primary somatosensory cortex in motor learning: An rTMS study. *Neurobiology of Learning and Memory*, *93*(4), 532-539.
- Walsh, R., & Hutchinson, M. (2007). Molding the sensory cortex: Spatial acuity improves after botulinum toxin treatment for cervical dystonia. *Movement Disorders*, *22*(16), 2443-2446.
- Wiestler, T., & Diedrichsen, J. (2013). Skill learning strengthens cortical representations of motor sequences. *Elife*, *2*, e00801.
- Woolsey, C. N., Erickson, T. C., & Gilson, W. E. (1979). Localization in somatic sensory and motor areas of human cerebral cortex as determined by direct recording of evoked potentials and electrical stimulation. *Journal of Neurosurgery*, *51*(4), 476-506.

- Yacoub, E., Shmuel, A., Pfeuffer, J., Van De Moortele, P.-F., Adriany, G., Andersen, P., Vaughan, J. T., Merkle, H., Ugurbil, K., & Hu, X. (2001). Imaging brain function in humans at 7 Tesla. *Magnetic Resonance in Medicine*, 45(4), 588-594.
- Zeuner, K. E., Bara-Jimenez, W., Noguchi, P. S., Goldstein, S. R., Dambrosia, J. M., & Hallett, M. (2002). Sensory training for patients with focal hand dystonia. *Annals of Neurology*, 51(5), 593-598.

7.8 Appendices

A. Travelling wave paradigm

A somatosensory travelling wave paradigm (Figure 7.26) involves sequential stimulation of digits with no off period and has been shown to be highly reproducible (Sánchez-Panchuelo et al., 2014). A full explanation of the travelling wave paradigm is given in Figure 7.26. Digit stimulation is performed in both the forwards and reverse order, with the stimulation order reversed to remove the haemodynamic lag. Digits are stimulated in the order D1 to D5 for the forward-order scan, and D5 to D1 for the reverse-order scan. Figure 7.26A shows an example time course from a voxel responding to stimulation of the index finger (D2) in the forward-order scan and Figure 7.26B shows the corresponding time course of the index finger from the reverse-order scan. To remove haemodynamic lag, the reverse-order scan is time-reversed (Figure 7.26C). It can be seen from Figure 7.26D, where the time-reversed reverse-order scan is plotted with the forward-order scan, that the two scans are mirror images of each other. The phase of the response is computed relative to acquisition time, and the point of symmetry between the forward-order scan and time-reversed reverse-order scan corresponds to 2.5 TR. The time-reversed reverse-order scan is then shifted by 1 TR period so the point of symmetry is moved forward by half a TR to 3 TR which makes the phase values easier to interpret (Figure 7.26E). A cosine function is fit to the responses, and the phase of the best fitting cosine function to the forward-order scan and the TR-shifted, time-reversed, reverse-order scan is averaged, which results in a direct relationship between phase and the location of the stimulation. The use of the forward and reverse scans removes haemodynamic lag, and the TR-shift removes the effect of slice time acquisition.

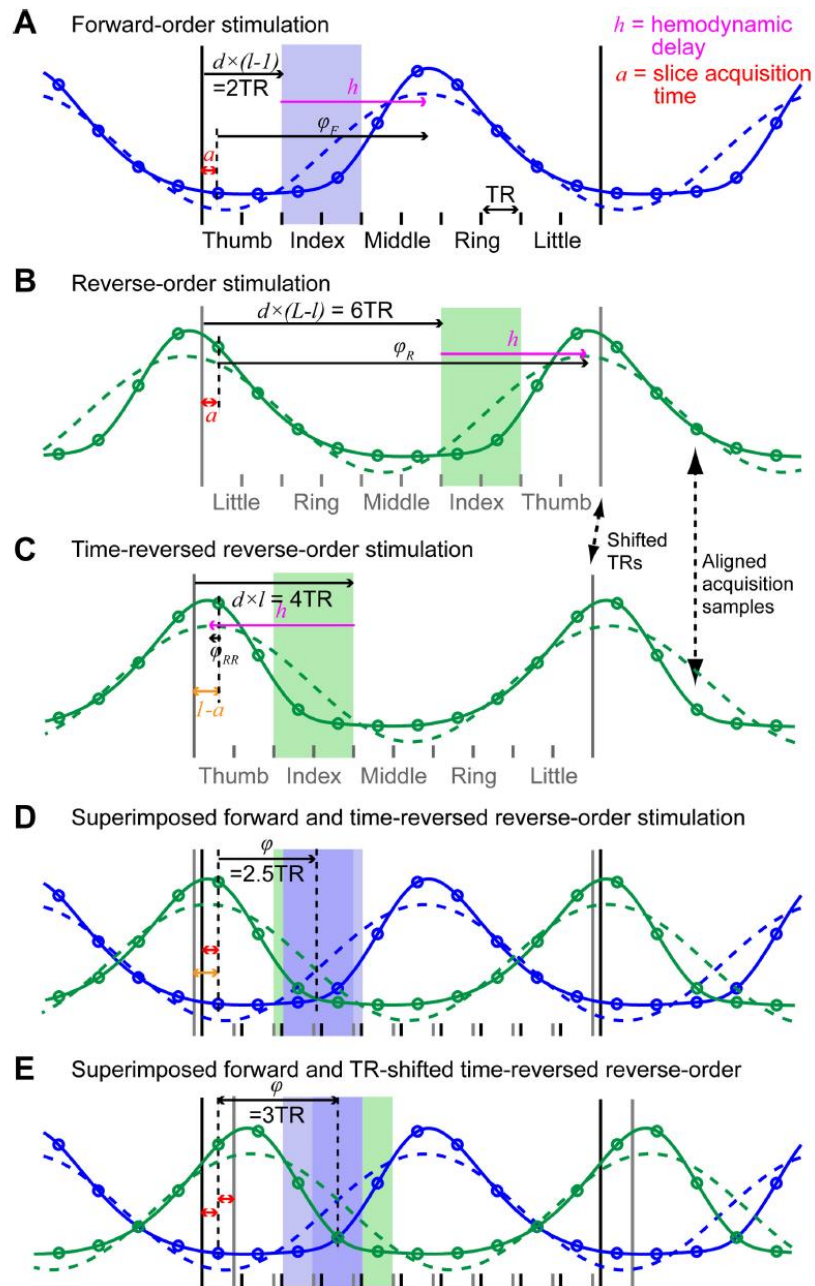


Figure 7.26. Schematic of the travelling wave paradigm. Solid line represents the time course of activation from a voxel. Dashed blue line represents the best-fitting cosine function. Circles represent each sampled time point, an unknown acquisition time, a , after the start of each TR period. (A) The response from an activated voxel from stimulation of the index finger, in the forward-order scan. (B) Reverse-order stimulation of the index finger. (C) The response from (B) time-reversed. (D) Forward-order stimulation, (A), superimposed with time-reversed reverse-order stimulation (C). (E) Forward-order stimulation, (A), superimposed with time-reversed reverse-order stimulation (C), shifted by 1 TR period to correct for slice timing acquisition. The forward-order and time-reversed, reverse-order runs are then averaged which cancels out the haemodynamic delay. This results in a direct relationship between phase and the location of the stimulation. Reproduced from (Besle et al., 2013).

B. Handedness questionnaire.

HANDEDNESS QUESTIONNAIRE

NAME

AGE

SEX

Were you one of twins, triplets at birth or were you single born?.....

*Please indicate which hand you habitually use for each of the following activities by writing **R** (for right), **L** (for left), **E** (for either).

Which hand do you use:

1. To write a letter legibly?
2. To throw a ball to hit a target?
3. To hold a racket in tennis, squash or badminton?
4. To hold a match whilst striking it?
5. To cut with scissors?
6. To guide a thread through the eye of a needle (or guide needle on to thread)?
.....
7. At the top of a broom while sweeping?
8. At the top of a shovel when moving sand?
9. To deal playing cards?
10. To hammer a nail into wood?
11. To hold a toothbrush while cleaning your teeth?
12. To unscrew the lid of a jar?

If you use the **RIGHT HAND FOR ALL OF THESE ACTIONS**, are there any one-handed actions for which you use the **LEFT HAND**? Please record them here:

.....

If you use the **LEFT HAND FOR ALL OF THESE ACTIONS**, are there any one-handed actions for which you use the **RIGHT HAND**? Please record them here:

.....

Mapping Touch, Handedness questionnaire, Final Version 1.0, 25/08/2017

1

C. Dice coefficients

Individual subject results of Dice coefficient for somatosensory task (dominant/affected hand) (Figure 7.27) somatosensory task (non-dominant/unaffected hand) (Figure 7.28) and the motor task (Figure 7.29).

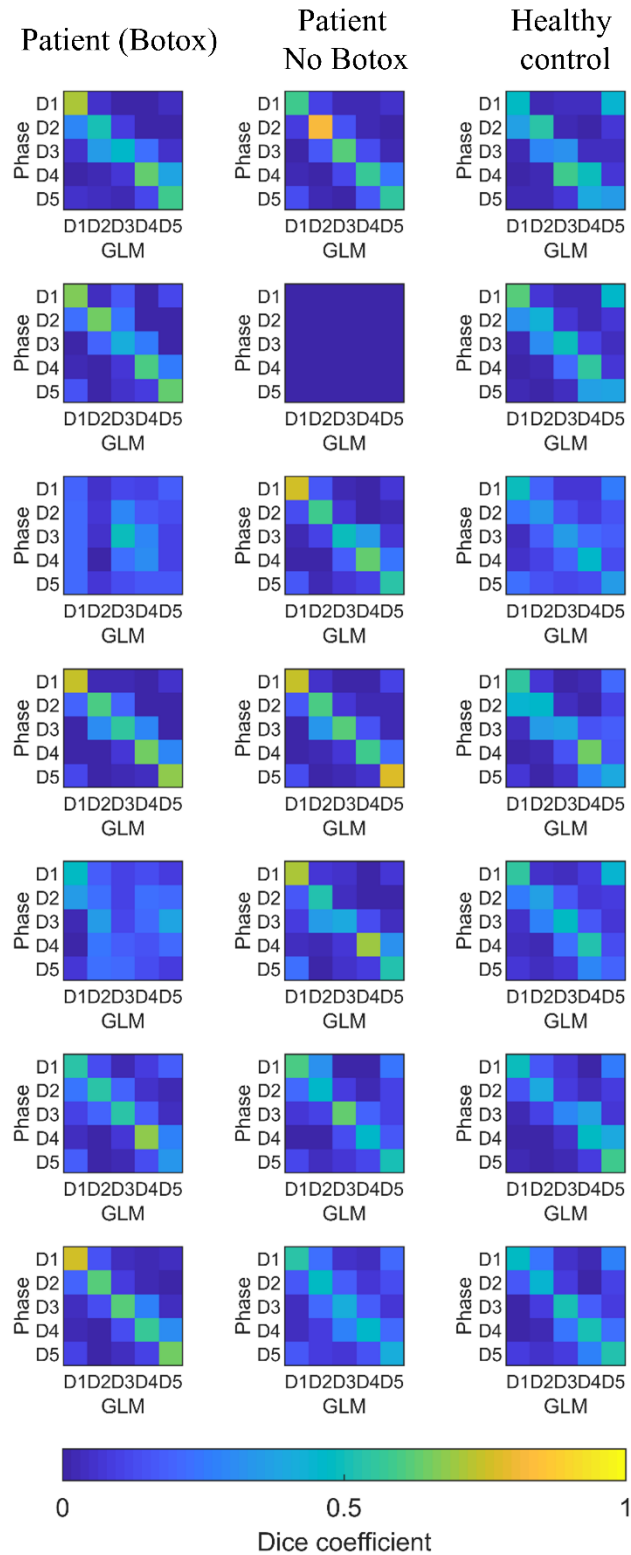


Figure 7.27. Dice coefficient between phase maps and winner takes all map from GLM analysis maps for somatosensory task on dominant/affected hand. Blue indicates low similarity and yellow indicates high similarity.

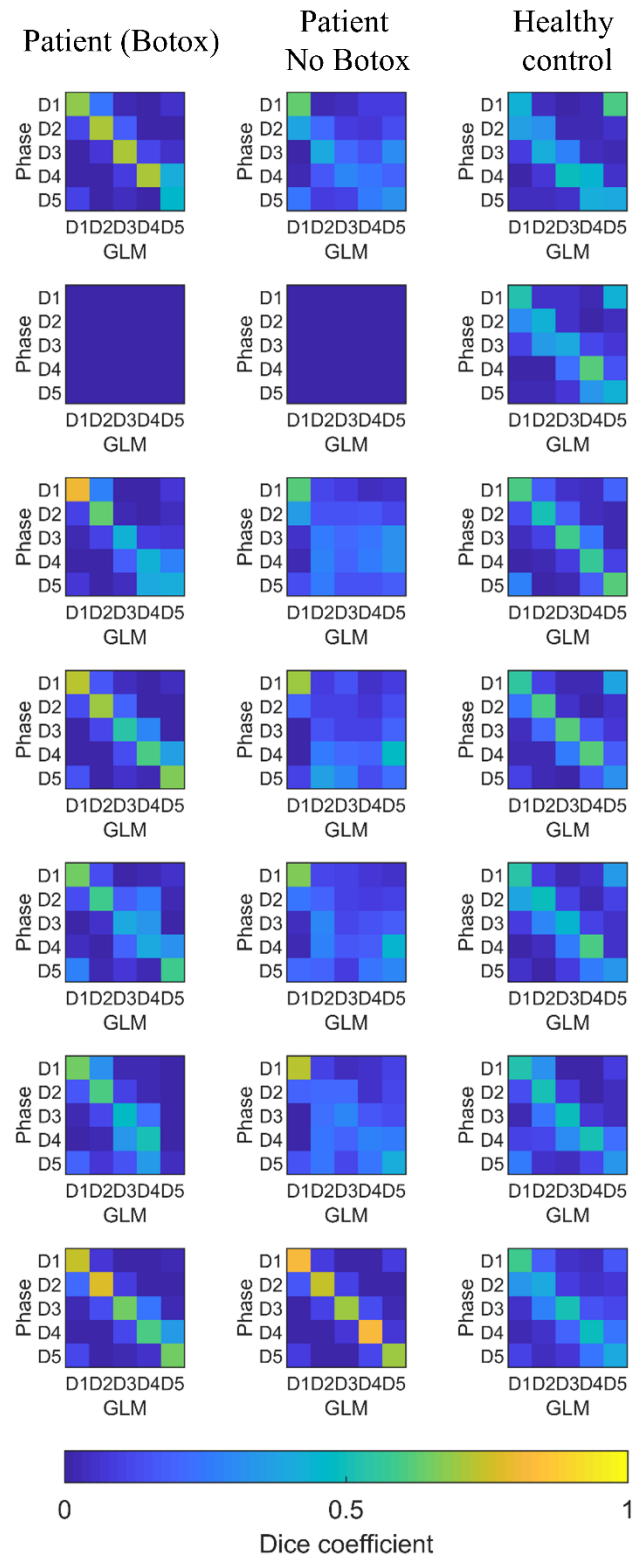


Figure 7.28. Dice coefficient between phase maps and winner takes all map from GLM analysis for somatosensory task on non-dominant/unaffected hand. Blue indicates low similarity and yellow indicates high similarity.

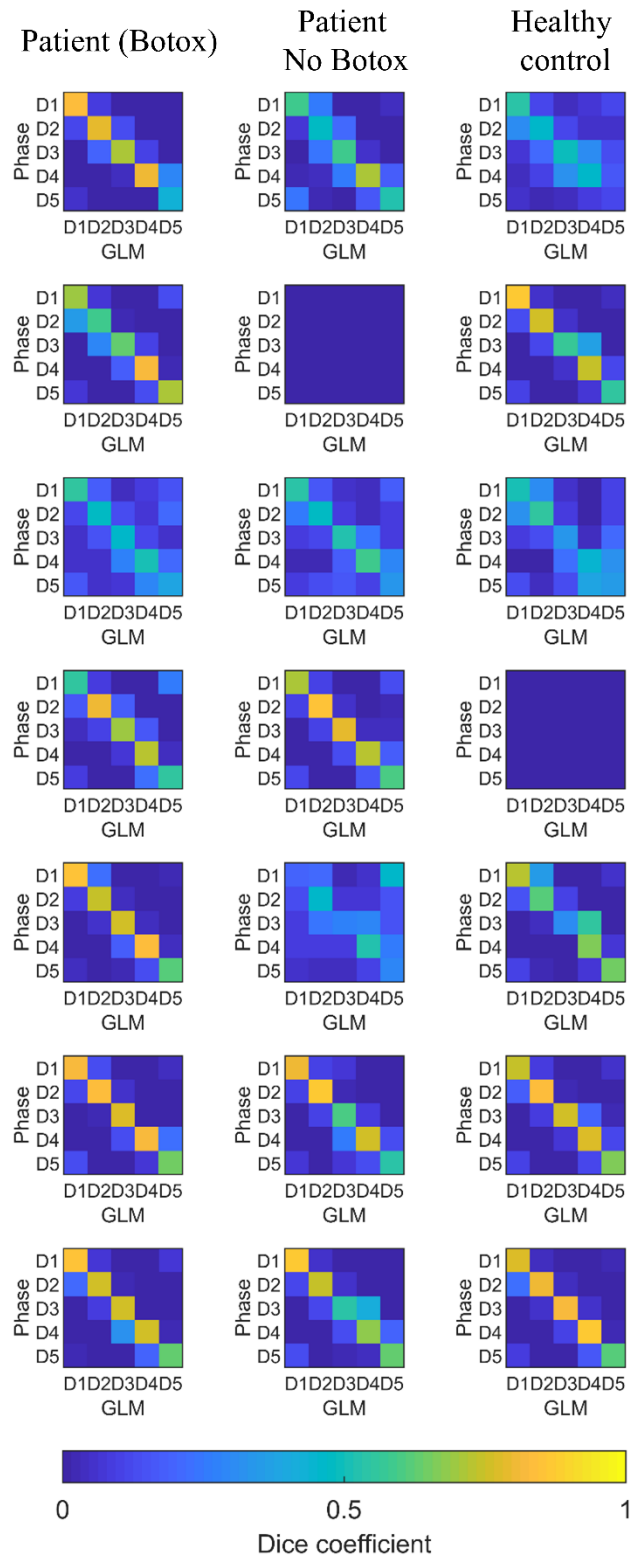


Figure 7.29. Dice coefficient between phase maps and winner takes all map from GLM analysis for somatosensory task on non-dominant/unaffected hand. Blue indicates low similarity and yellow indicates high similarity.

CHAPTER 8

8 Conclusion

8.1 Summary

The research presented in this thesis contributes to a growing body of work that aims to understand the characteristics and functional role of brain responses measured by MEG and fMRI. Together, this work highlights the potential and strengths of each of the imaging modalities for furthering our understanding of human brain function.

Specifically, Chapter 4 has shown that MEG post-stimulus responses are modulated by task duration. Importantly, the PMBR was shown to last up to 9 s in duration. This is significant as this length of time is longer than the majority of electrophysiology studies leave between trials. An implication of this is the possibility that differences in measured PMBR could, instead, be a result of differences in baseline period used, or, that differences between groups may be obscured if the PMBR does not fully return to baseline. Overall, this work strengthens the idea that the PMBR is of functional relevance as the PMBR was shown to systematically vary with task duration. These results will be of great importance to the rapidly expanding field of measuring PMBR changes in clinical research, where the PMBR has been shown to be altered in people with schizophrenia (Robson et al., 2016), multiple sclerosis (Barratt et al., 2017) and motor neurone disease (Proudfoot et al., 2017), to name but a few. In future, the task presented in this thesis could be applied to a clinical cohort to identify any changes in PMBR in health and disease.

Following the results of Chapter 4, further research was performed to investigate the functional role of the PMBR. This was done by exploring the functional networks present during a task. Chapter 5 used novel methods to show that functional networks form and dissolve on rapid timescales. In particular, this study showed that networks break down during the movement period, and are re-established during the post-movement period. These findings suggests the role of the PMBR is not solely related to inhibition, as previous studies have suggested (Pfurtscheller et al., 1996), but instead that the PMBR fulfils a role of re-establishing connectivity across the functional networks of the brain after a movement task. The second major finding, revealed with

hidden Markov model analysis, was that the PMBR can be described by increased frequency of transient beta events, typically lasting ~100 ms, in agreement with other studies (Little et al., 2018; Sherman et al., 2016). The idea that the PMBR consists of transient bursts and that changes in bursting activity relates to different stimulus durations provides new evidence that the PMBR has a distinct origin and functional role which still warrants further investigation.

In Chapter 6, the relationship between MEG and fMRI was investigated by applying the same paradigm as Chapter 4 and 5 to fMRI. fMRI measures of blood volume and blood oxygenation were explored, to better understand the origin and characteristics of the post-stimulus undershoot. The results of Chapter 6 showed that the BOLD post-stimulus undershoot is modulated by task duration, but not in the same way as the MEG response: increasing the grip duration increases the amplitude of the BOLD post-stimulus undershoot. This possibly suggests the post-stimulus undershoot is not entirely driven by neuronal activity. Measures of blood volume (CBV) showed a decrease in total blood volume in the post-stimulus period, with no change in arterial blood volume (aCBV). The decrease in total CBV, but not aCBV, suggests a reduction in venous CBV drives the VASO undershoot, which is the opposite of the balloon model (Buxton et al., 1998). However, a decrease in vCBV alone could not cause the BOLD post-stimulus undershoot; an undershoot would require a post-stimulus increase in CMRO₂ or reduction in CBF. Whilst both measures of CMRO₂ and CBF were attempted in this study, neither could be directly measured and therefore further work is needed to develop this study. However, the work presented provides strong evidence that the Balloon model is not the complete explanation for the BOLD response and further testing is needed to reveal the origins of the BOLD post-stimulus undershoot.

Finally, Chapter 7 highlights the potential use and challenges of BOLD fMRI in a clinical setting. Development of analysis methods showed that it was possible to use GLM analysis on a travelling wave paradigm, and that this can be used to measure overlap between cortical digit representations. However, even with optimised analysis strategies, the results of this study showed no significant differences between somatosensory representations of digits in patients with focal hand dystonia (FHD) compared to healthy controls. This is in contrast to what was hypothesised and what has been seen in previous studies (Bara-Jimenez et al., 1998; Butterworth et al., 2003). It is possible that this discrepancy is due to a small sample size, the effectiveness of

Botox treatment or additional noise at 7 T. Despite these limitations, it could be hypothesised that FHD does not alter sensory digit representation. This is a similar finding to a recent study of pain syndrome (Mancini et al., 2019). This new outcome may help improve the understanding of FHD.

8.2 The Future

The functional role of the PMBR is still unclear. The work in this thesis has laid the groundwork for future research into the PMBR, but more research is needed to understand its precise mechanism, especially if it is to be used as an indicator of brain health. In particular, there is a need to characterise how different movement types modulate the PMBR, whilst making sure to carefully control task parameters. Current MEG research is limited to experiments which are largely unnatural – as the experiments must be performed without moving, either seated or lying down, usually pressing a button. A new generation of MEG technology, OPM-MEG (Boto et al., 2018), enables MEG to be performed whilst moving, and with the possibility of in a virtual reality environment (Roberts et al., 2019), as has previously been done with EEG (Tromp et al., 2018), which could enable more realistic experiments to be performed, helping to understand the PMBR further and perhaps its relevance to task performance.

Similarly, the mechanisms behind the BOLD signal need to be fully understood before fMRI can be used widely in as a clinical tool. Considerably more work is required to determine what drives the post-stimulus undershoot. Future work could explore measuring cerebral blood flow (CBF) as well as CBV, which should be possible with the sequence developed in this thesis and an optimally performing ultra-high field MRI scanner. As well as CBF, future research should investigate the time course of venous CBV. This would help confirm the observed change in total CBV in this research. However, combining all these measures would pose a significant technological challenge. Taking the results of Chapter 5 and Chapter 6 together, a natural progression of this work would be to conduct an EEG-fMRI study, where transient beta events are modelled on a trial-by-trial basis and are input as regressors into the GLM, to better model the beta responses. However, MRI will cause artefacts on the EEG data, which might make beta bursts difficult to reliably detect. EEG can also introduce image artefacts into the MR data, which may reduce MR image quality and impact the ability

to measure CBF and CBV, though it can be done. Given the current evidence that post-stimulus responses are altered in neurological conditions and have been proposed as a biomarker of disease state, work needs to be carried out to gain a full understanding of the networks involved in the generation of post-stimulus responses and the functional relevance of this response in task performance, through a combination of electrophysiological and haemodynamic measures.

Further studies need to be carried out in order to validate the work of Chapter 7. If it is the case that FHD does not alter cortical representation of digits, more research will need to be conducted to understand FHD. Analysis of the other fMRI scans (such as the 5-minute resting state scan, an event-related paradigm and structural scans) and MEG data collected during this project will also help elucidate these results. A larger study with more patients could provide more evidence.

An interesting result of Chapter 7 was that the response to the motor task of a finger movement gives a large response in somatosensory cortex and little in the motor cortex, in agreement with other fMRI data using a similar motor task (Kolasinski et al., 2016). This shows the interconnectedness of motor and somatosensory cortex but raises an important point surrounding the relationship of responses measured with MEG and fMRI. MEG studies often show that the MRBD is localised to the somatosensory cortex whilst the PMBR is localised to the motor cortex in similar finger movement tasks (Jurkiewicz et al., 2006), which was what was observed in Chapter 4 for the grip-force task. It could be that this difference is highlighting that MEG and fMRI are not measuring the same effects. Or, it could be that the primary response to a simple finger movement in both modalities is in the somatosensory cortex, and the post-stimulus response is in the motor cortex. This is not what was found in Chapter 6 when the post-stimulus fMRI response was interrogated. However, further investigation with a finger movement task which is less motor-demanding than the grip-force task used in the early experimental chapters of this work is warranted. The post-stimulus response cannot be investigated from the fMRI data collected in Chapter 7 due to the travelling wave paradigm used. The relationship between fMRI and MEG evidently needs investigating further as where the PMBR is generated from and its relationship with the post-stimulus BOLD response will help understand its function and possible role in FHD.

Perhaps it is the case that our understanding of brain function using fMRI is still limited by its spatial and temporal resolution. In future, with more ultra-high field scanners (>7 T), which give higher signal, may be able to image the brain faster and with higher resolution that is currently possible. This might help us better understand the relationship between fMRI and neuronal activity.

8.3 References

- Bara-Jimenez, W., Catalan, M. J., Hallett, M., & Gerloff, C. (1998). Abnormal somatosensory homunculus in dystonia of the hand. *Annals of Neurology*, *44*(5), 828-831.
- Barratt, E. L., Tewarie, P. K., Clarke, M. A., Hall, E. L., Gowland, P. A., Morris, P. G., Francis, S. T., Evangelou, N., & Brookes, M. J. (2017). Abnormal Task Driven Neural Oscillations in Multiple Sclerosis: A Visuomotor MEG Study. *Human Brain Mapping*, *38*(5), 2441-2453.
- Boto, E., Holmes, N., Leggett, J., Roberts, G., Shah, V., Meyer, S. S., Muñoz, L. D., Mullinger, K. J., Tierney, T. M., & Bestmann, S. (2018). Moving magnetoencephalography towards real-world applications with a wearable system. *nature*, *555*(7698), 657-661.
- Butterworth, S., Francis, S., Kelly, E., McGlone, F., Bowtell, R., & Sawle, G. V. (2003). Abnormal cortical sensory activation in dystonia: An fMRI study. *Movement Disorders*, *18*(6), 673-682.
- Buxton, R. B., Wong, E. C., & Frank, L. R. (1998). Dynamics of blood flow and oxygenation changes during brain activation: The balloon model. *Magnetic Resonance in Medicine*, *39*(6), 855-864.
- Jurkiewicz, M. T., Gaetz, W. C., Bostan, A. C., & Cheyne, D. (2006). Post-movement beta rebound is generated in motor cortex: evidence from neuromagnetic recordings. *Neuroimage*, *32*(3), 1281-1289.
- Kolasinski, J., Makin, T. R., Jbabdi, S., Clare, S., Stagg, C. J., & Johansen-Berg, H. (2016). Investigating the Stability of Fine-Grain Digit Somatotopy in Individual Human Participants. *The Journal of Neuroscience*, *36*(4), 1113.
- Little, S., Bonaiuto, J., Barnes, G., & Bestmann, S. (2018). Motor cortical beta transients delay movement initiation and track errors. *bioRxiv*, 384370.
- Mancini, F., Wang, A. P., Schira, M. M., Isherwood, Z. J., McAuley, J. H., Iannetti, G. D., Sereno, M. I., Moseley, G. L., & Rae, C. D. (2019). Fine-grained mapping of cortical somatotopies in chronic complex regional pain syndrome. *Journal of Neuroscience*, *39*(46), 9185-9196.
- Pfurtscheller, G., Stancák, A., & Neuper, C. (1996). Post-movement beta synchronization. A correlate of an idling motor area? *Electroencephalography and Clinical Neurophysiology*, *98*(4), 281-293.
- Proudfoot, M., Rohenkohl, G., Quinn, A., Colclough, G. L., Wu, J., Talbot, K., Woolrich, M. W., Benatar, M., Nobre, A. C., & Turner, M. R. (2017). Altered Cortical Beta-Band Oscillations Reflect Motor System Degeneration in Amyotrophic Lateral Sclerosis. *Human Brain Mapping*, *38*, 237-254.
- Roberts, G., Holmes, N., Alexander, N., Boto, E., Leggett, J., Hill, R. M., Shah, V., Rea, M., Vaughan, R., & Maguire, E. A. (2019). Towards OPM-MEG in a virtual reality environment. *Neuroimage*, *199*, 408-417.
- Robson, S. E., Brookes, M. J., Hall, E. L., Palaniyappan, L., Kumar, J., Skelton, M., Christodoulou, N. G., Qureshi, A., Jan, F., Katshu, M. Z., Liddle, E. B., Liddle, P. F., & Morris, P. G. (2016). Abnormal visuomotor processing in schizophrenia. *Neuroimage Clin*, *12*, 869-878.
- Sherman, M. A., Lee, S., Law, R., Haegens, S., Thorn, C. A., Hämäläinen, M. S., Moore, C. I., & Jones, S. R. (2016). Neural mechanisms of transient neocortical beta rhythms: Converging evidence from humans, computational modeling, monkeys, and mice. *Proceedings of the National Academy of Sciences*, *113*(33), E4885.

Tromp, J., Peeters, D., Meyer, A. S., & Hagoort, P. (2018). The combined use of virtual reality and EEG to study language processing in naturalistic environments. *Behavior Research Methods*, *50*(2), 862-869.